Peptide Based Biomaterials via Thiol-ene Chemistry

Burcu Colak

2012-2016

Submitted in partial fulfilment of the requirements of the Degree of Doctor of Philosophy

Statement of originality for inclusion in research degree theses

I, Burcu Colak, confirm that the research included in this thesis is my own work or that where it has been carried out in collaboration with or supported by others, that is duly acknowledged below and my contribution indicated. Previously published material is also acknowledged below.

I attest that I have exercised reasonable care to ensure that the work is original, and does not to the best of my knowledge break any UK law, infringe any third party's copyright or other Intellectual Property Right, or contain any confidential material.

I accept that the college has the right to use plagiarism detection software to check the electronic version of this the thesis.

I confirm that this thesis has not been previously submitted for the award of a degree by this or any other university.

The copyright of this thesis rests with the author and no quotation from it or information derived from it may be published without the prior written consent of the author.

Signature Date 20.12.2016

Details of collaborations and publications:

Stefania Di Cio performed the AFM measurements. All analysis of the data was performed by me.

Part of Chapter 2 has been published.

Acknowledgment

This work could not be possible without funding from Queen Mary University of London and the Institute of Bioengineering and the help of my most patient, kind and supportive supervisor Julien E. Gautrot. I am very grateful that I have had the opportunity to work with him and I have very much enjoyed being part of his team.

My time in the laboratory would not have been enjoyable without the members of the Gautrot group; I thank them for being so friendly and inspirational throughout the years.

I would like to thank Julio C. S. Da Silvia and Thereza A. Soares for their collaboration on the submitted paper on thiol-ene chemistry, Helena Azevedo and Daniela S. Ferreira for their guidance with the HPLC studies, Remzi C. Becer for his assistance on the synthesis of poly(oxazoline)s and Stefania Di Cio for providing the AFM scans. I would also like to express my appreciation to Julien E. Gautrot, Madeline Ramstedt and Thereza for funding the opportunities to visit the workshops in Cambridge, Sweden and Brazil. Finally, I would like to express my gratitude to my parents, sister and partner for their love and emotional support throughout this project and also Onur Tasci, Sevda Dogan, Aziz Boybeyi and Berivan Ucak Dogan for proof reading my thesis

Abstract

Thiol-ene radical coupling is increasingly used for the biofunctionalisation of biomaterials and the formation of 3D hydrogels enabling cell encapsulation. Indeed, thiol-ene chemistry presents interesting features that are particularly attractive for platforms requiring specific reactions of peptides or proteins, in particular *in situ*, during cell culture or encapsulation: thiol-ene coupling occurs specifically between a thiol (from cysteine residues for example) and a non-activated alkene (unlike Michael addition); it is relatively tolerant to the presence of oxygen; it can be triggered by light, to trigger dynamic systems or for patterning. Despite such interest, little is known about the factors impacting thiol-ene chemistry *in situ*, under biologically relevant conditions. Here we explore some of the molecular parameters controlling photo-initiated thiol-ene coupling chemistry with a series of alkenes and thiols, including peptides, in buffered conditions. ^{1}H NMR spectroscopy and HPLC were used to quantify the efficiency of couplings and the impact of the intensity of UV exposure, pH of the buffer, as well as the molecular structure and local microenvironment close to alkenes and thiols to be coupled. Our studies demonstrate that molecular design should be carefully selected in order to achieve high biofunctionalisation levels in biomaterials with peptides.

Thiol-ene coupling enables the biofunctionalisation of solid surfaces by the immobilisation of biofunctional thiols to achieve surfaces with biological properties. In this work, we synthesised pOEGMA brushes and studied the thiol-ene coupling system with a series of thiols including peptides RGD and REDV. The polymer brush systems were investigated as 2D culture materials and the adhesive properties of biofunctional surfaces were studied with HUVECs. Since, thiol-ene chemistry can be photo-initiated; thiols could be patterned on surfaces using photo masks, imaged using epifluorescent microscopy and AFM. Patterning bioactive peptides means cells can be patterned and confined to known locations to study the effect of changes in the microenvironment and the cell features.

Synthetic biomimetic hydrogels have received much attention in the last decade. Here, thiol-ene chemistry was used to crosslink alkene functional polymers and enzymatically degradable peptidic thiols. This enabled to generate a robust system for the production of hydrogels of various stiffnesses and from different polymeric backbones. The gelation and enzymatic degradation of the gels were studied *in situ* using photo-rheology. Poly(oxazoline) hydrogel systems were investigated as 3D cell encapsulation materials and provided good cell viability. The control over the gelation kinetics, stiffness, biofunctionality and degradation kinetics makes these hydrogel materials attractive for future investigations as 3D cell culture systems.

Contents

Acknowledgment ii

Abstract iii

Abbreviations vii

List of Figures, Tables and Schemes ix

Chapter 1 1

Design of peptide-based biomaterials 1

1.1 Thiol-ene click chemistry 2
1.2 Polymer brushes for biomedical applications 14
1.3 Synthetic hydrogels for cell culture and tissue engineering 27
1.4 Summary 55

Chapter 2 57

Thiol-ene chemistry 57

2.1 Thiol-ene methodology 57
2.2 Summary 94
2.3 Experimental section 95

Chapter 3 109

Design of thiol-ene based hydrogels for 3D cell culture 109

3.1 General methodology 109

3.3 Cell encapsulation in 3D systems 128
3.4 Summary 143
3.5 Experimental section 144
Chapter 4 151
Polymeric brushes as biomaterials 151
4.1 Brush synthesis and activation via DSC 153
4.2 Thiol-ene coupling to POEGMA brushes 156
4.3 Cell adhesion to peptide functionalised polymer brushes 162
4.4 Patterning peptides on brushes 167
4.5 Summary 175
4.6 Experimental section 176
Chapter 5 183
Conclusion and future directions 183
References 187
Appendix 1 197
Appendix 2 213
Appendix 3 215

Abbreviations

AFM	atom force microscopy
ATR-FTIR	attenuated total reflectance fourier transform infrared
ATRP	atom-transfer radical polymerisation
BMP-2	bone morphogenetic protein 2
CDI	carbonyldiimidazole
CROP	cationic ring opening polymerisation
DMAP	4-(dimethylamino) pyridine
DMF	dimethylformaldehyde
DSC	disuccinimidyl carbonate
DTT	dithiothreitol
ESI	electron spray ionisation
ECM	extracellular matrix
FBS	foetal bovine serum
FTIR	fourier transform infrared
GC	Gas chromatography
GPC	gel permeation chromatography
HEPES	(4-(2-hydroxyethyl)-1-piperazineethanesulfonic acid)
^{1}H NMR	hydrogen nuclear magnetic resonance
HPLC	high performance liquid chromatography
hMSCs	human mesechymal stem cells

HUVECs	human umbilical vein endothelial cells
IRG2959	2-hydroxy-4'-(2-hydroxyethoxy)-2-methylpropiophenone
NMP	nitroxide-mediated polymerisation
NPC	4-nitrophenyl chloroformate
pDMAEMA	poly(dimethylamino)ethyl methacrylate
PDMS	poly(dimethyl siloxane)
PEG	poly(ethylene glycol)
PEG methyl ether thiol	poly(ethylene glycol) methyl ether thiol
PEGDT	poly(ethylene glycol) dithiol
PEGNB	poly(ethylene glycol) norbornene
pEtOx	poly(2-ethyl-2-oxazoline)
$pEtOx_{80}$ $Bu{=}Ox_{20}$	poly(2-ethyl-2-oxazoline) (80%) co-poly(2-3'butenyl-2-oxazoline) (20%)
PFA	paraformaldehyde
pGMA	poly(glycidyl methacrylate)
pHEMA	poly(hydroxyethyl methacrylate)
PI	photoinitiator
$pPhOx_{80}$ $Dc{=}Ox_{20}$	poly(2-phenyl-2-oxazoline) (80%) co-poly(2-9'-decenyl-2-oxazoline) (20%)
pOEGMA	poly oligo (ethylene glycol) methyl ether methacrylate
pOEGMA-AA	allylamine functionalised poly oligo (ethylene glycol) methyl ether methacrylate
pOEGMA-DSC	disuccinimidyl carbonate functionalised poly oligo (ethylene glycol) methyl ether methacrylate
QCM	quartz crystal microbalance
RAFT	reversible addition-fragmentation chain transfer polymerisation
SPR	surface plasmon resonance
TGA	thermo gravimetric analysis
UV	ultra violet
XPS	x-ray photoelectron spectroscopy

List of Figures, Tables and Schemes

Figure 1.1 Annual number of papers reported on "thiol-ene" coupling since year 2000, obtained from the web of knowledge. 2

Figure 1.2 Representation of the thiol-ene coupling reaction including the propagation, chain transfer and chain growth steps[29]. 4

Figure 1.3 a) A reaction profile showing relative free energies of the listed alkenes with methyl mercaptan and b) the kinetic model for the thiol-ene coupling reaction[29]. 5

Figure 1.4 Schematic showing the a) "grafting to" and b) "grafting from" methods. 16

Figure 1.5 Representation of the "brush" and "mushroom" regime[102]. 17

Figure 1.6 Modes or adsorption on polymer brushes[102]. 17

Figure 1.7 The biofunctionalisation of brushes a) via the brush system and b) through coupling reagents. 20

Figure 1.8 A representation of micro-contact printing for the generation of brush patterned surfaces and the adsorption of ECM proteins[107]. 23

Figure 1.9 Primary human epidermal keratinocytes were seeded on POEGMA patterns generated on gold, incubated for a) 0, b) 1, c) 3 and d) 7 days. Scale bar 100 µm[107]. 24

Figure 1.10 a) Example of a cell cluster with 2D and 3D views, scale bar 20 µm. b) Micro-epidermis array, scale bar 100 µm. Cells are stained with involucrin, α6 and DAPI[131]. 25

Figure 1.11 Condensation images showing a) hydrophilic thiol on squares (300 mesh), b) hydrophilic squares (2000 mesh) and c) hydrophilic thiol on mesh (300)[17]. 26

Figure 1.12 Representation of cells patterned on islands and their migration after biofunctionalisation with RGD peptide using thiol-ene coupling[21]. 26

Figure 1.13 The cell microenvironment. The properties of hydrogels can be maniplutaed to try to mimic features of a natural microenvironment[136]. 27

Figure 1.14 Formation of a poly(oxazoline) hydrogel using UV initiated thiol-ene coupling[152]. 30

Figure 1.15 Formation of a PEG hydrogel using thiol-ene coupling and its hydrolytic degradation products[1467]. 31

Figure 1.16 Fabrication of step and chain polymerised hydrogels[158]. 33

Figure 1.17 An illustration representing the synthesis of cationic gels (FC- fumaryl chloride, DMA- dodecyl bis(2-hydroxyethyl) methlammonium chloride and MSA- mercaptosuccinic acid)[162]. 36

Figure 1.18 Fabrication of hydrogel microarray using thiol-ene coupling[167]. 37

Figure 1.19 a) An illustration of photo-crosslinking and photodegradation of thiol-ene gels, b) the chemical structure of the photodegradable peptide and c) schematic of UV-mediated peptide degradation[171]. 38

Figure 1.20 Hydrogel mass loss as a function of a) collagenase concentration with 3 wt% gel and b) different concentrations of hydrogel with 1 U/mL collagenase[177]. 41

Figure 1.21 Fabrication of PEG nanofibre composites representing control ober the bioactivity and mechanial properties of the hydrogel[181]. 43

Figure 1.22 Mesechymal stem cells on soft (3kPa), soft-to-stiff (3-30kPa) and stiff (30kPa) substrates on day 1 and day 2. Red (phalliodin), blue (DAPI) and scale bar 100μm[5]. 44

Figure 1.23 The general method for the generation of photopatterned hydrogels[20]. 44

Figure 1.24 Fluroescent images of sequenctially patterned hydrogels: a) triangles with 5(6)-carboxyfluorescein, b) lines with rhodamine b and c) circles with 7-methoxycoumarine-2-acetic acid. d) Represents the merged channels and e) demostrates the depth of the patterns through the gel. Scale bars 100 μm[20]. 45

Figure 1.25 Fibroblasts attached on RGD patterned areas of hydrogel. Green (RGD-Alexa Fluor 488), Red (phalliodin), blue (DAPI) and scale bar is 200μm[189]. 46

Figure 1.26 Fibroblast morphology in 3D encapsulated gels of variable stiffness (represented by dry mass) over of 3 weeks. Images with and without enzyme sensitive crosslinker represented at week 3. PEG gels compared to collagen gel over 2 weeks. Cells stained with phalliodin and DAPI[143]. 51

Figure 1.27 hMSCs encapsulated in uniform and photopatterned hyaluronic acid hydrogels after 14 days. Cells stained with calcein, scale 100µm[198]. 53

Figure 2.1 Series of thiols (S1-6 and peptides) and alkenes (A1-A11). 59

Figure 2.2 ^{1}*H NMR spectra of the product peaks (a, b) and the alkene peaks (c) of the A1-S1 reaction at different UV exposure times (5-30 s).* 61

Figure 2.3 Impact of the time of UV exposure on the reaction conversion for A1 with a series of thiols. Reactions were performed with 2 mol% PI and 17 mW/cm^{2} *UVintensity.* 61

Figure 2.4 ^{1}*H NMR spectroscopy of the thiol-ene products of the reaction of thiols S1-6 with A1 in deuterated PBS with 2 mol% PI and 60s UV. a) S1, b) S2, c) S3, d) S4, e) S5 and f) S6.* 62

Figure 2.5 The impact of the buffer pH on the reaction conversion (60 s UV exposure) for A1 with thiols S1 and S4-S6. 64

Figure 2.6 ^{1}*H NMR spectroscopy of a) N-(2-chloroethyl)-4-pentenamide, b) 2-butenyl-2-oxazoline, c) 2-ethyl-2-oxazoline, d) pEtOx and e) pEtOxBu=Ox/ pOx(A10).* 67

Figure 2.7 FTIR spectra of a) 2-butenyl-2-oxazoline, b) 2-ethyl-2-oxazoline, c) pEtOx and d) pEtOxBu=Ox/ pOx (A10). 68

Figure 2.8 ^{1}*H NMR spectra of pMA*$^{-}$ *(A11).* 69

Figure 2.9 FTIR spectra of poly(methyl vinyl ether alt-maleic anhydride) and pMA^{-} *(A11).* 69

Figure 2.10 ^{1}*H NMR spectra of a) pDMAEMA, b) pDMAEMA propene (A7), c) pDMAEMA butene (A8), and d) pDMAEMA pentene (A9).* 71

Figure 2.11 FTIR spectra of a) pDMAEMA, b) pDMAEMA propene (A7), c) pDMAEMA butene (A8), and d) pDMAEMA pentene (A9) with highlighted stretching vibrations. 72

Figure 2.12 Normalised GPC traces for pOx (blue, M_n *6.3 kg/mol) and pDMAEMA (red,* M_n *67.9 kg/mol).* 73

Figure 2.13 Reaction conversion 60 s UV, photoinitiator 1 mM, A2-A6 or 300 s UV 2.5 mM, A7-A9) of S1 and the series of alkenes (A2-A9). See Fig. A1.1 for corresponding statistical analysis. 78

Figure 2.14 ^{1}*H NMR spectra of a) N,N-diethylpent-4-enamide (A2) b) N-allylacetamide (A3) c) N,N,N-triehtylprop-2-en-1-aminium (A4) d) N,N,N-triehtylbut-3-en-1-aminium (A5) and e) N,N,N-triehtylpent-4-en-1-aminium (A6).* 79

Figure 2.15 Impact of the addition of amino acids or electrolytes to the thiol-ene system, blue 10 mol% and red 100 mol%. See Fig. A1.4 for corresponding statistical analysis. 81

Figure 2.16 a) Reaction conversions quantified by ^{1}H NMR spectroscopy for 4 peptide sequences (300 s UV exposure, 2.5 mM initiator, 45 mM peptide). b) Reaction conversions quantified by HPLC for 7 peptide sequences (300 s UV exposure, 2.5 mM initiator, 45 mM peptide). c) Sequence of peptides with cysteines in green, glycines and serines in blue, charged amino acids (arginine and aspartic acid) in red and aromatic (phenylalanine and tyrosine) amino acids in purple. See Fig. A1.2-1.3 for corresponding statistical analysis. 85

Figure 2.17 Reaction conversion and remaining reagents measured for the coupling of GCGSY and A1 at different concentrations (300 s UV exposure, 2.5 mM initiator; dotted lines, product formed; full lines, unreacted peptide). 86

Figure 2.18 Reaction conversion and remaining reagents measured for the coupling of CRGSF/CGRSF and A1 at different concentrations (300 s UV exposure, 2.5 mM initiator). CRGSF (blue dotted lines, product formed; full lines, unreacted peptide) and CGRSF (red dotted lines, product formed; full lines, unreacted peptide). Lines are only intended to guide the eye. 87

Figure 2.19 Percentage of unreacted peptide measured for the coupling of GCGSF (blue), CGGSF (red), CDGSF (green) and CGDSF (purple) and pentenoic acid A1 at different concentrations (300 s UV exposure, 2.5 mM initiator). Lines are only intended to guide the eye. 88

Figure 2.20 Percentage product formed peptide measured for the coupling of GCGSF (blue), CGGSF (red), CDGSF (green) and CGDSF (purple) and pentenoic acid A1 at different concentrations (300 s UV exposure, 2.5 mM initiator). Lines are only intended to guide the eye. 89

Figure 2.21 ^{1}H NMR spectroscopy of the thiol-ene products of pentenoic acid (A1) with a) GCGSY, b) GCGSF, c) CDGSF and d) CRGSF. 90

Figure 2.22 Mass spec of the thiol-ene products of pentenoic acid (A1) and a) GCGSF (570 m/z)), b) CGGSF (570 m/z)), c) CRGSF (670 m/z) and d) CGDSF (629 m/z). 91

Figure 2.23 The impact of photoinitiator and peptide concentration (GCGSY) on the reagent conversion and product formation. Peptide concentrations were 4.5 mM (blue dotted lines, product formed; blue full lines, unreacted peptide) and 9 mM (red dotted lines, product formed; red full lines, unreacted peptide). 92

Figure 2.24 The impact of buffer type and degassing on peptide (GCGSY) conversion and product formed. PBS (blue dotted lines, product formed; full lines, unreacted peptide),

degassed PBS (red dotted lines, product formed; red full lines, unreacted peptide) and HEPES (green dotted lines, product formed; green full lines, unreacted peptide). 93

Figure 2.25 ^{1}H NMR spectroscopy of a) N,N-diethylpent-4-enamide (A2) b) N-allylacetamide (A3) c) N,N,N-triehtylprop-2-en-1-aminium (A4) d) N,N,N-triehtylbut-3-en-1-aminium (A5) and e) N,N,N-triehtylpent-4-en-1-aminium (A6). 102

Figure 2.26 FTIR spectra a) N,N-diethylpent-4-enamide (A2) b) N-allylacetamide (A3) c) N,N,N-triehtylprop-2-en-1-aminium (A4) d) N,N,N-triehtylbut-3-en-1-aminium (A5) and e) N,N,N-triehtylpent-4-en-1-aminium (A6) with highlighted stretching vibrations. 103

Figure 3.1 Demostration of a gelled hydrogel a) in a vial and b) free standing. Scale, 0.5 cm. 110

Figure 3.2 Schematic representation of hydrogel formation: a) alkene (green) functional polymeric backbone (blue) b) crosslinked using dithiols (red) and biofunctionalised using monothiols (turquiose), c) gel is shown with cell interactions to bioactive monothiols, d) cell culture in 3D hydrogel system. 111

Figure 3.3 FTIR spectra of the polymers (dotted lines) and corresponding gels (dehydrated) with PEGDT (full lines) a) pMA^{-} c) pOx and e) pDMAEMA^{+}. 113

Figure 3.4 TGA traces for the gels from PEGDT and a) pMA^{-}, b) pOx and c) pDMAEMA^{+} gels before (blue) and after submersion in PBS (red) and water (green), dotted lines represent the derivatives of the original TGA trace. Gelation was performed with thiol:ene ratio 0.5:1, 0.5 mol% PI and 120 s UV exposure at 17 mW/cm^{2} UV intensity. 115

Figure 3.5 The percentage of water present in the different backbone gels (S5, 225 mM) with PEGDT before swelling (blue), swollen in PBS (red), swollen in deionised water (green). Gelation was performed with thiol:ene ratio 0.5:1, 0.5 mol% PI and 120 s UV exposure at 17 mW/cm^{2} UV intensity. 116

Figure 3.6 The percentage swelling of the gels with in PBS (blue) and deionised water (red). Gelation was performed with thiol:ene ratio 0.5:1 and 120 s UV exposure at 17 mW/cm^{2} UV intensity. 117

Figure 3.7 The time sweep graphs for the pOx gel of different stiffnesses S3 (blue 135 mM), S4 (red, 180 mM) and S5 (green, 225 mM) with thiol:ene ratio 0.5:1, 0.5 mol% PI, 120 s UV exposure at 17 mW/cm^{2} UV intensity and 0.5 mol% PI. Filled markers correspond to G' (storage modulus) and empty markers are G'' (loss modulus). 119

Figure 3.8 Storage modulus for different stiffness gels (S3 blue, S4 red and S5 green) from different polymer backbones, 50% crosslinked with PEGDT using 120 s UV exposure and 0.5 mol% PI. 120

Figure 3.9 Frequency sweep (G') for series of gels pMA^- (blue), pOx (red) and $pDMAEMA^+$ (green), at different stiffness S3 (full lines), S4 (dotted lines), and S5 (broken lines). Gels were generated using 120 s UV exposure (17 mW/cm^2) and 0.5 mol% PI. 122

Figure 3.10 Amplitude sweep for series of gels pMA- (blue), pOx (red) and pDMAEMA+ (green), at different stiffness S3 (full lines), S4 (dotted lines), and S5 (broken lines). Gels were generated using 120 s UV exposure (17 mW/cm2) and 0.5 mol% PI. 122

Figure 3.11 A representation of the setup for a) photorheology for gelation and b) degradation, black lines represent the methacrylate functionalised glass coverslips. 123

Figure 3.12 Time sweep (10 h) of gels (S3, pOx) incubated in PBS or collagenase enzyme (0.25mg/mL) to confirm the degradation of the VPM gel by the selected enzyme. Gel compositions S3 VPM:PEGDT: 100:0 with enzyme (blue), 0:100 with enzyme (red) and 100:0 without enzyme (green). Results shown are of a single repeat. 125

Figure 3.13 Time sweep of different degradable gels incubated in collagenase enzyme (0.25mg/mL) showing varying rates of degradation over 24 h. Gel compositions S3 VPM:PEGDT incubated in enzyme: 100:0 (blue), 75:25 (red), 50:50 (green) and 25:75 (purple). Results shown are of a single repeat. 127

Figure 3.14 Cell viability of HUVECs encapsulated in non-degradable PEGDT crosslinked hydrogels of increasing stiffness (S3-S5), live dead assay was performed after 24h. Gels were generated with thiol:ene 0.5:1 ratio, 10 mol% RGD, 0.5 mol% PI, 120 s UV exposure and 50k cells/well. 130

Figure 3.15 Live/Dead assay of HUVECs encapsulated in nondegradable PEGDT crosslinked hydrogels of increasing stiffness. From left to right: control, S3, S4 and S5, after 24h, scale 100 µm, 50k cells/well. Live cells were stained green and dead cells red. Gels were generated with thiol:ene 0.5:1 ratio, 10 mol% RGD, 0.5 mol% PI and 120 s UV exposure. See Fig. A2.1 for corresponding statistical analysis. 130

Figure 3.16 Cell viability of dermal fibroblasts encapsulated in degradable hydrogels with various ratios of degradable:nondegradable crosslinker in S3 gels and also ratio 75:25 with S4 and S5 gels. Live dead assay was performed after 24h. Gels were generated with thiol:ene

0.5:1 ratio, 10 mol% RGD, 0.5 mol% PI and 120 s UV exposure. See Fig. A2.2 for corresponding statistical analysis. 133

Figure 3.17 Live/Dead assay of fibroblasts encapsulated in hydrogels of varying degradation and increasing stiffness. From left to right to bottom: control, S3 VPM:PEGDT 100:0, S3 25:75, S3 50:50, S3 75:25, S4 75:25, S5 75:25, after 24h, scale 100 µm, 100k cells/well. Live cells were stained green and dead cells red. Gels were generated with thiol:ene 0.5:1 ratio, 10 mol% RGD, 0.5 mol% PI and 120 s UV exposure. 133

Figure 3.18 Dermal fibroblasts at day 1 in S3 pOx gels with 10% RGD, 0.5 mol% PI, 120 s UV and VPM:PEGDT a) 0:100, b) 25:75, c) 50:50, d) 75:25 spread cells, e) 75:25 rounded cells, f) 100:0 spread cells and g) 100:0 rounded cells, stained with phalliodin (red) and DAPI (blue), 100k cells/well, scale bar 50 µm. Each image is represented with its corresponding z-stack on its right. 135

Figure 3.19 Dermal fibroblasts at day 7 in S3 pOx gels with 10% RGD, 0.5 mol% PI, 120 s UV and VPM:PEGDT a) 0:100, b) 25:75, c) 50:50, d) 75:25 and e) 100:0, stained with phalliodin (red) and DAPI (blue), 100k cells/well, scale bar 50 µm. Each image is represented with its corresponding z-stack on its right. 136

Figure 3.20 Dermal fibroblasts day 1 in pOx gels with 10% RGD, 0.5 mol% PI, 120 s UV and VPM:PEGDT 75:25 with varying stiffness a) S3 spread cells, b) S3 rounded cells, c) S4 spread cells, d) S4 rounded cells, e) S5 spread cells and f) S5 rounded cells, stained with phalliodin (red) and DAPI (blue), 100k cells/well, scale bar 50 µm. Each image is represented with its corresponding z-stack on its right. 139

Figure 3.21 Dermal fibroblasts at day day 7 in pOx gels with 10% RGD, 0.5 mol% PI, 120 s UV and VPM:PEGDT 75:25 with varying stiffness a) S3, b) S4 and c) S5, stained with phalliodin (red) and DAPI (blue), 100k cells/well, scale bar 50 µm. Each image is represented with its corresponding z-stack on its right. 140

Figure 3.22 Glass bottom PDMS wells in a petridish, diameter of each well is 8 mm. 148

Figure 4.1 Scheme representing the polymer brush formation, functionalisation and thiol-ene reaction. 153

Figure 4.2 The polymerisation kinetics of pOEGMA brushes followed by ellipsometry and the functionalisation through DSC coupling to obtain alkene functional brushes. Blue pOEGMA,

red pOEGMA-DSC and green pOEGMA-AA. a) The journey of the brush thickness and b) the degree of functionalisation of pOEGMA brushes. Trendlines were added to guide the eyes. 155

Figure 4.3 Series of thiols and peptides (S1-S8) reacted with pOEGMA-AA brushes using thiol-ene coupling. 157

Figure 4.4 A representation the thiol-ene functionalisation setup 157

Figure 4.5 The effect of UV exposure time and PI concentration on the thiol-ene reaction with pOEGMA brushes. Blue represents the thiol-ene coupling with S1 and red S2. Solid lines represent thiol-ene coupling with 5 mol% PI, dotted lines 2 mol% PI with 300 s UV exposure time. 158

Figure 4.6 The effect of pOEGMA brush thickness on the thiol-ene reaction with 5 mol% PI, 300s UV exposure time, blue-S1 and red-S2. Trendline was added to guide the eyes. 159

Figure 4.7 Representation of the degree of functionalisation of thiols (S1-8) on pOEGMA-AA (30-40 nm) surfaces. See Fig. A3.1 for corresponding statistical analysis. 160

Figure 4.8 Grazing angle FTIR spectra with 13 mm mirror, brushes and thiol-ene substrates on gold coated glass surfaces plotted from 800-1900 cm^{-1} and 2600-4000 cm^{-1} for a more detailed view: a) pOEGMA, b) pOEGMA-AA, c) S1 functionalised pOEGMA d) S2 functioanlised pOEGMA and e) S5 functionalised pOEGMA. Thiol-ene coupling was performed with 5 mol% PI and 300 s UV exposure. 161

Figure 4.9 HUVEC cell count on polymer brush substrates functionalised with various peptides (S3-6) (5 mol% PI, 300s UV) and collagen control. See Fig. A3.2 for corresponding statistical analysis. 163

Figure 4.10 HUVEC cell area on polymer brush substrates functionalised with various peptides (S3-6) (5 mol% PI, 300s UV) and collagen control. See Fig. A3.3 for corresponding statistical analysis. 163

Figure 4.11 Epifluorescent images of HUVECs seeded (15,000 cells/mL) on substrates stained with phalliodin (red) and DAPI (blue). Substrates from left to right represent, collagen, pOEGMA, pOEGMA-AA, REDV (S3), RDVE (S4), RGD (S5) and RGE (S6). Reactions were performed with 5 mol% PI and 300 s UV. 163

Figure 4.12 HUVEC cell count on methacrylate functionalised substrates functionalised with peptides (S3, S5-6) 166

Figure 4.13 HUVEC cell area on methacrylate functionalised substrates functionalised with peptides (S3, S5-6) 166

Figure 4.14 Epifluorescent images of HUVECs seeded (15,000 cells/mL) on substrates stained with phalliodin (red) and DAPI (blue). Substrates from left to right represent, collagen, methacrylate, REDV (S3), RGD (S5) and RGE (S6). 166

Figure 4.15 An illustration representing the thiol-ene patterning setup. 167

Figure 4.16 Epifluorescent images of FITC-RGE (S8) 50 µm circles and lined patterned substrates, scale 100µm. Reactions were performed with 5 mol% PI and 300 s UV exposure. 168

Figure 4.17 Gray values from epifluorescent images of S8 functionalised 50 µm lines (blue) an 168

Figure 4.18 Epifluorescent images of S8 functionalised 50 µm line patterned substrates with differing UV exposure time, scale 100µm. Reactions were performed with 5 mol% PI. 169

Figure 4.19 Gray value from epifluorescent images of S8 functionalised 50 µm line patterned substrates with differing UV exposure times: 300 s (blue), 180 s (red) and 60 s (green). Reactions were performed with 5 mol% PI. 169

Figure 4.20 Average gray value from epifluorescent images of S8 functionalised 50 µm line patterned substrates with differing UV exposure times: 300 s (blue), 180 s (red) and 60 s (green). Reactions were performed with 5 mol% PI. 169

Figure 4.21 Epifluorescent images of S8 functionalised 5x2 µm rectangle patterned substrates with differing UV exposure time, scale 100µm. Reactions were performed with 5 mol% PI. 171

Figure 4.22 Gray values from epifluorescent images of S8 functionalised 5x2 µm reactangle patterned substrates with differing UV exposure times: 300 s (blue), 180 s (red) and 60 s (green). Reactions were performed with 5 mol% PI. 171

Figure 4.23 Average gray value from epifluorescent images of S8 functionalised 5x2 µm patterned substrates with differing UV exposure times: 300 s (blue), 180 s (red) and 60 s (green). Reactions were performed with 5 mol% PI. 171

Figure 4.24 AFM topography scan of S1 rectangle (5x2µm) patterned substrate with 5 mol% PI and 300s UV exposure, scale 10µm. 172

Figure 4.25 Pattern analysis of S1 rectangles with differing UV exposure times: 300 s (blue), 180 s (red) and 60 s (green). Reactions were performed with 5 mol% PI. 172

Figure 4.26 A representation of HUVECs (7 500 cells/mL) on S5 : S8 (1:1) ring patterned substrates, scale bar 100µm. Reactions were performed with 5 mol% PI and 300 s UV

exposure. a) rings stained with FITC labelled peptide (green), b) nucleus were stained with DAPI (blue), c) cell cytoskeleton, actin were stained with phalliodin (red) an d) a representation of the merged channels. 174

Figure A1.1 The impact of PI concentration on the thiol-ene extent of reaction between PEG methyl ether thiol S5 and alkene A1 (45 µmol/mL) with 60 s UV. 197

Figure A1.2 The impact of UV intensity on the thiol-ene extent of reaction between alkene A1 and thiols S1 (blue line) and S5 (orange line) (45 µmol/mL), using 2 mol% of PI with respect to the thiol with 60 s UV. 197

Figure A1.3 HPLC traces for a) thiol-ene coupling reaction (45 mM) between GCGSY and pentenoic acid (A1), b) unreacted peptide GCGSY, c) pentenoic acid and d) PI IRG2959. 198

Figure A1.4 HPLC traces for the low concentration reaction with GCGSY and pentenoic acid (A1) from high to low concentration a) 45 mM, b) 9 mM, c) 4,5 mM and d) 1.8 mM. Reactions were performed with 5 mol% PI and 300 s UV exposure. 199

Figure A1.5 Normalised traces for unreacted peptide GCGSY (2.95 min)) and product peaks (15.9 min) for GCGSY and pentenoic acid (A1) at different reaction concentrations: 45 mM, 9 mM, 4,5 mM and 1.8 mM. Reactions were performed with 5 mol% PI and 300 s UV exposure. 200

Table 2.1 A list of reaction conversions from ^{1}H NMR spectroscopy for series of thiols and alkenes with variable concentration of PI, UV exposure time (s) and thiol: alkene ratio. 75

Table 3.1 The concentrations of the components used for each gel type in molar concentration and weight percent. Gels were made using thiol:ene 0.5:1 ratio, 0.5 mol% PI and 120 s UV exposure. 119

Table 3.2 Storage modulus obtained for different backbone hydrogels at three different concentrations, modulus are reported from the frequency sweep for the measurement at 1 Hz. 120

Table 3.3 The concentration of components used to make each gel type in molar concentration and weight percent. S3 gels with thiol:ene 0.5:1 and PI 0.5 mol% 124

Table 3.4 The concentration of the components used to make different stiffness gels (S3-S5) in molar concentration and weight percent. pOx gels with thiol:ene 0.5:1, 10 mol% RGD and PI 0.5 mol%. 129

Table 3.5 The concentration of the components used to generate pOx gels in molar concentration and weight percent. Gels were made using thiol:ene 0.5:1 ratio, 10 mol% RGD, 0.5 mol% PI and 120 s UV exposure. 131

Table 3.6 Protocol to make 200 µL gels, solutions were exposed to UV for 120s, 0.5 mol% PI, units in columns are in microlitres (except stiffness)..... 147

Table 3.7 Protocol to make 200 µL gels, 50 µL was put in each well and exposed to UV for 120s, 10 mol% RGD, 0.5 mol% PI, units in columns are in microlitres (except stiffness). 150

*Table A1.1 Summary of statistical data analysis obtained for the percentage conversion with S1 and A2-A9 (see Fig. 2.13). n.s., non significant; *, p < 0.05; **, p < 0.01: ***, p < 0.001. ..... 200*

*Table A1.2 Summary of statistical data analysis obtained for the percentage peptide product formation via ^{1}H NMR spectroscopy (see Fig. 2.16). n.s., non significant; *, p < 0.05; **, p < 0.01: ***, p < 0.001. ..... 201*

*Table A1.3 Summary of statistical data analysis obtained for the percentage peptide product formation via HPLC (see Fig. 2.16). n.s., non significant; *, p < 0.05; **, p < 0.01: ***, p < 0.001. .... 202*

*Table A1.4 Summary of statistical data analysis obtained for the percentage reaction conversion in the presence of amino acids and electrolytes (see Fig. 2.15). n.s., non significant; *, p < 0.05; **, p < 0.01: ***, p < 0.001. ..... 203*

*Table A2.1 Summary of statistical data analysis obtained for the percentage cell viability of HUVECs encapsulated in different stiffness gels (see Fig. 3.14). n.s., non significant; *, p < 0.05; **, p < 0.01: ***, p < 0.001. ..... 213*

*Table A2.2 Summary of statistical data analysis obtained for the percentage cell viability of dermal fibroblasts encapsulated in hydrogels (see Fig. 3.16). n.s., non significant; *, p < 0.05; **, p < 0.01: ***, p < 0.001. ..... 214*

*Table A3.1 Summary of statistical data analysis obtained for the percentage functionalisation with a series of thiols (see Fig. 4.7). n.s., non significant; *, p < 0.05; **, p < 0.01: ***, p < 0.001. ..... 215*

*Table A3.2 Summary of statistical data analysis obtained for the number of cells on substrates (see Fig. 4.9). n.s., non significant; *, p < 0.05; **, p < 0.01: ***, p < 0.001. ..... 216*

*Table A3.3 Summary of statistical data analysis obtained for the cell area on substrates (see Fig. 4.10). n.s., non significant; *, p < 0.05; **, p < 0.01: ***, p < 0.001. ..... 217*

Scheme 1.1 Mechanism of a) free radical thiol-ene coupling and b) nucleophile initiated Micheal addition[27]. 3

Scheme 1.2 Representation of the CROP mecanism[42]. 10

Scheme 2.1 Synthesis of a) 2-butenyl-2-oxazoline monomer through N-(2-chloroethyl)-4-pentenamide and b) the pOx co-polymer from 2-ethyl-2-oxazoline and 2-butenyl-2-oxazoline monomers. 66

Scheme 2.2 Functionalisation of poly(methyl vinyl ether alt-maleic anhydride) to generate poly(maleic amide co-acid)/ pMA$^-$ (A11). 69

Scheme 2.3 Synthesis of pDMAEMA propene (A7), pDMAEMA butene (A8), and pDMAEMA pentene (A9, pDMAEMA$^+$) from pDMAEMA. 70

Scheme 2.4 Synthesis of N,N-diethylpent-4-enamide (A2). 99

Scheme 2.5 Synthesis of N-allylacetamide (A3). 100

Scheme 2.6 Synthesis of N,N,N-triehtylprop-2-en-1-aminium (A4), N,N,N-triehtylbut-3-en-1-aminium (A5) and N,N,N-triehtylpent-4-en-1-aminium (A6) from triethylamine. 101

Scheme 4.1 A representation of the polymer brush synthesis, functionalisation and thiol-ene coupling reactions. 154

Chapter 1

Design of peptide-based biomaterials

Research in the biomaterials field has grown exponentially in the last decades. There is more and more need for novel material design and synthesis. The applications of biomaterials in various fields are expanding, and more efforts focus on the design of new biomaterials which display controlled interactions with cells and tissues at biointerfaces (polymer films, polymer brushes, and hydrogels) and mimic various aspects of biological environments[1-4]. Many have studied such 2D systems looking at the cell behaviour to the material at interface[5-7], however, researchers are realising the importance of the 3D environment. Other researchers have developed biomaterials and hydrogels appropriate for studying and controlling interactions between cells and their matrix in 3D (bio-mimetic 3D environment for cell culture) [8, 9]. This is still a challenging field as it requires precise control over the chemistry and material synthesis, the functionalisation of biomaterial with biologically active molecules and a lack of cytotoxicity. Thiol-ene coupling provides an excellent tool for this purpose and is one of the focuses here.

1.1 Thiol-ene click chemistry

In 2001, Sharpless *et al*. introduced the concept of click chemistry[10]. This new concept referred to highly selective reactions, readily proceeding under aerobic and ambient atmospheric conditions, not or little affected by molecular complexity and highly efficient, resulting in high yields and ease of isolation of product. A number of click chemistry systems have been developed and have had a considerable impact in the fields of chemistry, biochemistry and materials science[11-14]. One of the most classic examples of click chemistry is the copper(I)-catalysed azide-alkyne cycloaddition[15, 16], but recently thiol-alkene (thiol-ene) and thiol-alkyne (thiol-yne)[17-19] couplings have attracted some attention, they make use of readily available chemical functions present in the structure of polymers and materials as well as peptides and proteins[17-19]. Thiol-ene chemistry has been studied since the 1900s and has been applied in various fields of contemporary chemistry, including organic synthesis, polymer chemistry, materials chemistry, surface functionalisation and bioconjugation[20-24].

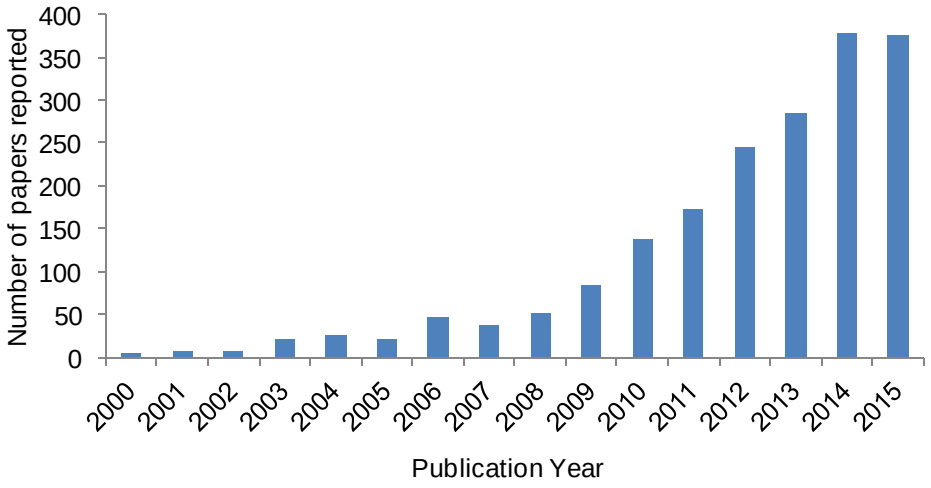

Figure 1.1 Annual number of papers reported on "thiol-ene" coupling since year 2000, obtained from the web of knowledge.

1.1.1 Mechanism and kinetics

Thiol-ene coupling was generalised to two methods, free radical addition and catalysed thiol Michael addition, represented in Scheme 1.1. Both types of thiol-ene coupling reactions are known to proceed via step growth polymerisation and therefore have been employed in many polymer synthesis procedures[25]. The catalysed thiol Michael addition is more likely to occur with electron deficient alkenes[26]. Catalysts include strong bases, Lewis acids, organometallics and metals. The free radical addition reaction proceeds via the elimination of the hydrogen radical from the thiol by a carbon centred radical initiator species, followed by the propagation where the thiyl radical adds across the carbon-carbon double bond, where the thiol-ene coupling reaction is thermodynamically favourable[27].

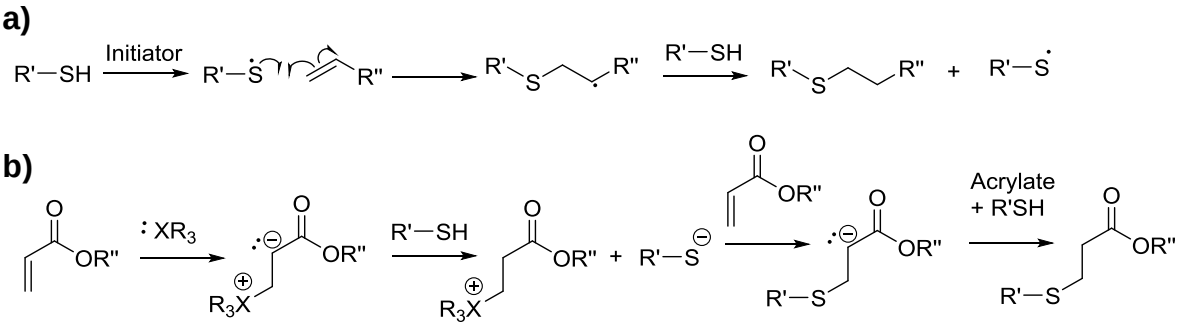

Scheme 1.1 Mechanism of a) free radical thiol-ene coupling and b) nucleophile initiated Micheal addition[27].

Kinetic studies of the thiol-ene coupling reaction provide greater insight into understanding the overall chemical process. Cramer *et al.* investigated the thiol-ene coupling reaction in more mechanistic detail and modelled the reaction kinetics[28]. Findings showed that the chain transfer step was the rate-limiting step and the reaction had first order kinetics.

Computational analysis can also be performed to support and further investigate effects seen in experimental data. Northrop *et al.* produced computational results on the kinetic analysis of the radical initiated thiol-ene coupling reaction with a model thiol and a series of 12 alkenes in the gas phase[29]. Reaction and transition-state enthalpies, free energy calculations and the electronic structure calculations were used to determine the factors controlling the energy activation barriers. During the thiol-ene coupling reaction the thiol radical reacts with an alkene (propagation) however, it is also possible for a carbon radical to react with an alkene species (homopolymerisation) to initiate chain growth, illustrated in Fig. 1.2.

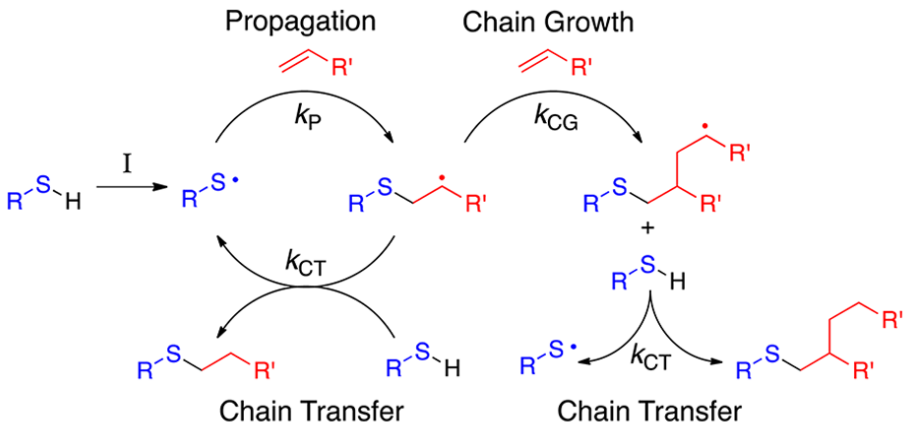

Figure 1.2 Representation of the thiol-ene coupling reaction including the propagation, chain transfer and chain growth steps[29].

The addition of the thiyl radical to the alkene (free energy of propagation) ranges from highly exothermic to slightly endothermic (Fig. 1.3a). For alkenes that have a positive free energy of propagation, the formation of the carbon radical intermediate was thermodynamically reversible. However, the overall thiol-ene coupling reaction was exothermic and it drove the reaction. The forward and reverse rate constants were calculated for the addition of the thiyl radical to the alkene to obtain a fuller understanding of the reaction.

Northrop *et al*. also produced a kinetic model of the thiol-ene coupling reaction (Fig. 1.3b). Alkenes with high propagation barriers and stable radical intermediates were predicted to have faster rate of reactions and alkenes with low propagation barriers and less stable radical intermediates are expected to have slower rate of reactions due to the reversibility of the propagation step. They argue that changing the experimental conditions will vary the reaction kinetics of each system however, will not affect the relative order of reactivity of the 12 alkenes. Their kinetic model was compared to experimental studies from other researchers and showed a general agreement. Northrop and co-workers have shown greater understanding of the activation energies of the thiol-ene coupling reaction and therefore, their overall reactivity. Computational studies show a good insight into the factors relevant to the reactivity of the thiol-ene coupling reaction, however, it is important to be able to obtain results experimentally.

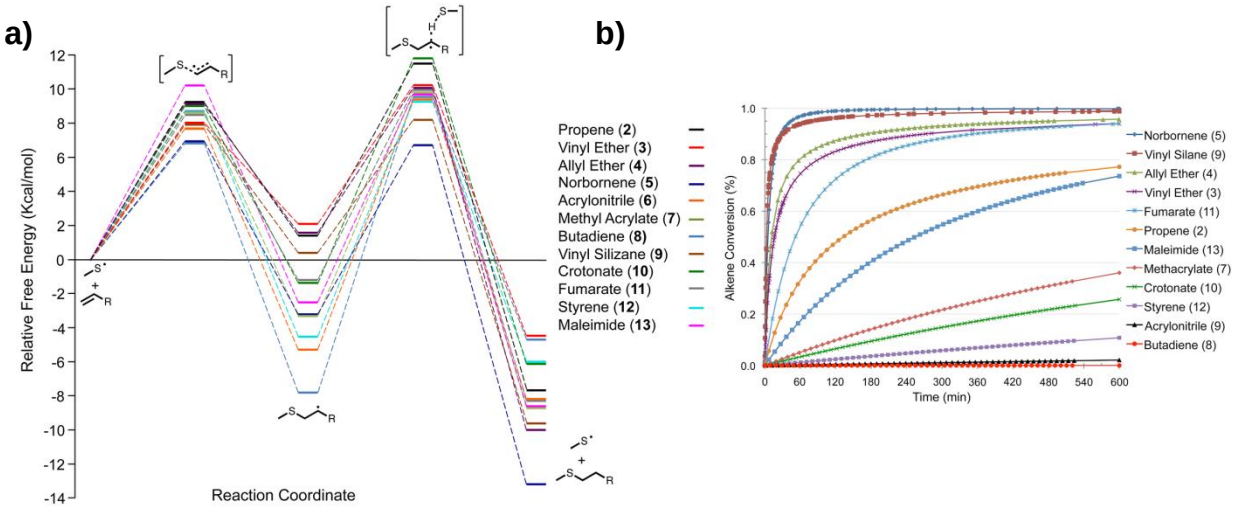

Figure 1.3 a) A reaction profile showing relative free energies of the listed alkenes with methyl mercaptan and b) the kinetic model for the thiol-ene coupling reaction[29].

1.1.2 Factors influencing free radical-based thiol-ene couplings

Thiol-ene chemistry was classified as a click reaction after Sharpless *et al.* reported[10]. However, some researchers have found that the thiol-ene coupling reaction does not work as efficiently as proposed for some type of systems. Here we explore some of these features.

The free radical thiol-ene initiation can be generated by a wide variety of systems including many thermal and photoinitiators[19]. Uygun *et al*. studied the thiol-ene coupling reaction with thiol functionalised polystyrene and a series of alkenes and also, an alkene functionalised polystyrene and 3-mercaptopropioic acid[30]. The reactions were performed in organic solvent and initiated by various photo and thermal radical initiators (4 hours UV irradiation or heating). The conversions were determined by ^{1}H NMR spectroscopy (via the consumption of the alkene peak). Results from the library showed that the lowest conversions were obtained from thermal initiators and the highest by photoinitiators, which is also in agreement with similar work by others[19]. A kinetic study was performed neat with a thiol-ene coupling system and monitored using FTIR spectroscopy[30]. Uygun *et al.* concluded that thermal initiators perform with lower conversions because high temperatures favoured side reactions. Other researchers have also reported that the alkene conversion is usually higher than the thiol conversion; the homopolymerisation of alkene substituents is thought to be favourable in some conditions[31-33]. This effect could be related to the rate constants of the reaction components.

Cramer *et al.* reported that for some alkenes the propagation kinetic constant was greater than the rate constant for hydrogen abstraction from the thiol[33].

It is vital to investigate the impact of other variables on the thiol-ene coupling reaction. Lecamp *et al.* investigated the influence of temperature, photoinitiator concentration and UV light intensity on the thiol-ene coupling reaction using photocalorimetry and FTIR spectroscopy. Increasing the reaction temperature resulted in homopolymerisation and the consumption of the double bonds leading to lower thiol-ene coupling efficiencies. Decreasing the UV intensity from 18.1 to 3.7 mW/cm^2 resulted in slower reaction kinetics. Moreover, increasing the photoinitiator concentration resulted in a higher reaction rate and higher ultimate conversion of the material. Studies showed that the investigations of the reaction parameters are crucial in order to create a robust system for the production of materials. Johnson *et al*. also investigated the impact of temperature and UV exposure time on the thiol-ene photopolymerisation using FTIR spectroscopic analysis[31]. This enabled them to generate a large data set, and therefore perform high throughput analysis which would be beneficial for those who are modelling or optimising experimental protocols.

In organic solvents and neat conditions, the kinetics of thiol-ene couplings has been reported to proceed faster with electron-rich alkenes[34, 35]. Slower reaction rates were observed with electron deficient molecules, but still allowed couplings to occur[27, 36]. Other reactivity rules have been established, highlighting the importance of the respective rates of thiyl radical addition and transfer[28, 37, 38]. For example, thiol-ene chemistry is thought to be low yielding with allylic and benzylic compounds, due to the hydrogen abstraction by thiyl

radicals from the allylic and benzylic positions and therefore the formation of the stabilised radical species[37].

Important reactivity differences were also reported between polymer-small molecule[19] and polymer-polymer conjugation[39]. Koo *et al*. investigated the effect of molecular size on the thiol-ene reaction efficiency[35]. Findings showed that conditions used to conjugate small molecules to polymers were inefficient when applied to polymer-polymer systems. The thiol-ene coupling between two polymers was reduced due to competitive bimolecular termination reactions[35], this is in good agreement with work reported by Derboven *et al*.[39]. Koo *et al.* concluded that these termination reactions are unavoidable and advised that radical thiol-ene reactions used for macromolecular systems should not be referred to as "click" reactions[35].

1.1.3 Poly(oxazoline)s as candidates for thiol-ene coupling

The mechanistic detail of thiol-ene coupling has been discussed; researchers have also put their efforts to understanding the systems that work well or limit the reaction efficiency. Here we focus on oxazolines as polymeric candidates for their use in the biomaterials field. When used conjunction with thiol-ene coupling it is possible to generate materials with unique features[40]. This thesis will focus on thiol-ene coupling used together with polymers for the generation of biomaterials; therefore, suitable biocompatible polymeric candidates are required to fulfil this purpose.

There is an exponential increase in the synthesis of biocompatible polymers used for medical applications especially poly(oxazolines), many reviews have discussed the potential applications of these materials[3, 41-44]. Various other polymers have been developed and investigated for specific applications (discussed further in later sections).

Oxazoline monomers are widely available in different substituted forms and therefore, have a great potential to generate various polymeric networks without the need for monomer synthesis. Polymers produced from 2-methyl and 2-ethyl oxazolines, their homopolymers and co

mers are known to be non-cytotoxic even at high concentrations[45] and have been proposed as alternatives to PEG [46].

Poly(oxazoline)s are formed by the CROP mechanism represented in the illustration (Scheme 1.2)[41]. The CROP mechanism is a living polymerisation, which means that it provides great control over the molecular weight dispersity (narrowdispersity) during synthesis.

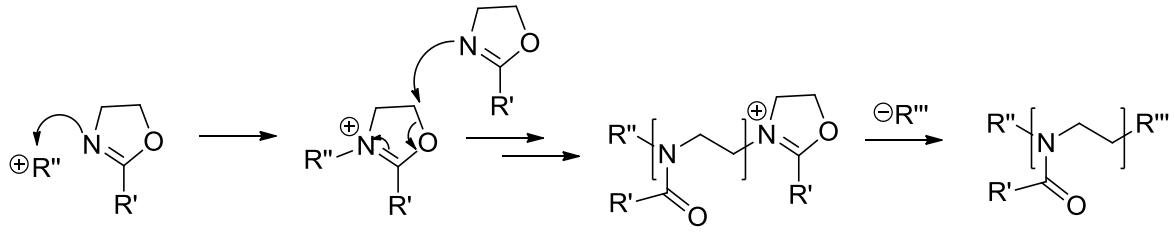

Scheme 1.2 Representation of the CROP mecanism[41].

Using microwave reactors have become very popular for organic synthesis because it shortens the relative time used for the reaction. Kelly and co-workers produced a library of poly(oxazoline) hydrogels using this method[47]. Ratios of ethyl, phenyl and phenylene-1,3-bis-(2-oxazoline) monomers were reacted in a microwave with methyl tosylate as the initiator. After purification the polymer product was obtained in high yields (+95%). Recently, almost all poly(oxazoline)s synthesised are generated using similar systems[48]. Hoogenboom *et al*. produced a library of triblock co-poly(oxazoline)s consisting of different ratios of methyl, ethyl, nonyl and phenyl oxazoline monomers with narrow dispersities (< 1.33)[49]. They characterised the micellisation behaviour of the polymers and showed insight into the design of polymers for further use in drug delivery applications. Poly(oxazoline)s on their own provides a potential for their use in the biomaterials field. With the combination of thiol-ene coupling it is possible to generate materials without having to sequence polymers monomer by monomer.

In order to generate thiol-ene coupling systems with polymers, it is crucial to have thiol or alkene functionalities present in the polymers. Cesana *et al.* synthesised an oxazoline monomer with a thiol functionalised end group[46]. The thiol functionalised monomer was copolymerised with different ratios of ethyl

oxazoline. These materials provide a potential for the use of oxazolines for thiol-ene coupling.

Gress *et al*. synthesised an oxazoline monomer containing an alkene functionality which was further polymerised[22]. Four different molecular weight homopolymers were generated and reacted with a series of thiols. Also, an alkene functional co-polymer with ethyl was generated. The synthesis of the alkene functional monomer and the co-polymer showed interest in other research groups and was studied further. This work enlightened studies produced by Schenk *et al.* [23, 47]. They produced alkene functional $pEtOx_{80}Bu{=}Ox_{20}$ hydrophilic and $pPhOx_{80}Dc{=}Ox_{20}$ hydrophobic co-polymers and crosslinked them with a tetra-functional thiol using free radical photo-initiated thiol-ene chemistry[23]. The formed network was used to coat substrates for photoresist applications. Alkene functional oxazoline polymers provide an excellent potential for biomaterials applications.

The co-polymer comprised of the butenyl monomer synthesised by Gress *et al.* has a great potential due to its ease of synthesis and availability of functionality. This monomer can be co-polymerised with ethyl monomers to generate alkene functional polymers of required ratios. Schenk *et al*. has enlightened researchers for the use of thiol-ene coupling to crosslink these systems and generate networks. Since oxazolines are known to be non-toxic[45], this provides a great prospective for these materials to be further investigated in the bioengineering field[40] and is one of the highlights of this thesis. Applications for polymeric systems together with thiol-ene coupling have been discussed in more detail in the biomaterials sections.

1.1.4 Biofunctionalisation with thiol-ene chemistry

The biofunctionalisation of biomaterials is important to confer bioactive properties essential to their use in a wide range of applications, including medical implants[50, 51], tissue engineering scaffolds[52], cell culture platforms for cell expansion and *in vitro* assays[53], drug delivery systems and imaging probes[54]. Typically, proteins and peptides are adsorbed or coupled to biomaterials to alter cell phenotype or tissue response. One essential element for the design of biocompatible materials is the ability to couple proteins or peptides to biomaterials *in situ,* in the presence of cells, in mild conditions and with non-toxic reagents. Such *in situ* biofunctionalisation can be applied for the design of 3D hydrogels encapsulating cells, for tissue engineering or as *in vitro* models[40, 55-58], or the development of controlled dynamic cell-based assays[21, 59].

Click chemistry has received much attention for the design of biofunctional platforms, owing to the efficiency of click couplings in mild conditions and at low concentrations (often desired due to the cost of proteins or peptides). The conditions required are so mild that even sunlight was reported to initiate free radical thiol-ene coupling (in the presence of a photoinitiator)[27]. Also, oxygen and water inhibition, typically preventing conventional radical reactions and polymerisations, can often be neglected in thiol-ene reactions[27, 60].

Many researchers have investigated the factors influencing the thiol-ene reactions in organic solvents[19, 35, 39] or neat conditions[31-33]; however, when using this as a tool for biofunctionalisation, it is important to understand the reaction in aqueous buffers, so far, none has been reported to our knowledge.

Peptides are the main candidates used for the biofunctionalisation of materials. The naturally occurring cysteine amino acid has a thiol functional group present on its side chain, and therefore can be incorporated into peptide sequences and used for thiol-ene coupling for the biofunctionalisation of materials[21, 40, 61, 62]. Even though this system is widely used, the thiol-ene reaction efficiency with peptides sequences has not been reported. It is important to consider the reactivity of cysteine residues in peptide sequences. The thiol-ene reactivity of the cysteine may be affected by the neighbouring amino acids in the sequence through charge or hydrophobicity, this work has been investigated in this thesis.

1.2 Polymer brushes for biomedical applications

The control and manipulation of interfaces between materials and biological systems is an expanding area in the field of biomaterials. A variety of processes have been developed to design interfaces. Surface engineering using polymers is a versatile platform and can be used to alter the characteristics at interfaces: hydrophilicity, chemical reactivity, topography, mechanics, surface charge, adhesion, protein resistance and conductivity[63-69]. To this aim, research in the field of polymer brushes has grown exponentially in the past couple of decades. Polymer brushes are defined as polymer chains covalently attached to a surface, forming a dense polymer coating, potentially swollen with solvent[69-71]. Polymer brushes are chemically stable making them well-suited for storage and cell culture applications. Their composition can be controlled using various monomers which allowed the control of the chemical functionalities present, they have a defined architecture and their precise location on the surface can be controlled using patterning techniques[69, 72]. This provide a new platform for controlling biointerfaces, offering manipulation of surfaces physio-chemical and biochemical properties and therefore making them more suited to a variety of applications.

1.2.1 Properties of polymer brushes

It is important to understand and be able to control interfaces for their application in various fields. In particular polymer brushes are attractive since many of their features can be controlled and manipulated: brush architecture and chemistry, grafting density and brush thickness [72, 73]. These features allow for the fine tuning of the surface properties: hydrophilicity, surface energy[74-76], diffusion of molecules and particles, binding[77-80], adsorption of biomolecules[81-85] and cell adhesion[86-88].

Surface bound polymer brushes can be generated via the "grafting to" or "grafting from" method (Fig. 1.4). The "grafting to" method relates to the attachment of readily made polymer chains to surfaces via an anchoring step. The "grafting from" method relates to polymer chains grown from initiator moieties, coupled to the surface to achieve a brush structure[71, 83]. Therefore, the interest in "grafting from" polymer brushes has triggered the development of surface initiated polymer chemistry. Various radical initiated controlled polymerisation techniques have been applied to achieve brushes[69]: ATRP[89-92], RAFT[92-94], NMP[95, 96], and iniferter polymerisation[97]. Since the early developments of polymer brushes, a wide range of materials have be exploited as polymer brushes surfaces.

The behaviour and properties of polymer brushes are determined by their chemistry and architecture[69, 98-100]. The ability to form brushes with various chemical functionalities has produced brushes with a range of surface properties (bioactivity, bioinertness, tribology, and hydrophilicity) and the architecture allowed for the manipulation of features modulating the brush behaviour.

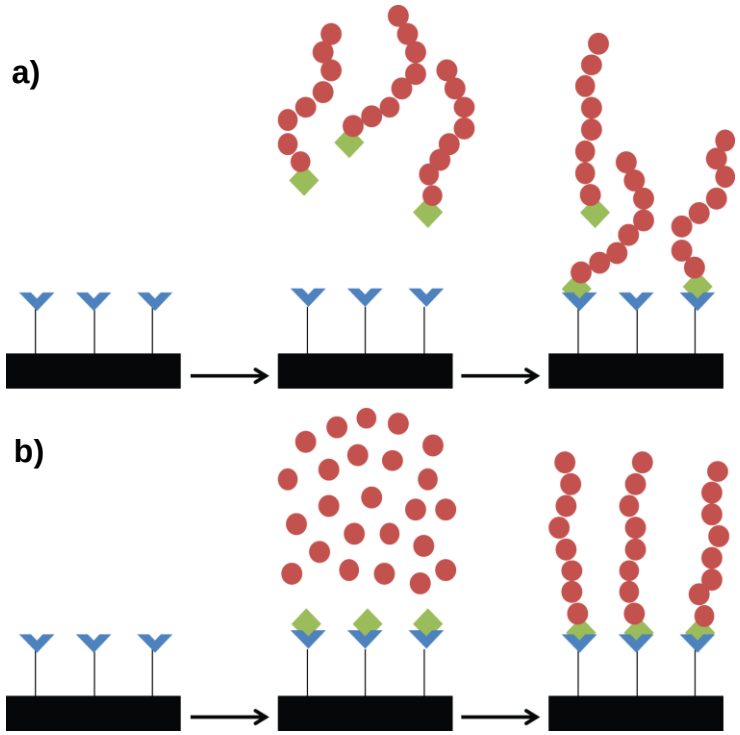

Figure 1.4 Schematic showing the a) "grafting to" and b) "grafting from" methods.

One of the key architectural features is the grafting density (number of chains per area). The chain density is determined by the conformation of that brushes prefer to adopt, the initial density of initiators and the efficiency with which these initiators give rise to polymer chains. At high densities, the polymer chains tend to be extended with a partial orientation ("brush" regime), whereas at low densities the polymer chains randomly coil and distribute across the surface ("mushroom" regime, Fig. 1.5). The adopted grafting density and brush conformation affects the surface behaviour and physio-chemical properties.

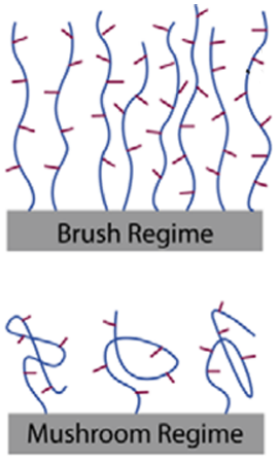

Figure 1.5 Representation of the "brush" and "mushroom" regime[101].

Some polymer brush surfaces allow the adsorption of biomolecules (proteins). The adsorption is mainly a result of hydrophobic, electrostatic or hydrogen bonding interactions[102, 103]. Three different scenarios have been proposed for the adsorption of biomolecules to the polymer brush surfaces Fig. 1.6[104]. The primary adsorption describes the adsorption of biomolecules to the underlying substrate. Secondary adsorption is restricted to interactions at only the outermost surface of the brush. Ternary adsorption is a result of low free energy of adsorption to the underlying substrate and high attraction energy of the brush. Adsorption is also controlled by the conformation of the brush as well as the size of the biomolecules.

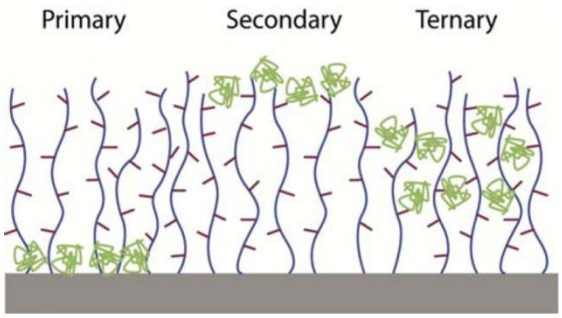

Figure 1.6 Modes or adsorption on polymer brushes[101].

On the other end of the spectrum are polymer brushes that are resistant to protein adsorption. The interaction of proteins with surfaces can be measured using SPR or QCM. pOEGMA Brushes were the first to be studied and reported as protein resistance coatings[89, 105]. The stability of pOEGMA brushes at ambient conditions and when exposed to cell culture conditions were studied[106]. Results showed that the methoxy-terminated brushes were stable at ambient conditions and up to 7 days in cell culture conditions. However, the hydroxy-terminated brushes were less stable, after prolonged exposure to cell culture conditions brushes showed detachment as films. This could possibly be due to the presence of dimethacrylate in commercially available hydroxy-terminated monomers, therefore resulting in some crosslinking behaviour between the brush structures and associated swelling with the presence of good solvents, resulting in surface detachment as films.

1.2.2 Biofunctionalisation of polymer brushes

The wealth of chemical functionalities available with polymer brushes enables the attachment and immobilisation of biomolecules. Biofunctionalisation can be achieved using many methods. Proteins can directly be adsorbed onto brush surfaces if protein-brush interactions are strong. Polyelectrolytes are usually good candidates for such strategy, as they don't require coupling agents and proteins can be simply adsorbed via electrostatic forces, Christman *et al.* immobilised heparin on poly(styrenesulfonate) surfaces[107]. Although pOEGMA brushes are known for their protein resistance, counter-intuitively it is possible to irreversibly adsorb proteins on pOEGMA brush surfaces[108]. In such case, it is thought that upon dehydration of the surface, the protein-brush interaction is increased and the entangled nature of brushes prevents the desorption of proteins when immersed in buffer.

Simple protein adsorption isn't compatible with all brush systems and therefore, it is necessary to develop other methods for biofunctionalisation, of which chemical coupling is introduced. Coupling chemistry provides a good tool for functionalisation since polymer brushes can readily be designed with many chemically reactive components: carboxylic acids, amines, hydroxyls and epoxides. Depending on the final system required, brushes can be reacted directly to achieve the desired biofunctionality or be coupled with coupling agents to achieve various other functionalities to then further functionalise with biomolecules illustrated in Fig. 1.7. Two important coupling agents commonly used include DSC[109, 110] and NPC[87, 111], which are popular due to their availability and mild reaction conditions. Biotin and RGD were coupled to pOEGMA brushes using DSC and NPC as coupling agents.[87, 109] pHEMA was

functionalised with leucine and serine amino acids using NPC as the coupling agent.[112] Results from Neutron reflectivity measurements show that the uppermost part (20nm depth) of the brush is more likely to be functionalised with denser brushes, whereas with lower density brushes a more homogeneous coupling was observed. pOEGMA brushes were coupled to achieve maleimide functional chains that were reacted with cysteine terminated peptide sequences using Michael addition to achieve biofunctionalisation[113]. pOEGMA brushes were functionalised with a cysteine-terminated RGD peptide sequence using thiol-ene and thiol-yne photoinitiated coupling chemistry[21]. The density of peptide was controlled via changing the initial concentration of the peptide in the reaction solution. Neutral brushes (pHEMA, pOEGMA) were activated using DSC, NPC and CDI to couple larger biomolecules such as proteins: lysozyme[114], streptavidin[109], and antibodies[115].

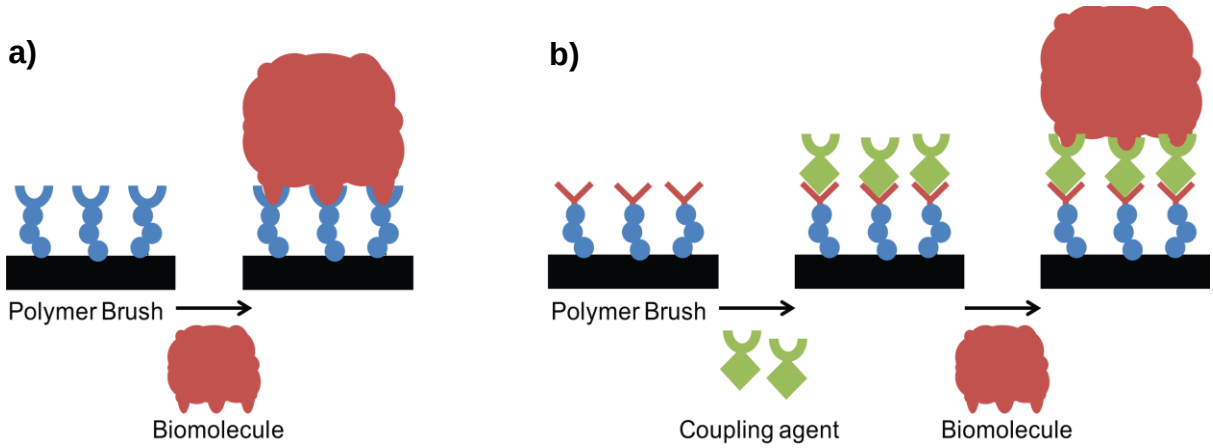

Figure 1.7 The biofunctionalisation of brushes a) via the brush system and b) through coupling reagents.

Biofunctionalisation plays an important role for controlling materials-cell interfaces and therefore, polymer brushes constitute an attractive tool to be used for the coating of biomaterials for biomedical applications. Polymer brushes can be used to introduce bioactivity with the coupling of bioactive

peptides that can promote cell adhesion and culture. Cell adhesive properties can be achieved with the introduction of peptides that are known to have cell adhesive properties; widely used RGD (from fibronectin, collagen I, laminin α_1 and vitronectin)[116] and PHSRN derived from fibronectin (HUVECs, mouse fibroblasts, adipose stem cells)[87, 117-121], GFOGER derived from collagen I used to promote the cell adhesion and differentiation of osteoblasts[86, 111, 122] and REDV used to promote the adhesion and migration of endothelial cells[123].

1.2.3 Patterned brushes for the development of cell-based assays

Classical cell culture conditions do not reflect the true cellular microenvironment and therefore give rise to artefacts and irreproducibility. Cells feel a flat and rigid substrate which does not represent the characteristics of an *in vivo* environment. Micro-engineering techniques allow to control and manipulation of cells and their extra-cellular matrix at the cellular to sub-cellular scales[124]. Micro-scale systems allow the study single cells or a collection of cells with added complexity and dynamic behaviour. These features can be added using patterning techniques which can be achieved with a range of methods: photolithography, micro-contact printing and photopatterning.

One approach that has been particularly successful consists of the use of ATRP initiators that are deposited between areas protected by a photoresist[125, 126]. After the initiation step, polymer brushes are grown from the initiator patterned areas only and therefore result in micrometer-patterned brushes. Although this method provides good micrometer sized resolution and is compatible with many systems, it requires multiple steps.

Micro-contact printing is an alternative adopted by many researchers since it is a faster method to produce patterns in larger numbers[106]. A monolayer of initiator is applied using a patterned stamp, usually a surface patterned PDMS cast against a master generated via photolithograph (Fig. 1.8)[106]. After initiation the brushes are grown as before. Micro-contact printing avoids the few extra steps required by repeated photolithography, although a master and stamp are still required. Gold surfaces were patterned with thiol functionalised

initiators and pOEGMA brushes were grown from these surfaces with good control of micrometer features[89, 106].

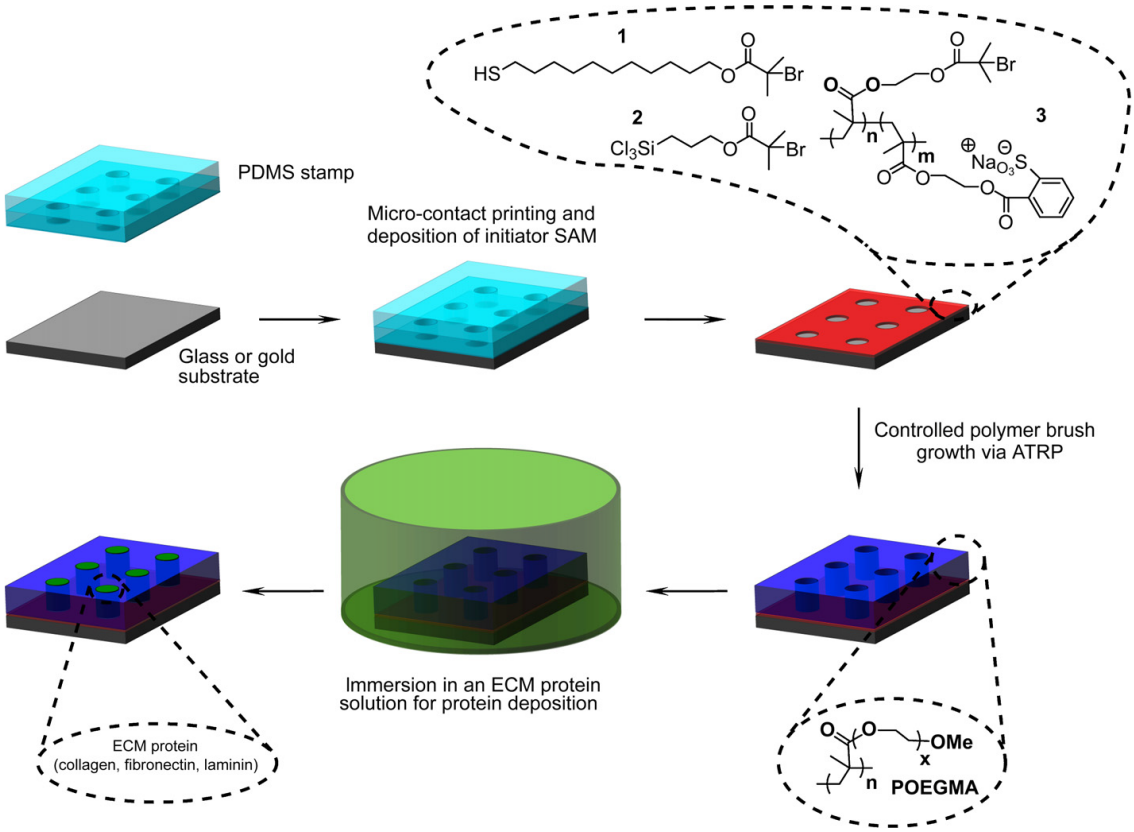

Figure 1.8 A representation of micro-contact printing for the generation of brush patterned surfaces and the adsorption of ECM proteins [106].

Direct photopatterning of brushes is compatible with a wider range of substrates and provides good control over the micrometer sized patterns, although it requires the mask to be compatible with the monomer solution (therefore often ruling out the use of acetate masks). Li *et al*. adsorbed a photoreactive initiator on the surface of plastic substrates and initiated the polymer brush growth[127]. They seeded osteosarcoma cells on the substrates and showed the attachment of clustered cells on the patterned areas.

Initiator patterned surfaces can obtained by etching monolayers of initiator using deep-UV light prior to the growth of polymer brushes from the protected

areas[128, 129]. This method is advantageous over other photolithography and a micro-contact printing technique since it is direct, in one single step, and avoids the diffusion factor occurring in micro-contact printing.

For cell patterning, the brush chemistry is also an important aspect as well as the method used to produce the patterns. pOEGMA brushes have proved to be good candidates for cell patterning due to their high protein resistance and chemical stability[106]. It has been used to study and control single cell spreading, cell shape and the formation of clusters of cells attached to patterns of different shapes and sizes (Fig. 1.9)[89, 106].

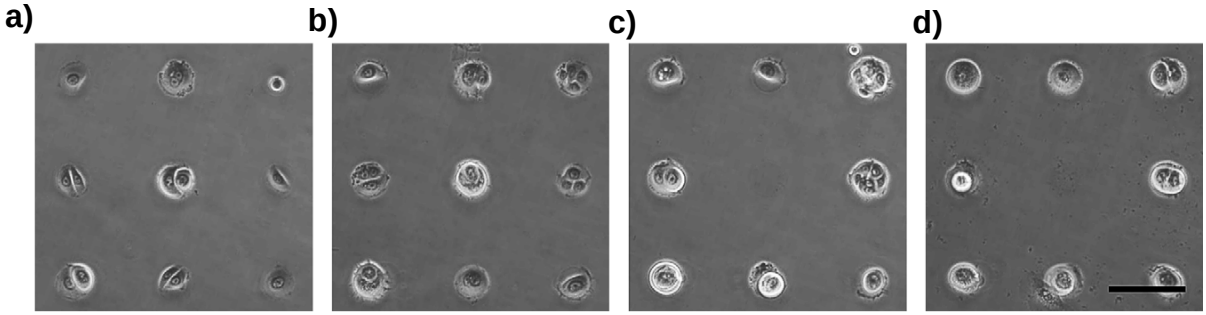

Figure 1.9 Primary human epidermal keratinocytes were seeded on POEGMA patterns generated on gold, incubated for a) 0, b) 1, c) 3 and d) 7 days. Scale bar 100 µm[106].

It was found that larger patterns allowing the attachment of cell clusters could self organise and be manipulated to mimic tissue like structures. Gautrot *et al*. patterned polymer brush islands to mimic the human micro-epidermis and studied the stem cell differentiation on the islands (Fig 1.10)[130].

Proteins were immobilised on the surface of thiol functionalised substrates using photo-initiated thiol-ene coupling. Patterns were generated in various sizes and dimensions using alkene functionalised proteins. Patterns of well defined shape were produced homogenously over large distances[131]. Similarly, Hensarling *et al*. used photo-initiated thiol-yne chemistry to click thiols onto the

surface of pGMA brushes and generated patterns using a photomask[17]. Alkyne functionalised surfaces were functionalised with a given thiol using a photomask, then reacted once more without a mask, covering the total surface of the brushes with two thiols and therefore generating chemical micropatterns. This technique enabled to create textured surfaces of controlled surface chemistry, as evidenced by condensation images showing differential hydrophilicity at the generated patterned areas. Condensation images show the water droplets selectively generated from areas functionalised with hydrophilic thiols (Fig. 1.11).

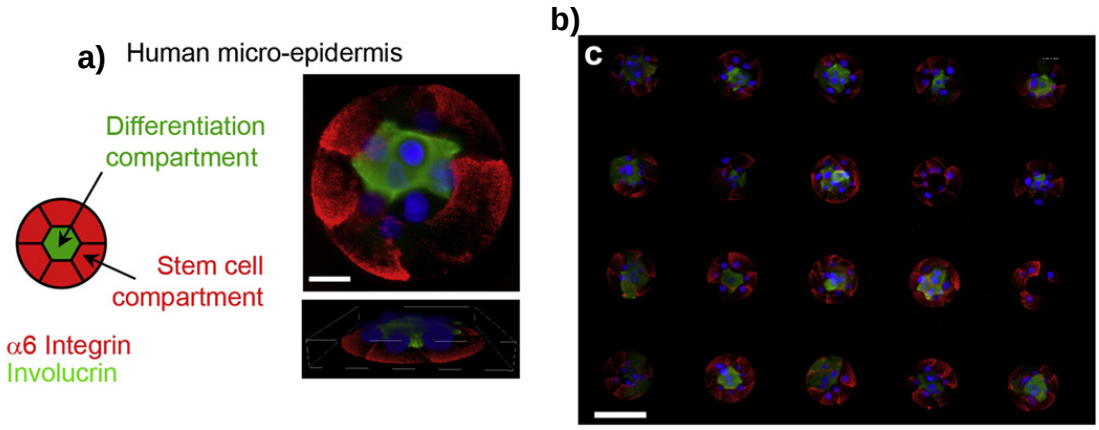

Figure 1.10 a) Example of a cell cluster with 2D and 3D views, scale bar 20 µm. b) Micro-epidermis array, scale bar 100 µm. Cells are stained with involucrin, α6 and DAPI[130].

Costa *et al*. used micro-contact printing and pOEGMA brushes to produce unprotected (gold substrate) islands where cells attached[21]. Thiol-ene chemistry was then used to functionalise the pOEGMA brushes with RGD peptides. Results show the migration of cells from confined gold patterns to the brush surface, as it was functionalised with an RGD peptide (Fig. 1.12). The migration of cells on RGD functionalised substrates was concentration dependent. Cells migrated more quickly with higher concentration of RGD, and did not migrate with the RGE control substrates.

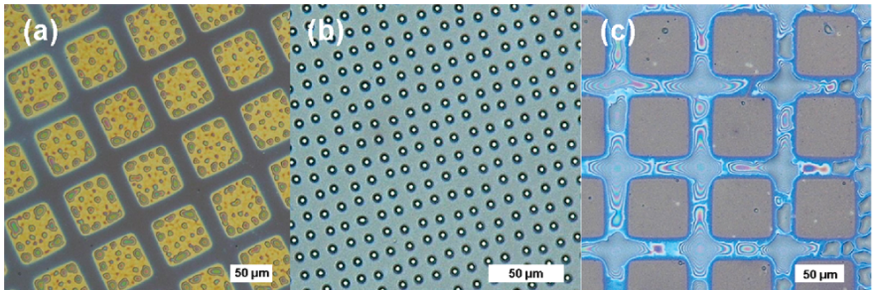

Figure 1.11 Condensation images showing a) hydrophilic thiol on squares (300 mesh), b) hydrophilic squares (2000 mesh) and c) hydrophilic thiol on mesh (300)[17].

Patterning can also be performed on homogeneous brush surfaces using photopatterning, small molecules and biomolecules can be patterned on brush surfaces using this method. Tan *et al*. functionalised the surface of pGMA brushes with alkenes, whereby they used photoinitiated thiol-ene chemistry to attach small molecules and biomolecules presenting thiol groups[132]. They characterised the efficiency of functionalisation and used photomasks to form circular patterns of a thiol on homogenous brush surfaces (characterised by AFM).

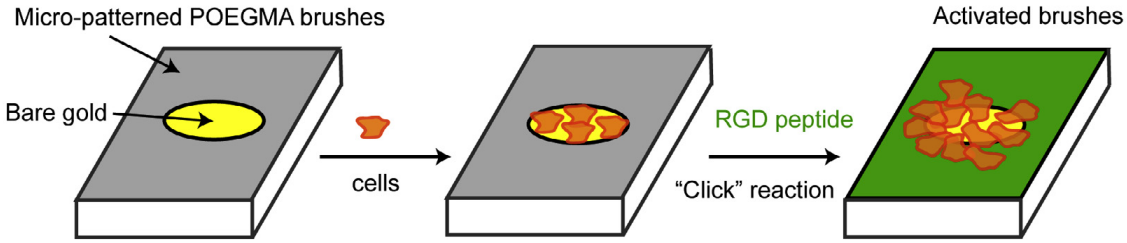

Figure 1.12 Representation of cells patterned on islands and their migration after biofunctionalisation with RGD peptide using thiol-ene coupling[21].

1.3 Synthetic hydrogels for cell culture and tissue engineering

Research in the field of tissue engineering has grown exponentially. Initially, inert materials were used as scaffolds for cells where, proteins and peptides were used to promote adhesion[133]. With time, it is now clear that cells interact with the extracellular matrix and require to degrade as well as deposit novel matrix proteins[4, 134]. Therefore, it is important to design new functional biomaterials that provide structural support as well as sustain cellular spreading, cell migration, stimulate specific membrane receptors, capture growth factors and can be remodelled[135]. The schematic image in Fig. 1.13 represents these features. Hydrogel materials combining these different properties are still elusive. So that the full potential of hydrogels can be exploited for the design of biomaterials for tissue engineering, novel platforms must be developed.

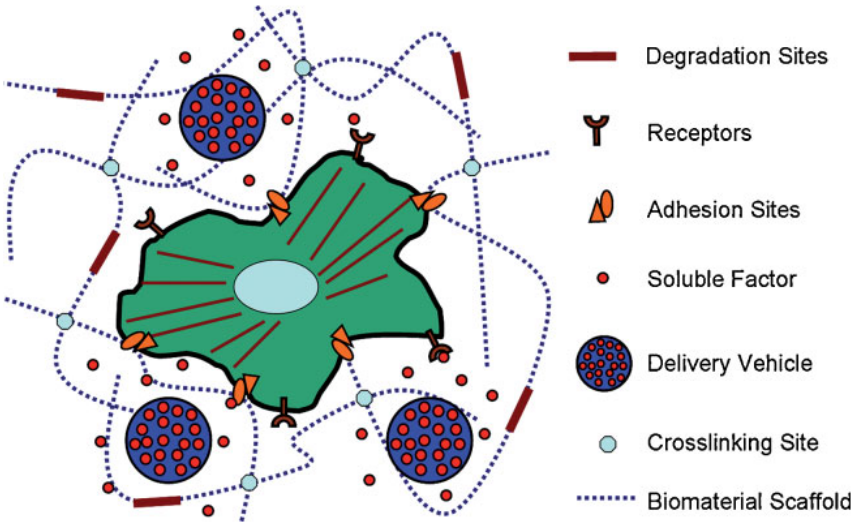

Figure 1.13 The cell microenvironment. The properties of hydrogels can be maniplutaed to try to mimic features of a natural microenvironment[135].

The design of synthetic materials has been a growing aspect in the field of hydrogels for biomedical applications, although natural offer interesting advantages for design of the cell-material interface[136]. However, traditionally used hydrogels based on naturally derived components (such as fibrin gels, Matri-gel or collagen gels) display poor control over the properties of the materials and these properties usually cannot be manipulated with ease[137]. Synthetic or semi synthetic materials provide an advantage over natural materials, as their chemistry can be well controlled to achieve a range of different mechanical and chemical properties[5, 55, 59, 138], they can be incorporated with biologically active molecules to ensure good control over the biological properties (e.g. cell adhesion, migration, proliferation and differentiation)[139, 140]. With this respect, many researchers focused on the production of novel synthetic hydrogel systems. Initially, hydrogels were used to study cell-material behaviour at 2D interfaces as with polymer brushes[21], however, to the field has come to realise the greater potential of hydrogels as 3D materials. Many have started to focus on using hydrogels as 3D biomimetic systems to study and culture many cell types[141-144]. This presents a significant advantage over many biomaterial systems; the development of hydrogels as 3D interacting materials opens up doors for new applications in the biomedical field and in the pharmaceutical industry.

1.3.1 Crosslinking of hydrogels

The new applications for synthetic hydrogels require the development of various chemical techniques for the synthesis and crosslinking of hydrophilic polymer networks. The coupling chemistry used to produce such networks is required to work in mild and aqueous conditions, as well as negligible toxicity if generating 3D systems due to the presence of cells. Synthetic hydrogels require the cross linking of linear polymers to form networks with specific chemical and mechanical properties. Thiol-ene coupling chemistry developed by Sharpless *et al*. is a commonly used system to crosslink hydrogel materials[145, 146]. Thiol-ene chemistry is also suitable as it works efficiently under mild and ambient conditions and is known to occur well under aqueous conditions. Photo-initiated thiol-ene coupling or Michael additions have been developed as non-cytotoxic methods for the production of 3D systems[5, 8, 59]. Thiol-ene coupling also displays another important advantage: it is suitable to be used to couple biologically relevant molecules (usually in the form of peptides) to synthetic materials. Michael addition works under alkaline conditions which can promote disulfide formation, the crosslinking is spontaneous and therefore does not allow for spatially control, however for photopolymerisation these issues are bypassed[9]. Crosslinking via thiol-ene coupling for hydrogels proceeds via free radical addition generated from a photoinitiator upon exposure to UV light. Recently groups have reported the use of visible light and other initiators for curing hydrogels via a thiol-ene mechanism[56, 144, 147-149]. This seems like an interesting approach, as UV exposure can be slightly toxic to cells or may induce DNA mutations, and such systems would avoid the use of any UV exposure for sensitive cell types.

Naturally derived polymeric backbones have also been crosslinked via thiol-ene coupling, such as polysaccharides (i.e. hyaluronic acid and dextran), which were reacted with a series of thiols using photoinitiated thiol-ene[150]. The reaction proceeded in aqueous media and resulted in high coupling efficiency within a few minutes. Bioactive peptides were used as thiol crosslinkers for the generation of hydrogels.

Dargaville *et al*. explored poly(oxazoline)s as backbones for hydrogels[151]. Co-polymers of 2-(dec-9-enyl)-2-oxazoline and 2-methyl-2-oxazoline or 2-ethyl-2-oxazoline were synthesised and crosslinked with a dithiol in ethanol to form hydrogels (Fig. 1.14). The gels were characterised by photorheology and their aqueous swelling behaviour was studied. It was concluded that the degree of swelling in water was tuneable based on the hydrophilicity of the starting co-polymer and the proportion of alkenes present. The dithiol crosslinker was also made hydrolytically cleavable, introducing these materials for potential applications in the biomaterials field.

Figure 1.14 Formation of a poly(oxazoline) hydrogel using UV initiated thiol-ene coupling[151].

Shih and co-workers prepared PEG hydrogels with either photoinitiated thiol-ene coupling or Michael addition (Fig. 1.15)[145]. Results showed that the photoinitiated thiol-ene displayed higher degree of cross linking and occurred

at faster gelling times, resulting in lower mass swelling ratio. The hydrolytic degradation of the ester bonds in the material was investigated and the effect of the pH was observed. Results showed that the material was stable under acidic conditions at pH 6.0, however increased in swelling under basic conditions (pH 7.4 and pH 8.0). The degradation was thought to be governed by the hydrolysis of the ester and also by a base catalysed oxidation of the thioether bond which forms between the thiol and alkene. The studies also showed that a decrease in the crosslinking density and the decrease of the macromer concentration increased the swelling of the material.

Dove *et al*. generated poly(carbonate) grafted PEG hybrid hydrogels using thiol-ene coupling[152]. They studied the morphology of the gels using cryogenic scanning electron microscope and showed that the size of the pores could be controlled by varying the length of the PEG linker. This feature allowed controlling the swelling properties and also the rate of hydrolytic degradation of the gels.

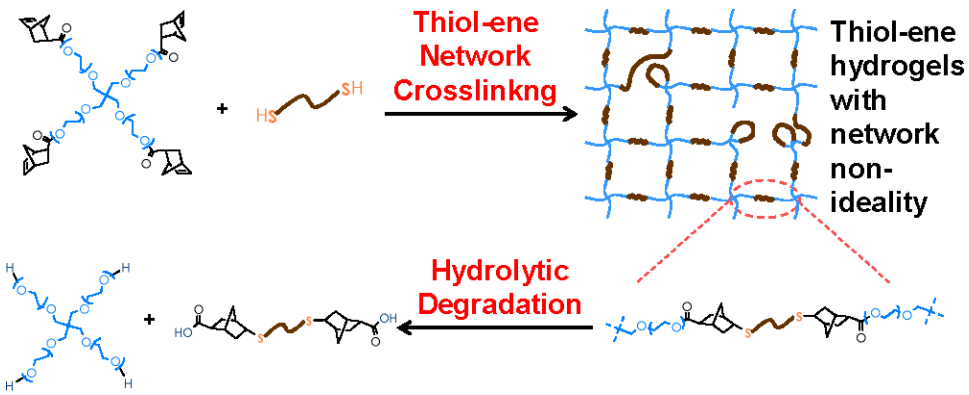

Figure 1.15 Formation of a PEG hydrogel using thiol-ene coupling and its hydrolytic degradation products[145].

1.3.2 Controlling the mechanical properties of hydrogels

Control over the crosslinking density of synthetic hydrogels allowed to generate materials with variable stiffness. Matrix stiffness plays an important role to control cellular behaviour and influences the ability of cells to change their phenotype and gene expression, for example resulting in their differentiation[6, 153]. It was found that fibroblasts, endothelial cells and neutrophils spreading on materials with controlled stiffness showed abrupt changes in cell morphology when in sparse culture, especially in the stiffness range of 3 kPa, below which no actin stress fibres were present[7]. However, when cell-cell contact was apparent, this was ignored, the cell morphology did not change significantly as a function of matrix stiffness. Thiol-ene coupling was used to produce PEG hydrogels of varying stiffness 4-29 kPa[154]. These hydrogels were tailored with cell adhesive sequences (RGDS, VGVAPG) and the behaviour of valvular interstitial cells was studied. Results showed an increase in α-smooth muscle actin expression with materials containing high (1.2 mM) concentrations of CGVGVAPG peptide regardless of the substrate stiffness. Yang *et al*. investigated the coupling of different molecular weight PEG alkenes (2-8 kDa) with trifunctional thiol crosslinkers to produce a series of 4 hydrogels (175-555 kPa)[155]. Olofsson and co-workers functionalised PEG backbones (2k, 6k, 10k and 20k) with allyl dendrons to generate tetra-functional crosslinkable PEG[146]. Hydrogels were produced in ethanol, and crosslinked with tri-functional thiols. The swelling of these hydrogel, their rheological properties and hydrolytic degradation were characterised. Results showed that the molecular weights of the PEG strongly influenced the final properties of the hydrogel. Higher molecular weight hydrogels resulted in increased swelling behaviour, less hydrolytic stability (pH 10) and influenced

the hydrogel stiffness (Young's modulus was reported, 106 MPa to 6 MPa for PEG-2k to PEG-20k hydrogels respectively). Mosiewicz *et al*. investigated a new method for the manipulation of hydrogel stiffness[156]. They used caging chemistry in combination with Michael addition to increase the crosslinking density at required site, able to achieve stiffness-patterned materials (3-8 kPa) which were used to study the migration of mesechymal stem cells and the impact of changes in stiffness.

The relationships between macroscopic and microscopic properties of hydrogels are of particular interest to the materials science community. Tibbitt *et al*. compared the mechanical properties of chain and step polymerised PEG hydrogels (Fig. 1.16)[157]. They concluded that step polymerised hydrogels shows increased mechanical integrity and homogeneity. These hydrogels were also designed to degrade upon UV light exposure. Degradation was studied for both step- and chain-polymerised hydrogels; however, the rate of erosion was faster for the step polymerised hydrogel due to the lower networking density.

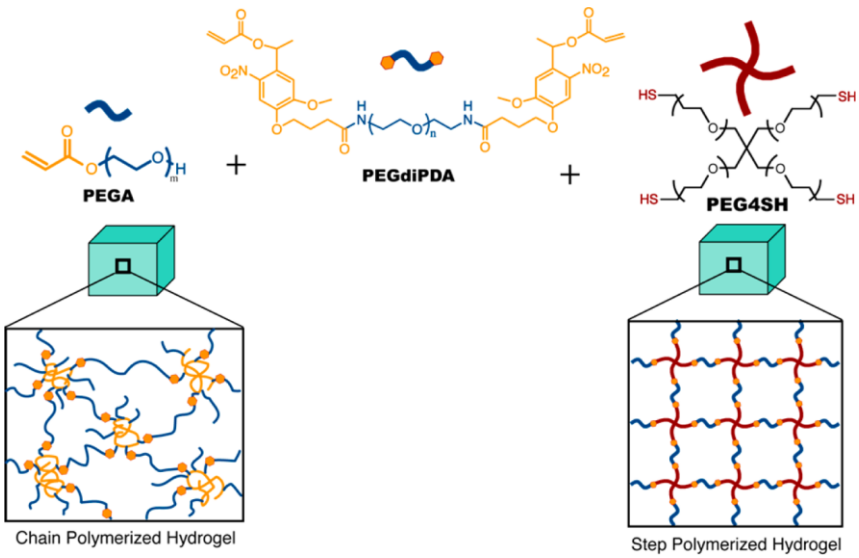

Figure 1.16 Fabrication of step and chain polymerised hydrogels[157].

Grube *et al*. studied the differences and similarities of macroscopic and microscopic mechanical properties of thiol-ene polymerised hydrogels compared to polyacrylamide gels and paid particular attention to their inhomogeneity[158]. Mechanical measurements showed that for both type of gels the inhomogeneity varied by varying the concentration, while the macroscopic properties at particular concentrations were similar. Observations by light scattering showed that the gel inhomogeneity is affected by the method of preparation. Results showed that thiol-ene coupled gels appeared more homogeneous than polyacrylamide gels.

1.3.3 Biofunctionalisation of hydrogels

The success of biomaterials in tissue engineering and regenerative medicine depends on cell-matrix interactions and their performance *in vivo*. There is a need for well define and tuneable matrices. This can be achieved by the introduction of bioactive molecules into the hydrogel network, usually in the form of peptides mimicking the function and activity of proteins.

Toepke and co workers generated PEG hydrogels with controlled stiffnesses, using various concentrations of 4 and 8 arm PEG crosslinked with either a dithiol or 4 arm thiols and characterised their formation, demonstrating their ability to tune mechanical properties in the range of Pa to ~600 kPa[62]. They further introduced an RGD sequence using thiol-ene coupling and studied the attachment of fibroblasts. They found that the amount of peptide incorporated in the hydrogel was proportional to the initial amount in the pre-polymer solution.

Fittkau and co-workers investigated the spreading and mobility of cells in PEG hydrogels[61]. They incorporated a selection of YIGSR (laminin β_1- $\alpha_3\beta_1$, $\alpha_4\beta_1$, $\alpha_6\beta_1$)[159], PHSRN (fibronectin- $\alpha_5\beta_1$)[120, 160] and RGD (fibronectin, collagen I, laminin α_1 and vitronectin- $\alpha_v\beta_1$) into their system and seeded endothelial or smooth muscle cells onto the hydrogel surfaces. Results showed that there was little adhesion and spreading of cells on YIGSR and PHSRN surfaces alone. However, when combined with RGD, YIGSR showed an enhanced migration of endothelial cells but not smooth muscle cells. Research in this field has been developing since, combining peptides to achieve stronger cell behaviour, these systems allow to tune and specifically control different cell types by manipulating surfaces with various active peptides.

Apart from cell adhesion and degradation, other bioactive properties have been conferred to hydrogels via their molecular engineering. For example, hydrogels have been designed to display antibacterial properties. Du *et al.* used thiol-ene chemistry to produce cationic PEG hydrogels (Fig. 1.17)[161]. The cationic moieties were introduced via the connection of ammonium groups to PEG chains. These hydrogels showed strong antibacterial properties to Gram-negative and Gram positive bacteria.

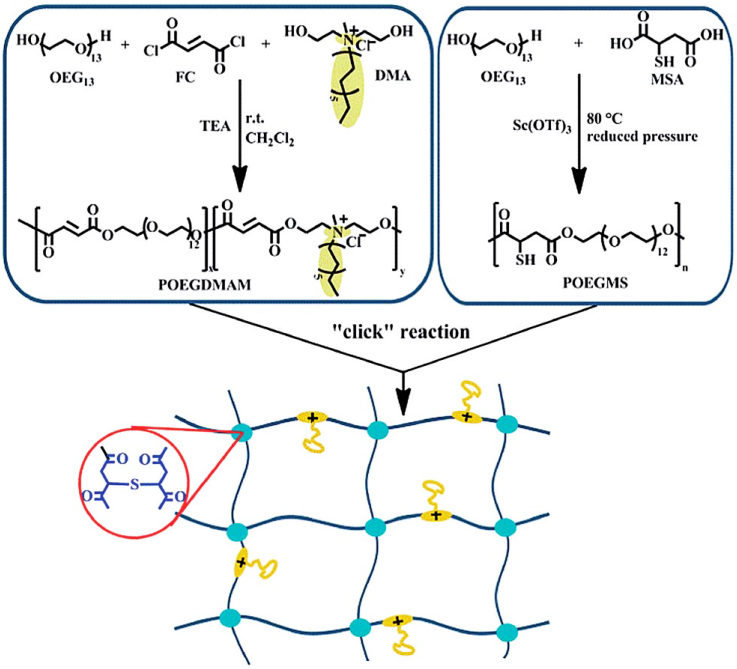

Figure 1.17 An illustration representing the synthesis of cationic gels (FC- fumaryl chloride, DMA- dodecyl bis(2-hydroxyethyl) methlammonium chloride and MSA- mercaptosuccinic acid)[161].

Lundberg and co-workers generated PEG hydrogel coatings for marine anti-fouling applications[162]. They produced a library of hydrogels with different structural compositions by varying the length of PEG chains. These systems were evaluated for the impact of curing, degradation and anti-fouling properties. Results showed that ester free hydrogels were more stable (with respect to hydrolytic degradation) and increasing the PEG chain length resulted in accelerated degradation. The antifouling properties were evaluated

using protein adsorption methods of BSA and marine bacteria. Cleophas *et al*. incorporated a highly active antimicrobial peptide into a PEG hydrogel network using photoinitiated thiol-ene coupling[163, 164]. The hydrogel system proved to be antimicrobial to gram-positive and negative strains demonstrating its potential for applications against biofilm forming bacteria.

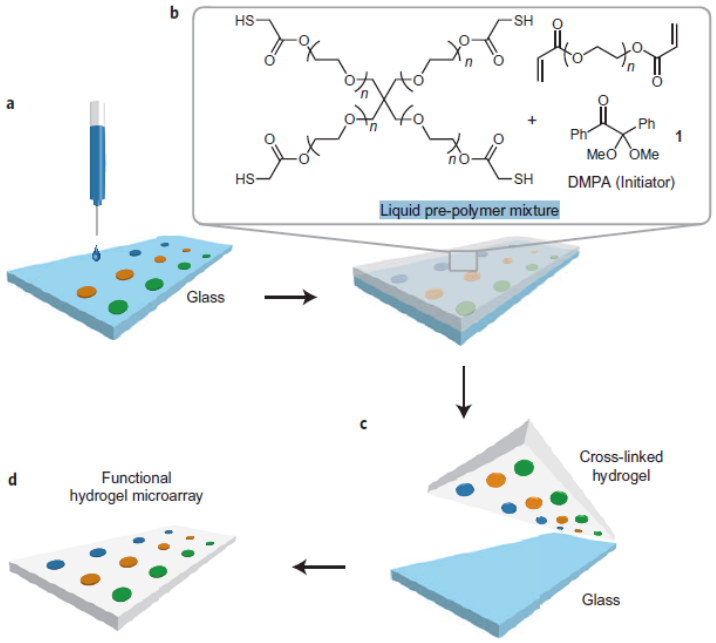

Figure 1.18 Fabrication of hydrogel microarray using thiol-ene coupling[165].

Gupta *et al*. generated a high-throughput system to fabricate PEG hydrogels functionalised with various biomolecules (Fig. 1.18)[165]. The robust nature of thiol-ene coupling allowed for the production of hydrogel microarrays with high yield, under user-friendly and mild reaction conditions and with minimal amounts of active biomolecules required. This is an interesting system that can be used for the incorporation of many active peptides for screening with different cell types. They seeded fibroblasts on peptide functionalised microarrays and studied the attachment of cells; cells only adhered to arrays bound with RGD. They also tested the microarray system for the binding of fluorescent dyes.

1.3.4 Degradation of hydrogels

The behaviour of cells interacting with biomaterials is determined not only by the introduction of bioactive peptides or biomacromolecules allowing for cell adhesion or growth factor signalling, but also by the possibility for cells to remodel their matrix. This has led researchers to generate degradable hydrogel networks. Much of the research focused on the production of hydrolytically degradable networks, usually maintained with the incorporation of ester linkages in polymer backbones[152]. Under buffered conditions the ester linkages break over time, making space for cells to lay their own matrix[166-168]. Other researchers have developed photodegradable networks[167, 169]. Ki *et al*. used a photolabile peptide to crosslink PEGNB gels via visible light-mediated thiol-ene coupling (Fig. 1.19)[169]. The peptide cleaved in the presence of UV light, producing a photodegradable system. Photodegradation allows to change the mechanics of gels, this is an interesting feature and it could potentially be used to partially degrade networks to study the invasion of cells through self-directed routes in 3D cell-gel system.

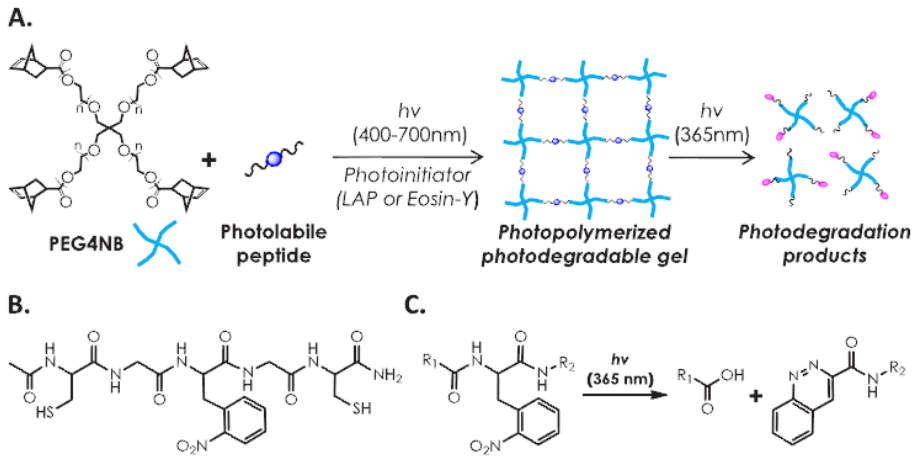

Figure 1.19 a) An illustration of photo-crosslinking and photodegradation of thiol-ene gels, b) the chemical structure of the photodegradable peptide and c) schematic of UV-mediated peptide degradation[169].

Another approach consists in using enzymatically cleavable peptides. The versatility of coupling chemistries such as thiol-ene reaction or Michael addition allowed to introduce peptides as crosslinkers with cysteines present at both ends of the sequence[170]. Peptide sequences can be altered to suit the required application and therefore they can be designed to mimic the enzymatic degradability of specific proteins (or in response to specific enzymes). This is a fast-growing field that has proved very successful for controlling matrix modelling, so far.

Patterson *et al*. investigated up to 29 peptide sequences that are known to be degradable by MMP-1, MMP-2 and plasmin[171, 172]. Michael addition was used to crosslink the peptides and form PEG hydrogels. Michaelis-Menten analysis showed that peptides have various k_{cat} values, associated with each enzyme. Hydrogels with lower k_{cat} values degraded slower. The graded increase in k_{cat} values for various peptides can be used to engineer hydrogels with degradation properties tuned to the enzymes and therefore cell types. Bracher and co-workers crosslinked PEG hydrogels with peptides sensitive to various enzymes and assessed the sprout formation of fibroblasts or smooth muscle cells from cellular spheroids[57]. This data suggests that using enzyme specific peptide crosslinkers has the capability to regulate cell specific invasion and growth.

Degradation rates can also be controlled by manipulating the ratio of degradable to non-degradable crosslinkers. Chwalek and co-workers combined enzyme sensitive and insensitive peptides as crosslinkers and studied the release of VEGF and also the impact of such design on cell behaviour[173]. The enzymatic degradation was increased with the introduction

of insensitive (non-degradable) peptides; this was thought to increase the accessibility of enzymatically cleavable sites in the gel. Gels that degraded faster and released VEGF showed enhanced endothelial cell invasion in 3D encapsulated systems. They concluded that the combination of sensitive and insensitive peptide crosslinkers amplified the gel degradation and influenced the endothelial cell morphogenesis which was surprising. However, this study also considered the influence of VEGF released from the hydrogel and therefore, this could have played an important impact on the cell behaviour. Hence, the cell morphogenesis observed may not only be affected by the degradation rate but also the release of VEGF.

Degradable hydrogels have also been developed for the delivery of biomolecules[174]. Holloway and co-workers generated a MMP sensitive hyaluronic acid based hydrogels for the delivery of BMP-2 for bone repair applications[175]. They produced gels of varying stiffness by altering the crosslinking density, either through polymer concentration or maleimide functionalisation of hyaluronic acid. Dithiol functionalised peptide (GCRDVPMS↓MRGGDRCG) was used as the degradable sequence. Results show the degradation of the hydrogel and release of BMP-2, specifically in the presence of collagenase II. Fig. 1.20 Reports the percentage of mass loss with different concentrations of collagenase II and with different concentration hydrogels.

Shih *et al*. studied PEGNB hydrogels (4 wt%, 2 kPa) crosslinked with bis-cysteine peptides that were either sensitive (CGGY↓C) or insensitive (CGGGC) to chymotrypsin[145]. The non-sensitive peptide material showed faster swelling and loss of elastic modulus than the material containing the

chymotrypsin sensitive peptide. Similar behaviour was reported by Chwalek *et al*.[173]. The argument that was made to account for this observation was that the presence of a tyrosine in the chymotrypsin sensitive sequence facilitated steric hindrance (and perhaps aggregation), yielding slower degradation[145]. This enzymatic degradation study led to the production of PEG4NB materials containing different ratios of CGGGC: CGGY↓C (100:0, 75:25, 50:50, 25:75, and 0:100). When immersed in a chymotrypsin solution, materials containing more sensitive peptides showed surface erosion. This is interesting; with 2 kPa gels we would expect the diffusion of enzymes into the gels and the degradation of the bulk rather than through surface erosion.

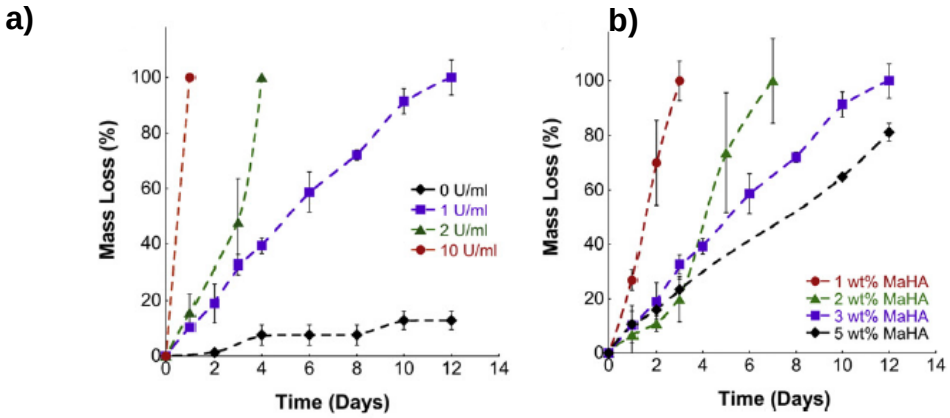

Figure 1.20 Hydrogel mass loss as a function of a) collagenase concentration with 3 wt% gel and b) different concentrations of hydrogel with 1 U/mL collagenase[175].

Peptides are expensive especially when required in large sequences and quantities. This is sometimes a limitation for the generation of new biomaterials since larger quantities of material is required for further investigations. Jo and co-workers investigated the use of a plasmin-sensitive tri-amino acid peptide as a crosslinker to generate PEG hydrogels[176]. In vitro and in vivo degradation experiments were performed and showed the infiltration of cells into the gels and their ability to be remodelled.

1.3.5 Hydrogels for 2D cell culture

Many hydrogels have been studied as 2D systems for cell culture. The biointerface plays an important role for determining the cell response to these materials. Many hydrogels have been functionalised with biomolecules such as peptides to allow cell adhesion specifically via integrins and crosslinked to enable enzymatic degradation[177]. An important research effort has also focused on the study of the impact of hydrogel mechanics on cell phenotypes such as adhesion[178], spreading[7, 179], migration[180], proliferation[181] and differentiation[5, 182]. These are important aspects for understanding cell-material interactions enabling to produce more advance systems.

In 2013, Farrugia *et al*. synthesised an alkene functional poly(oxazoline) co-polymer and cross-linked it with a dithiol using photoinitiated thiol-ene reaction[40]. A 10% w/v hydrogel was produced under aqueous conditions. These hydrogels were cell repulsive. Hydrogels containing bioactive peptides or thiols (0-25%) were generated: CRGDSG, CRDGSG and 2-mercaptoethanol, the remaining alkenes were reacted with DTT to form a crosslinked network. The effect of such composition on the behaviour of human dermal fibroblasts was investigated. Hydrogels containing the RGD integrin binding motif showed an increased level of fibroblast attachment. However, the percentage of incorporated peptide did not change the level of cells attached but did change the cell morphology. With increasing loading of RGD peptide, the orientation of the actin fibres became more aligned.

Goktas and co-workers reported an interesting approach for the biofunctionalisation of hydrogels of variable stiffness[179]. They introduced self-assembled peptide amphiphile nanofibres into PEG hydrogels to create

composite hydrogels, changing the concentration of PEG allowed to produce gels of variable stiffness (Fig. 1.21). They studied the impact of the mechanical properties and biofunctional nanofibres on Saos-2 cell attachment and spreading. More cells adhered to the softer gels with RGD functional fibres; however the cells on stiff RGD showed more spreading. Cells were also encapsulated into the PEG gels with and without RGD fibres, the cells showed better viability with the fibres present.

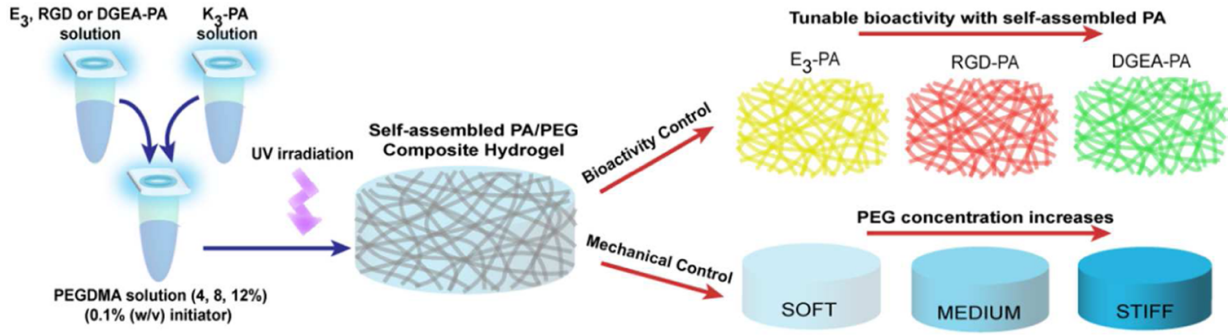

Figure 1.21 Fabrication of PEG nanofibre composites representing control ober the bioactivity and mechanial properties of the hydrogel[179].

Biological processes are dynamic in nature, and the stiffness of materials is an important property, however, much of the systems produced are static[5]. Guvendiren and co-worker created a new platform that stiffens hydrogels (3-30 kPa) in the presence of cells with the application of external light; this allowed to study the cell response to the changing environment. They studied the system using rheology and confirmed the increase in stiffness over an order of magnitude. Mesenchymal stem cells were seeded on soft, soft-to-stiff and stiff gels (Fig. 1.22). Cells remained rounded on soft gels and their spreading increased as the gel was stiffened. They studied the generation of traction forces by cells and their differentiation to osteogenic (on stiff) and adipogenic (soft) lineages.

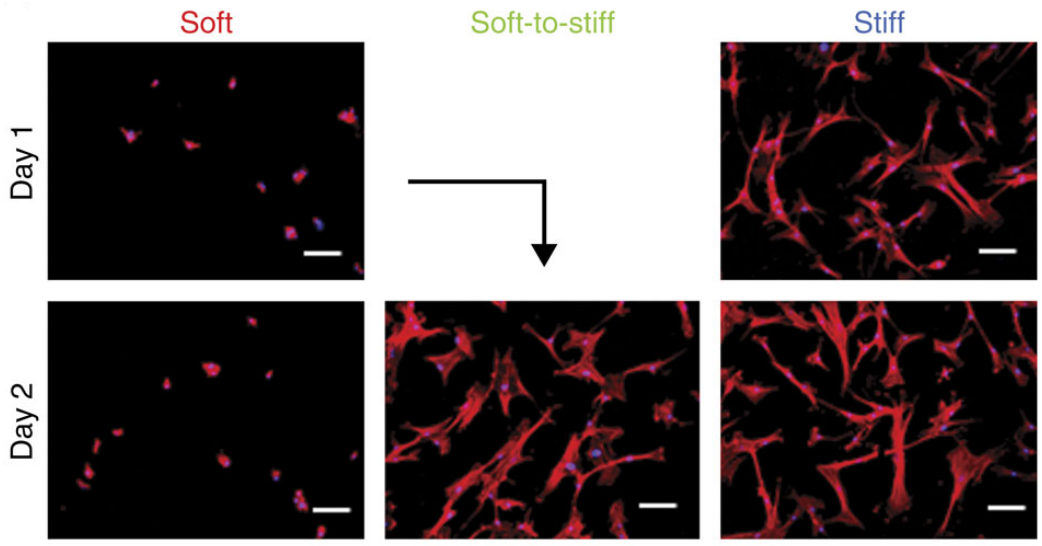

Figure 1.22 Mesechymal stem cells on soft (3kPa), soft-to-stiff (3-30kPa) and stiff (30kPa) substrates on day 1 and day 2. Red (phalliodin), blue (DAPI) and scale bar 100μm[5].

In 2008, Rydhom and co-workers patterned hydrogel chemistry with RGD using photochemistry and a mask[133]. Fibroblasts were seeded on these surfaces; cells adhered to the RGD functionalised areas. Since then the area of patterning biomolecules[183, 184] and gel mechanics[20, 185] have received much attention.

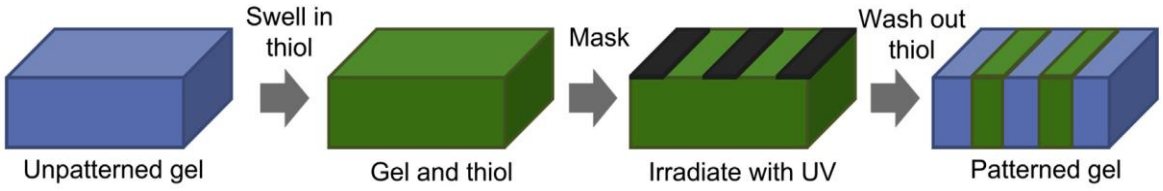

Figure 1.23 The general method for the generation of photopatterned hydrogels[20].

Gramlich *et al*. patterned hyaluronic hydrogels using UV initiated thiol-ene coupling (thiol: norbornene)[20]. They patterned with dithiols to initiate further crosslinking and also monothiols to vary the biochemical properties of the gels. Results showed a significant increase in mechanical stiffness when patterned with dithiol crosslinkers, but no difference with monothiols. They synthesised

hydrogels and swelled them in the thiol containing solution, samples were irradiated with UV through a photomask and the remaining thiols were washed out to results in either mechanical or chemically patterned hydrogels (Fig. 1.23). The UV exposure time during patterning was varied; they showed that the intensity of the fluorescence increased as more dye reacted with the gels, however, longer UV exposure times result in photobleaching, therefore, an optimum amount of UV exposure is required (Fig. 1.24). Gramlich and co-workers also demonstrated the patterning of different dyes and shapes within the same hydrogel. They report the patterning of chemical and mechanical signals that allowed introducing heterogeneity into hydrogels for the manipulation of the cell microenvironments.

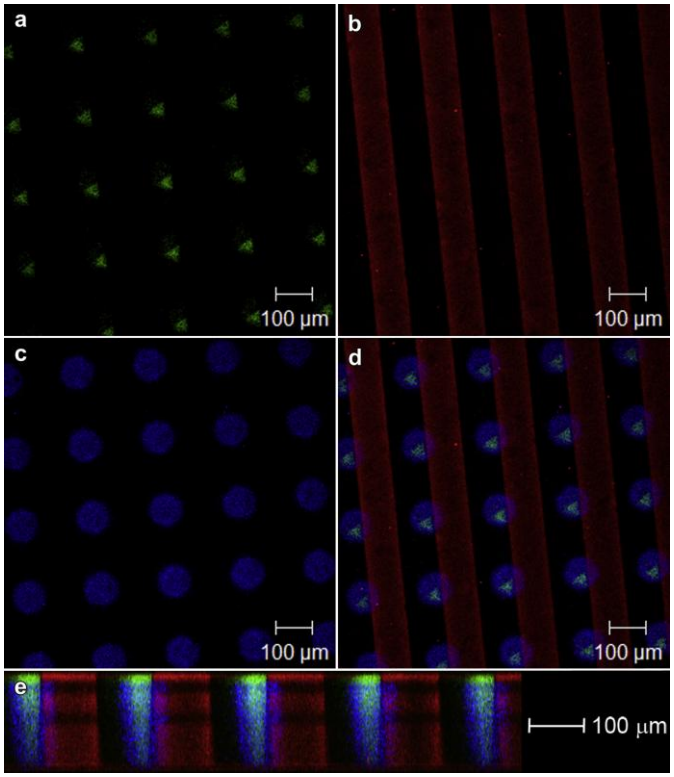

Figure 1.24 Fluroescent images of sequenctially patterned hydrogels: a) triangles with 5(6)-carboxyfluorescein, b) lines with rhodamine b and c) circles with 7-methoxycoumarine-2-acetic acid. d) Represents the merged channels and e) demostrates the depth of the patterns through the gel. Scale bars 100 µm[20].

DeForest and co-workers used photoinitiated thiol-ene to pattern hydrogels with bioactive peptides (RGD)[186]. They observed a change in cell morphology in the peptide patterned areas confirming the importance of biofunctionalisation and the specificity of their materials to sustain integrin-mediated cell adhesion. They further developed their system to generate photoreversible patterning of biomolecules[187]. They introduced RGD patterns and seeded fibroblasts to observe the attachment in RGD patterned areas only (Fig. 1.25). Then they activated the photocleavable site on the RGD to detach the biomolecule from the surface of the gel, with this the cells also detached from the patterned areas.

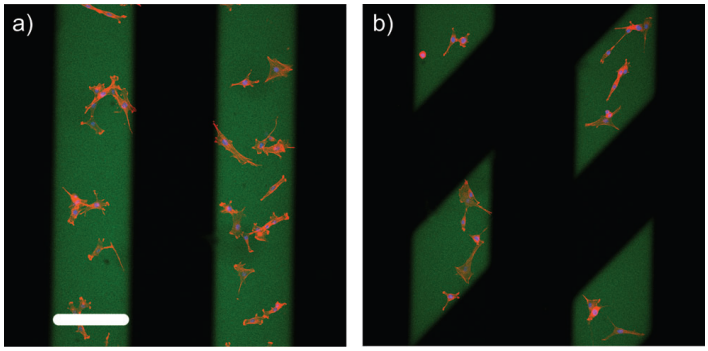

Figure 1.25 Fibroblasts attached on RGD patterned areas of hydrogel. Green (RGD-Alexa Fluor 488), Red (phalliodin), blue (DAPI) and scale bar is 200μm[187].

1.3.6 Hydrogels to control the 3D microenvironment of cells

Much of the research reporting cell-hydrogel interactions has focused on 2D materials; however, this does not reflect the true biological environment. For this it is crucial to develop new platforms for 3D biomimetic hydrogels. This will enable to better understand cellular responses to the microenvironment, a collection of factors including soluble cytokines and growth factors, cell-cell interactions and matrix interactions[188]. Understanding such interactions will allow to considerably expanding our repertoire of biomaterials for applications in the biomedical field, in particular for regenerative medicine. In 2009, DeForest *et al*. encapsulated cells within click hydrogels for the first time[186]. This advanced the potential of click hydrogel systems as 3D matrices for cell culture. This has led to a shift in the trend in this field, with researchers using click hydrogels focusing on 3D rather than 2D systems[142, 189, 190]. The most common methods for creating 3D cell-gel constructs are with collagen or Matri-gel, however the gelation of these materials cannot be controlled precisely and these matrices cannot be designed readily[191].

Neumann *et al.* used photo-initiated thiol-ene coupling to generate PEG hydrogels from 8-armed PEGNB whereby the crosslinks contained hydrolytically degradable caprolactone segments[192]. They encapsulated chondrocytes in the hydrogels for up to 4 weeks and assessed the degradation of the gels and also the deposition of ECM proteins over time. Results showed an increase in compressive modulus from 7 to 28 days as a result of matrix deposition. These results were interesting, they did not use peptides to introduce biofunctionality or enzymatic degradation into these gels, the cells responded well by laying their own matrix. They concluded that hydrolytically

degradable hydrogels provide a promising platform for cartilage tissue engineering.

Patterson *et al.* used Michaelis-Menten analysis to show that peptides have various k_{cat} values for enzymes[171, 172]. Fibroblasts were encapsulated in hydrogels crosslinked with various enzyme active peptides. Results showed that hydrogels with higher k_{cat} values degraded faster and this correlated with increased cell proliferation and cell spreading, over a time course of 26 days. Hence, peptides displaying different degradation rates can be used to engineer and fine tune hydrogels to suit a range of different cell types in 3D cultures.

In 2010, Bott *et al*. generated a series of degradable PEG based hydrogels and compared them to collagen as materials for 3D fibroblast culture[142]. They concluded that cell proliferation can be manipulated through the alteration of the gel properties. Mechanical characteristics highly influence the cell behaviour, acting as a barrier at 2.5 wt% (1.2 kPa). Cell spreading decreased with increasing stiffness, fibroblasts generated interconnected multicellular networks with 1.5% (0.25 kPa) and 2% gels (Fig 1.26). Enzyme-sensitive and insensitive cell-gel constructs were compared at week 3, reduced cell spreading was observed for enzyme insensitive gels. Collagen constructs showed highly dense cellular network formation. Comparison of the PEG and collagen gels showed that differences in viscoelastic behaviour may influence the mechanisms cells use to remodel their matrix.

To better understand the role of biophysical and biochemical cues on cell migration, 3D PEG hydrogels with various crosslinking density, controlling the matrix stiffness, were used to study the behaviour of preosteoblastic cells[139]. Migration behaviour was strongly dependant on the hydrogel stiffness with two

regimes recognized: cells migrate faster in non-degradable soft hydrogels and in enzyme degradable gels at high stiffness. Raeber *et al*. investigated the migration of fibroblasts with response to cyclic mechanical loads[140]. Results showed that cells increased their proteolytic migration activity and orientated themselves in the direction of principal strain, cells preferred to move parallel to the principal strain axis.

Matrix degradability also plays an important role in cell morphology and cell fate. Khetan and co-workers compared covalently crosslinked and physically crosslinked proteolytically cleavable hydrogels to better understand the role of degradation on cell morphology and differentiation[8]. They conclude that the differentiation of hMSCs is directed through degradation-mediated cellular tractions, directly correlated with gel mechanics and cell shape. Cells that displayed increased spreading and high tractions favoured osteogenesis in soft gels and the opposite for adipogenesis, in stiff gels. Importantly, this is the exact opposite of what is observed on 2D gels[193] or in non-degradable 3D gels[194]. With the introduction of secondary crosslinking to increase crosslinking density, cells can be switched from osteogenesis to adipogenesis.

Hydrogels based on naturally occurring materials have been used as 3D encapsulation materials for cells. Gelatin crosslinked hydrogels have received attention for 3D cultures. Gelatin can offer an alternative method to hyaluronic based gels and this material is much cheaper. In 2012, Fu *et al*. introduced thiol functional groups to the gelatin backbone and crosslinked using PEG diacrylate using thiol-ene to generate hydrogels[195]. Unmodified gelatin was incorporated with PEG diacrylate to generate gels that were not covalently crosslinked. Both gelatin hydrogels were studied with encapsulated fibroblasts

and assessed over 28 days. Fibroblasts in physically incorporated gels were rounded and in thiol-ene gels were spread with cellular network formation. In 2014, Mũnoz and co-workers, functionalised gelatin with norbornene, crosslinked with PEG tetrathiol to form hydrogels using photoinitiated thiol-ene coupling[143]. They compared physically crosslinked gelatin gels with covalently crosslinked thiol-ene gels for hMSCs encapsulation. Results showed that cells cultured in the thiol-ene gels promoted faster and higher degree of cell spreading.

Hydrogels based on PEG and naturally occurring polymers such as hyaluronic acid have been very successfully applied to cell culture in 2D and 3D[138], however natural polymers are typically associated with important batch-to-batch variations and can be very expensive, whilst PEG is not ideally suited for molecular design as only its end chains can be functionalised easily (and its synthesis relies on the use of highly toxic, mutagenic and potentially explosive ethylene oxides and derivatives). New materials for 3D hydrogel systems are required to overcome these aspects should find applications the biomaterials field. After PEG and hyaluronic clickable hydrogels, a new class of polymers that display promising features is poly(oxazoline)s. These polymers are being adapted for 3D cultures. The cytotoxicity of poly(oxazoline) based hydrogel networks on human dermal fibroblasts was studied[40]. Cells were encapsulated in CRGDSCG (0-25%) DTT crosslinked gels. Live/dead assay were performed at 1 and 8 days, 80% of the cells were viable for hydrogels containing the bis-cysteine peptide. The gels were reported to be highly transparent which enabled the imaging of cells using confocal microscopy, making this hydrogel system an interesting potential candidate for further uses. pOx Hydrogels were

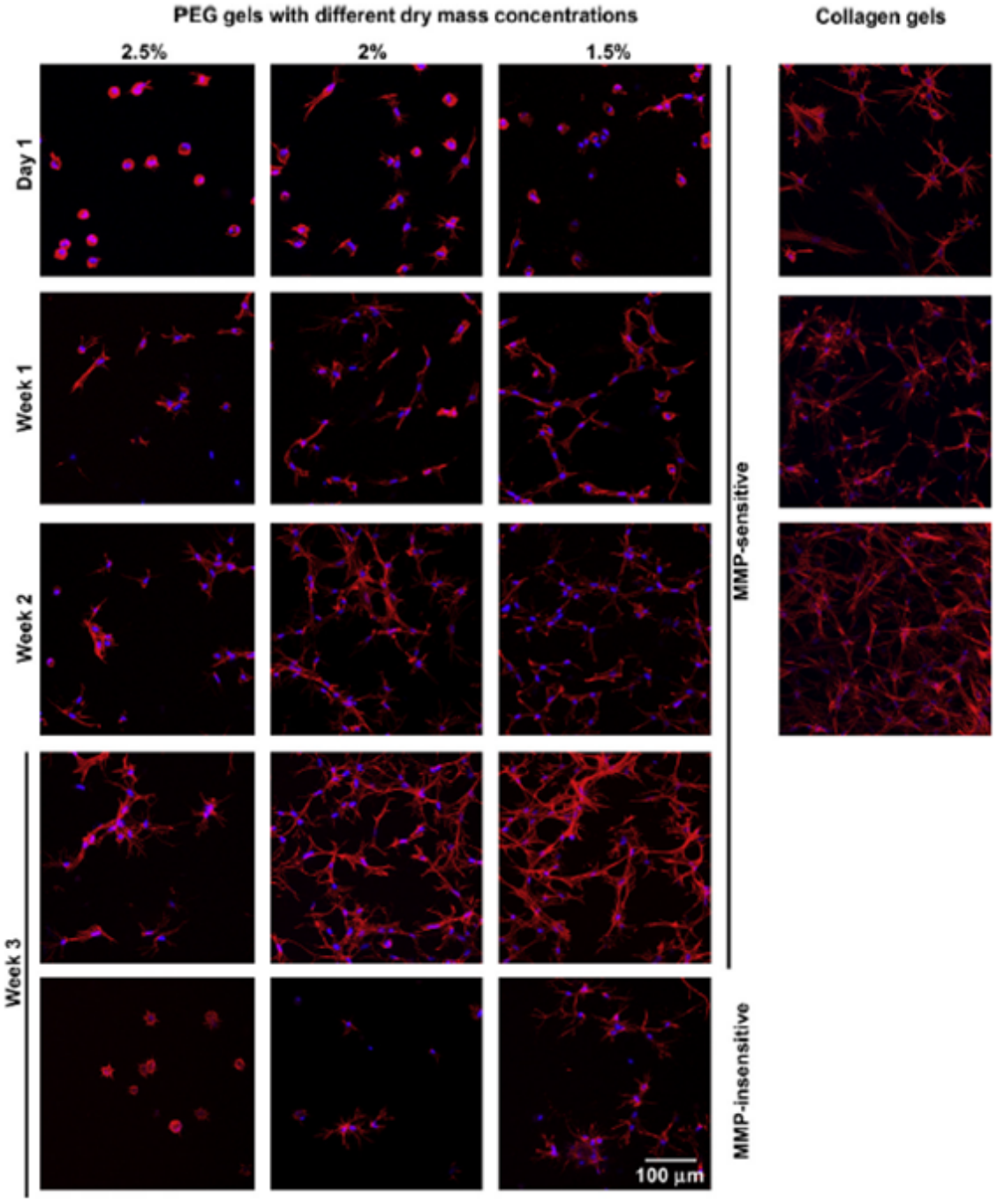

Figure 1.26 Fibroblast morphology in 3D encapsulated gels of variable stiffness (represented by dry mass) over of 3 weeks. Images with and without enzyme sensitive crosslinker represented at week 3. PEG gels compared to collagen gel over 2 weeks. Cells stained with phalliodin and DAPI[142].

made from 10% weight/volume polymer and showed moduli ranging from 3.5-10 kPa. The range of stiffness achieved is comparable to PEG and hyaluronic acid gels[9, 145, 150, 157, 174, 189]. However, in some cases it is possible to achieve higher stiffnesses with PEG gels. This is because pOx gels require a larger

quantity of polymer to achieve similar crosslinking densities. This is related to the lower percentages of alkenes present in the polymer and the number of crosslinks made per chain polymer. pOx polymers require more development to achieve higher densities of alkene functionalisation.

Spatial control over hydrogels and therefore cell behaviour can be achieved by further crosslinking and also patterning adhesive peptides[9, 55, 189]. Hyaluronic acid hydrogels were crosslinked using a degradable peptide, then crosslinked further at UV initiated sites with non-degradable crosslinks[196]. This system allowed to pattern gels with different crosslinking densities in the different patterned regions and enabled to control cell morphology together with the spatial distribution of these phenotypes. Where cells were in degradable gels they adopted spread morphology, and were rounded when in UV initiated gels. (Fig. 1.27). The manipulation of the microenvironment may be valuable in the development of hydrogels systems for advanced tissue engineering purposes. Hence biophysical cues in hydrogels can be manipulated in both space and time. Mosiewicz and co-workers, demonstrated the use of a light beam to increase the crosslinking density in applied regions with cells present in 3D hydrogel platforms, creating a micro-patterned environment that cells recognise after culture[183].

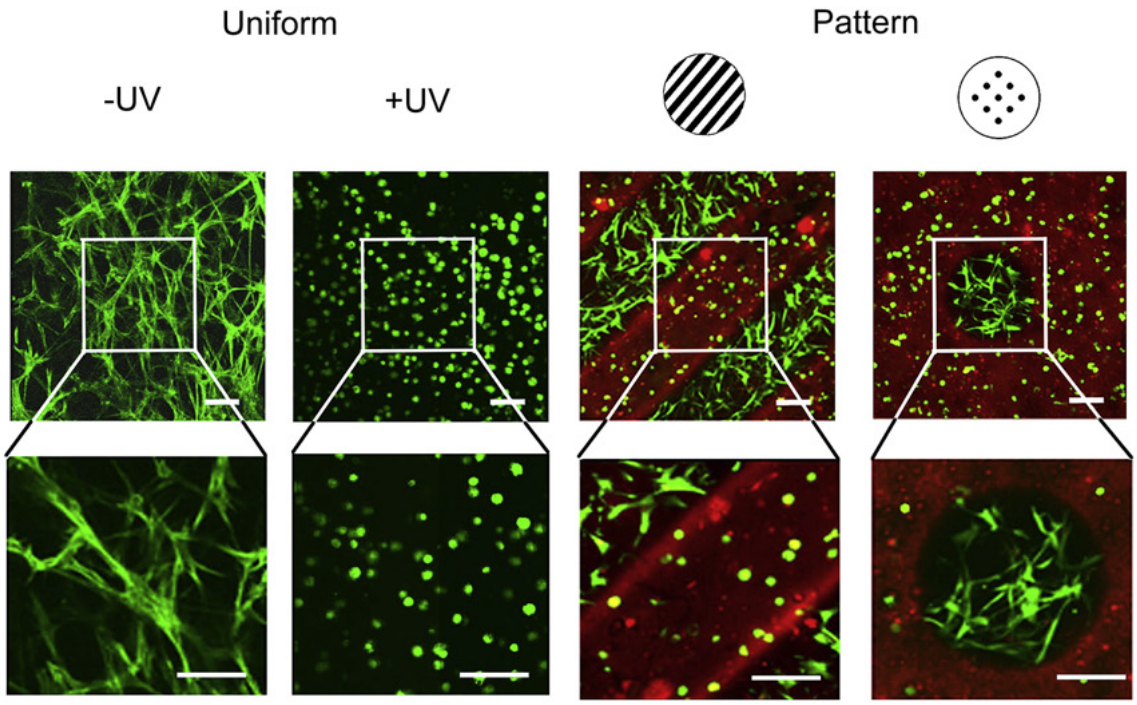

Figure 1.27 hMSCs encapsulated in uniform and photopatterned hyaluronic acid hydrogels after 14 days. Cells stained with calcein, scale 100μm[196].

Signalling pathway analysis can be used to study active molecular processes in tissue development and progression of cancer. These studies are usually employed on 2D surfaces, however, these do not directly relate to the true *in vivo* environment. To assist with the studies in this field, some has employed the used of synthetic hydrogels as 3D culture systems[197]. Loessner *et al*. compared 2D and 3D cultures systems with epithelial ovarian cells[141]. They concluded that the design of hydrogels and their ability to be manipulated for various features,their long term stability in culture conditions, makes hydrogel systems more versatile and physiologically relevant for the investigation of cancer models in 3D environments.

Photo-initiated thiol-ene crosslinked enzyme degradable hydrogels were used for studying cell growth, morphology, drug resistance and cancer stem cell marker expression in pancreatic ductal adenocarcinoma, a platform for which

cells were encapsulated in 3D[198]. Kraehenbuehl and co-workers used PEG hydrogels to direct differentiation of P19 embryonal carcinoma cells as a model[199]. Matrix elasticity, protease sensitivity and concentration of the adhesive peptide RGD were modulated to evaluate the effect of such composition on differentiation. 3D hydrogel systems allow for the study of cell behaviour in response to a variety of features.

The ability to control the features of hydrogels makes them suitable for 3D cell culture systems. Hydrogels provide a selection of properties that can be manipulated during cell encapsulation: chemistry, gelation, mechanics, biofunctionalisation, degradation and patterning. They allow for the study of cell behaviour in response to manipulations in the microenvironment. 3D cell culture systems allowed to study the adhesion, migration, proliferation and differentiation of cells. The ability to control the cell microenvironment plays a crucial role in understanding why cells make the choices they do.

1.4 Summary

Thiol-ene coupling has received much attention in the last decades especially after the report by Sharpless *et al.* where it was classified as a click reaction[10]. Factors influencing the reaction efficiency have been reported; type of photoinitiator, temperature, UV exposure time, photoinitiator concentration, UV light intensity and thiol-ene ratio. Thiol-ene coupling has been applied in the field of polymer synthesis and functionalisation, has been particularly studied in organic solvents, in concentrated solutions or neat monomer systems[29, 200-203]. Whereas these conditions are perfectly suited to macromolecular design, they are often poorly adapted to the biofunctionalisation of biomaterials and the *in situ* preparation of hydrogels for 3D cell culture. Indeed, for such applications, low concentrations and reactions in buffers preserving the structure of proteins or the viability of cells are required. Therefore, it is important to study and understand the behaviour of thiol-ene chemistry in biologically relevant conditions and contexts.

A wide variety of strategies have been developed to create produce biomaterials with cellular function. The focus of this review was placed on polymeric brush systems and hydrogel networks. Polymer brushes and their physical and chemical properties were discussed[101]. Reports showed that brush systems are suitable materials for biofunctionalisation. It is possible to achieve biofunctionalisation by coupling cysteine containing peptides using thiol-ene coupling[21, 132]. Also, photoinitiated thiol-ene could be used to produce patterned brushes with variable features. All these features showed that polymeric brush materials are suitable systems for 2D cell culture.

Researchers have come to realise the importance of the microenvironment during cell culture. For this they have placed focus on the synthesis of 3D cell culture materials. Hydrogel systems provide a good base for this type of biomaterial. Many researchers have developed their gel systems by focusing on various physical and biochemical features of the gels; stiffness, gelation, biofunctionality and degradation. The combination of these aspects has allowed generating hydrogels that are fully applied as 3D culture materials[142].

The aim of this project is to characterise the factors influencing the thiol-ene reaction under aqueous buffered conditions, specifically studying the impact of UV exposure time and light intensity, PI concentration and pH of buffer with a series of thiols and alkenes including polymers and peptides. The application of thiol-ene coupling with polymer brushes systems and their application as 2D cell culture materials. The synthesis and characterisation of polymeric alkenes and their formation of hydrogels through thiol-ene coupling. The ability to manipulate various characteristics of the gel (stiffness, biofunctionality and degradation) and to test the hydrogel as a 3D cell culture material.

Chapter 2

Thiol-ene chemistry

2.1 Thiol-ene methodology

Recently, the robustness and simplicity of thiol-ene chemistry, the mild conditions required and the availability of alkene functions as side chains of macromolecules (including those not activated towards polymerisation or Michael additions) and that of thiols present in proteins and peptides, specifically through cysteine residues, have contributed to its popularity for biofunctionalisation and hydrogel formation. Thiol-ene chemistry was used for the biofunctionalisation of surfaces and polymer brushes, for example for the generation of protein patterns or the design of dynamic cell-based assays via *in situ* peptide coupling[21, 132]. Hydrogels have also been produced via thiol-ene based crosslinking[20, 62, 145]. In many of these systems, thiol-ene coupling is used to confer biofunctionality and bioactivity to the corresponding biomaterials, through the use of peptide sequences presenting cysteine residues[142, 150, 163, 183]. This strategy was applied to confer cell adhesion to biomaterials and culture platforms[21] and dicysteine peptides were used to

crosslink polymers and form enzymatically degradable hydrogel networks[40, 145, 176, 204].

Despite such interest in applying thiol-ene coupling to biomaterials chemistry, little is known of the impact of structural parameters controlling the efficiency of thiol-ene coupling in buffered and physiological conditions. Compared to more traditional systems used in polymer functionalisation and the curing of resins, the impact of the chemistry of the biomaterials to be functionalised on thiol-ene coupling is not well established. Similarly, rules and guidelines controlling the reactivity of peptides via radical thiol-ene reactions have not been investigated systematically. In particular, the impact of changes in the molecular environment of the reactive centres, which have been directly implicated in the regulation of disulfide exchanges for example[205, 206], has not been systematically studied but should contribute to simplify and standardise the use of thiol-ene radical coupling for bioconjugation and biofunctionalisation of biomaterials. Such understanding will also be essential to control reaction conditions in biologically relevant conditions (for example, during cell encapsulation in 3D hydrogels, *in vitro* or for *in vivo* delivery) and to manage and address toxicity and mutagenicity concerns. Here we systematically study some of the reaction parameters (pH, concentration, type of medium) and structural factors (chemistry of polymer backbones, thiols and cysteine-bearing peptides) controlling radical thiol-ene coupling in biologically relevant buffers. To this aim, we developed simple methodologies, using ^{1}H NMR spectroscopy and HPLC, to quantify reaction efficiencies. We identify important rules for the design of the chemical structure of thiol-ene based biomaterials.

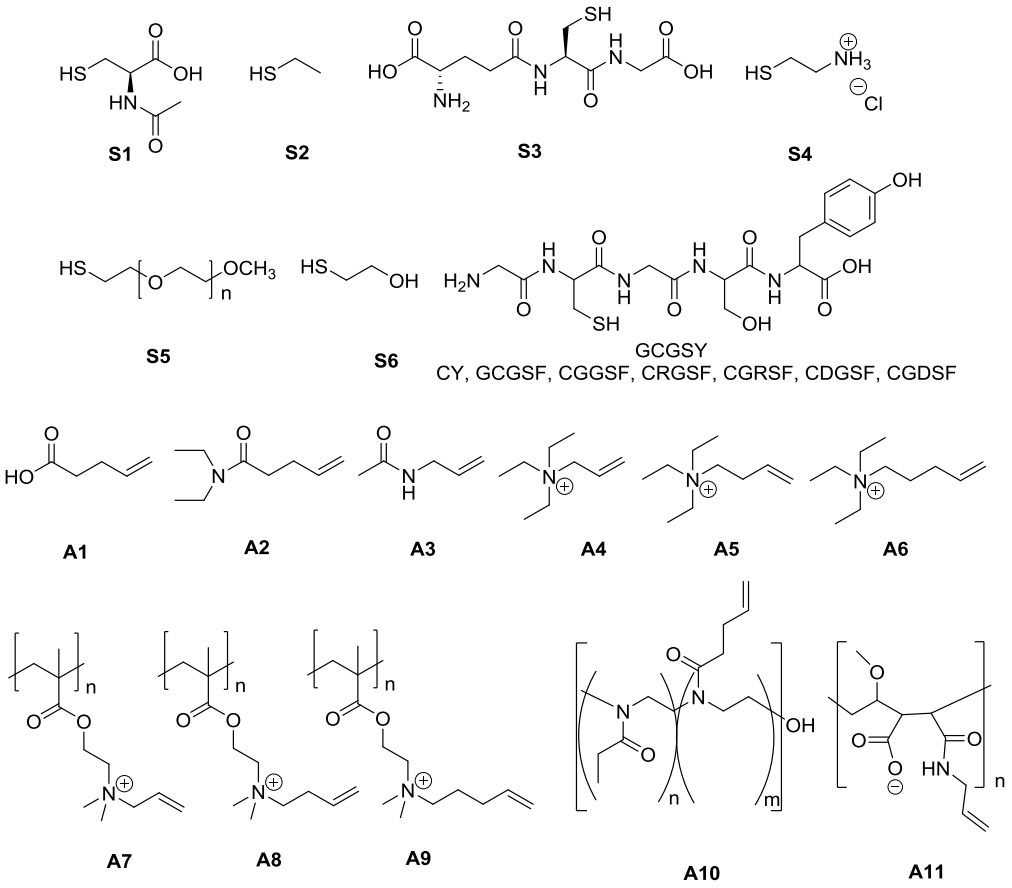

Figure 2.1 Series of thiols (S1-6 and peptides) and alkenes (A1-A11).

2.1.1 Design of a model system to study thiol-ene coupling.

The reaction of a range of thiols (**S1-5**) with pentenoic acid **A1**, in equimolar concentrations, was used as a model system to monitor the coupling of thiols to alkenes in buffered conditions relevant to biofunctionalisation (Fig. 2.1). These molecules were selected based on their solubility in PBS, simplicity of chemical structure and low molar masses. The efficiency of coupling was assessed via ^{1}H NMR spectroscopy, via the integration of the peaks at 4.8-5.1 and 5.8-5.9 ppm, corresponding to olefinic protons, and that of the peaks at 1.5-1.68 and 2.54-2.61 ppm, corresponding to the formation of thioethers (Fig. 2.2). However, the peaks at 4.8-5.1 ppm were almost always distorted by the presence of the water peak at 4.8 ppm, therefore this peak was no longer used for the conversion calculations. The single proton peak at 5.8-5.9 ppm was not affected by the water peak and was chosen as the reference peak for all experiments. In some cases ^{1}H NMR spectroscopy phase and baseline corrections were performed to achieve a straight baseline at zero, integrations of peaks were measured most accurately and consistently.

We first investigated the effect of UV exposure time on the efficiency of the thiol-ene reaction (Fig. 2.3). Reactions with thiols **S1-5** all reached 92-100% in 45 s of exposure to UV light, however, the reaction was sensitive to the molar mass of the reactants and associated steric hindrance, as the rates of coupling of PEG methyl ether thiol **S5** and *l*-glutathione **S3** were the slowest. Fig 2.4 shows the ^{1}H NMR spectroscopy for the thiol-ene reaction products. For the rest of our studies, an exposure time of 60 s was used as conversions did not significantly improve between 45 s and this time point. In addition, we investigated the impact of the photoinitiator concentration and the intensity of the UV light on the extent of reaction (Fig. A1.1 and A1.2). We found that at an

initiator concentration of 2 mol% (1 mM, conversions were already reaching a plateau. The UV exposure time had a clear impact on reaction conversions, with coupling efficiencies reaching a plateau near 10 mW/cm^2.

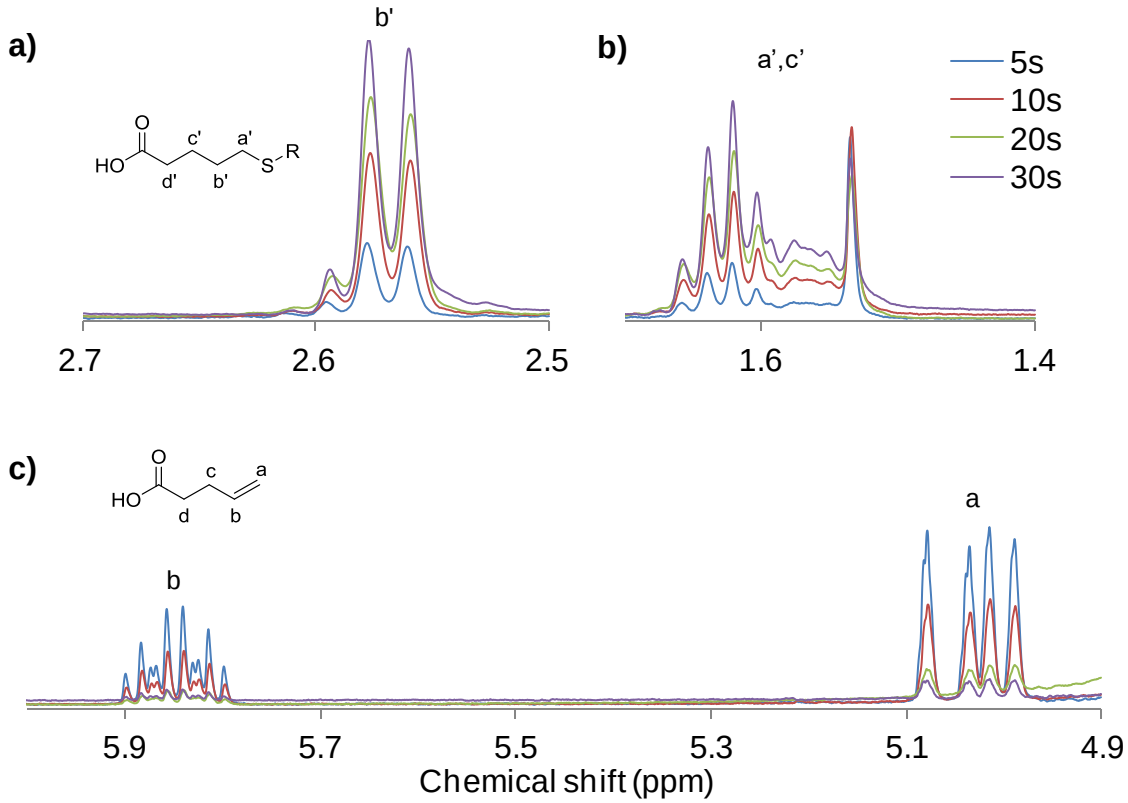

Figure 2.2 ^{1}H NMR spectra of the product peaks (a, b) and the alkene peaks (c) of the A1-S1 reaction at different UV exposure times (5-30 s).

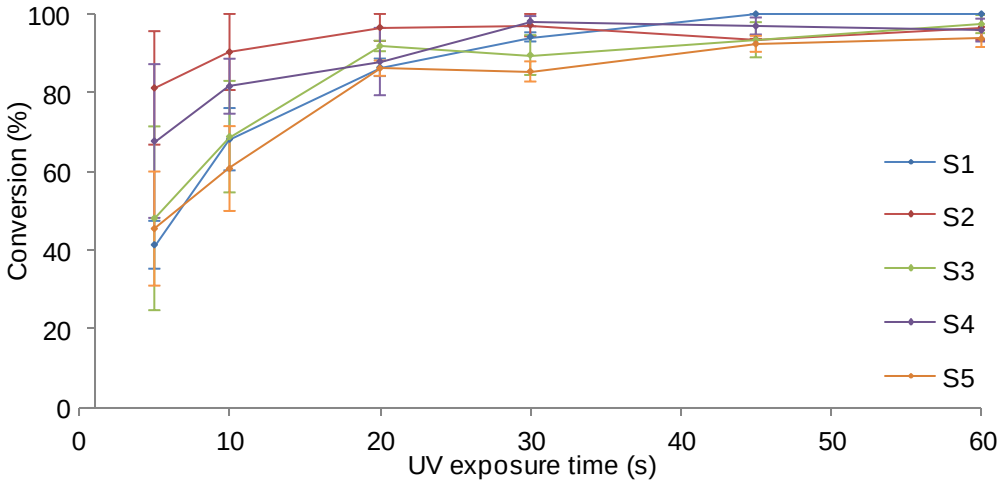

Figure 2.3 Impact of the time of UV exposure on the reaction conversion for A1 with a series of thiols. Reactions were performed with 2 mol% PI and 17 mW/cm^2 UVintensity.

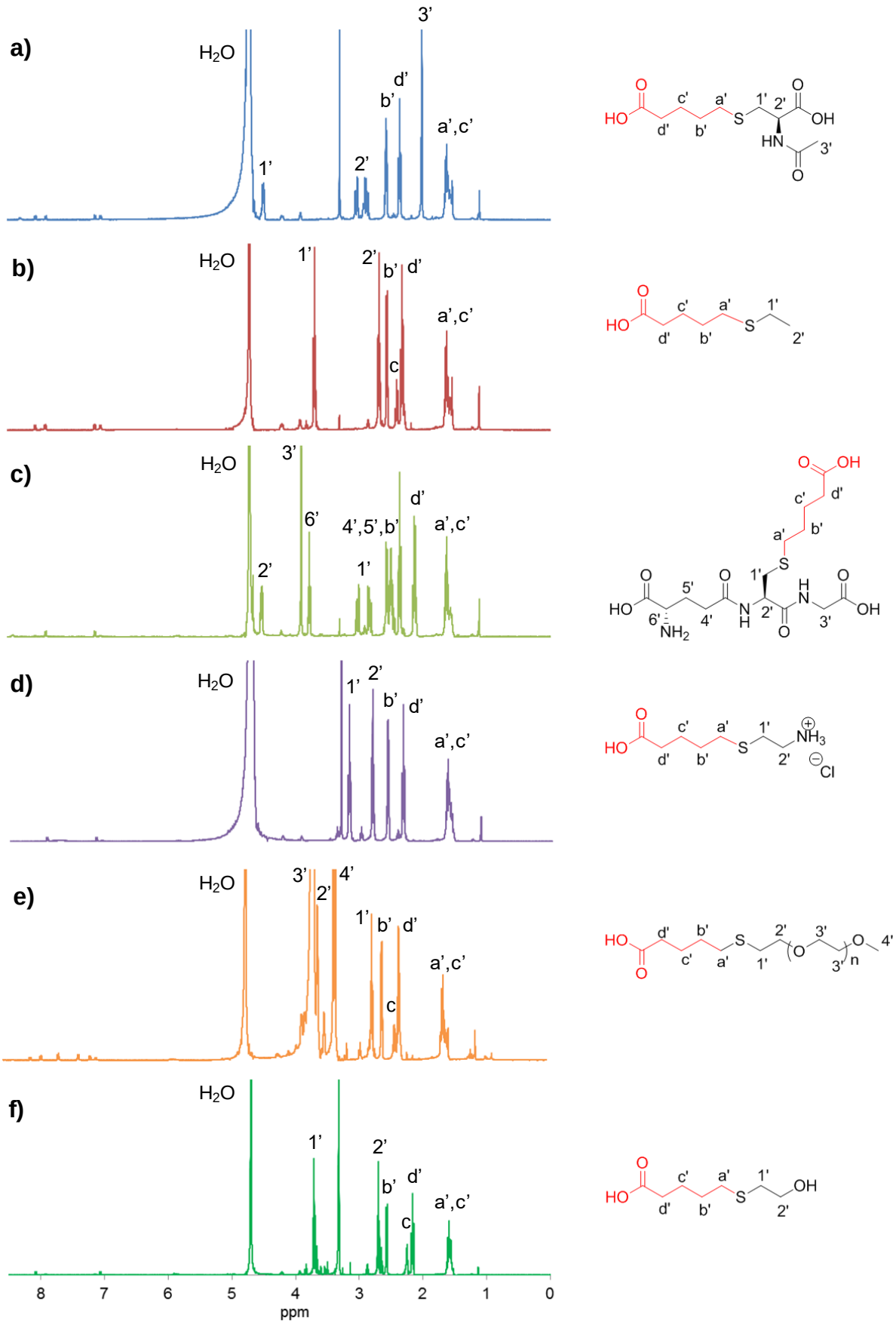

Figure 2.4 ^{1}H NMR spectra of the thiol-ene products of the reaction of thiols S1-6 with A1 in deuterated PBS with 2 mol% PI and 60s UV. a) S1, b) S2, c) S3, d) S4, e) S5 and f) S6.

2.1.2 Impact of pH of the buffer

Having determined optimised reaction conditions, the thiol-ene coupling of thiols **S1**, **S4**, **S5** and **S6** with alkene **A1** was monitored next as a function of pH (Fig. 2.5). Reactions were performed in PBS with 2 mol% of photoinitiator, a UV power of 17 mW/cm^2 and 60 s of UV exposure time. The pH of the deuterated buffer was adjusted using NaOD and DCl and conversions were calculated based on ^{1}H NMR spectra as in Figure 2.2. There were some difficulties adjusting the pH of the cocktail especially around the pK_a of the thiol, patience was required. Reaction efficiencies were at their maximum (between 92 and 100%) between pH 4 and 7, except for thiol **S6**, which showed a minor decrease to c.a. 84%. The reaction deteriorates with increasing pH and coupling efficiencies fall to 0% above pH 9 to 11, depending on the thiol. Indeed, in this pH range, the formation of increasing concentrations of thiolates prevents the formation of thiyl radicals and does not afford any notable coupling (Fig. 2.5).

We hypothesized that differences in the pH at which reaction efficiencies rapidly collapse were attributable to differences in the pK_a of the four thiols tested. Indeed, the pK_a's of these thiols should be influenced by the occurrence of intramolecular hydrogen bonds. Therefore, we calculated the pK_a of the thiols **S1**, **S4**, **S6** and a diethylene oxide thiol modelling PEG **S5** in the presence and absence of intramolecular hydrogen bonds. This work was performed by our collaborators in Brazil and is described in more detail[207].

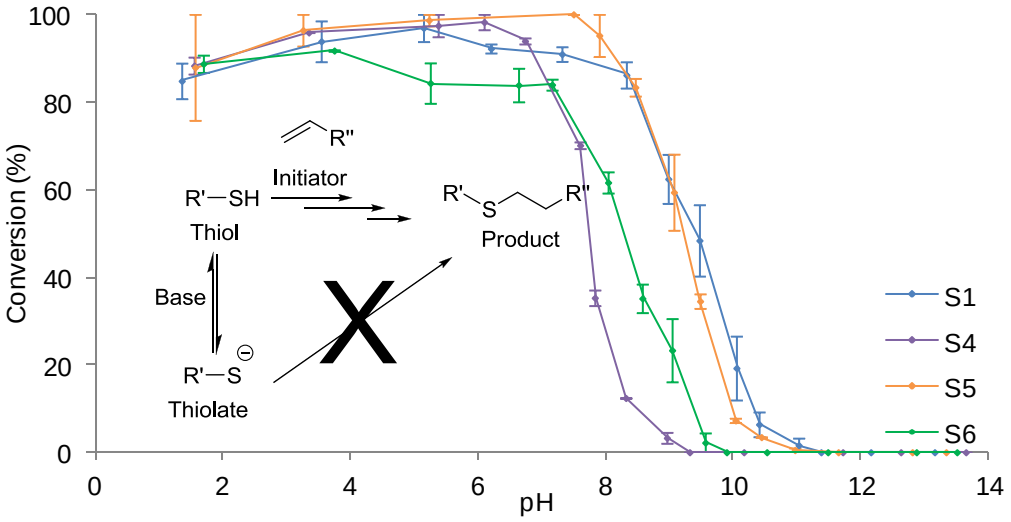

Figure 2.5 The impact of the buffer pH on the reaction conversion (60 s UV exposure) for A1 with thiols S1 and S4-S6.

2.1.3. Synthesis of thiol-reactive water soluble polymers

This section discusses the synthesis of polymeric alkenes suitable for thiol-ene coupling and for the production of hydrogels (Chapter 3). Three different types of polymeric backbones with different chemical and physical properties were generated. A neutral co-polymer (A10, pOx), with a known percentage of alkenes, negatively charged (A11, pMA^-) polymer derived from a maleic anhydride polymer and positively charged polymers (A7-A9 $pDMAEMA^+$) derived from pDMAEMA.

The neutral co-polymer pOx is an interesting polymer that has started to receive attention from the field of biomaterials by many research groups[42, 44, 137, 208]. The monomers are commercially available or can be synthesised[22, 209] easily to generate a variety of polymers/ co-polymers with interesting chemical and physical properties[210, 211]. Thiol-ene crosslinked pOx hydrogels have been investigated as cell culture materials[40] and for photoresist applications[151]. Here we discuss the synthesis of a butenyl monomer and polymerisation with ethyl oxazoline.

The alkene functional butenyl monomer was synthesised using a 2 step process. 2-chloroethylamine and pentenoyl chloride were reacted under inert gas (Scheme. 2.1). The intermediate product was purified by extraction and reacted with potassium hydroxide to obtain the close ring oxazoline monomer[22].

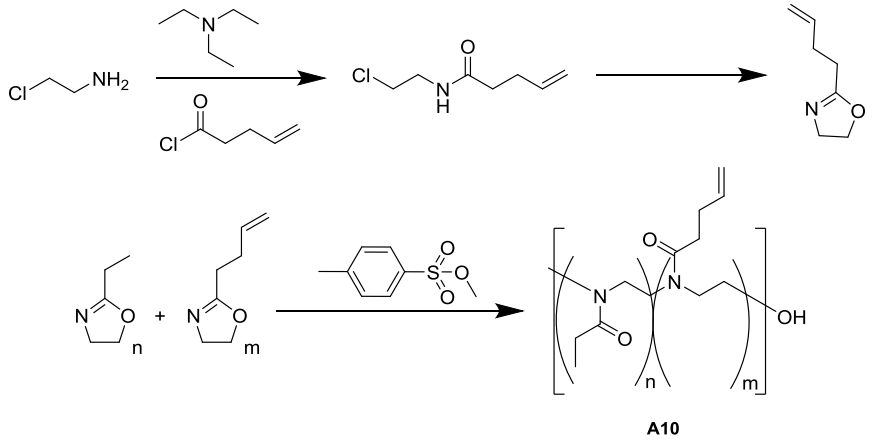

A10

Scheme 2.1 Synthesis of a) 2-butenyl-2-oxazoline monomer through *N*-(2-chloroethyl)-4-pentenamide and b) the pOx co-polymer from 2-ethyl-2-oxazoline and 2-butenyl-2-oxazoline monomers.

A mixture of ethyl: butenyl monomers 80:20 was polymerised using microwave synthesis; the polymerisation was initiated with methyl tosylate and terminated with water. The reaction conversion was close to 100% by GC (not shown) and ^{1}H NMR spectroscopy,

Each product was analysed by ^{1}H NMR spectroscopy and FTIR spectroscopy for the confirmation of the structures (Fig. 2.6 and 2.7). The assignment for each peak is indicated on the structures. By ^{1}H NMR spectroscopy the obtained polymers contained 13-17% alkene functionality indicating the partial termination of the reaction during synthesis (Fig. 2.6e). This feature is also supported by the measurements made by GPC (discussed later). The mol% of alkene for the pOx (A10) was calculated from the ^{1}H NMR spectroscopic analysis and used for thiol-ene coupling reactions.

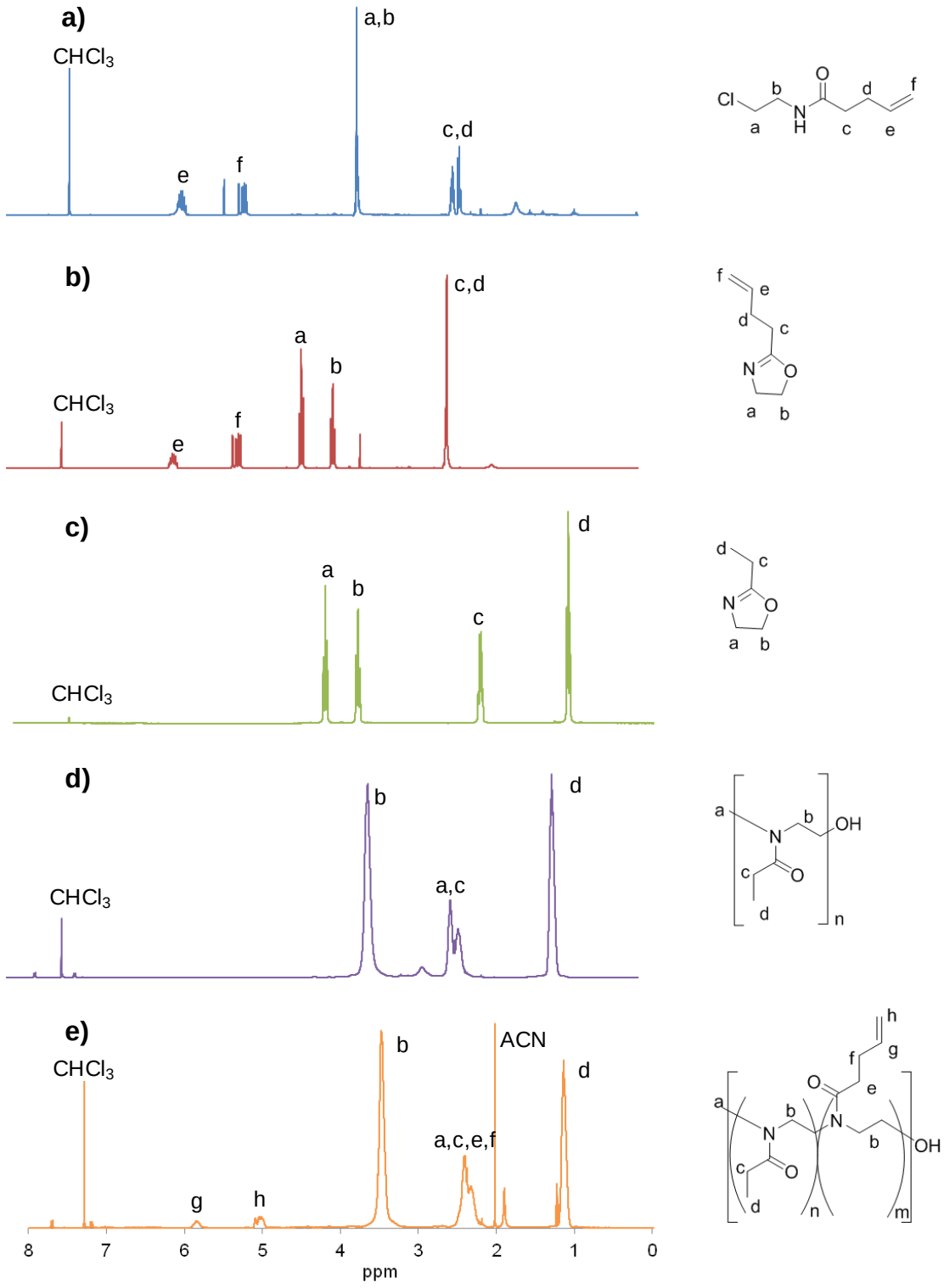

Figure 2.6 ^{1}H NMR spectroscopy of a) *N*-(2-chloroethyl)-4-pentenamide, b) 2-butenyl-2-oxazoline, c) 2-ethyl-2-oxazoline, d) pEtOx and e) pEtOxBu=Ox/ pOx(A10).

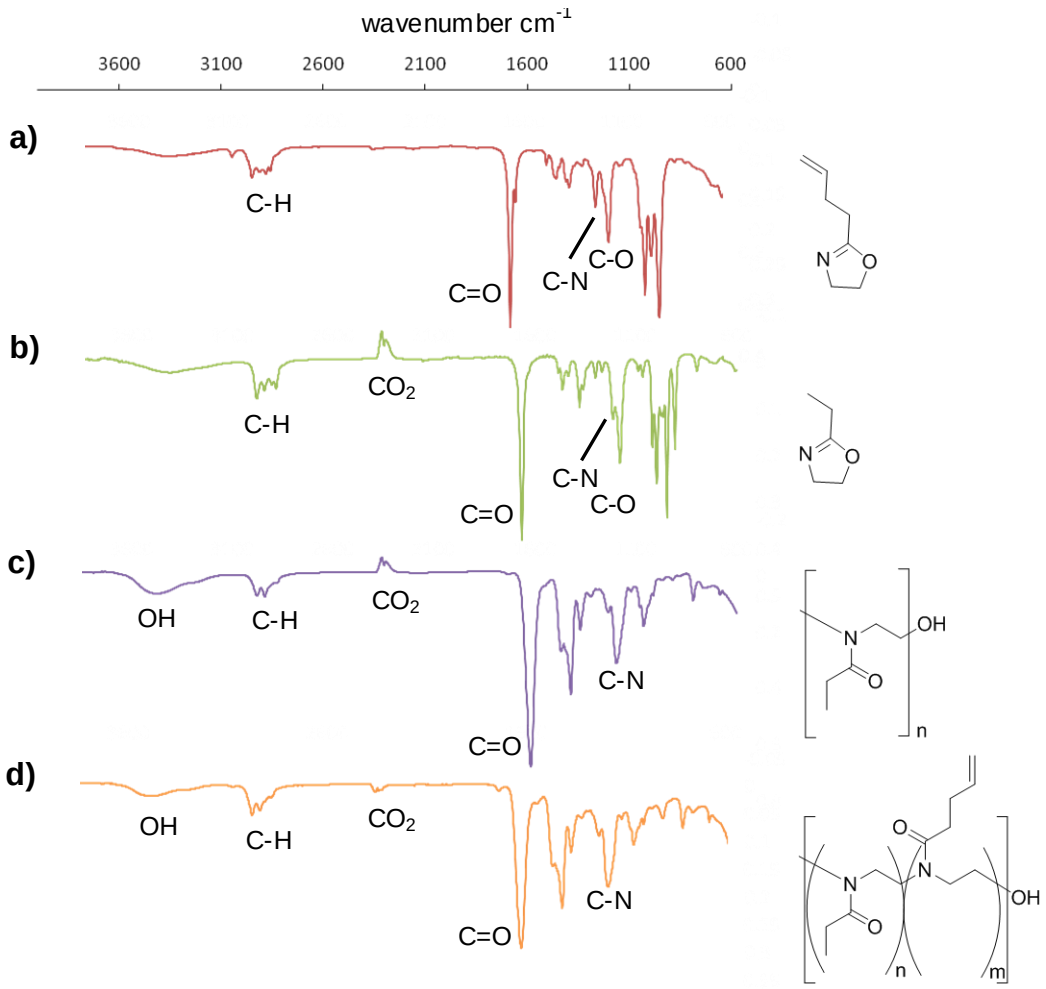

Figure 2.7 FTIR spectra of a) 2-butenyl-2-oxazoline, b) 2-ethyl-2-oxazoline, c) pEtOx and d) pEtOxBu=Ox/ pOx (A10).

The second polymer of interest was a negatively charged maleic acid polymer derived from a commercially available maleic anhydride polymer and allylamine (Scheme 2.2). This polymer was of particular interest, it can be functionalised with ease to obtain alkene functionality and suitable for thiol-ene reactions. Brafman *et al*. printed an array of synthetic polymers and tested these as surfaces to support the self-renewal and pluripotency of stem cells[212]. They found that out of the 91 polymers tested, poly(methyl vinyl ether-alt-maleic anhydride) supported the long term attachment, proliferation and self-renewal of cells. Cells maintained their characteristic morphology and expressed high levels of pluripotency markers. There could be a greater

potential for this polymer in the biomaterials field, and therefore we chose to study this polymer as a negatively charged backbone for thiol-ene coupling and hydrogel formation. The maleic acid co-polymer was characterised using ^{1}H NMR spectroscopy and FTIR spectroscopy to confirm its structure (Fig. 2.8 and 2.9). Full functionalisation was apparent by ^{1}H NMR spectroscopy (ratio n:m 4:96).

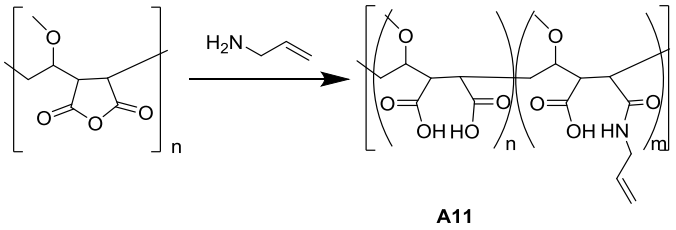

Scheme 2.2 Functionalisation of poly(methyl vinyl ether *alt*-maleic anhydride) to generate poly(maleic amide co-acid)/ pMA^{-} (A11).

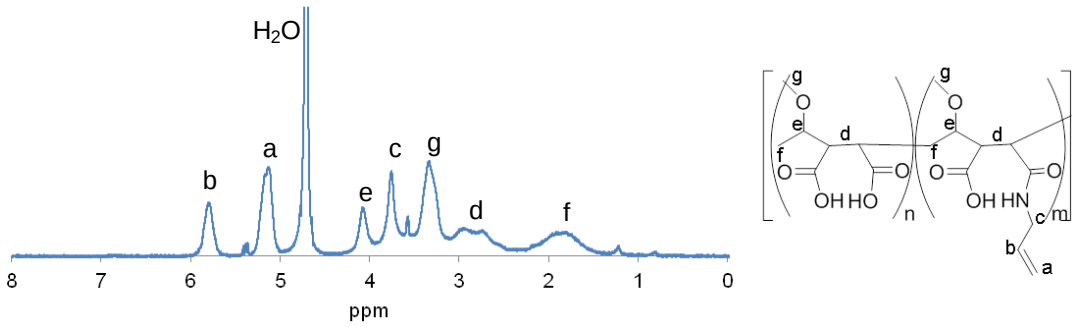

Figure 2.8 ^{1}H NMR spectroscopy of pMA^{-} (A11).

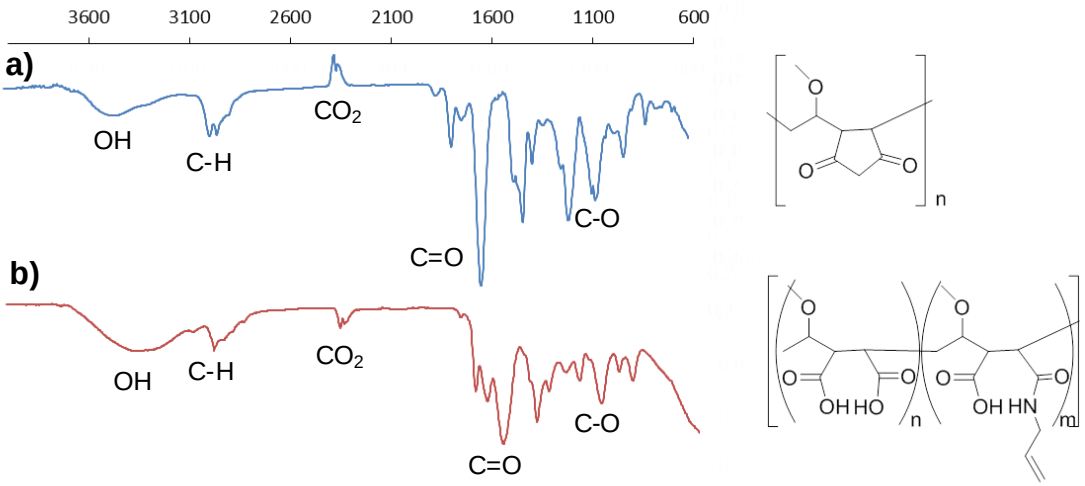

Figure 2.9 FTIR spectra of poly(methyl vinyl ether *alt*-maleic anhydride) and pMA^{-} (A11).

The third class of polymers focused in the thesis are the pDMAEMA functionalised derivatives (A7-9). These polymers are positively charged therefore can be interesting in comparison to the negatively charged and neutral polymers for thiol-ene coupling. pDMAEMA has been reported as a hemocompatible polymer making it interesting as a biomaterial[213]. Others have reported the use of pDMAEMA polymer brush systems for gene delivery and antibacterial surfaces[101, 214, 215]. The pDMAEMA backbone can easily be functionalised with a series of alkyl halides to achieve quaternary functionalised positively charged polymers[216]. The functionalised pDMAEMA behaves as a polyelectrolyte and can also be interesting for pH responsive materials[217-219].

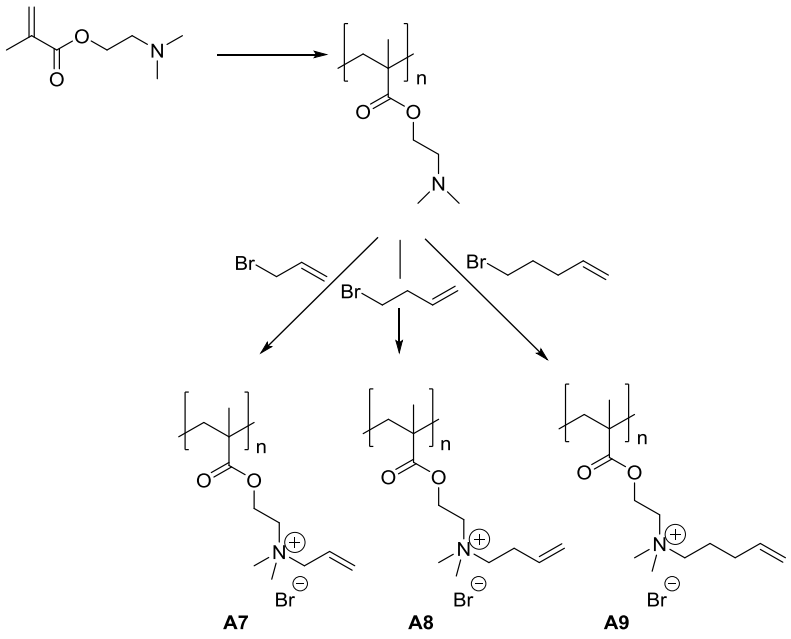

Scheme 2.3 Synthesis of pDMAEMA propene (A7), pDMAEMA butene (A8), and pDMAEMA pentene (A9, pDMAEMA^{+}) from pDMAEMA.

The charged pDMAEMA derivatives were functionalised using allylbromide, bromo-butene or bromo-pentene (Scheme 2.3) and purified by precipitation. The polymers were characterised with ^{1}H NMR spectroscopy and FTIR

spectroscopy to confirm their structures (Fig. 2.10 and 2.11). Full conversion to the alkene was observed by ^{1}H NMR spectroscopy. The alkene functional pDMAEMA backbones (A7-9) showed very different thiol-ene coupling efficiencies to one another (discussed in section 2.1.5).

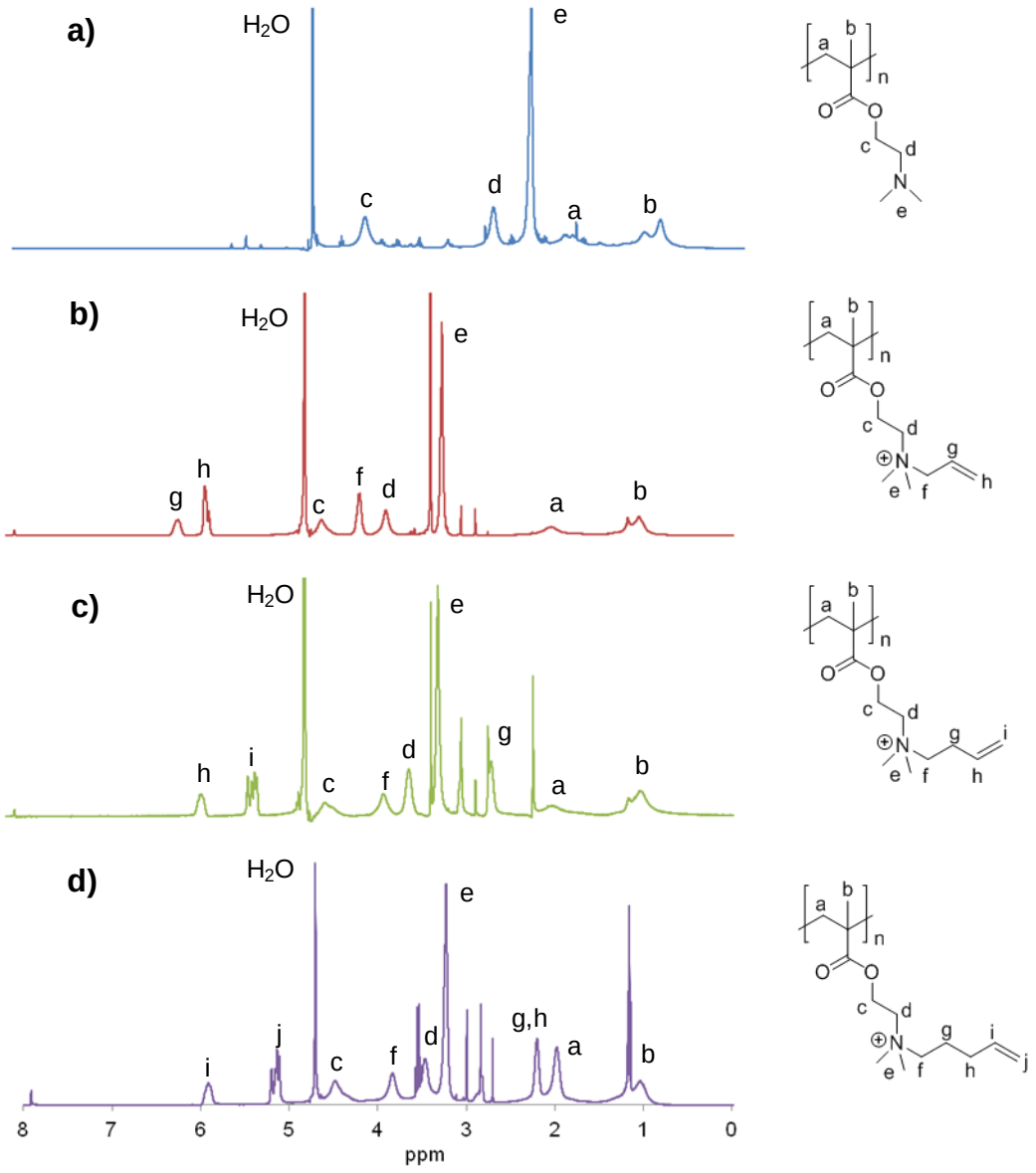

Figure 2.10 ^{1}H NMR spectroscopy of a) pDMAEMA, b) pDMAEMA propene (A7), c) pDMAEMA butene (A8), and d) pDMAEMA pentene (A9).

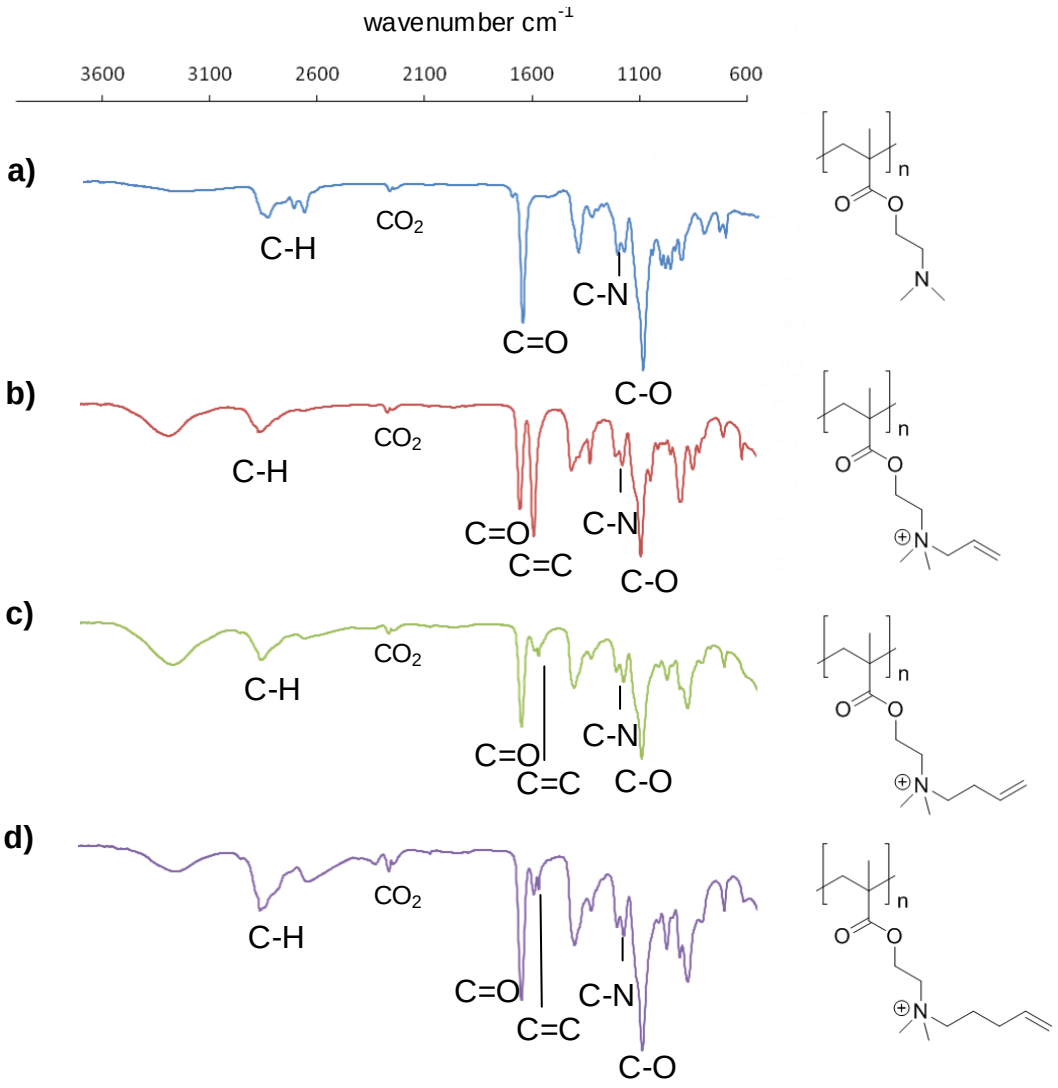

Figure 2.11 FTIR spectra of a) pDMAEMA, b) pDMAEMA propene (A7), c) pDMAEMA butene (A8), and d) pDMAEMA pentene (A9) with highlighted stretching vibrations.

GPC analysis was performed to measure the molecular masses of the generated polymers (Fig. 2.12). The pOx (13% alkene) GPC trace shows the average M_n as 6.3 kg/mol with the lowest molecular weight of the polymer series followed by pDMAEMA 67.93 kg/mol (before functionalisation) and poly(methyl vinyl ether *alt*-maleic anhydride) 20.0 kg/mol (quoted from the manufacturer). The dispersity, $Đ_M$ of pDMAEMA and pOx show good control over the dispersity (1.60 and 1.62, respectively) of the chain length during synthesis. The pOx trace showed tailing towards the lower molecular weight, indicating that the reaction is partially terminated during the polymerisation. Some other researchers have achieved dispersity, $Đ_M$ closer to 1 with various pOx systems; however this is not a drawback for the application of this material[22, 220]. The pMA^- polymer is negatively charged, it formed good adhesion with the column and therefore, could not be measured using GPC. The pDMAEMA was further functionalised to obtain alkene functional chains. Overall, the molecular weight and dispersity of the synthesised polymers are in good line with the required application.

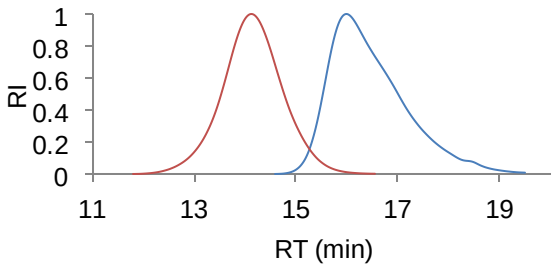

Figure 2.12 Normalised GPC traces for pOx (blue, Mn 6.3 kg/mol) and pDMAEMA (red, Mn 67.9 kg/mol).

2.1.4. Efficiency of thiol-ene coupling on macromolecules

Thiol-ene reactions perform efficiently with small molecules in neutral or slightly acidic buffered conditions with 2 mol% PI and short UV exposure times (60 s). It is more difficult to achieve high reaction efficiencies with macromolecules as reported previously by Koo *et al*.[35]. In this study, we will focus on the optimisation of the thiol-ene reaction with polymer-small molecule and polymer-polymer systems.

The polymers synthesised in section 2.1.3 were coupled to thiols S1, S4 and S5, the conditions were optimised by varying the thiol:ene ratio, PI concentration and UV exposure time, reaction conversions are reported in Table 2.1. Negatively charged alkene functional polymer A11 was reacted with S1 using 1:1 thiol-ene reaction, 2 mol% PI and 60 s UV exposure resulting in 47% reaction efficiency. Increasing the UV exposure time to 300 s increased the conversion to 69% and increasing the concentration of thiol (2:1, 5:1) resulted in 87% conversion. Similar reaction behaviours were observed with neutral polymer A10. Although increasing the thiol concentration improved the reaction conversion, it is not suitable for the hydrogel systems discussed in Chapter 3.

We made an interesting observation, the reaction between A11 and S4 performed better than with S1; this could be related to the electrostatic attraction between the two components. Neutral polymer A10 did not show the same behaviour, the reaction efficiency decreased when compared to S1.

The thiol-ene reaction efficiencies decreased when performed with polymer-polymer systems (A9/A10/A11:S5) compared to the small molecule-polymer

system (with S1 or S4). For this the percentage of PI was increased to 5 mol%, the thiol-ene reactions performed with higher efficiency (in bold).

Table 2.1 A list of reaction conversions from ^{1}H NMR spectroscopy for series of thiols and alkenes with variable concentration of PI, UV exposure time (s) and thiol: alkene ratio.

Thiol	Alkene	Ratio thiol:ene	PI (mol%)	UV (s)	Conversion (%)
S1	A11	1:1	2	60	47
S1	A11	1:1	2	300	69
S1	A11	2:1	2	300	87
S4	A11	1:1	5	300	99
S4	A11	2:1	2	300	87
S5	A11	1:1	2	300	75
S5	A11	5:1	2	300	87
S5	**A11**	**1:1**	**5**	**300**	**83**
S5	A11	2:1	5	300	95
S1	A10	1:1	2	60	87
S1	A10	1:1	2	300	95
S1	A10	2:1	2	300	100
S4	A10	1:1	2	300	29
S4	A10	1:1	5	300	51
S4	A10	2:1	2	300	51
S5	A10	1:1	2	300	41
S5	A10	2:1	2	60	49
S5	A10	2:1	2	300	94
S5	**A10**	**1:1**	**5**	**300**	**92**
S5	A10	1:1	10	300	94
S1	A7	1:1	2	300	7
S1	A7	1:1	5	300	14
S5	A7	1:1	2	60	4
S1	A8	1:1	5	300	98
S1	A9	1:1	5	300	99
S5	**A9**	**1:1**	**5**	**300**	**53**
CY	A1	1:1	2	60	40
CY	**A1**	**1:1**	**5**	**300**	**60**

Polymer A7, a propene functional pDMAEMA was reacted with S1 and S5, the thiol-ene reaction performed very poorly. Derivatives A8 and A9 performed much better with both S1 and S5, the reasons for this was discussed in more detail in section 2.1.5.

Thiol containing dipeptide CY was reacted with alkene A1 using the initial and macromolecular optimised thiol-ene reaction conditions. A 20% increase was observed for the reaction efficiency.

We concluded that 5 mol% PI and 300 s UV with 1:1 thiol:ene ratio performed to satisfactory reaction efficiencies, and therefore the thiol-ene reactions with polymers and peptides were followed using these conditions.

2.1.5 Impact of the chemical structure close to the alkene moiety

Thiol-ene coupling having direct applications in the bioconjugation of proteins and peptides to polymers and small molecules presenting alkene functions[150] and for the formation of degradable hydrogels[57, 172, 196], we next examined the role of the local chemical structure close to the alkene moiety. In addition to the negatively charged alkene **A1**, we tested the reactivity of *N*-acetyl *l*-cysteine **S1** with neutral alkene amides **A2** and **A3** and positively charged alkenes **A4-9** (see Fig. 2.13). The neutral alkene amide **A2** reacted with high efficiency with **S1** (73%), but the allyl amide derivative **A3** showed a 71% drop in reactivity compared to that of **A1**. In addition, the allyl ammonium derivative **A4** only reacted 4% with **S1**.

We proposed that the close proximity (one CH_2 group only) of the alkene moiety and the nitrogen atom in **A3** and **A4** could account for the lack of reactivity of these two molecules with **S1**. Therefore we examined the coupling of **S1** to **A5** and **A6**, which display two and three methylene groups between the ammonium group and the alkene moiety, respectively (A5 A4 p 0.000118, A6 A4 p 0.0000161). The reaction efficiency was restored to near completion in both cases (see Fig. 2.13). Similarly, polyelectrolyte **A7**, presenting olefinic ammonium residues showed poor reactive thiol-ene coupling with **S1** (5%), but polyelectrolyte **A8** and **A9** with extended aliphatic chains reacted well (> 99%, A8 A7 p 0.0.0000020, A9 A7 p 0.0000010).

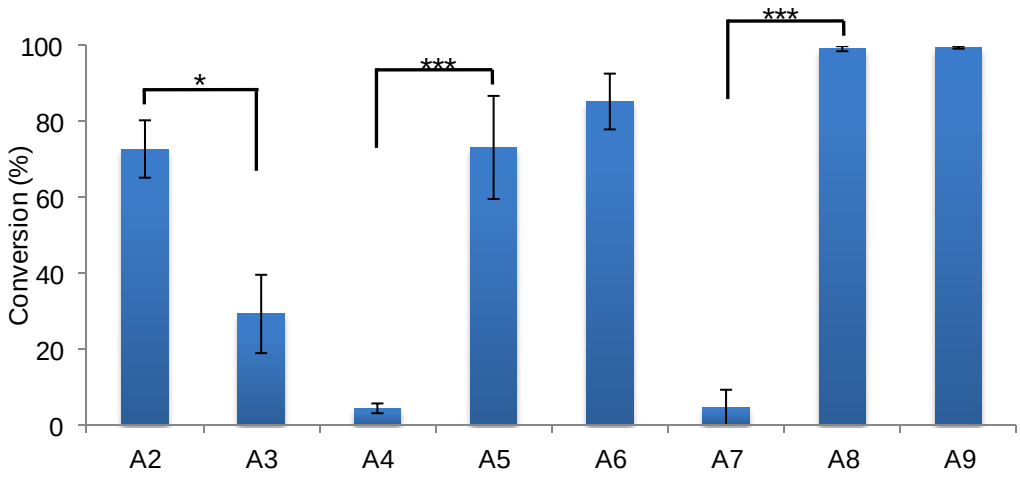

Figure 2.13 Reaction conversion 60 s UV, photoinitiator 1 mM, A2-A6 or 300 s UV 2.5 mM, A7-A9) of S1 and the series of alkenes (A2-A9). See Fig. A1.1 for corresponding statistical analysis.

Before working with pDMAEMA functionalised polymers, we were working with pGMA functionalised with iodomethane to achieve a quaternary pGMA structure with a positive charge (not shown). Thiol-ene reactions with the pGMA polymers served very difficult. Initially we thought this may be due to the presence of iodide and performed the pottasium iodide reaction shown in Fig. 2.15. Since the thiol-ene reaction was affected by the presence of iodide, we changed the iodomethane to allylbromide and functionalised the pGMA through this process to achieve the same polymer structure with a bromide ion instead of an iodide. However, the thiol-ene reactions still performed very badly. On exchange of the polymer system to pDMAEMA, with the allyl functional version (**A7**) we continued to see the same behaviour. In order to overcome this problem we decided to extend the carbon chain length between the charge and the alkene, and with the difference of a single carbon we saw dramatic differences. Working with an extended chain allowed for the full conversion of the alkenes. Computational modelling was performed to investigate the reasons to why this is the case, and is described in more detail in the submitted paper.

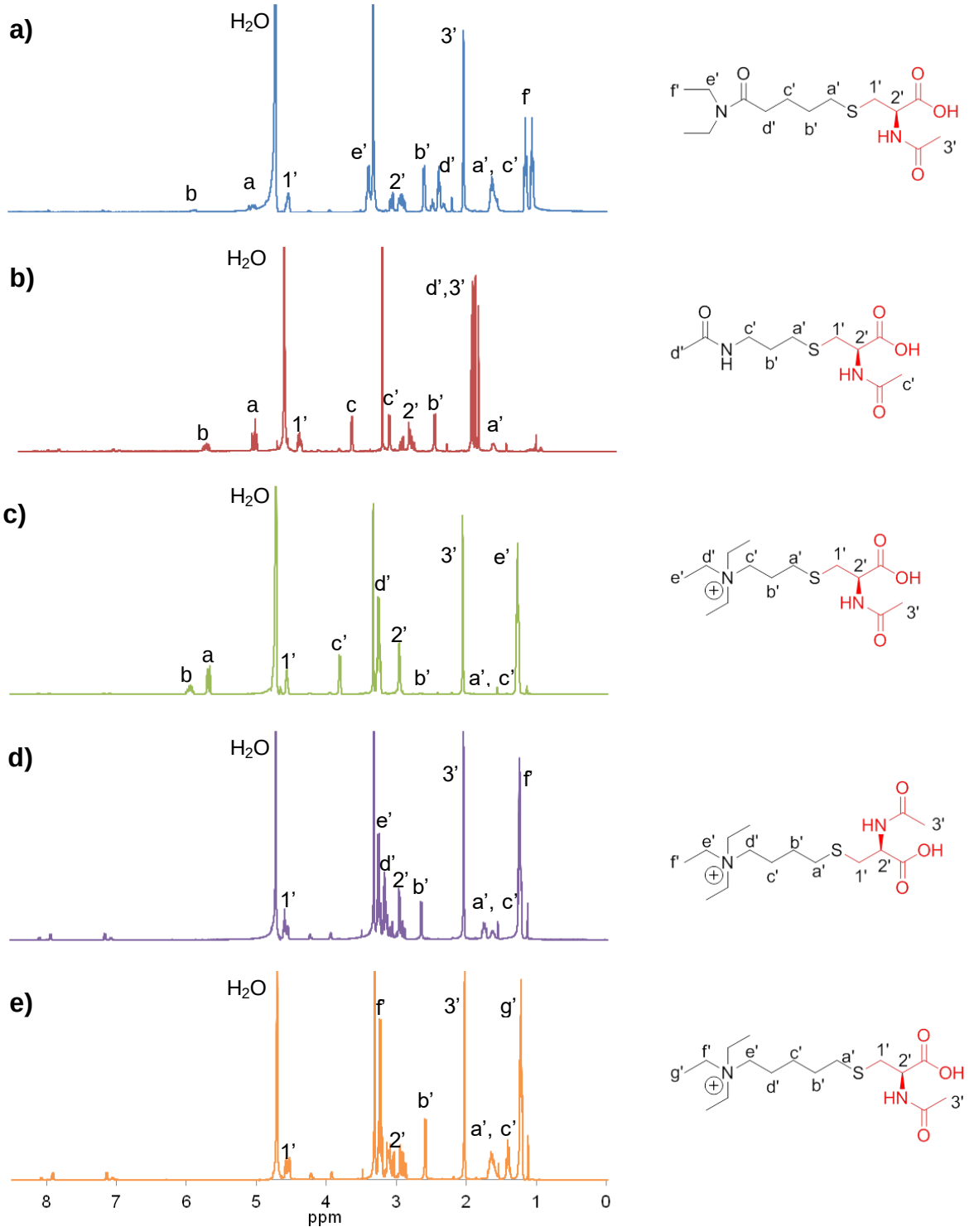

Figure 2.14 ^{1}H NMR spectroscopy of a) *N,N*-diethylpent-4-enamide (A2) b) *N*-allylacetamide (A3) c) *N,N,N*-triehtylprop-2-en-1-aminium (A4) d) *N,N,N*-triehtylbut-3-en-1-aminium (A5) and e) *N,N,N*-triehtylpent-4-en-1-aminium (A6).

2.2.6 Impact of the composition of the molecular environment

Next, the impact of other molecules present in the reaction medium was examined. We carried out thiol-ene reactions between **S1** and **A1** in the presence of amino acids and different electrolytes (Fig. 2.15). Reaction mixtures containing **S1** and **A1** in deuterated PBS, with 2 mol% photoinitiator were spiked with a range of amino acids and electrolyte at two different molar ratios. The resulting solutions were then adjusted to pH 7 using NaOD or DCl, as free amino acids can change the pH of the resulting mixtures, and exposed to 60 s of UV light (17 mW/cm^2, Fig. 25). As before, ^{1}H NMR spectroscopy was used to study the efficiency of the reactions. Generally, thiol-ene coupling in the presence of a range of amino acids with neutral hydrophilic, hydrophobic or charged structures remained efficient, with most conversion levels between 73 and 93% (n.s., p 0.976-1), confirming the very good tolerance of thiol-ene chemistry to a large range of functionalities.

Amongst the neutral amino acids tested, proline, glycine and the hydrophobic phenylalanine and tyrosine did not show any significant decrease in coupling compared to the control (non-spiked) conditions. Glutamine, serine and leucine showed a modest 11% decrease in coupling, although not significant. Although the reasons for this slight decrease are not clear, in the case of leucine it could arise from possible proton abstraction to form stable tertiary radicals. The presence of tryptophan also resulted in a strong decrease in coupling (15%, n.s.), potentially due the olefinic character of the double bond in the pyrrole ring and the possibility of addition of thiyl radicals to this moiety. Hence thiol-ene coupling may not be compatible with peptide sequences displaying high

ratios of tryptophan residues compared to cysteines, although 10% seems to be well tolerated.

Amongst the charged amino acids tested, the negatively charged aspartic acid resulted in a 12% decrease in coupling (n.s.), perhaps due to weak acid-base interactions with thiol moieties, resulting in some level of deprotonation. Three positively charged amino acids were tested, the primary amine lysine, the imidazole-derivative histidine and the guanidine derivative arginine (Fig. 2.15). Histidine did not affect the coupling of **S1** to **A1**, possibly due to its low pK_a and therefore neutral character at physiological pH. In contrast, both lysine and arginine decreased the reaction efficiency by 20 to 13%, possibly through electrostatic stabilisation of the thiolate form of **S1**.

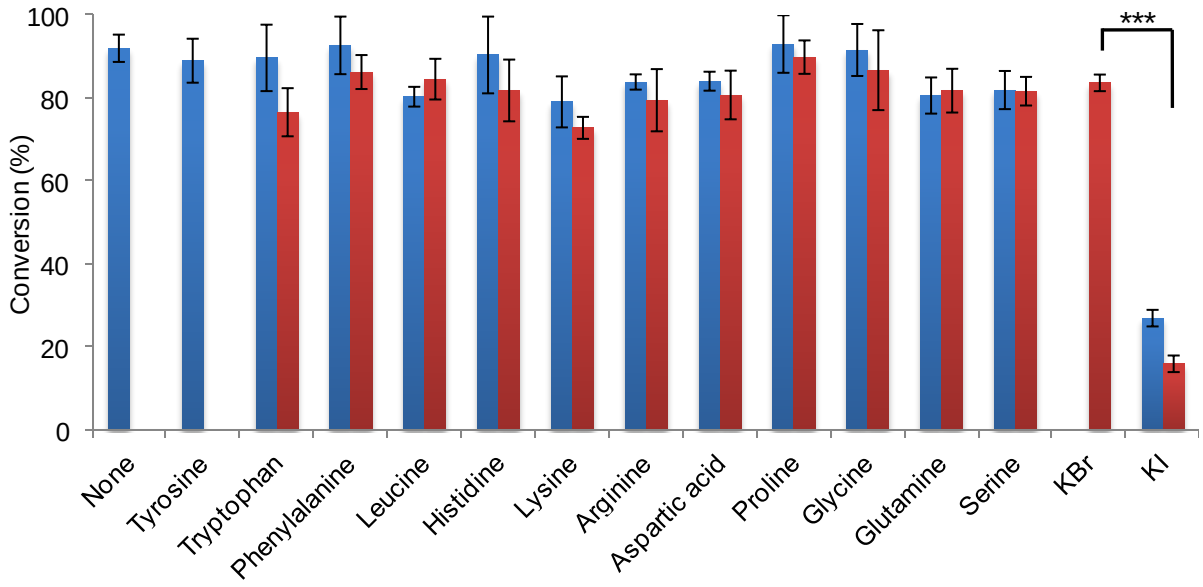

Figure 2.15 Impact of the addition of amino acids or electrolytes to the thiol-ene system, blue 10 mol% and red 100 mol%. See Fig. A1.4 for corresponding statistical analysis.

Finally, the effects of different electrolytes, in particular different halides were examined. This was the result of our observation that allyl ammonium iodide does not significantly react via thiol-ene coupling (results not shown). Such

behaviour led us to test whether bromides and iodides had an impact on thiol-ene coupling. Therefore, we added equimolar amounts of potassium bromide and potassium iodide to reaction mixtures of **S1** and **A1**. We found that potassium iodide efficiently quenched the coupling (KI 10 control p 0.0000496, KI control 100 p 0.0000011), whereas the bromide electrolyte had a minor effect (84%, KBr control p 1, Fig. 2.15). This is consistent with electron transfer and quenching phenomena observed with halides[221] and the lower standard reduction potential of iodine atoms compared to bromine[222].

2.2.7 Impact of the chemical structure of cysteine-terminated peptides

The impact of the chemical structure in the vicinity of the thiol, specifically a cysteine within a peptide sequence, was investigated next, due to the potential importance of molecular design on reactivity and bioconjugation. In particular, we monitored the impact of aromatic amino acids; the vicinity of charges and the position of the cysteine residue on coupling efficiencies. To do so, we used a combination of ^{1}H NMR spectroscopy (to determine the extent of coupling) and HPLC (to explore the role of concentration and buffer on the coupling efficiency). Mass spectrometry was performed on the thiol-ene samples to confirm the molecular weight of the formed product (Fig. 2.22). We selected sequences of pentameric amino acid peptides for this study, with the ultimate residue being aromatic to allow UV monitoring via HPLC, and reacted them with alkene **A1** (integrations of the peaks were performed manually). We found that tyrosine in the sequence resulted in a decrease of the coupling efficiency compared to phenylalanine (Fig. 2.16c), in slight contrast to our results on the reaction of **A1** with **S1** in the presence of single amino acids (Fig. 2.15). Perhaps this is a result of the increased concentration of tyrosine in the reaction mixture with the present peptide (100% compared to cysteine) as the single amino acid tyrosine was not sufficiently soluble to be tested at concentrations above that of 10% of *N*-acetyl *l*-cysteine (above 4.5 mM). However, the results showed that despite the larger molar mass of peptide GCGSF (compared to *N*-acetyl *l*-cysteine), high conversions (86% by ^{1}H NMR spectroscopy see Fig. 2.16a; 100% by HPLC see Fig. 2.16b) could be

reached. Hence peptide coupling via thiol-ene reaction can be efficient at moderate concentrations (45 mM) and in buffered conditions.

The position of the cysteine residue in the peptide sequence was also found to be important to improve thiol-ene coupling efficiency (Fig. 2.16c). Two main cysteine-based sequences are commonly found in the literature to couple peptides via thiol-ene reaction or Michael addition: CGGXX[62, 174] and GCGXX[57, 142, 177, 183, 196]. We explored the impact of the position of the cysteine on the reaction efficiency and found a marked decrease in coupling when the cysteine residue was placed in the ultimate position (68 ± 1.53% by HPLC n.s. p 0.123 CGGSF-GCGSF). This is perhaps due to the local chemical structure of the resulting CGGSF peptide as the thiol finds itself two carbons away from a primary amine, as in cysteamine **S4**. Cysteamine **S4** was found to quickly lose reactivity just above neutral pH (Fig. 2.5), due to a decrease in the pK_a of its thiol group. Our results indicate that similar effects take place in the case of cysteine-terminated peptides, leading to a slight decrease in coupling efficiency in PBS (pH 7.4), highlighting that GCGXX type of sequences should be preferred for the design of peptide sequences for bioconjugation and biofunctionalisation.

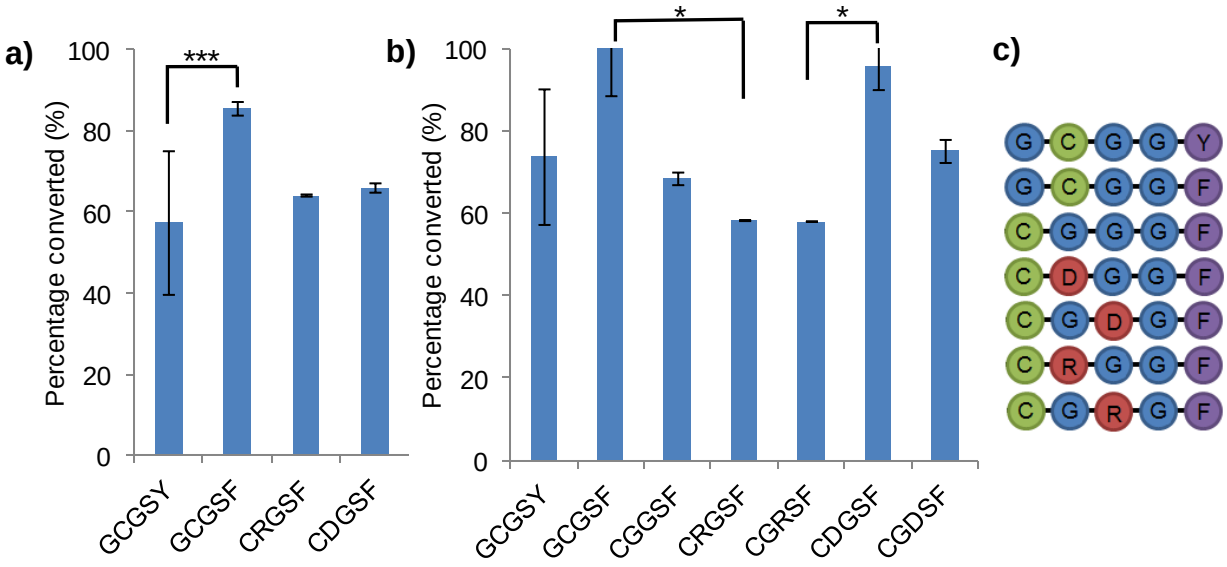

Figure 2.16 a) Reaction conversions quantified by ^{1}H NMR spectroscopy for 4 peptide sequences (300 s UV exposure, 2.5 mM initiator, 45 mM peptide). b) Reaction conversions quantified by HPLC for 7 peptide sequences (300 s UV exposure, 2.5 mM initiator, 45 mM peptide). c) Sequence of peptides with cysteines in green, glycines and serines in blue, charged amino acids (arginine and aspartic acid) in red and aromatic (phenylalanine and tyrosine) amino acids in purple. See Fig. A1.2-1.3 for corresponding statistical analysis.

Neighbouring amino acids were also found to have a modest impact on thiol-ene efficiency (Fig. 2.16c). The introduction of the negatively charged amino acid residue aspartic acid directly adjacent to the cysteine or separated from it by a glycine resulted in a slight increase in coupling efficiency (directly adjacent: 66% by ^{1}H NMR spectroscopy; 96% by HPLC; separated by a glycine: 75% by HPLC; n.s. p 0.516 CDGSF CGDSF from HPLC). In contrast, the positively charged amino acid arginine had a negative effect on the thiol-ene reaction, whether when introduced directly next to the cysteine or separated from it by a glycine (64% by ^{1}H NMR spectroscopy for CRGSF; both CRGSF and CGRSF 58% by HPLC; n.s. p 1 CRGSF CGRSF, p 0.024 CRGSF GCGSF from HPLC). These results suggest that the local chemical structure around the thiol moiety plays a modest role on the thiol-ene coupling, but still impacts on its efficiency. The opposite effects of positively and negatively charged neighbouring amino acids imply that they could stabilise and

destabilise thiolates, respectively. This hypothesis, based on our observations made at different pH (Fig. 2.5), should result in the associated changes in reactivity, as observed in Fig. 26c.

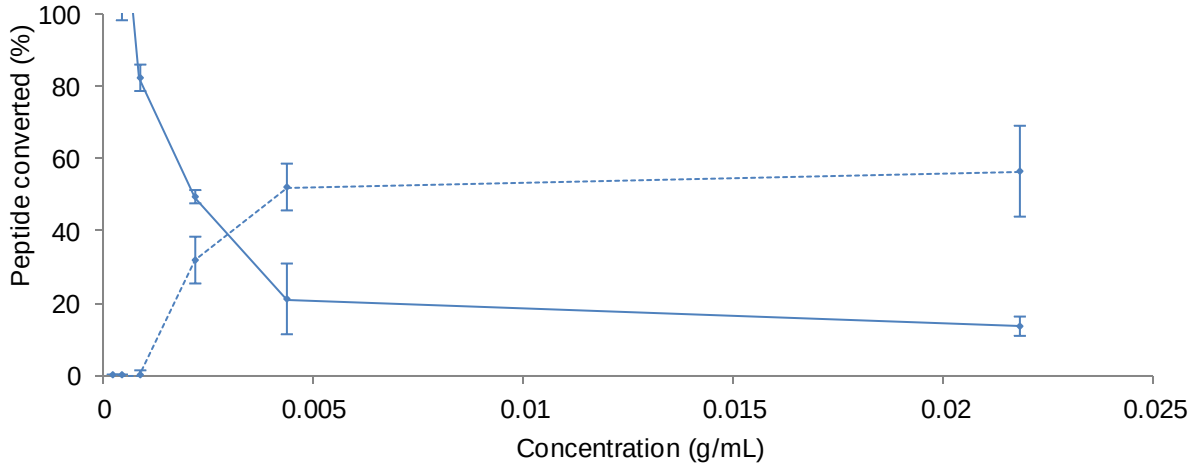

Figure 2.17 Reaction conversion and remaining reagents measured for the coupling of GCGSY and A1 at different concentrations (300 s UV exposure, 2.5 mM initiator; dotted lines, product formed; full lines, unreacted peptide).

To explore further what parameters impact on thiol-ene reaction, we examined the role of concentration on the efficiency of the coupling. This is particularly relevant to bioconjugation methods (in particular for coupling to proteins and antibodies), which can require low concentrations to be used. The concentrations of all reagents (including that of the photoinitiator) were changed by identical factors by direct dilution of the most concentrated stock solution and the thiol-ene coupling of GCGSY to pentenoic acid **A1** was monitored via HPLC. We found symmetric trends for the evolution of the starting peptide (unreacted) and that of the product and also a decrease in the peptide conversion (%) at lower concentration, suggesting a loss of reactive radicals during the reaction at low concentrations. Below concentrations of 4.5 mM, no substantial product formation was observed. In addition, the sum of product and reagent concentrations only accounted for 90% of the total thiol amounts initially used (Fig. 2.17). This suggest that below a concentration of

4.5 mM of thiol species are quenched by other species (or processes) present in the reaction milieu.

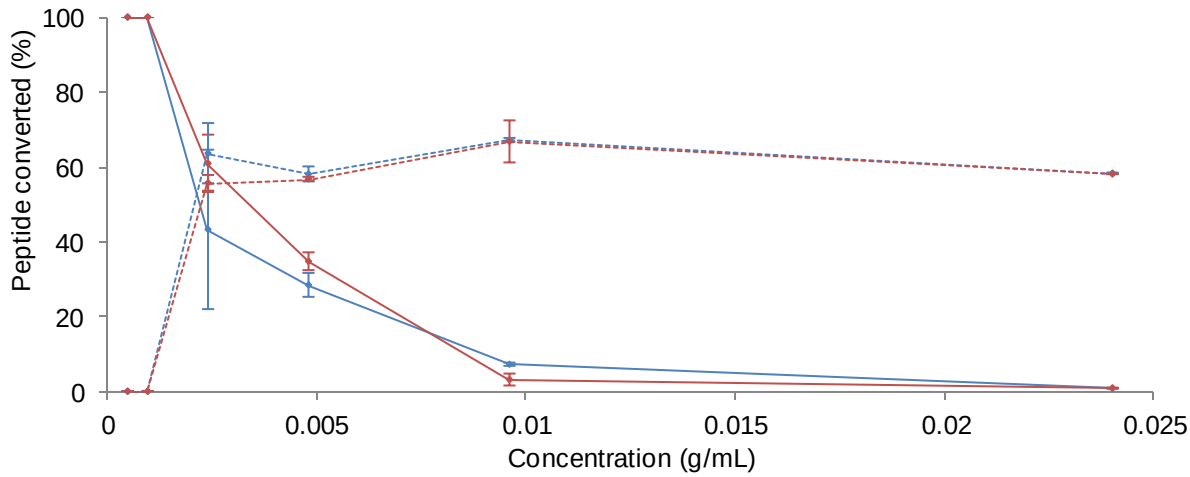

Figure 2.18 Reaction conversion and remaining reagents measured for the coupling of CRGSF/CGRSF and A1 at different concentrations (300 s UV exposure, 2.5 mM initiator). CRGSF (blue dotted lines, product formed; full lines, unreacted peptide) and CGRSF (red dotted lines, product formed; full lines, unreacted peptide).

In contrast, the changes in reagent and product concentrations observed with arginine-containing peptides were not symmetrical (Fig. 2.18). The product formation remained unchanged (between 56 and 67%) over a range of starting peptide concentration of 4.5 to 45 mM, the relative concentration of starting peptide changed from 0% (at high concentrations of 45 mM) to 61% (for a starting concentration of peptide of 4.5 mM). Hence our results suggest that at high concentrations, a substantial fraction of the reacted peptides are not contributing to product formation and are presumably converted to other species via side-reactions. This could imply that radical-radical coupling reactions, which would be more sensitive to concentration than other side-reactions (as their rate would depend on the square of the radical concentration), are frequent at high concentrations. Hence such bimolecular recombination was found to dominate termination in polymer-polymer couplings mediated by thiol-ene chemistry[35].

There were some difficulties with the experiments performed in this section. We wanted to monitor the thiol-ene reaction with respect to the reaction concentration at very low concentrations. For this we performed the thiol-ene reaction up to 0.09 mM concentrations (not shown). However after 1.8 mM the integrations of the product and peptide peaks became arbitrary. This could possibly be related to the lack of UV activity of the peptides measured at the lower concentrations and therefore limits the lowest concentration at which these reactions can be monitored.

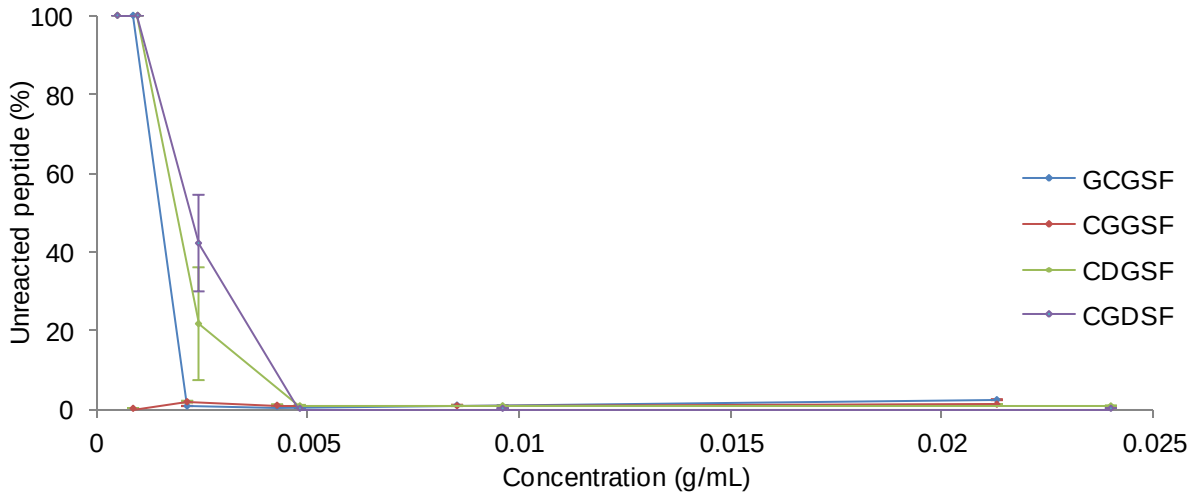

Figure 2.19 Percentage of unreacted peptide measured for the coupling of GCGSF (blue), CGGSF (red), CDGSF (green) and CGDSF (purple) and pentenoic acid A1 at different concentrations (300 s UV exposure, 2.5 mM initiator).

We also examined the role of concentration on the efficiency of the coupling for the peptides GCGSF, CGGSF, CDGSF and CGDSF with A1. We found that the percentage of unreacted peptide for the aspartic acid containing sequences increased at 4.5 mM concentrations indicating that the reaction is limited at low concentrations (Fig. 2.19). Replacing the aspartic acid with a glycine CGGSF resulted in very low percentage of unreacted peptide even at 0.9 mM concentrations. When the terminal cysteine was moved to the second

position in the sequence GCGSF, the percentage of unreacted peptide increased after 1.8 mM concentrations.

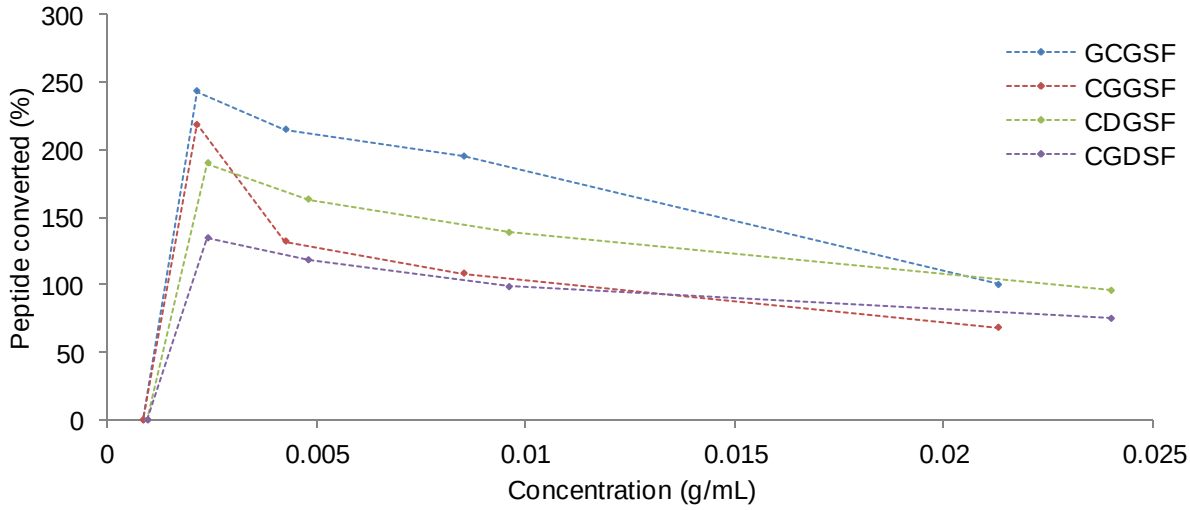

Figure 2.20 Percentage product formed peptide measured for the coupling of GCGSF (blue), CGGSF (red), CDGSF (green) and CGDSF (purple) with pentenoic acid A1 at different reaction concentrations (300 s UV exposure, 2.5 mM initiator).

The corresponding percentage of product formed for each peptide is shown in Fig. 2.20. The findings show over 100% product formation for these peptides, at low reaction concentrations. We propose that these aberrant conversions may be due to hidden peaks associated with impurities eluting together with the product peak. These impurities can be neglected at high concentrations, but when these are reduced. Although such impurities may only be present in low concentrations, they may display substantially higher extinction coefficients than the peptides studied. All calibration curves for the peptide series are consistent and fit with exponential functions, presumably as a result of the adsorption of peptides on the glassware and plasticware used for the preparation of the solutions. HPLC is the most sensitive technique we could use to measure reaction efficiencies, but a possible approach to investigate the presence of impurities would be to isolate the peak fractions using HPLC and perform mass spectroscopy on each individual peak or use a HPLC with

integrated mass spectroscopy to detect all fragments. This may give a better indication of any underlying peaks and whether they are separable from the product.

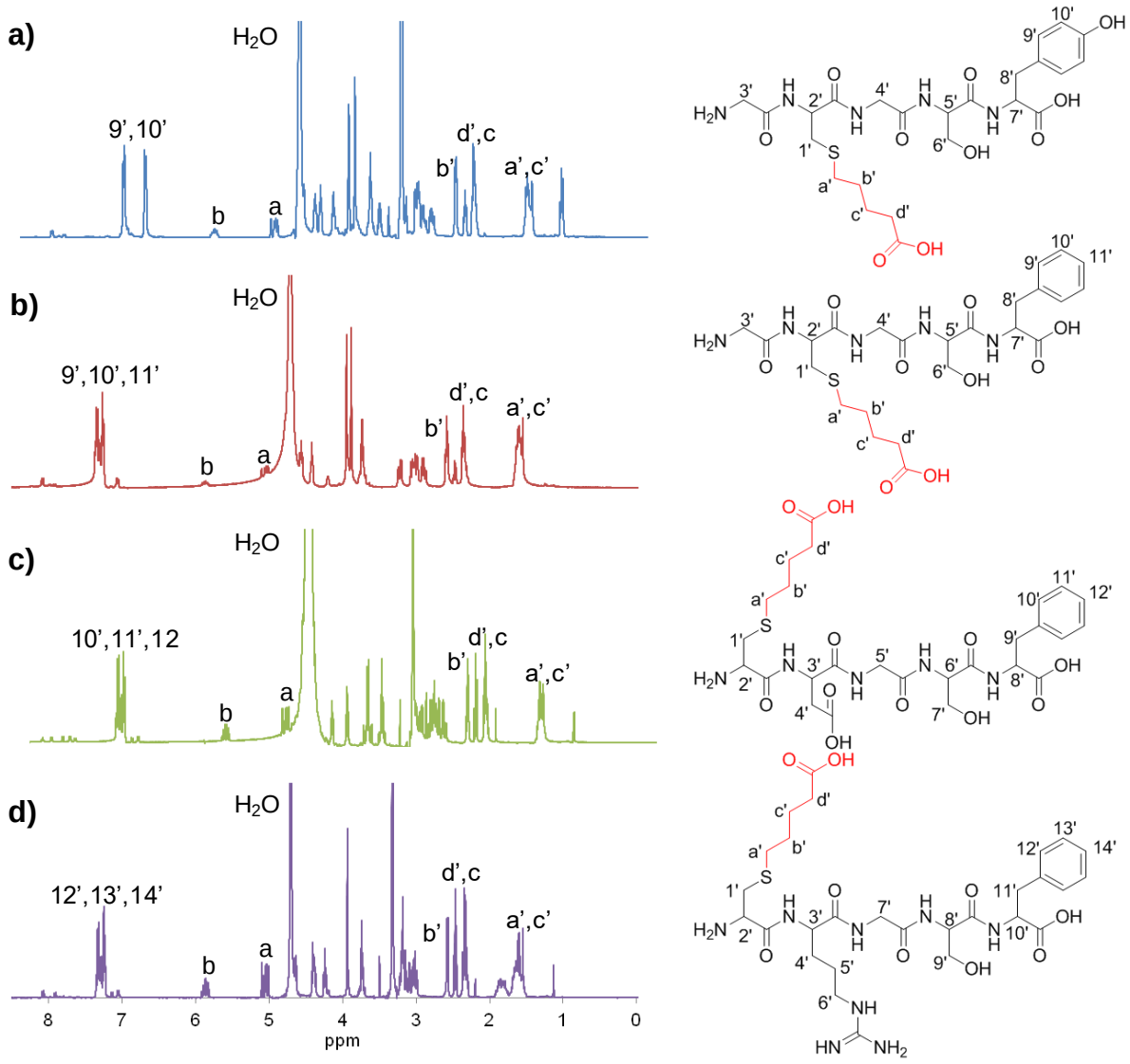

Figure 2.21 ^{1}H NMR spectroscopy of the thiol-ene products of pentenoic acid (A1) with a) GCGSY, b) GCGSF, c) CDGSF and d) CRGSF.

Mass spectrometry was performed on the thiol-ene coupled peptides reacted at 45 mM concentration with 2.5 mM PI and 300 s UV exposure. Findings showed that the expected masses for the peptide products were present for all the samples measured (Fig. 2.22). Disulfide peptide couplings were not

570

a)

observed for any of the peptide reaction mixtures and hence the side reactions observed with the HPLC reactions could be related to other products.

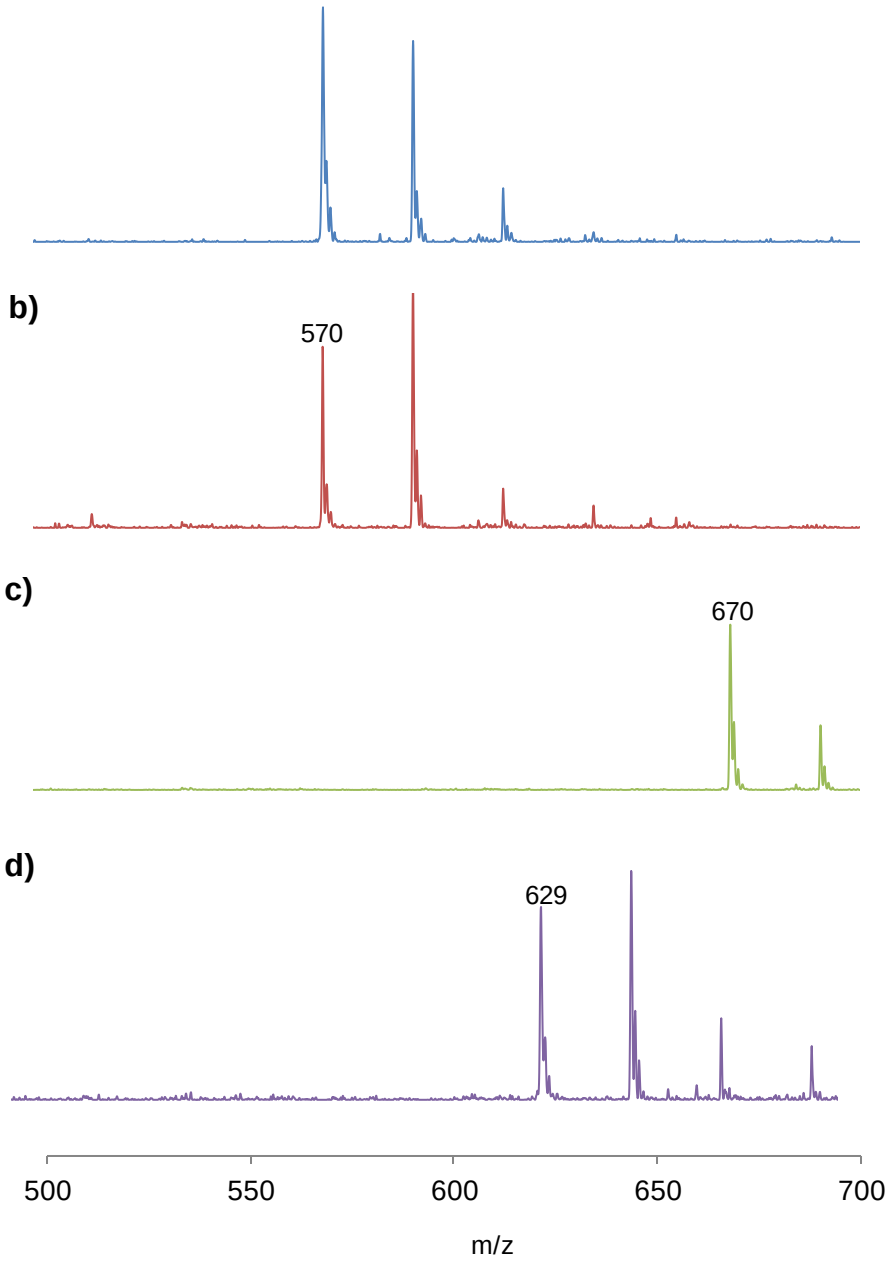

Figure 2.22 Mass spectrometry of the thiol-ene products of pentenoic acid (A1) and a) GCGSF (570 m/z)), b) CGGSF (570 m/z)), c) CRGSF (670 m/z) and d) CGDSF (629 m/z).

2.2.8 Impact of competitive radical quenching mechanisms

Thiol-ene couplings are thought to be relatively insensitive to the presence of oxygen as rate transfer of carbon-based radicals to thiols are typically one order of magnitude higher than their quenching by oxygen[223, 224]. However, as the concentration of thiols decreases (for example in cases for which only low concentrations of reagents, proteins or peptides are practically usable), transfer rates may become dominated by oxygen quenching. Therefore, we tested whether such events significantly occur in peptide coupling via thiol-ene chemistry. We studied the impact of the concentration of photoinitiator on the reaction efficiency with the peptide GCGSY at two different concentrations (4.5 and 9 mM, Fig. 2.23), corresponding to 5- and 10-fold dilutions compared to experiments reported in Fig. 2.24c. We found no effect of the photoinitiator concentration, within the range tested, on the consumption of thiols or the formation of product, although the latter levels were higher by c.a. 8% at peptide concentrations of 9 mM.

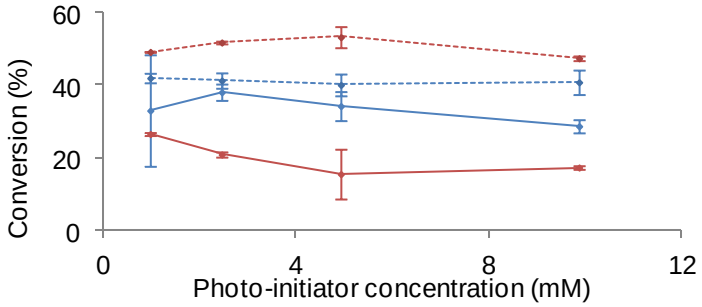

Figure 2.23 The impact of photoinitiator and peptide concentration (GCGSY) on the reagent conversion and product formation. Peptide concentrations: 4.5 mM (blue) and 9 mM (red). Dotted lines are product formed and full lines are unreacted peptide.

In addition, we carried out experiments at different thiol concentrations in degassed PBS buffer, to reduce the concentration of oxygen (Fig. 2.24). We found that although the levels of thiol consumption were comparable, the formation of product was significantly impaired (down to 21%). These

experiments suggest that oxygen is not the agent responsible for the quenching of radicals and the loss of product formation at higher concentrations (45 mM), but rather protects thiols against such reactions. In addition, our results imply that the reduced coupling observed at lower concentrations of thiols is not due to quenching by oxygen species but rather a simple reflection of reduced reaction rates. Therefore thiol-ene coupling displays some of the hallmarks of an oxygen-tolerant reaction, even at low reagent concentrations. Interestingly, we found that the choice of buffer is more important than reducing the concentration of oxygen. When couplings were carried out in HEPES buffer (pH 7, Fig. 2.24), we found a reduction in product formation and thiol consumption, perhaps indicating that tertiary amines from the buffer (present at 10 mM concentrations) can trap some of the radicals and reduce the reaction rate. Therefore, the presence of competing species other than oxygen appears as a limiting factor for thiol-ene coupling in buffers relevant to biofunctionalisation of biomaterials. In this respect, phosphate buffers appear as good media for thiol-ene based conjugation, biofunctionalisation and hydrogel formation.

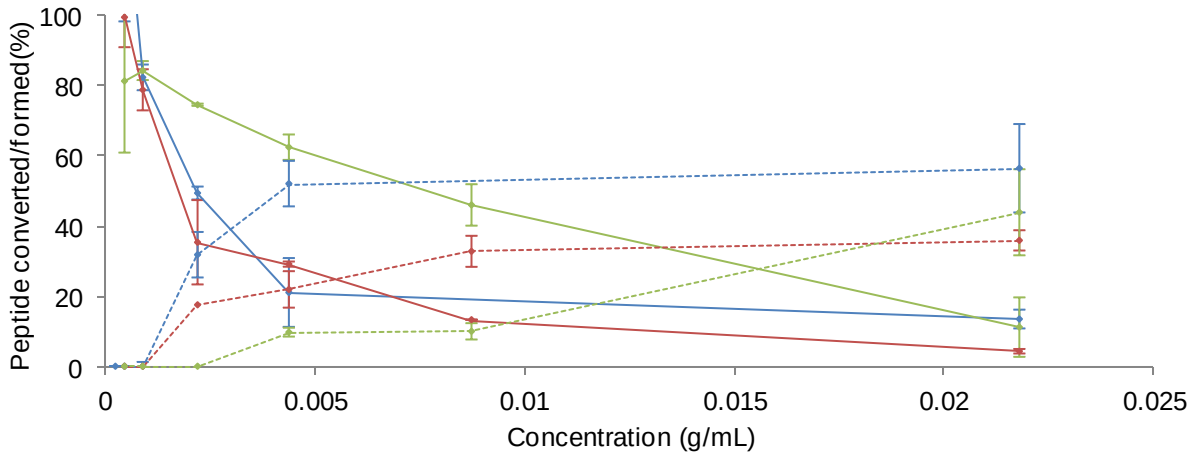

Figure 2.24 The impact of buffer type and degassing on peptide (GCGSY) conversion and product formed. Buffers: PBS (blue), degassed PBS (red) and HEPES (green). Dotted lines are product formed and full lines are unreacted peptide.

2.2 Summary

Thiol-ene chemistry displays interesting features for the biofunctionalisation of biomaterials. The present study focused on the determination of some of the parameters controlling thiol-ene efficiency in buffered conditions relevant to the coupling of peptides and potentially proteins to biomaterials. Our results demonstrate that the coupling of small molecules in buffered conditions occurs with high efficiency, although restricted by size, presumably via a diffusion-controlled mechanism. However, the pH of the environment has dramatic effects on the efficiency of the reaction. Changes in the chemical composition of the reaction medium, the local structure of the alkene as well as the thiol, in particular in the case of cysteine-bearing peptides, also impact coupling efficiencies. These observations have important implications in the development of biofunctionalisation strategies, for example for the design of peptide sequences allowing the control of biochemical and physical properties of peptide-based biomaterials and hydrogels. In contrast, the use of thiol-ene chemistry for coupling of proteins and antibodies to surfaces and biomaterials remains challenging and our results indicate that the low thiol concentrations typically used when coupling such larger biomacromolecules would result in considerably lower rates of reactions. These issues should be addressed for thiol-ene coupling to be included in the toolbox of methodologies compatible with the precise, regioselective coupling of proteins and antibodies to biomaterials and biosensors.

2.3 Experimental section

2.3.1 Materials

PEG methyl ether thiol (average M_n 1 kg/mol), *N*-acetyl *l*-cysteine (99%), cysteamine hydrochloride (97%), *l*-glutathione reduced (98%), ethanethiol (97%), 2-mercaptoethanol (99%), 4-pentenoic acid (97%), IRG2959 or 2-hydroxy-4'-(2-hydroxyethoxy)-2-methylpropiophenone (98%), phosphate buffered saline tablet, allylamine (98%), triethylamine (99%), diethylamine (99.5%), 4-pentenoyl chloride (98%), allyl bromide (97%), 5-bromo-1-pentene (95%), 4-bromo-1-butene (97%), acetic anhydride (98%), 2-(dimethylamino)ethyl methacrylate (contains 700-1000 ppm monomethyl ether hydroquinone as inhibitor, 98%), ethyl α-bromoisobutyrate (98%), ethanol (99.8%), 2,2'-bipyridine (>99%), copper (I) chloride (>99.995% trace metals basis), poly(methyl vinyl ether *alt*-maleic anhydride) (M_w ~216 kg/mol average M_n ~80 kg/mol), 2-chloroethylamine hydrochloride (99%), 2-ethyl-2-oxzoline (99%), methyl p-toluenesulfonate (97%), deuterium oxide (99.9% atom% D), deuterium chloride solution (37 wt% in deuterium oxide, 99% atom% D), sodium deuteroxide (40% in deuterium oxide 99 atom% D), hydrochloric acid (37%), anhydrous magnesium sulphate (99.5%), sodium bicarbonate (99.7%), sodium chloride (99.5%), sodium hydroxide (97%), dichloromethane (99.5%), anhydrous dichloromethane (99.8%), anhydrous dimethylformamide (99.8%), methanol (HPLC 99.9%), tetrahydrofuran (99.9%), ethyl acetate (99.7%), diethyl ether (99%), petroleum ether 40-60, acetonitrile (HPLC 99.9%), heptane (HPLC 99%), dimethylformamide (pharmaceutical secondary standard) and silica gel were purchased from Sigma Aldrich. Potassium carbonate (99%), and chloroform (AnalaR 0.6% of ethanol) were purchased

from VWR. Potassium permanganate (98%) was purchased from Alfa Aesar. Chloroform-D (99.8%) was purchased from Cambridge Isotope Laboratories Inc. Cellulose ester dialysis membrane (M_w 3,-5 kg/mol) was purchased from Spectrum laboratories Inc. Custom peptides GCGSY, GCGSF, CGGSF, CRGSF, CGRSF, CDGSF and CGDSF were purchased from Proteogenix, France.

2.3.2 Instrumentation

^{1}H NMR spectroscopy was produced using Bruker AV 400 and AVIII 400, abbreviations for the peaks: s- singlet, d-doublet, t-triplet, q-quartet, dt-doublet of triplets, dq-doublet of quartets, tt-triplet of triplets and m-multiplet. ATR-FTIR spectroscopy were produced using a Bruker Tensor 27 spectrometer equipped with a MCT detector, results were acquired at a resolution of 16 cm^{-1} and a total of 128 scans per run in the region of 600-4000 cm^{-1}, abbreviations for the peaks: s-strong, m-medium and w-weak. The UV light used to initiate reactions was the Omnicure series 1500. The radiometer used to measure the UV light intensity was from International light technologies, ILT 1400-A radiometer photometer. HPLC analysis was conducted using a Waters separations module instrument equipped with a 2489 UV/Vis detector, a reversed-phase C18 Atlantis T3 3 µm 4.6 x 150 mm column, a reversed-phase C18 Atlantis T3 5 µm 3 x 50 mm guard column and a water/acetonitrile gradient. All samples were filtered through 0.2 µm supor membrane pore before analysis. GPC analysis were performed using an Agilent 1260 Infinity system equipped with an refractive index and variable wavelength detector, 2 PLgel 5 µm mixed-C column (300 x 7.5 mm), a PLgel 5 mm guard column (50 x 7.5 mm) operated

in DMF with NH_4BF_4 (5 mM). The instrument was calibrated with poly(methyl methacrylate) standards (5.5 to 46.9 kg/mol). All samples were filtered through 0.2 µm nylon 66 before analysis. Mass spectrometry (ESI) was performed using Agilent 6310 Ion Trap (350 °C dry temperature, 40 psi nebulizer, 10 l/min dry gas, scanned 80-2200 m/z, average of 5 spectra). All spectra were measured in the positive mode in acetonitrile.

2.3.3 Statistical analysis

All data were analysed by Tukey's test and significance was determined by * $p < 0.05$, ** $p < 0.01$: *** $p < 0.001$. A full summary of statistical analysis is provided in the Fig. A1.1-A1.4.

2.2.4 Thiol-ene reaction for NMR monitoring

Deuterated-PBS was prepared (1 PBS tablet per 200 mL deuterium oxide) in a volumetric flask. This solution was used for the thiol-ene experiments. Thiol (45.4 µmol, 45 mM) and alkene (45.4 µmol, 45 mM) 1:1 ratio were dissolved in deuterated-PBS (1 mL). IRG2959 solution was prepared in methanol (0.198 M, 0.0444 g/mL). To thiol-ene solution (0.5 mL) was added 2 mol% (1 mM, 5 µL, for all small molecules) or 5 mol% (2 mM, 12.5 µL, for polymers or peptides) photoinitiator in methanol. The samples were irradiated with UV (17 mW, 350-500 nm) for a known amount of time (60 s for small molecules, power 1.02 J/cm^2; 300 s for polymers and peptides, 5.1 J/cm^2) and analysed by ^{1}H NMR spectroscopy. The conversion was calculated through the consumption of the single proton alkene peak (reference) with respect to the formation of the two

product peaks, the average of the two calculations were taken to obtain the average percentage conversion. Certain variables controlling the thiol-ene reaction were investigated; UV irradiation time, photoinitiator concentration, pH of the solution and intensity of UV irradiation with a series of thiols and alkenes. The pH of the solutions were adjusted using the Hanna instruments pH meter.

2.3.5 Thiol-ene reaction for HPLC monitoring

The peptides were dissolved in PBS at known concentrations (45.4 µmol, 45 mM) then diluted to known concentrations and measured using HPLC connected to a UV detector (275 nm for tyrosine containing sequences and 254 nm for phenylalanine containing sequences) for the peptide calibration. Atlantis T3 3 µm 4.6x150 mm column was used with a solvent gradient; from 0-20 min acetonitrile: water 2:98 to 15:85, 20-25 min 30:70, 25-35 min 100:0, and 35-40 min 2:98. Reaction mixtures containing peptide: pentenoic acid **(A1)** 1:1 and photoinitiator 5 mol% (2.5 mM) were prepared and reacted using UV for 300 s then diluted and measured using HPLC for the reaction calibration. IRG2959 solution was prepared in methanol (0.198 M, 0.0444 g/mL). For the low concentration reaction, mixtures containing peptide: pentenoic acid **(A1)** 1:1 and photoinitiator 5 mol% (2.5 mM) were prepared, diluted to known concentrations then reacted using UV for 300 s. HPLC traces were analysed for the product formation and unreacted peptide via a calibration, typical traces are shown in Fig. A1.3-1.5.

2.3.6 Synthesis of *N,N*-diethylpent-4-enamide (A2)

Diethylamine (1 eq., 0.0253 mol) was dissolved in anhydrous dichloromethane (7 mL) and the flask was placed in an ice bath. Triethylamine (1 eq.) was added, then pentenoyl chloride (1 eq.) dropwise with vigorous stirring. The content turned brown and contained salts.

Dichloromethane (100 mL) was added to the mixture and extracted from hydrochloric acid (0.5 M, 30 mL three times), sat. sodium bicarbonate (30 mL three times) and brine (30 mL three times). The aqueous layers were washed with dichloromethane and recovered. The organic phases were combined, dried over magnesium sulphate and evaporated to yield a brown oil 3.02 g. δ_H (400 MHz; $CDCl_3$) δ 1-1.1 (6H, dt), 2.32 (4H, m), 3.2-3.3 (4H, dq) 4.9-5 (2H, m) and 5.7-5.8 (1H, m) (Fig. 2.25). *v/cm*$^{-1}$ ~2900 (w, C-H), 1643 (s, C=O) and 1432 (m, C=C) (Fig. 2.26).

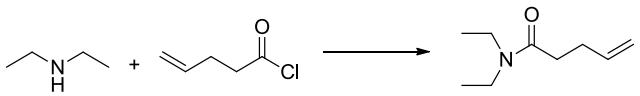

A2

Scheme 2.4 Synthesis of *N,N*-diethylpent-4-enamide (A2).

2.3.7 Synthesis of *N*-allylacetamide (A3)

Allylamine (1 eq., 0.0294 mol) and triethylamine (1 eq.) were dissolved in tetrahydrofuran (10 mL), then acetic anhydride (5 eq., 0.147 mol) was slowly added with stirring and the mixture was heated to 50 ºC for 24 h resulting in a brown solution. The solvent was evaporated and a column was performed in petroleum ether: ethyl acetate (1:1), then graduated to ethyl acetate. The solvent was evaporated to yield a brown oil 3.458 g. δ_H (400 MHz; D_2O) δ 2.0 (3H, s), 3.7 (2H, d), 5-5.1 (2H, m) and 5.7-5.8 (1H. m) (Fig. 2.25). *v/cm*$^{-1}$ ~2900 (w, C-H), 1641 (s, C=O), 1548 (m, C=C) and 1284 (m, C-N) (Fig. 2.26). Similar types of reactions were performed to generate similar products[225].

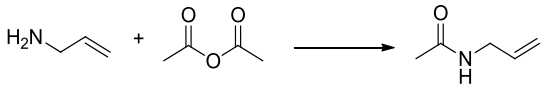

A3

Scheme 2.5 Synthesis of *N*-allylacetamide (A3).

2.3.8 Synthesis of *N,N,N*-triehtylprop-2-en-1-aminium (A4), *N,N,N*-triehtylbut-3-en-1-aminium (A5) and *N,N,N*-triehtylpent-4-en-1-aminium (A6)

Triethylamine (1.25 eq., 0.0310 mol) was dissolved in diethyl ether (5.5 mL), then was added allyl bromide (1 eq., 0.0248 mol) or 4-bromo-1-butene (1 eq.) or 5-bromo-1-pentene (1 eq.), the reaction was heated 50 ºC for 17 h. The solution was evaporated using pressure. Diethyl ether was added and the solution was dried twice more to yield a white powder (17), yellow oil (18 and 19). *N,N,N*-triethylprop-2-en-1-aminium **(A4)** δ_H (400 MHz; D_2O) δ 1.3 (9H, t), 3.3 (6H, q), 3.8 (2H, d), 5.6-5.7 (2H, m) and 5.8-5.9 (1H, m) (Fig. 2.25). *v/cm*$^{-1}$ ~2900 (w, C-H), 1398 (m, C=C) and 1170 (m, C-N) (Fig. 2.26). *N,N,N*-triethylbut-3-en-1-aminium **(A5)** δ_H (400 MHz; D_2O) δ 1.2 (9H, t), 2.4 (2H, dt), 3.1 (2H, m), 3.2 (6H, q), 5.1-5.2 (2H, m) and 5.6-5.7 (1H, m) (Fig. 2.25). *v/cm*$^{-1}$ ~2900 (w, C-H), 1398 (m, C=C) and 1170 (m, C-N) (Fig. 2.26). *N,N,N*-triethylpent-4-en-1-aminium **(A6)** δ_H (400 MHz; D_2O) δ 1.2 (9H, t), 1.7 (2H, tt), 2.1 (2H, dt), 3-3.1 (2H, m), 3.2 (6H, q), 3.8 (2H, d), 5-5.1 (2H, m) and 5.7-5.8 (1H, m) (Fig. 2.25). *v/cm*$^{-1}$ ~2900 (w, C-H), 1403 (m, C=C) and 1178 (m, C-N) (Fig. 2.26). Similar products were generated using similar methodology [226].

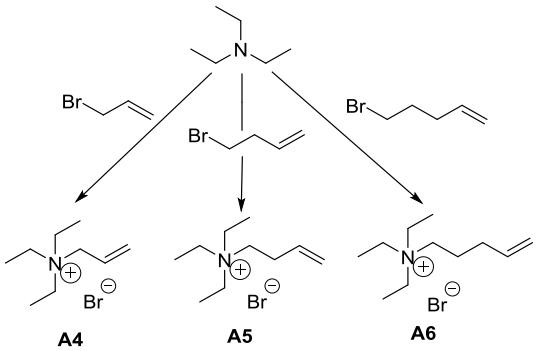

Scheme 2.6 Synthesis of *N,N,N*-triehtylprop-2-en-1-aminium (A4), *N,N,N*-triehtylbut-3-en-1-aminium (A5) and *N,N,N*-triehtylpent-4-en-1-aminium (A6) from triethylamine.

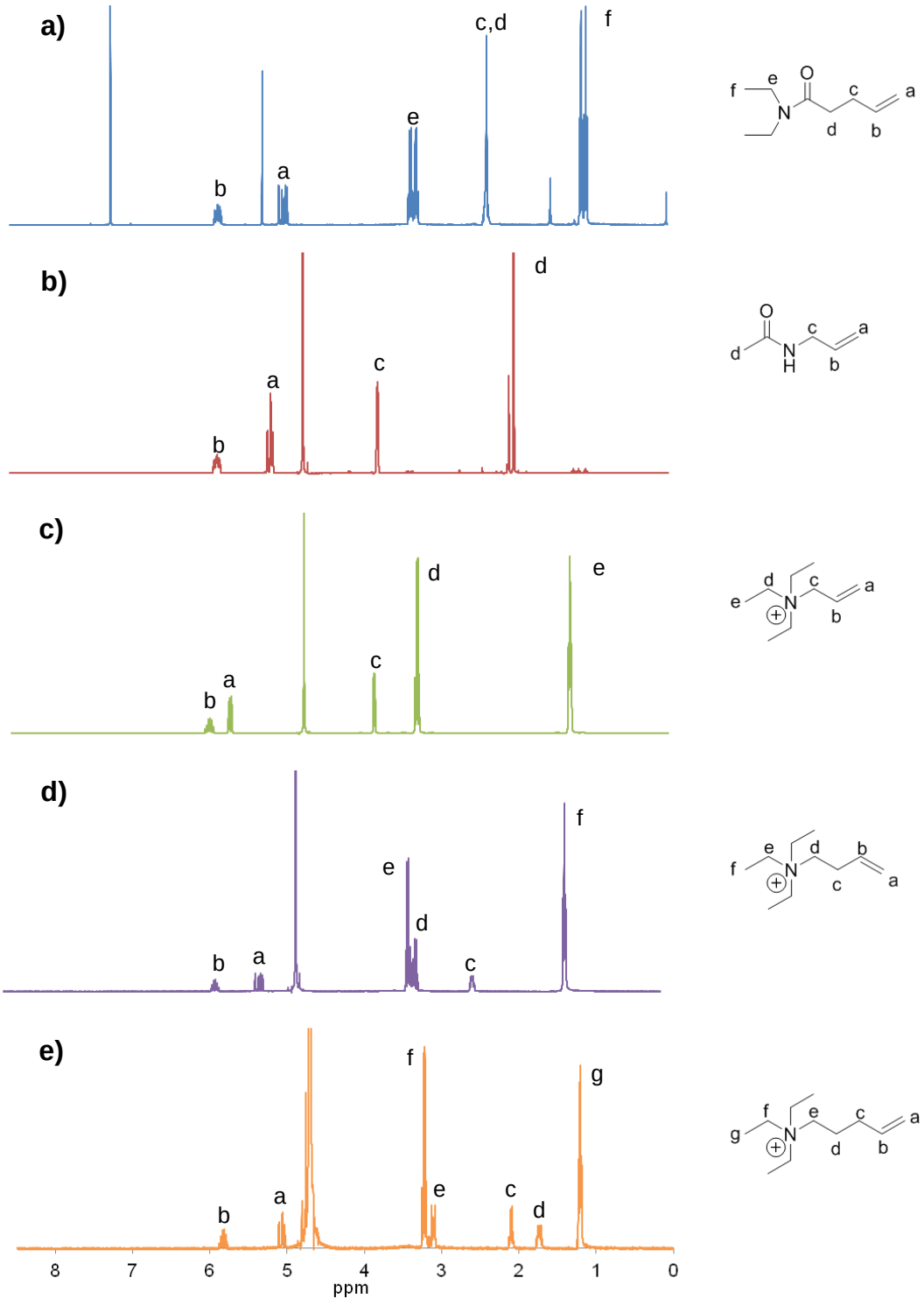

Figure 2.25 ^{1}H-NMR of a) *N,N*-diethylpent-4-enamide (A2) b) *N*-allylacetamide (A3) c) *N,N,N*-triehtylprop-2-en-1-aminium (A4) d) *N,N,N*-triehtylbut-3-en-1-aminium (A5) and e) *N,N,N*-triehtylpent-4-en-1-aminium (A6).

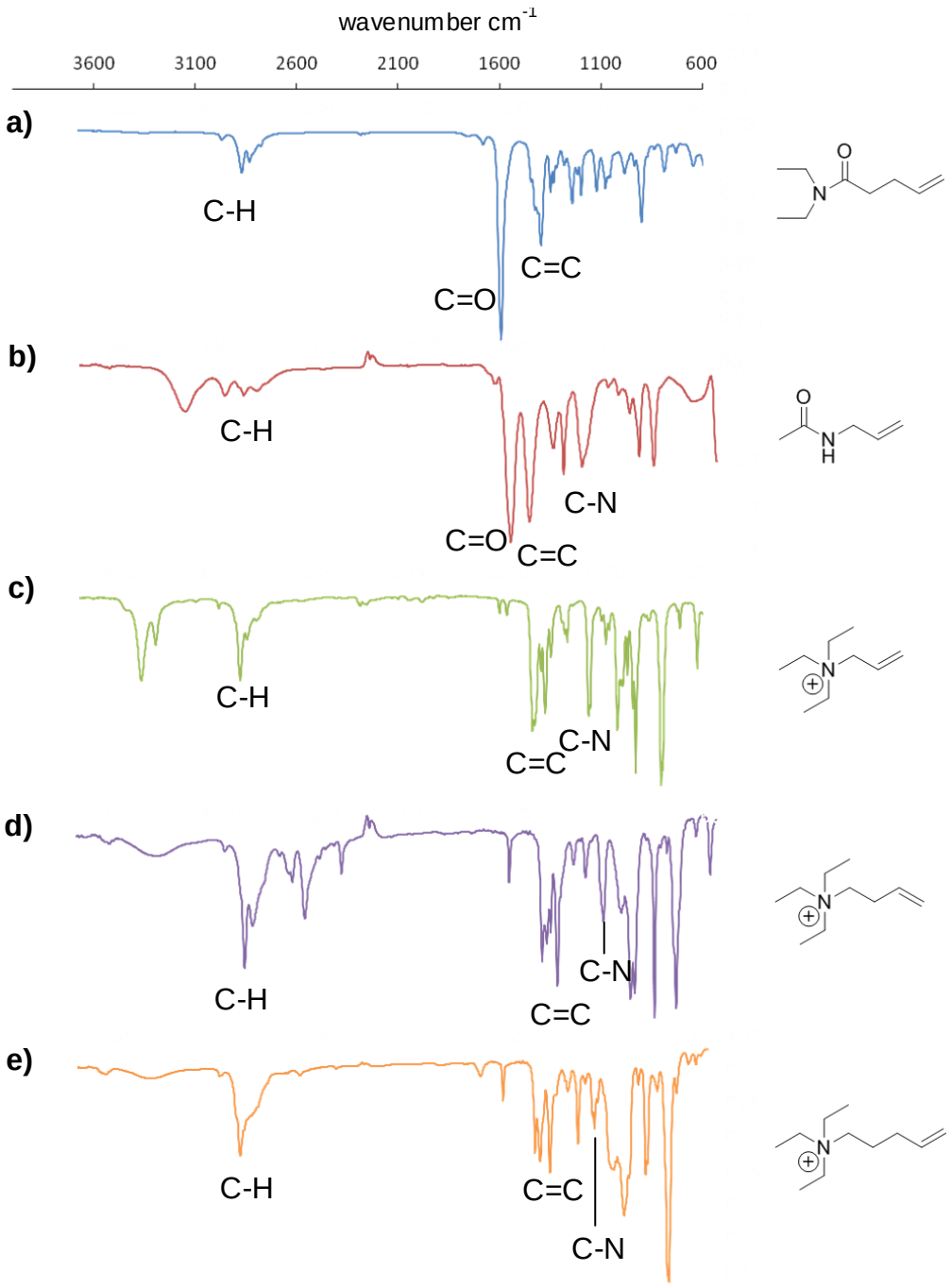

Figure 2.26 FTIR a) *N,N*-diethylpent-4-enamide (A2) b) *N*-allylacetamide (A3) c) *N,N,N*-triehtylprop-2-en-1-aminium (A4) d) *N,N,N*-triehtylbut-3-en-1-aminium (A5) and e) *N,N,N*-triehtylpent-4-en-1-aminium (A6) with highlighted stretching vibrations.

2.3.9 Synthesis of pDMAEMA

pDMAEMA synthesis was modified from another protocol[214]. A solution with ethanol: deionised water (1:4) was prepared and degassed for 30 min. 2-(dimethylamino)ethyl methacrylate (0.0954 mol) was weighed into a flask containing ethyl α-bromoisobutyrate (0.00037 mol), dissolved in ethanol-water (7.5 mL) and degassed for 30 min. Into a second flask was weighed 2,2'-bipyridine (0.00019 mol), dissolved in ethanol-water solution (7.5 mL) and degassed for 30 min. To the 2,2'-bipyridine solution was added copper (I) chloride (0.00019 mol), the brown solution was sonicated for 10 minutes. The catalyst solution was transferred to the monomer solution and the reaction was stirred under inert atmosphere for 5 h, 50 ºC. The ethanol was evaporated and the water freeze dried. The remaining solid was dissolved in tetrahydrofuran and added to silica gel (20 g), agitated for 1 h, filtered and concentrated using a rotary evaporator, then precipitated in heptane, filtered and dried under reduced pressure (pDMAEMA). GPC, M_n 67.9 kg/mol, $Đ_M$ 1.6 (Fig. 2.12). δ_H (400 MHz; D_2O) δ 0.75-1.2 (3H, m), 1.7-2.0 (2H, m), 2.3 (6H, s), 2.6-2.8 (2H, m) and 4.1 (2H, m) (Fig. 2.10). ν/cm^{-1} ~2900 (w, C-H), 1720 (s, C=O), 1261 (m, C-N) and 1100 (s, C-O) (Fig. 2.11). Characterisation showed comparative product formation[214].

2.3.10 Functionalisation of pDMAEMA to pDMAEMA propene (A7), pDMAEMA butene (A8), pDMAEMA pentene/ pDMAEMA^{+}(A9)

pDMAEMA (1eq., 1 g, 0.0064 mol) was dissolved in dimethylformamide (10 mL), then was added allyl bromide (5eq., 0.031 mol), 4-bromo-1-butene or 5-bromo-1-pentene (2.5eq., 0.015 mol) and the reaction was heated overnight at 70 ºC. Precipitated in diethyl ether and the remaining solid was dissolved in methanol and precipitated in diethyl ether, the recovered polymer was precipitated from methanol twice more. The polymer was recovered and dried under reduced pressure. pDMAEMA propene **(A7)** δ_H (400 MHz; D_2O) δ 0.80-1.3 (3H, m), 1.8-2.1 (2H, m), 3.2 (6H, s), 3.6-3.9 (2H, m), 4.0-4.1 (2H, m), 4.4-4.6 (2H, m) 5.7-5.9 (2H, m) and 6.0-6.2 (1H, m) (Fig. 2.10). *v/cm^{-1}* ~2900 (w, C-H), 1727 (s, C=O), 1660 (s, C=C), 1272 (m, C-N) and 1150 (s, C-O) (Fig. 2.11). pDMAEMA butene **(A8)** δ_H (400 MHz; D_2O) δ 0.75-1.2 (3H, m), 1.8-2.1 (2H, m), 2.6-2.7 (2H, m), 3.2 (6H, s), 3.4-3.6 (2H, m), 3.7-4.0 (2H, m), 4.3-4.6 (2H, m) 5.3-5.4 (2H, m) and 5.8-5.9 (1H, m) (Fig. 2.10). *v/cm^{-1}* ~2900 (w, C-H), 1726 (s, C=O), 1646 (w, C=C), 1247 (m, C-N) and 1149 (s, C-O) (Fig. 2.11).pDMAEMA pentene **(A9)** δ_H (400 MHz; D_2O) δ 0.85-1.4 (3H, m), 1.9-2.1 (2H, m), 2.1-2.3 (4H, m), 3.3 (6H, s), 3.4-3.5 (2H, m), 3.7-4.0 (2H, m), 4.3-4.6 (2H, m) 5.0-5.2 (2H, m) and 5.8-6.0 (1H, m) (Fig. 2.10). *v/cm^{-1}* ~2900 (w, C-H), 1727 (s, C=O), 1643 (w, C=C), 1243 (m, C-N) and 1137 (s, C-O) (Fig. 2.11).

2.3.11 Synthesis of *N*-(2-chloroethyl)-4-pentenamide

2-chloroethylamine hydrochloride (1.2 eq., 0.092 mol) was measured into a round bottom flask and purged with inert gas for 30 minutes. Then was added anhydrous dimethylformamide (80 mL). The flask was put into an ice bath and under inert gas, triethylamine (2.5 eq., 0.194 mol) was added followed by dichloromethane (75 mL) and pentenoyl chloride (1 eq., 0.077 mol) was added. The reaction was stirred in a water bath for 24 h under inert atmosphere. A brown solution and cream precipitate formed.

The flask content was added into a separation funnel with dichloromethane (200 mL). With the addition of dichloromethane, the precipitate dissolved. The organic solution was extracted from hydrochloric acid (1M, 500 mL four times), sat. sodium carbonate (500 mL twice) then from brine (500 mL four times). The organic layers were recovered and dried over magnesium sulphate. The organic layer was evaporated to yield a brown oil. δ_H (400 MHz; $CDCl_3$) 2.2-2.35 (4H, m), 3.55 (4H, m), 4.9-5.0 (2H, m) and 5.7-5.9 (1H, m) (Fig. 2.6).

2.3.12 Synthesis of 2-butenyl-2-oxazoline monomer

Into oven dried glassware was added crushed potassium hydroxide (1eq., 0.08 mol) and the system was purged with inert gas for 30 min[22]. Dry methanol (40 mL) was added and then N-(2-chloroethyl)-4-pentenamide (1eq.). The reaction was heated to 70 ºC for 24 h. The potassium chloride salt was filtered and the remaining solution was evaporated. The content was distilled over calcium hydride to yield a clear oil. δ_H (400 MHz; $CDCl_3$) 2.4 (4H, m), 3.8 (2H, t), 4.3 (2H, t), 5.0-5.1 (2H, m) and 5.8-5.9 (1H, m) (Fig. 2.6). ν/cm^{-1} ~2900 (w, C-H),

1675 (s, C=O), 1174 (w, C-N) (Fig. 2.7). Characterisation showed comparative product formation[22].

2.3.13 Synthesis of polyethyl oxazoline

2-Ethyl-2-oxazoline distilled over calcium hydride (100 eq., 0.1 mol) (δ_H (400 MHz; $CDCl_3$) 1.0 (2H, t), 2.2 (1H, q), 3.7 (2H, t) and 4.1 (2H, t), *v*/cm^{-1} ~2900 (w, C-H), 1672 (s, C=O), 1172 (w, C-N), and anhydrous acetonitrile (20 mL) were measured into a microwaveable flask containing a magnetic stirrer. Then was added methyl *p*-toluenesulfonate (1 eq.) over a flow of inert gas. The reaction was heated using a microwave, 140 ºC for 30 minutes[23]. The reaction was terminated with a drop of water and the precipitated in cold diethyl ether three times. The remaining polymer was recovered and dried under reduced pressure. The reaction proceeded to full conversion via ^{1}H spectroscopy. δ_H (400 MHz; $CDCl_3$) 1.0 (2H, m), 2.2-2.4 (4H, m) and 3.5 (2H, m) (Fig. 2.6). *v*/cm^{-1} ~3400 (br, O-H), ~2900 (w, C-H), 1625 (s, C=O), 1184 (w, C-N) (Fig. 2.7).

2.3.14 Synthesis of polyoxazoline co-polymer, pOx (A10)

2-Ethyl-2-oxazoline distilled over calcium hydride (80 eq., 0.08), 2-butenyl-2-oxazoline (20 eq.) and anhydrous acetonitrile (20 mL) were measured into a microwaveable flask containing a magnetic stirrer. Then was added methyl *p*-toluenesulfonate (1 eq.) over a flow of inert gas. The reaction was heated using a microwave, 140 ºC for 30 minutes[23]. The reaction was terminated with a drop of water and the precipitated in cold diethyl ether three times. The remaining polymer was recovered and dried under reduced pressure. The reaction proceeded to full conversion via GC (not shown) and ^{1}H NMR

spectroscopy. δ_H (400 MHz; $CDCl_3$) 1.1 (2H, m), 2.1-2.5 (8H, m), 3.4 (2H, m), 5.0 (2H, m) and 5.8 (1H, m) (Fig. 2.6). *v*/cm^{-1} ~3400 (br, O-H), ~2900 (w, C-H), 1633 (s, C=O), 1180 (w, C-N) (Fig. 2.7). GPC M_n 6.3 kg/mol, $Đ_M$ 1.62 (Fig.2.12). Characterisation showed comparative product formation[23].

2.3.15 Poly(maleic amide co-acid), pMA$^-$ (A11)

Allylamine (1 eq., 0.08 mol) was dissolved in acetonitrile (250 mL). Poly(methyl vinyl ether *alt*-maleic anhydride) (1eq.) was dissolved in acetonitrile (200 mL) in a second flask. *v*/cm^{-1} ~3400 (br, O-H), ~2900 (w, C-H), 1620 (s, C=O), 1066 (w, C-O) (Fig. 2.9). The poly(methyl vinyl ether *alt*-maleic anhydride) solution was slowly added to the amine solution with vigorous stirring. On addition of poly(methyl vinyl ether *alt*-maleic anhydride) to the allylamine, a white precipitate formed. The mixture was stirred at 70 °C for 24 h and room temperature for 48 h. The acetonitrile was evaporated and the remaining solid dissolved in sat. sodium bicarbonate solution (100 mL) and extracted from chloroform (200 mL three times). The aqueous layer was recovered and precipitated in hydrochloric acid (1.2 M, 400mL). The precipitate was dissolved in water and dialysed. The remaining polymer was recovered by freeze drying. δ_H (400 MHz; D_2O) 1.3-2.2 (2H, m), 2.5-3.0 (2H, m), 3.1-3.5 (3H, m), 3.6-3.8 (2H, m), 4.0-4.2 (1H, m), 5.0-5.3 (2H) and 5.6-5.9 (1H, m) (Fig. 2.8). *v*/cm^{-1} ~3400 (br, O-H), ~2900 (w, C-H), 1556 (s, C=O), 1388 (w, C-N) and 1072 (w, C-O) (Fig. 2.9).

Chapter 3

Design of thiol-ene based hydrogels for 3D cell culture

3.1 General methodology

Interest in hydrogel materials is growing exponentially; they have been applied in the field of tissue engineering as 2D and 3D cell culture models[142, 144, 195] as well as drug delivery systems[175, 227], coatings[228] and medical devices[229]. Hydrogel systems have widely been explored using natural and synthetic systems. One of the important aspects for the hydrogel design is the gelation. Gelation can occur through chain growth polymerisation or step growth polymerisation, the mechanical properties for each type of gel differ to one another[157]. A popular crosslinking chemistry for step growth polymerisation is Michael addition where the gelation is spontaneous above room temperature, however, alkaline conditions are required to initiate the reaction[9] and the gelation kinetics cannot be controlled well. Here we explore photoinitiated thiol-ene chemistry as the method used to form hydrogels from three different backbones, gelation occurs at neutral pH and is initiated with UV light, providing good control over the gelation kinetics and ability to control other

features of the gel (stiffness, bioactivity, degradation). The three polymeric backbones (A9-A11) studied differ in their chemical and physical characteristics. The physio-chemical properties of the hydrogels are likely to impact on the mechanical behaviour as well as the bioactivity of the hydrogels. Therefore, we aimed to generate three types of hydrogels with very different chemistries and charge densities. The polymer-polymer thiol-ene reaction efficiencies were explored in the previous chapter. Here we replace the mono-functional PEG thiol with di-functional PEGDT to crosslink the polymer backbones for the formation of a gel network (Fig. 3.1). The gel properties were characterised using FTIR spectroscopy, TGA and rheology. The polymer crosslinker was also be exchanged to a dicysteine containing peptide sequence to form proteolytically degradable hydrogels and biofunctionality could be added to the gel using mono-cysteine functional peptide sequences. These materials can be useful for 3D cell cultures. A schematic representation of work in this chapter is shown in Fig 3.2.

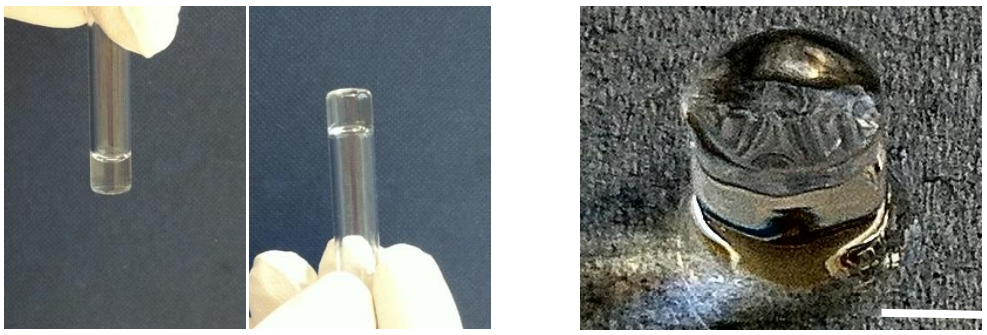

Figure 3.1 Demostration of a gelled hydrogel a) in a vial and b) free standing. Scale, 0.5 cm.

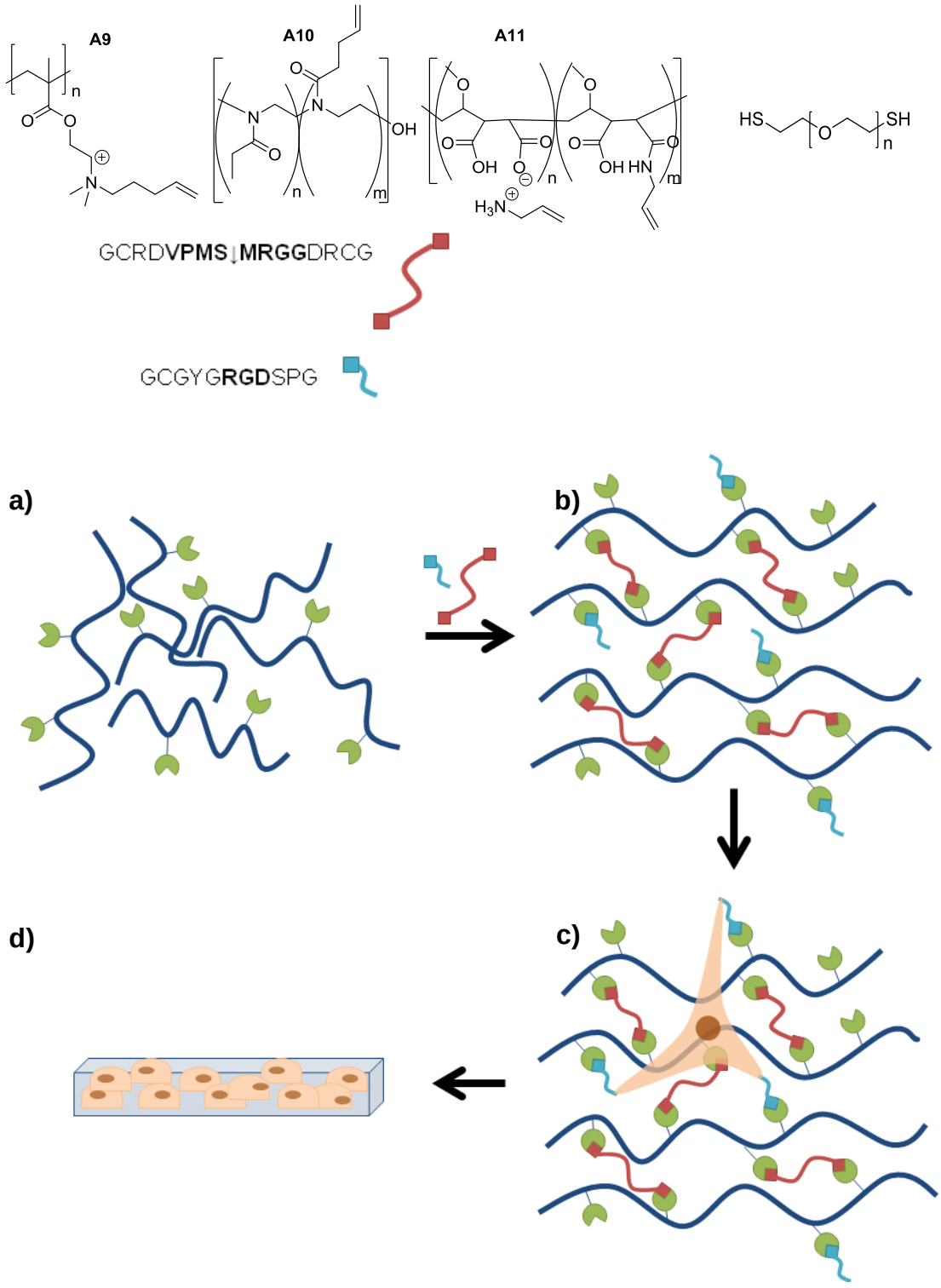

Figure 3.2 Schematic representation of hydrogel formation: a) alkene (green) functional polymeric backbone (blue) b) crosslinked using dithiols (red) and biofunctionalised using monothiols (turquiose), c) gel is shown with cell interactions to bioactive monothiols, d) cell culture in 3D hydrogel system.

3.2. Hydrogel crosslinking and characterisation

3.2.1 FTIR spectroscopy

Hydrogels were produced using three different alkene functional polymeric backbones and PEGDT (50 mol% with respect to the alkene functions) as the crosslinker. The gels were dehydrated using a freeze dryer and ATR-FTIR spectroscopy was performed on the dry gels (Fig.3.3). The dehydrated gels (full lines) were compared to the associated polymers (dotted lines). The assigned peaks for the polymers are also present in the dry gels. Carbonyl C=O peaks can be seen at 1580 cm^{-1} (pMA^-), 1630 cm^{-1} (pOx) and 1700 cm^{-1} ($pDMAEMA^+$), the vibrations at 2800-2900 cm^{-1} correspond to C-H stretching[230]. Peaks at 1190 cm^{-1} (pOx) and 1270 cm^{-1} ($pDMAEMA^+$) correspond to the C-N stretching vibrations. The peaks at 3400-3500 cm^{-1} correspond to O-H vibrations indicating that these polymers could have hydroscopic properties.

FTIR spectroscopic analysis showed an increase in the intensity of the C-O stretching vibration at 1100 cm^{-1} (pMA^-), 1110 cm^{-1} (pOx) and 1095 cm^{-1} ($pDMAEMA^+$) compared to the original FTIR spectra for the polymers. The increase in intensity is related to the addition of PEG into the material during crosslinking[230]. This effect is less pronounced for the pOx gels, since less crosslinks are present (13% alkene functional groups) and there is less PEG in the hydrogel, as the intensity of the corresponding band in the FTIR spectrum of pOx reflects.

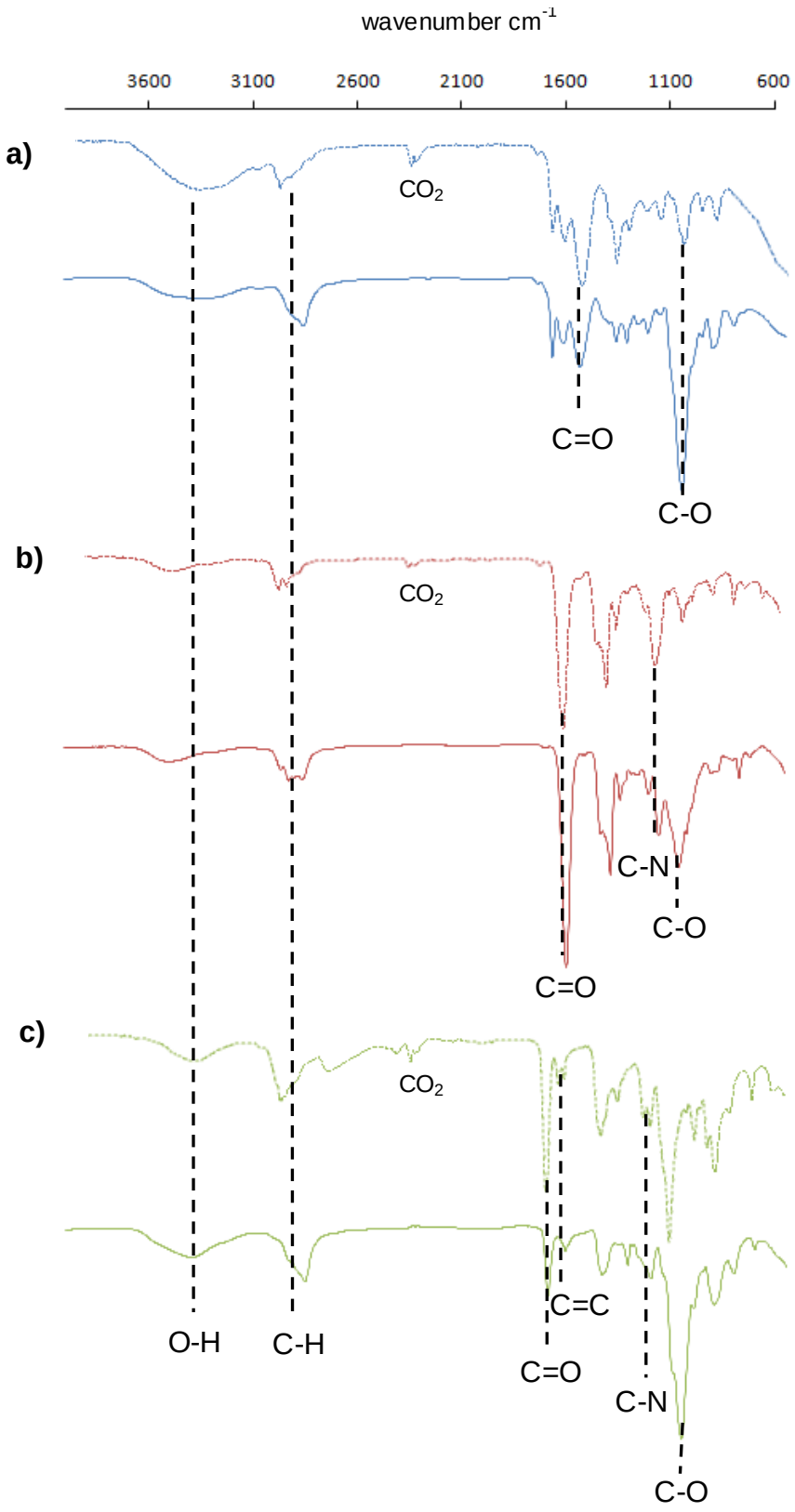

Figure 3.3 FTIR spectra of the polymers (dotted lines) and corresponding gels (dehydrated) with PEGDT (full lines) a) pMA^- c) pOx and e) $pDMAEMA^+$.

3.2.2 TGA

3.2.2 Swelling of the hydrogels

Hydrogels were produced using the three polymeric backbones (A9-A11) and PEGDT as the crosslinker (stiffness S5, 225 mM), the traces are shown in Fig. 3.4. All gels were crosslinked at 50 mol% with respect to the percentage of alkene functionalities present in the polymer (and based on 13% alkene functional groups in the case of pOx). The starting concentration of alkene was kept constant for all gels, rather than keeping the weight percent of the polymer constant. This is because we wanted to crosslink a known percentage of the alkenes, making the rest of the alkenes available for other types of functionalisation (i.e. peptide biofunctionalisation). Traces show the presence of water peaks corresponding to the majority of the gels (Fig. 3.4). The derivatives for the traces are shown to better show the peak intensities related to the degradation of the products relative to the temperature. Polymer degradation was observed at 350 °C for pMA^-, 390 °C for pOx and 360 °C for $pDMAEMA^+$ hydrogels. The intensity of the polymer peak decreased for pOx after incubation in PBS and deionised water; this is because the water to polymer ratio increased. Hydrogels with pMA^- and $pDMAEMA^+$ did not show a significant effect because the percentage of swelling was much lower.

The hydrogels were characterised using TGA before and after swelling in PBS or deionised water (equation 3.1 and 3.2). TGA was used to measure the amount of water present in the gels (Fig. 3.5). Results show that the percentage of water increasesdwhen submerged in PBS or water for all gels, the dimensions of the gels also increased slightly (not shown).

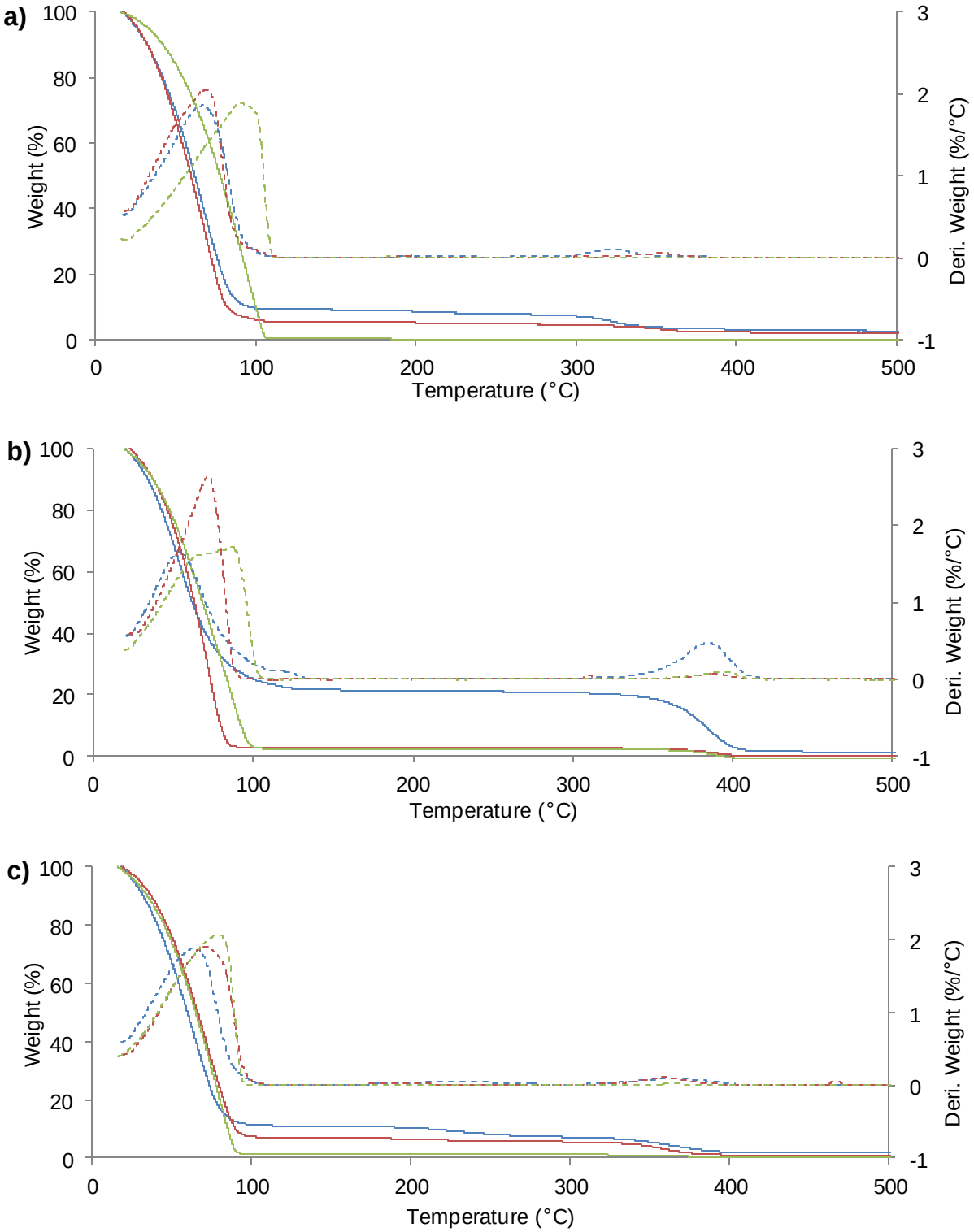

Figure 3.4 TGA traces for the gels from PEGDT and a) pMA^-, b) pOx and c) $pDMAEMA^+$ gels before (blue) and after submersion in PBS (red) and water (green), dotted lines represent the derivatives of the original TGA trace. Gelation was performed with thiol:ene ratio 0.5:1, 0.5 mol% PI and 120 s UV exposure at 17 mW/cm^2 UV intensity.

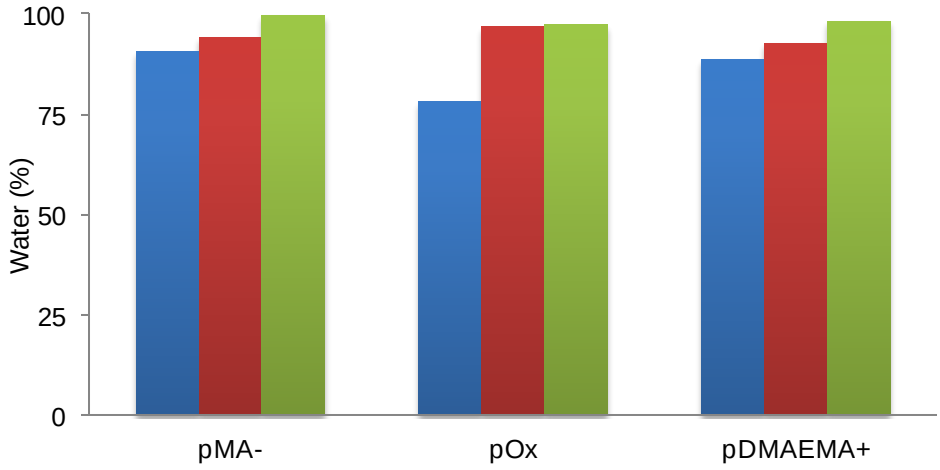

Figure 3.5 The percentage of water present in the different backbone gels (S5, 225 mM) with PEGDT before swelling (blue), swollen in PBS (red), swollen in deionised water (green). Gelation was performed with thiol:ene ratio 0.5:1, 0.5 mol% PI and 120 s UV exposure at 17 mW/cm^2 UV intensity.

The results show that the pMA$^-$ and pDMAEMA$^+$ hydrogels swell less than the pOx hydrogels (Fig. 3.6). Indeed, the pOx hydrogel displayed a higher degree of swelling in PBS and water (near 19%) when compared to the other two polymers (PBS 3.5-4.0%, water 9.0-9.5%) (Fig. 3.6). Farrugia reported the swelling behaviour for 2.5-10 wt% gels, swelling ratio 15-20[40]. This is comparable to our system. The pOx hydrogel reported here is made from 17.9 wt% polymer yielding 19% swelling.

Gels from pMA$^-$ and pDMAEMA$^+$ displayed higher crosslink densities per polymer chain, making the gel stronger and less susceptible to deformation when submerged in aqueous solution. All gels were generated in PBS; however, some swelling in PBS was still apparent. More swelling was observed for samples submerged in water; this is thought to be due to the increased osmotic pressure associated with the reduced ionic strength of the medium. The pOx polymer only displayed 13% of the monomers presenting an alkene functionality and only half contributing to crosslinking. This means that

the starting polymer content for pOx was higher (wt%) compared to the two other hydrogels. Hence it is not surprising that this resulted in a more swollen structure. In addition, the anticipated greater distance between effective crosslinks should result in higher swelling, as predicted by Oyen *et al*.[231].

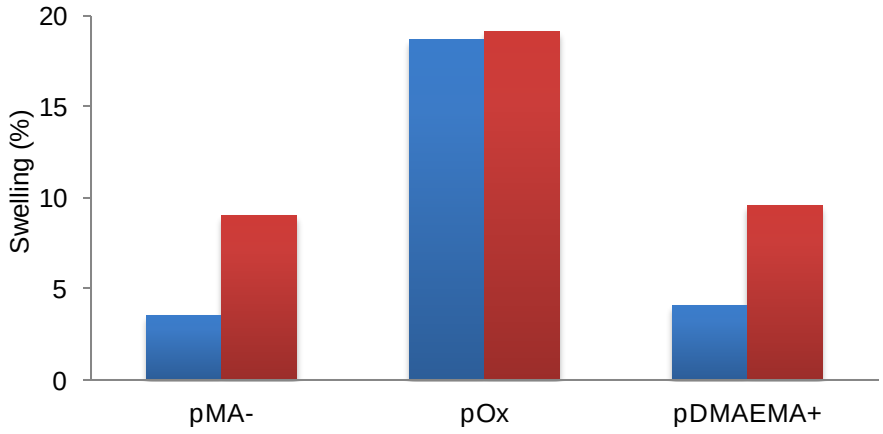

Figure 3.6 The percentage swelling of the gels with in PBS (blue) and deionised water (red). Gelation was performed with thiol:ene ratio 0.5:1 and 120 s UV exposure at 17 mW/cm^2 UV intensity.

Oyen *et al.* explained that when the molar mass between crosslinks decreased, the gels are less likely to deform and therefore, less swelling was observed[231]. Our results fit with this behaviour, the pOx gels have a greater distance between crosslinks and the swelling is a lot higher (the definition of swelling reported by Oyen *et al.* is absolute, with respect to the dry polymer). The TGA results for our work seem to show that the percentage of dry polymer in the swollen gels are very small, probably as a result of defects and looping during crosslinking, resulting in many chains not being incorporated in the network, or the lack of 100% efficiency in the thiol-ene coupling. In conclusion, the characterisation for the thiol-ene coupling efficiency may not be enough, the characterisation of the gel mechanics and crosslinking efficiency were required to better understand the crosslinking system.

3.2.3 Photo-rheology

Photo-rheology was used to characterise the crosslinking process *in situ* and the final mechanical properties of the resulting PEGDT crosslinked hydrogels. An UV activated method was setup to study the gelation of the gels. Others also used a similar method to monitor gelation[151]. Liquid mixtures of the gel components containing photoinitiator were added to the methacrylate functionalised glass slide on the quartz plate, UV light was turned on after 30 s into the time sweep measurement and kept on for 120 s, during this time the loss and storage modulus of these gels were measured, frequency and amplitude sweeps were also performed. Methacrylate functionalised glass slides were used in the setup, the methacrylate functionality and *in situ* gelation allowed for the incorporation of the alkenes on the surface of the glass into the hydrogels system and therefore avoiding any slippages during the measurement process (Fig. 3.11). The evolution of the storage and loss modulus as a function of time (during and after curing), for the pOx hydrogels of different stiffness, is represented in Fig 3.7. Initially the loss modulus was similar to the storage modulus, reflecting the liquid behaviour of the sample. With UV exposure after 30 s delay, the storage modulus increased sharply due to the formation of intermolecular crosslinks, exceeding the loss modulus[150]. All gels were crosslinked 50 mol% with respect to the percentage of alkene functionalities in the polymer (pOx, 13% alkene functional).

Table 3.1 The concentrations of the components used for each gel type in molar concentration and weight percent. Gels were made using thiol:ene 0.5:1 ratio, 0.5 mol% PI and 120 s UV exposure.

Stiffness	Thiol-ene conc^{n} (mM)	Wt% pMA^{-}	Wt% pOx	Wt% pDMAEMA^{+}	Wt% PEGDT	Wt% PI
S3	135	2.9	10.7	2.7	3.4	0.076
S4	180	3.8	14.3	3.6	4.5	0.1
S5	225	9.59	17.9	4.6	5.6	12.67

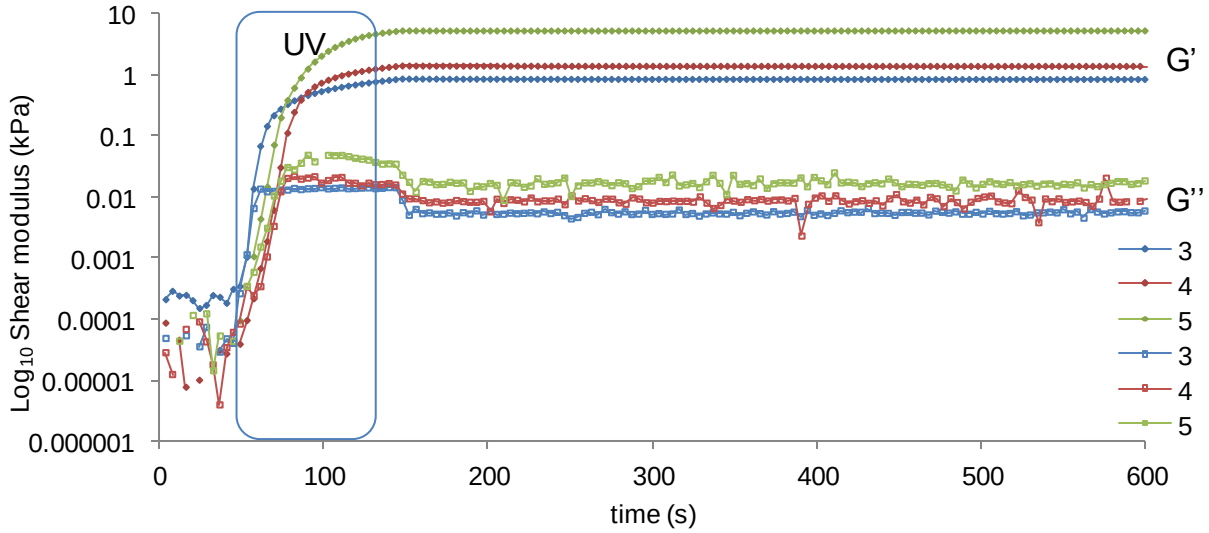

Figure 3.7 The time sweep graphs for the pOx gel of different stiffnesses S3 (blue 135 mM), S4 (red, 180 mM) and S5 (green, 225 mM) with thiol:ene ratio 0.5:1, 0.5 mol% PI, 120 s UV exposure at 17 mW/cm^{2} UV intensity and 0.5 mol% PI. Filled diamond markers correspond to G' (storage modulus) and empty square markers are G'' (loss modulus).

The different stiffness materials were formed by changing the total concentration of material in PBS (blue, 135 mM, S3 < red, 180 mM, S4 < green, 225 mM, S5) (refer to Table 3.1). The storage modulus values were obtained from the frequency graphs (displacement= 1e^{-4} rad; frequency= 0.1 to 100Hz) (Table 3.2 and Fig. 3.9). The pOx polymer forms the softer gel of the three backbones. This is thought to result from the greater spacing between alkenes along this backbone, and as a result an increase distance between crosslinks. pMA^{-} polymer forms the stiffest gel of the three backbones, consistent with the less swelling observed for this polymer (see Fig. 3.6). The higher modulus and lower percentage swelling observed for pMA^{-} gel is not

surprising. The results can be explained referring to the thiol-ene coupling reaction efficiency. The pMA^- polymer performed to higher reaction efficiencies than the $pDMAEMA^+$ when reacted with thiol S5 (Table 2.1), therefore, it is likely that the crosslinking efficiency was better and this was reflected on the modulus obtained for the gels. In all cases, stiffer gels were obtained by increasing the concentration of material in the initial mixture (blue < red < green in Fig. 3.8), as expected and common with other hydrogels[7, 142, 179].

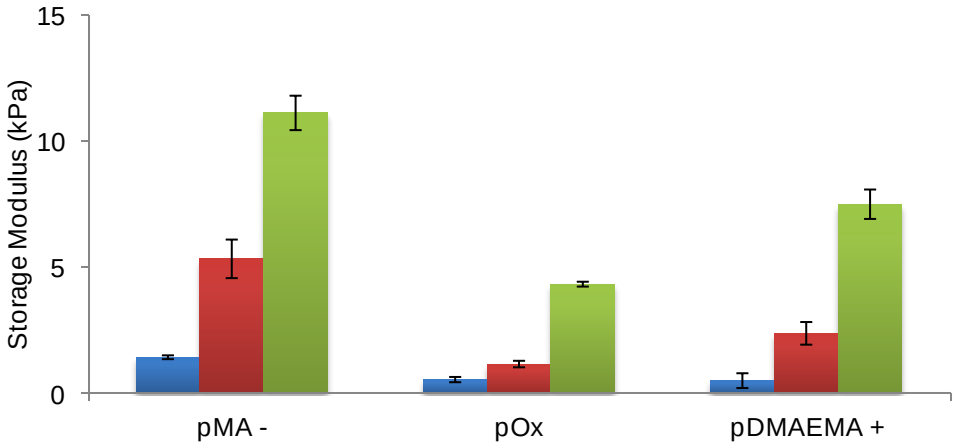

Figure 3.8 Storage modulus for different stiffness gels (S3 blue, S4 red and S5 green) from different polymer backbones, 50% crosslinked with PEGDT using 120 s UV exposure and 0.5 mol% PI.

Table 3.2 Storage modulus obtained for different backbone hydrogels at three different concentrations, modulus are reported from the frequency sweep for the measurement at 1 Hz.

Stiffness	Polymer backbone	Average storage modulus (kPa)
S3	pMA^-	1.41
S4	pMA^-	5.30
S5	pMA^-	11.08
S3	pOx	0.52
S4	pOx	1.14
S5	pOx	4.30
S3	$pDMAEMA^+$	0.48
S4	$pDMAEMA^+$	2.35
S5	$pDMAEMA^+$	7.47

Frequency sweeps were performed to analyse the effect of strain rate on gel mechanics (Fig. 3.9). Generally, soft gels displayed a strong frequency dependent modulus, compared to stiffer gels. This was particularly the case for pOx gels. Hence, a marked increase in modulus was observed for soft pOx gels (S3 and S4) and soft pDMAEMA$^+$ gels (S3), at high frequencies. On the contrary, the softest pMA$^-$ gel (S3) displays some thinning behaviour, with a slight decrease in the storage modulus at higher frequencies.

Such frequency-dependent response may arise from: a) the storage modulus is determined by covalent bonds, chain segments and whole molecular length of the polymers, variations in the length of chain segments and distance between crosslinks (crosslinking degree) would inevitably lead to a range of relaxation times in response to the dynamic stress applied. The storage modulus of the softest polymer with low crosslink density show more frequency dependence; b) a typical viscoelastic material is expected to display low level of frequency dependence below the glass transition of a material as only covalent bonds and short chain segments with fast relaxation times respond the stress at different frequency. The long chain segments do not have sufficient time to relax at high frequencies; c) water molecules are mobile within the deformed network and cannot rearrange fast enough at high frequencies, leading to stiffening of the hydrogel (poroelastic effect)[231].

Therefore, the more concentrated the gel, the shorter the chain segment length of the corresponding polymers, the lower the water content and the less frequency dependent the gel is. The profiles observed for the soft pOx (S3 and S4) and pDMAEMA$^+$ (S3) gels show that the modulus of these gels increase at higher frequencies (Fig 3.9). The pOx polymer has a longer chain segment,

owing to the presence of fewer alkenes per chain. Hence it is not surprising that pOx gels display stronger frequency dependence. The frequency dependent behaviour observed for pDMAEMA$^+$ (S3) may result to the high hydration of this polymer, displaying permanent positive charges for each repeat unit, and therefore an increase poroelastic effect. The slight decrease in modulus observed at high frequencies for pMA$^-$ S3 may be due to damage sustained by the network at high shear rates.

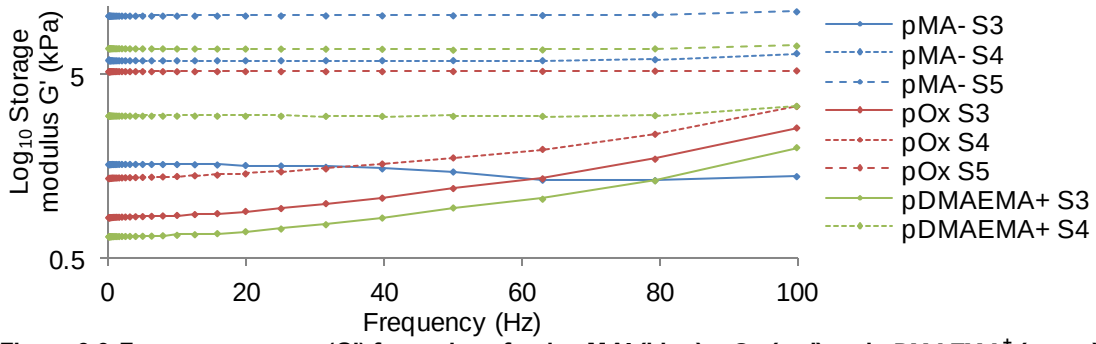

Figure 3.9 Frequency sweep (G') for series of gels pMA$^-$ (blue), pOx (red) and pDMAEMA$^+$ (green), at different stiffness S3 (full lines), S4 (dotted lines), and S5 (broken lines). Gels were generated using 120 s UV exposure (17 mW/cm^2) and 0.5 mol% PI.

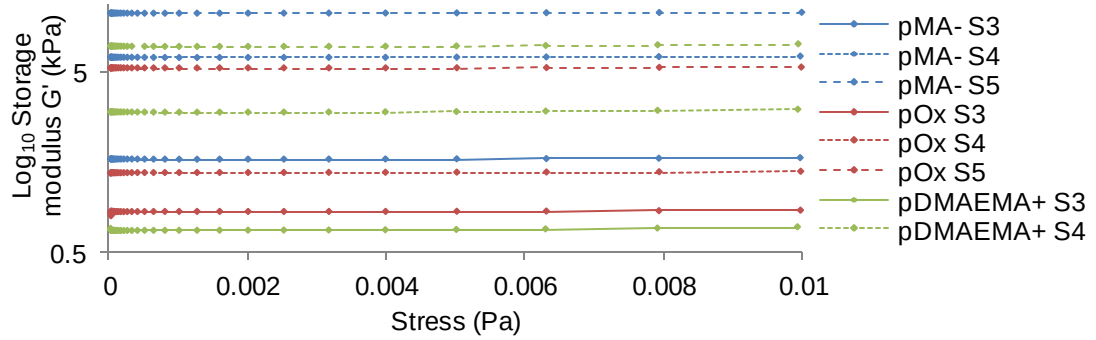

Figure 3.10 Amplitude sweep for series of gels pMA- (blue), pOx (red) and pDMAEMA+ (green), at different stiffness S3 (full lines), S4 (dotted lines), and S5 (broken lines). Gels were generated using 120 s UV exposure (17 mW/cm2) and 0.5 mol% PI.

Amplitude sweep experiments were performed to ensure the samples were tested in the linear viscoelastic region (Fig. 3.10). The gels composed of the three backbones of different stiffness confirm that measurements were taken in the linear viscoelastic region.

3.2.3 Formation of degradable hydrogels and enzymatic degradation

The hydrogel systems studied can be made biodegradable by exchanging the PEGDT crosslinker for an enzyme sensitive peptide crosslinker. Here we explore the VPM enzyme sensitive peptide as the crosslinker, which degrades in the presence of collagenase and MMP[232]. The combination of the enzyme sensitive peptide crosslinker with different ratios of PEGDT can be used to achieve control over the degradation kinetics. Rheology was used to study the change in the storage modulus (time sweep) over the degradation time when incubated (at ambient temperature) in collagenase enzyme solution (0.25 mg/mL in PBS). Kharkar *et al*. used a similar system to monitor the degradation of photo-cleavable gels[167]. The photo-rheology setup for gelation and degradation is represented in Fig. 3.11. All gels were crosslinked at 50 mol% with respect to the concentration of alkene functionalities in the polymer (17% alkene functional pOx, 135 mM, S3).

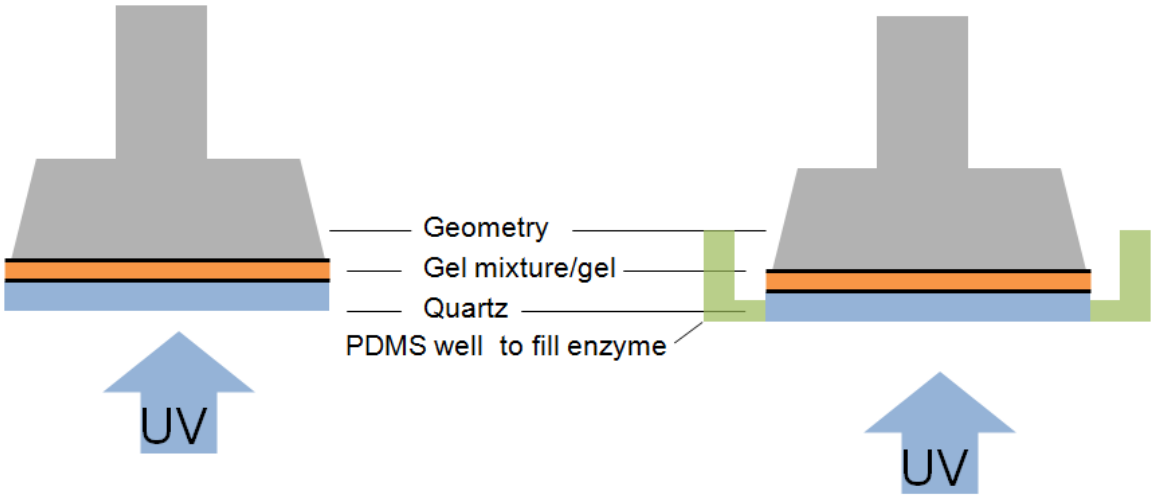

Figure 3.11 A representation of the setup for a) photorheology for gelation and b) degradation, black lines represent the methacrylate functionalised glass coverslips.

The gel degradation studies were performed with *in situ* monitoring of the storage modulus during gelation and degradation, by incubation in either PBS or enzyme solution. Initially, the collagenase enzyme was tested for its ability to degrade the VPM gel. The gel showed a decrease in storage modulus over time (10 h) when incubated in the enzyme solution, confirming the success of the enzymatic cleavage of the degradable peptide crosslinking our hydrogels (Fig. 3.12). The VPM crosslinked gels were also incubated in PBS as a control. Our observations did not highlight any degradation of the VPM-based hydrogels in PBS, confirming the activity and specificity of the VPM peptide to selectively promote enzymatic degradation rather than hydrolytic break down of the hydrogel network.

PEGDT crosslinked hydrogels were also incubated in collagenase solutions, showing no degradation over time, with a constant storage modulus for 10 h, further confirming the enzymatic selectivity of the VPM crosslinks as the main component for the degradation the networks. Other researchers studied the degradation of VPM compared to other degradable peptide crosslinkers and confirmed that the VPM peptide is degradable by collagenase at various concentrations[175].

Table 3.3 The concentration of components used to make each gel type in molar concentration and weight percent. S3 gels with thiol:ene 0.5:1 and PI 0.5 mol%.

VPM:PEGDT	Thiol-ene conc^{n} (mM)	Wt% pOx	Wt% VPM	Wt% PEGDT	Wt% PI
0:100	135	8.2	0	3.4	0.076
25:75	135	8.2	1.5	2.6	0.076
50:50	135	8.2	2.9	1.7	0.076
75:25	135	8.2	4.3	0.85	0.076
100:0	135	8.2	5.7	0	0.076

There are clear mechanical differences for gels crosslinked with either PEGDT or VPM. The VPM gels are much softer (4 kPa) difference than the PEGDT even though the concentrations of the gel components were the same. This is thought to be related to the molecular size of the crosslinkers. The length of the crosslinker could affect the stiffness of the gel; shorter crosslinkers (PEGDT) produce stiffer gels compared to VPM. For gels with differing ratios of crosslinker for the control over degradation, the gels composed of increasing ratios of PEGDT have a larger storage modulus (Fig. 3.13). It is possible that the difference in stiffness could be related to the reaction efficiencies of the thiol-ene reactions with PEGDT and VPM, the lack of reaction efficiency could lead to softer gels.

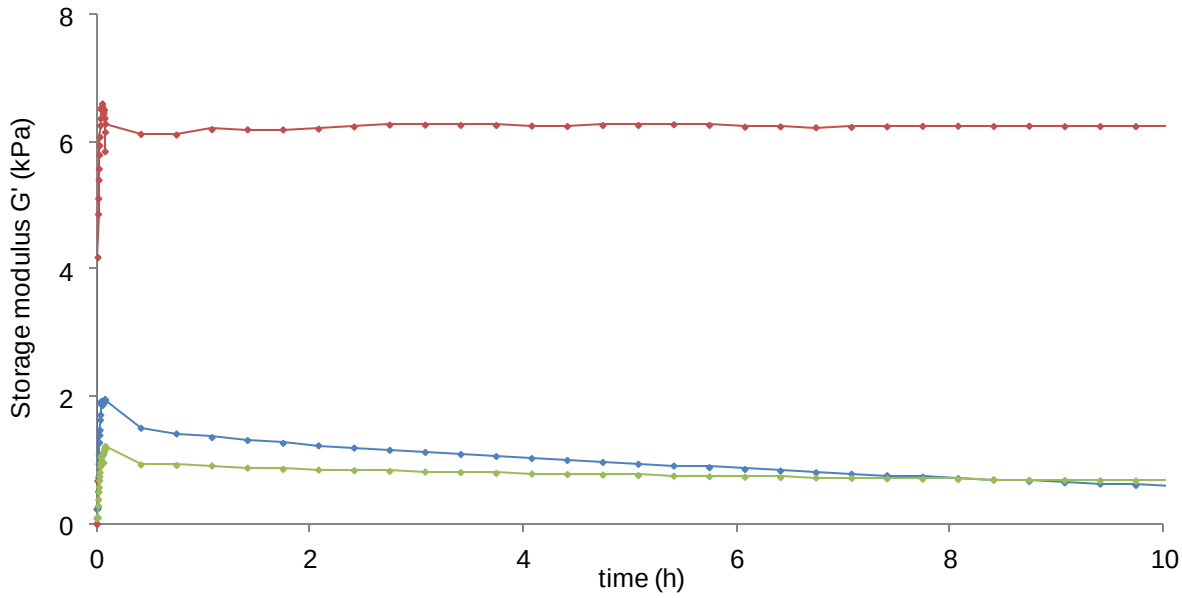

Figure 3.12 Time sweep (10 h) of gels (S3, pOx) incubated in PBS or collagenase enzyme (0.25mg/mL) to confirm the degradation of the VPM gel by the selected enzyme. Gel compositions S3 VPM:PEGDT: 100:0 with enzyme (blue), 0:100 with enzyme (red) and 100:0 without enzyme (green). Results shown are of a single repeat.

The VPM peptide is sensitive to numerous MMP's including collagenase I (MMP-1), gelatinase A (MMP-2) and gelatinase B (MMP-9)[232]. Turturro *et al*. investigated the degradation of VPM crosslinked gels with collagenase I (1

µg/mL) and results showed complete degradation in 4 days for thin gels (0-2 mm) and 12 days for thick gels (8-10 mm). Patterson *et al*. calculated the degradation time of given peptide sequences when in the presence of enzymes[171]. Their results for VPM containing sequences show degradation from 1-3 days with 10 nM MMP-1 and 2-7 days with 20 nM MMP-2. Holloway *et al.* investigated the degradation of VPM crosslinked hyaluronic acid gels (3 wt%, 30% crosslinkable functionalisation), they incubated gels in collagenase II solutions (0, 1, 2 and 10 U/mL) and observed degradation within 12 days at low concentrations and 1 day for high concentrations of enzyme[175]. In comparison to our system, the gels reported degraded slower. This is a result of the lower concentration of enzymes they have used and may also be linked to the reduced number of crosslinks per chain for the pOx gels, enabling faster degradation.

It is important to be able to control features such as degradation; one approach consists of varying the ratios of degradable and non-degradable crosslinks in the gel (Table 3.3). Here we explored different ratios of degradable (VPM) to non-degradable (PEGDT) crosslinker and the rate of degradation of the corresponding hydrogels, using *in situ* monitoring of the storage modulus through rheology (Fig. 3.13). Results show that with increasing concentrations of the non-degradable crosslinker, the rate of enzymatic degradation decreases (monitored over 24 h): VPM: PEGDT 100:0 > 75:25 > 50:50 > 25:75. Differences observed in initial storage modulus of the corresponding gels are due to the ratios of VPM: PEGDT.

This method enabled control over the degradation kinetics. Some researchers have also explored this method[173] and others have explored the use of different peptide sequences that have varying degradation kinetics to specific enzymes, therefore being able to control the cell activity in these gels[171, 172].

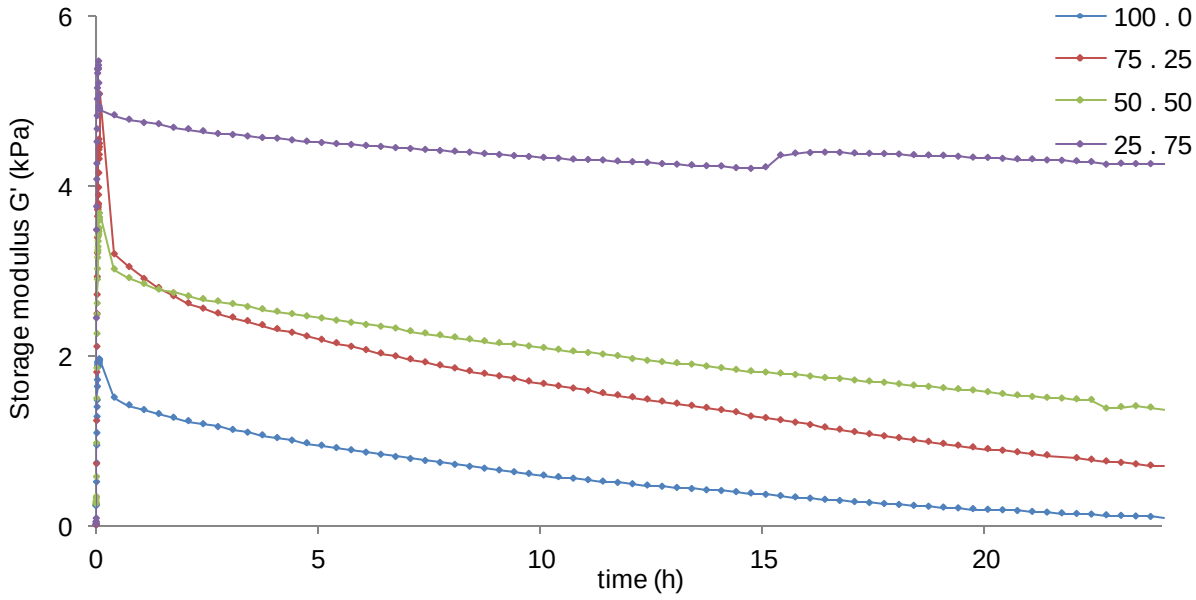

Figure 3.13 Time sweep of different degradable gels incubated in collagenase enzyme (0.25mg/mL) showing varying rates of degradation over 24 h. Gel compositions S3 VPM:PEGDT incubated in enzyme: 100:0 (blue), 75:25 (red), 50:50 (green) and 25:75 (purple). Results shown are of a single repeat.

3.3 Cell encapsulation in 3D systems

Hydrogel systems are designed and developed for applications in the bioengineering field. The success of hydrogels depends on their ability to behave as biomimetic systems with suitable protein-matrix and cell-matrix interactions. Therefore, it is crucial to choose suitable backbones, crosslinkers and associated coupling chemistry to form the networks. In addition, the components used to generate these systems are required to be non-toxic. In this work, the cytotoxicity of pOx hydrogels was investigated with two cell types, HUVECs and dermal fibroblasts. HUVECs and dermal fibroblasts were encapsulated in the gels and the toxicity was observed after 24 h. We were interested in using dermal fibroblasts as one of our cells types in the hydrogel system; these systems could be used to generate wound healing and *in vitro* skin models[116]. Similarly, HUVECs in hydrogels are applied as in vitro vasculogenesis or tissue engineering models[233].

3.3.1 Cell viability

To make 3D cell-gel constructs, cocktails containing the polymer backbone (pOx), crosslinker (50 mol% with respect to the alkene functions in polymer backbone), RGD (10 mol%) for cell matrix adhesion, PI (0.5 mol%) and PBS were prepared (Table 3.4 for HUVECs and Table 3.5 for fibroblasts), the cells (HUVECs or dermal fibroblasts) were added, the mixture (50 µL) was added into glass bottom PDMS wells and cured using UV exposure (120 s). Gels were washed with PBS and medium before incubation. The toxicity of the 3D encapsulated cells was investigated after 24 h using a live/dead assay. The toxicity assay was performed with HUVECs using non-degradable gels (using 13% alkene functional pOx) and fibroblasts with different ratios of degradable gels (using 17% alkene functional pOx) and at different stiffness.

It was difficult to produce high quality images for 3D cell cultures because of the fluorescence of cells at the different layers. This is even more difficult when using standard cell culture well plates. For this reason we generated glass bottom PDMS wells. They are easy to make and cost considerable cheaper than glass bottom culture plates.

Table 3.4 The concentration of the components used to make different stiffness gels (S3-S5) in molar concentration and weight percent. pOx gels with thiol:ene 0.5:1, 10 mol% RGD and PI 0.5 mol%.

Stiffness	Thiol-ene conc^{n} (mM)	Wt% pOx	Wt% PEGDT	Wt% RGD	Wt% PI
S3	135	10.7	3.4	1.5	0.076
S4	180	14.3	4.5	1.9	0.1
S5	225	17.9	5.6	2.3	12.67

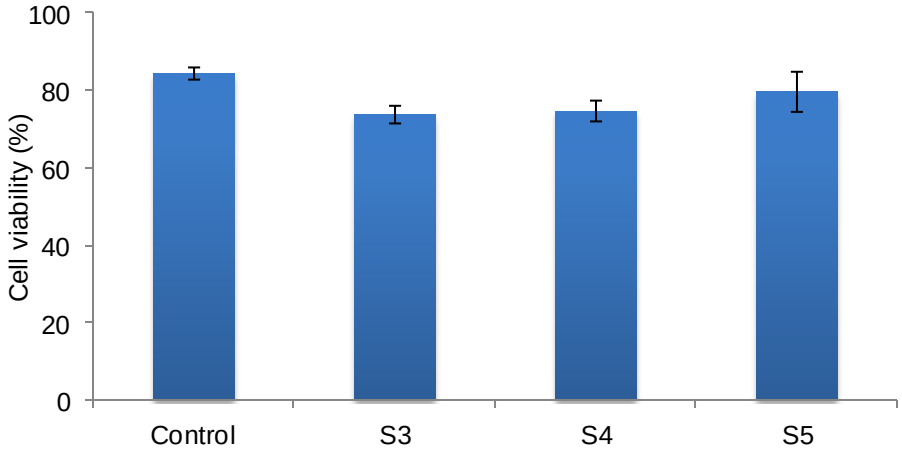

Figure 3.14 Cell viability of HUVECs encapsulated in non-degradable PEGDT crosslinked hydrogels of increasing stiffness (S3-S5), live dead assay was performed after 24h. Gels were generated with thiol:ene 0.5:1 ratio, 10 mol% RGD, 0.5 mol% PI, 120 s UV exposure and 50k cells/well.

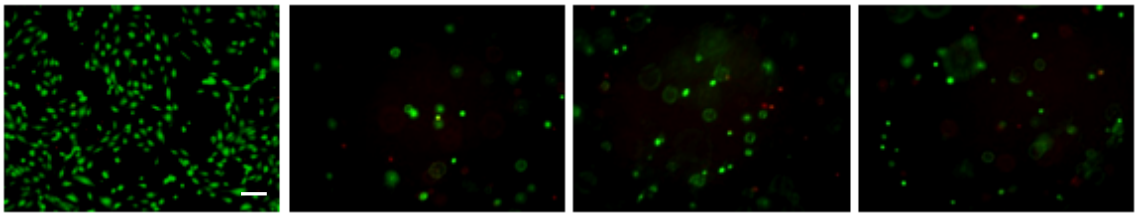

Figure 3.15 Live/Dead assay of HUVECs encapsulated in nondegradable PEGDT crosslinked hydrogels of increasing stiffness. From left to right: control, S3, S4 and S5, after 24h, scale 100 µm, 50k cells/well. Live cells were stained green and dead cells red. Gels were generated with thiol:ene 0.5:1 ratio, 10 mol% RGD, 0.5 mol% PI and 120 s UV exposure. See Fig. A2.1 for corresponding statistical analysis.

HUVECs were encapsulated in varying stiffness non-degradable pOx-PEGDT hydrogels to investigate the effect of gel stiffness on cytotoxicity (Fig. 3.14 and 3.15). Gel stiffness increases along the following trend: S3 (135 mM, 0.5 kPa) < S4 (180 mM, 1.1 kPa) < S5 (225 mM, 4.3 kPa). Results show over 73-80% viable cells in all gels. A Tukey test was performed, however, there is no significant difference between the samples measured. Positively charged $pDMAEMA^{+}$ and negatively charged pMA^{-} gel networks were studied as 3D encapsulation materials, however $pDMAEMA^{+}$ showed 100% cell death and pMA^{-} gels were difficult to assess due to problems with the staining (not shown).

For comparison, Sawicki *et al.* reported 87% and 81% viable cells (hMSCs) after 3 days in 10 wt% PEG peptide gels polymerised using 1 and 5 minutes UV exposure[189]. Their results showed a slight decrease in cell viability with increased UV exposure time. Lin *et al*. also generated PEG gels crosslinked with DTT using UV initiated thiol-ene coupling[197]. They encapsulated different densities of hepatocytes (derived from carcinoma cells). Results showed 80% cell viability for gels for 5 million cells/mL and 95% cell viability for 20 million cells/mL. From this we can conclude that using less UV exposure time and larger densities of cell encapsulation may lead to better cell viability.

Table 3.5 The concentration of the components used to generate pOx gels in molar concentration and weight percent. Gels were made using thiol:ene 0.5:1 ratio, 10 mol% RGD, 0.5 mol% PI and 120 s UV exposure.

VPM:PEGDT	Thiol-ene conc^{n} (mM)	Wt% pOx	Wt% PEGDT	Wt% VPM	Wt% RGD	Wt% PI
S3 0:.100	135	8.2	0	3.4	1.5	0.076
S3 25:.75	135	8.2	1.5	2.6	1.5	0.076
S3 50:.50	135	8.2	2.9	1.7	1.5	0.076
S3 75:.25	135	8.2	4.3	0.85	1.5	0.076
S3 100:.0	135	8.2	5.7	0	1.5	0.076
S4 75:.25	180	10.9	3.4	1.9	1.9	0.1
S5 75:.25	225	13.6	4.2	2.4	2.3	12.67

Similarly, dermal fibroblasts were encapsulated in various degradable pOx-VPM:PEGDT gels to study the effect of the crosslinker composition and degradability of the matrix on initial cell viability (Fig. 3.16 and 3.17). We selected a stiffness 2-6 kPa (S3) for this assay. Results show comparable levels of cell viability for a wide range of VPM/PEGDT crosslinker compositions (typically in the range of 82-88%), apart from the 25/75 ratio of VPM/PEGDT. Farrugia *et al*. encapsulated fibroblasts in gels with a similar poly(oxazoline)

backbone (3.4-4.5 kPa)[40]. They generated a series of gels by varying the crosslinker ratio CRGDSCG: DTT 0:1, 0.05:0.95, 0.1:0.9 and 0.25:0.75. After studying the cells for 1 and 8 days, they reported 80-90% viable cells with more dead cells in gels crosslinked with DTT only. The cells seem to show rounded morphology even after 8 days (concluded from the representative images reported). The reduced viability at higher PEGDT ratios are thought to arise from the toxicity of the batch of PEGDT crosslinker that was used for these studies, although the nature of the contaminant thought to be responsible for this behaviour is unknown. This behaviour was not observed with the HUVEC study where the gels were only composed of PEGDT crosslinks, the previous studies were performed with a different batch of PEGDT, and the difference in behaviour could be related to the batch to batch differences in PEGDT (item is bought) synthesis and purification.

Hydrogels composed of VPM: PEGDT 75:25 crosslinker ratios with increasing gel stiffness were investigated for their cell viability. Results show no significant differences for the cell viability at 24 h between the varying stiffness gels, all falling between 83 and 86%.

For comparison, Mũnoz *et al*. encapsulated hMSCs in thiol-ene crosslinked gelatin gels with DTT, results showed 97 and 91% cell viability after 24 h for 4 and 8 wt% gels[143]. Their results did not show any significant difference for the cell viability in different stiffness gels. Fu *et al*. also investigated modified gelatin and PEG crosslinked gels (10 wt%) for fibroblast encapsulation. Results showed 87% cell viability at 24 h which increased to 93% after 28 days with apparent cell spreading[195]. From these we can assume that small

differences in gel stiffness do not have a significant impact on cell viability and also, cell viability may increase with longer culture periods.

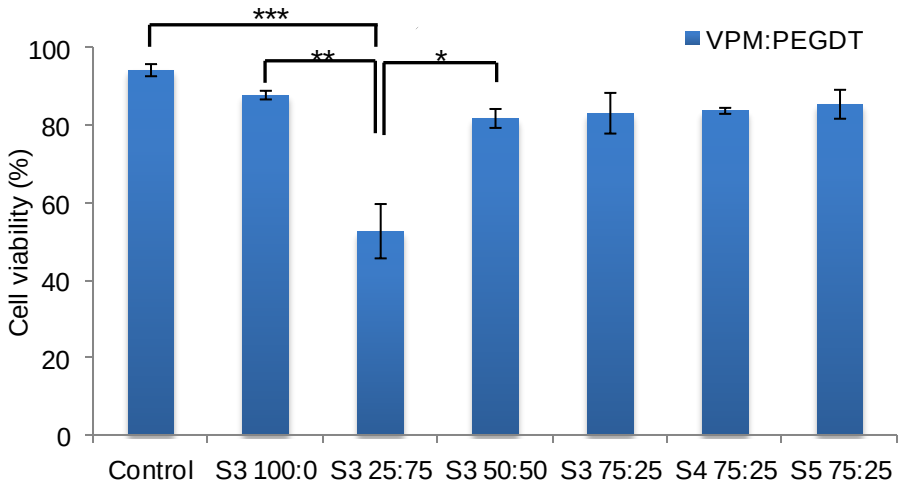

Figure 3.16 Cell viability of dermal fibroblasts encapsulated in degradable hydrogels with various ratios of degradable:nondegradable crosslinker in S3 gels and also ratio 75:25 with S4 and S5 gels. Live dead assay was performed after 24h. Gels were generated with thiol:ene 0.5:1 ratio, 10 mol% RGD, 0.5 mol% PI and 120 s UV exposure. See Fig. A2.2 for corresponding statistical analysis.

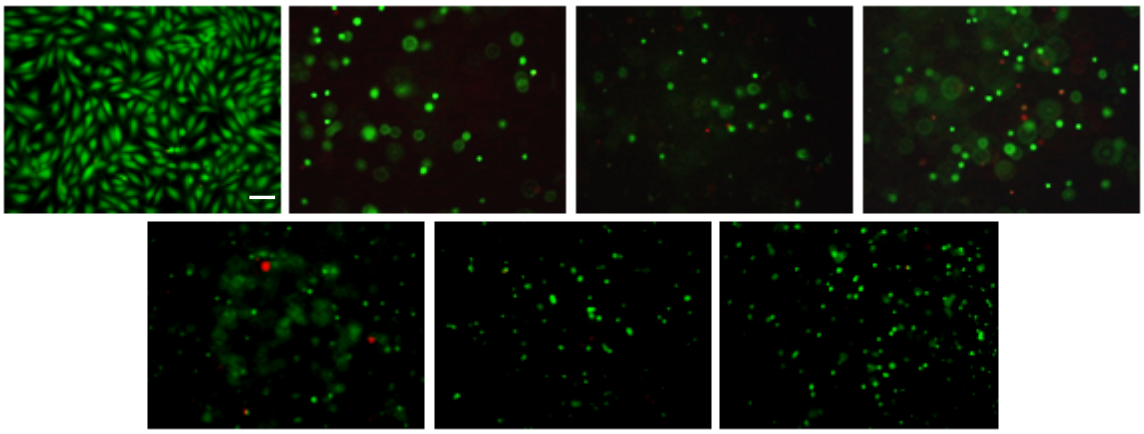

Figure 3.17 Live/Dead assay of fibroblasts encapsulated in hydrogels of varying degradation and increasing stiffness. From left to right to bottom: control, S3 VPM:PEGDT 100:0, S3 25:75, S3 50:50, S3 75:25, S4 75:25, S5 75:25, after 24h, scale 100 µm, 100k cells/well. Live cells were stained green and dead cells red. Gels were generated with thiol:ene 0.5:1 ratio, 10 mol% RGD, 0.5 mol% PI and 120 s UV exposure.

3.3.2 Cell spreading in 3D hydrogels

Dermal fibroblasts were encapsulated in 3D pOx hydrogels with different crosslinker compositions and mechanical properties and their spreading (and invasion of the matrix) was examined for 14 days after seeding. pOx Gels with 50 mol% crosslinker (with respect to alkenes) and 10 mol% RGD were used for these studies. The ratio of degradable (VPM) to non-degradable (PEGDT) crosslinker was altered, VPM:PEGDT 0-100%. We also examined the effect of stiffness with VPM:PEGDT 75:25 gels for differences in the cell morphology. The cells were fixed and stained after 1 or 7 days with phalloidin and DAPI, then imaged using confocal microscopy equipped with a z-axis scan.

Cells encapsulated in S3 PEGDT only gels (0:100) were rounded at day 1 and 7 (Fig. 3.18a and Fig 3.19a) and also up to day 14 (not shown). PEGDT gels are not degradable and therefore restrict the spreading, movement and growth of cells. In comparison, gels containing only the degradable crosslinker (VPM) showed spread cells at day 1 and 7 (Fig. 3.18f and Fig. 3.19e) and day 14 (not shown), however cells displayed 2D morphologies, implying that the cells had enzymatically degraded the gel to the point where the gel matrix could no longer support the cells. Sometimes cells in the degradable gels did not show the 2D behaviour, but showed some evidence of deformation and elongation of cells in 3D gels (Fig. 3.18g). We propose that the gelation achieved for the pOx gels is too close to the gelation point and that partial degradation of the network results in its dissolution, without retaining a mechanically strong scaffold (at least at the scale of single cells) for the time of the experiment. Hence, although we sometimes observed partially deformed cells in VPM only gels, usually we observed 2D cellular spreading for these samples.

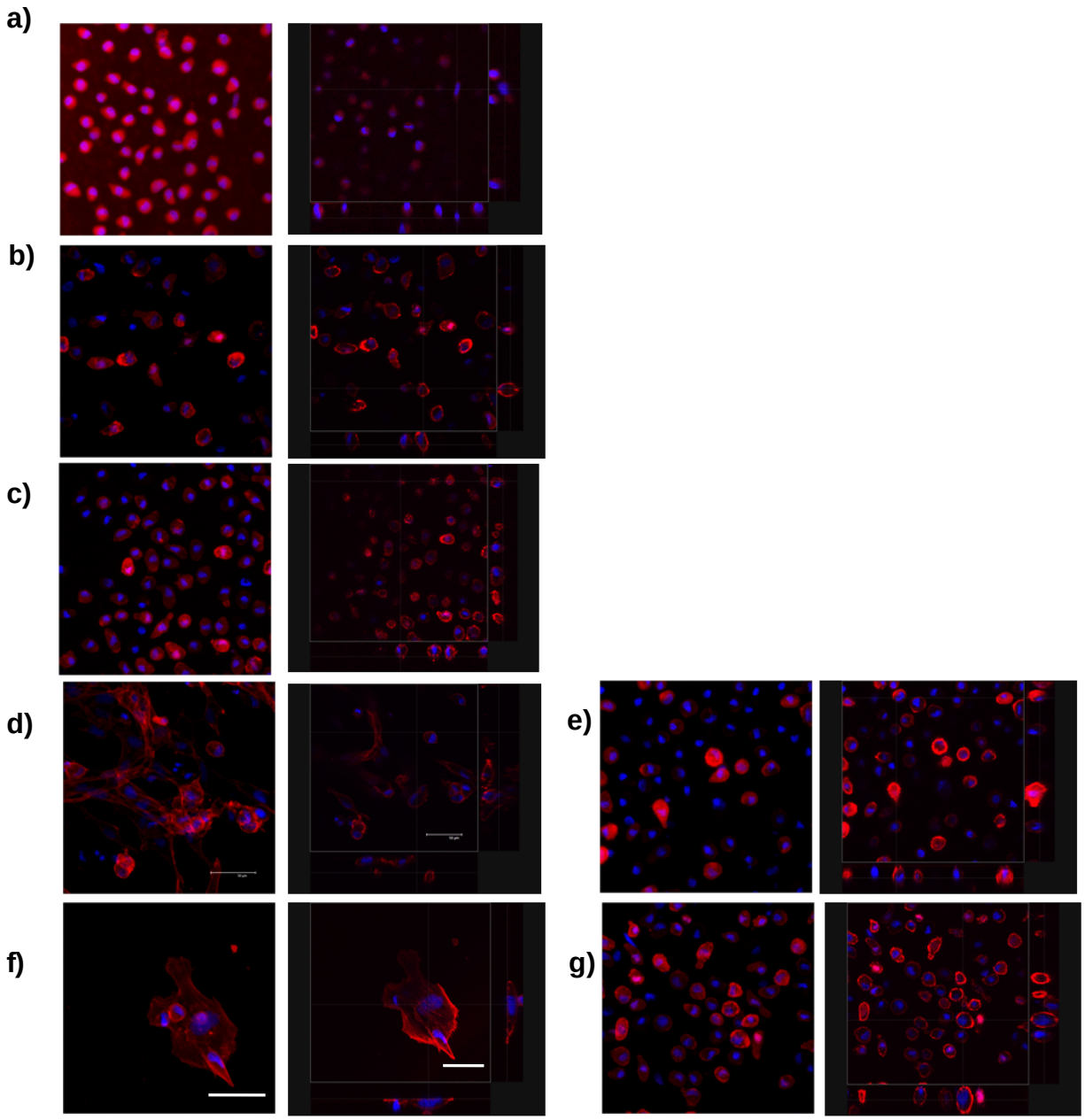

Figure 3.18 Dermal fibroblasts at day 1 in S3 pOx gels with 10% RGD, 0.5 mol% PI, 120 s UV and VPM:PEGDT a) 0:100, b) 25:75, c) 50:50, d) 75:25 spread cells, e) 75:25 rounded cells, f) 100:0 spread cells and g) 100:0 rounded cells, stained with phalliodin (red) and DAPI (blue), 100k cells/well, scale bar 50 µm. Each image is represented with its corresponding z-stack on its right.

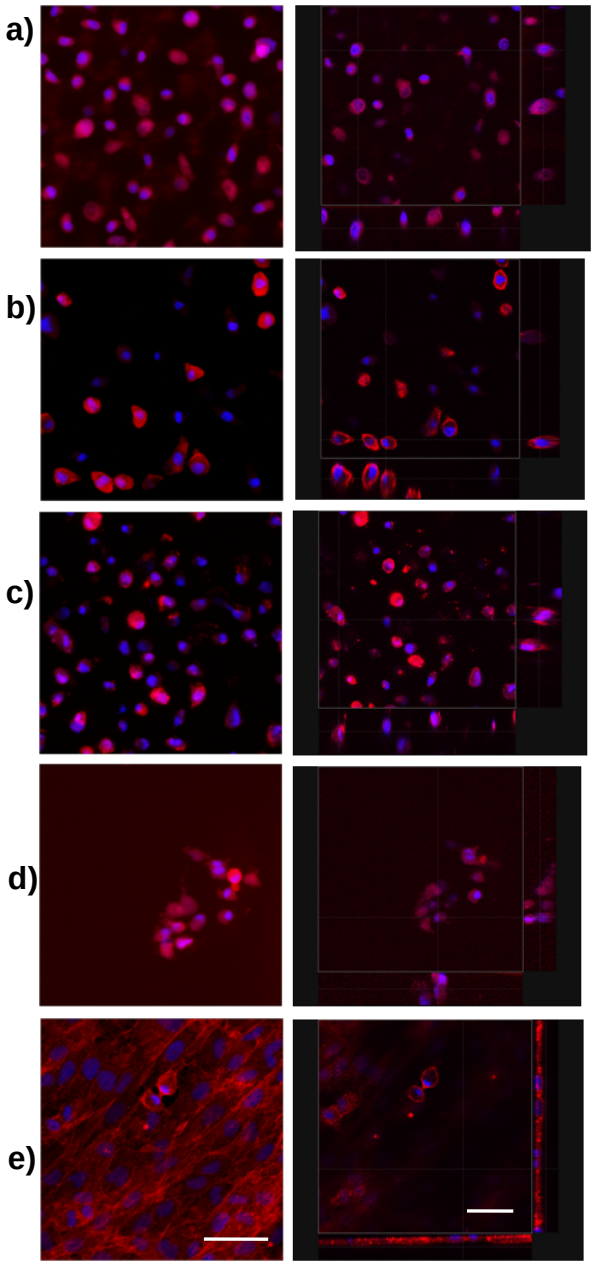

Figure 3.19 Dermal fibroblasts at day 7 in S3 pOx gels with 10% RGD, 0.5 mol% PI, 120 s UV and VPM:PEGDT a) 0:100, b) 25:75, c) 50:50, d) 75:25 and e) 100:0, stained with phalliodin (red) and DAPI (blue), 100k cells/well, scale bar 50 µm. Each image is represented with its corresponding z-stack on its right.

Since cells in the 3D hydrogels crosslinked purely using PEGDT or VPMdid not show controlled invasion into the matrix , mixtures of degradable and non-degradable crosslinkers were used to crosslink POx hydrogels and the resulting cell morphologies were studied. Gels (S3) with or less than 50% of VPM showed no or very little deformation of cells (qualitative analysis) at day 1 and 7 (Fig. 3.18b and Fig. 3.19b VPM:PEGDT 25:75; Fig. 3.18c and Fig.

3.19c, 50:50) and up to 14 days (not shown). Interestingly, increasing the ratio of VPM in the gel (S3) had a positive effect on the cell morphology at day 1 (Fig. 3.18d); fibroblasts in gels containing 75% VPM 25% PEGDT showed spreading, with the formation of a 3D network. Cell-cell contacts and distortion of cell shape were clearly apparent. However, this behaviour was not reproducible and, in several experiments cells seeded in 75:25 VPM:PEGDT pOx hydrogels displayed more rounded morphologies with only moderate cell elongation and protrusion formation (Fig. 3.18e). The rounded morphology was also observed at day 7 (Fig. 3.19d) and 14. In this case too, we hypothesise that a relatively poor control of the crossover from network to dissolved branched polymer is resulting in this behaviour, but that the presence of some PEGDT allowed slightly better control of the matrix degradation, compared to pOx gels purely crosslinked with VPM. This lack of control of the crosslinking and degradation rate may arise from a number of factors such as: 1, moderate thiol-ene coupling efficiency (as presented in Fig. 2.16, thiol-ene coupling efficiency with peptides is typically in the range of 58-100% by HPLC); 2, relatively low number of crosslinking alkenes per polymer chain (8 per chain based on 17% alkenes); 3, the use of a dithiol crosslinker only (rather than a multifunctional crosslinker); 4, too fast degradation rates observed for VPM peptides[171, 172], meaning that cells may be able to locally degrade the matrix very fast; 5, too high cell densities, resulting in high concentrations of enzymes able to degrade the peptide crosslinkers used.

The gelation and resulting storage modulus for gels crosslinked with PEGDT and/or VPM are different to one another (seen from the rheology Fig. 3.12).

The lack of control over the stiffness for the different crosslinker ratio gels introduces a variable factor that could have an impact on the cell behaviour.

To overcome some of the difficulties with the 3D gels, a series of experiments were performed. Various concentrations of cells in gels at the given gel condition (S3 75:25) were embedded in the gel matrix, however, cells showed no spreading (not shown). The medium was changed to a fresh bottle to ensure that the cells were provided with fresh and sufficient nutrients, however no changes were observed.

The stiffness of the hydrogels containing 75:25 VPM:PEGDT was altered next and the impact of stiffness on cell morphology was studied. Gel stiffness used for the degradation experiments is 0.52 kPa (S3) reported for PEGDT. Next the gel stiffness was increased from 0.52 kPa (S3) to 1.14 kPa (S4) and 4.3 kPa (S5) by increasing the concentration material in the gels. As the stiffness of the gel increased from 0.52 to 4.3 kPa, less spreading was generally observed (day 1). However, the important variation observed in cell spreading prevented us to quantify reliably this phenomenon. Fig. 3.20 and 3.21 presents the range of morphologies observed for the different conditions at day 1 (most spread morphologies observed on the two left columns and most rounded morphologies on the two right columns) and day 7. Conditions with 1.14 and 4.3 kPa showed no cell-cell interactions, only some cell sprouting and modest cell elongation, indicating relatively little matrix degradation and remodelling. Cells in the stiffest hydrogels (S5) showed some evidence of clustering, perhaps indicating that local degradation may occur in these conditions, but do not allow substantial remodelling of the matrix. At day 7 the cells showed very

little distortion of the cell morphology (Fig. 3.21) and followed similar behaviour to samples on the right two columns for day 1 (Fig. 3.20).

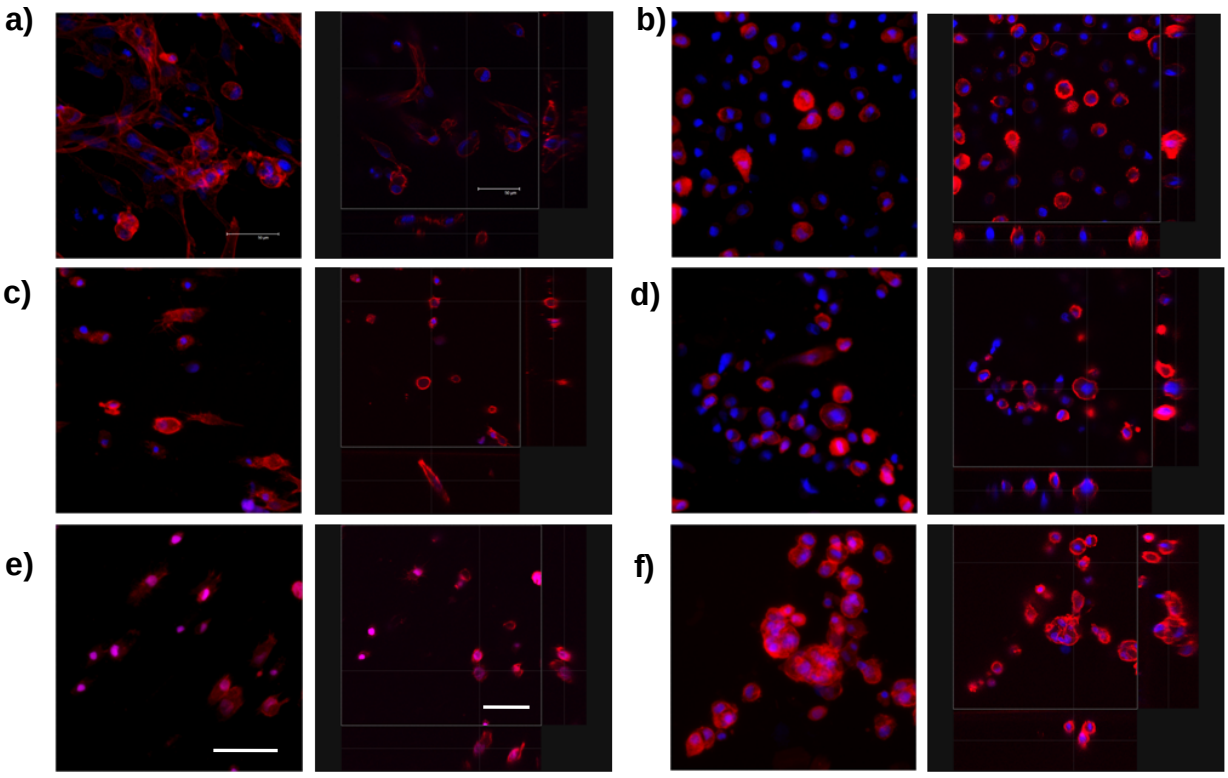

Figure 3.20 Dermal fibroblasts day 1 in pOx gels with 10% RGD, 0.5 mol% PI, 120 s UV and VPM:PEGDT 75:25 with varying stiffness a) S3 spread cells, b) S3 rounded cells, c) S4 spread cells, d) S4 rounded cells, e) S5 spread cells and f) S5 rounded cells, stained with phalliodin (red) and DAPI (blue), 100k cells/well, scale bar 50 µm. Each image is represented with its corresponding z-stack on its right.

Although the gels from charged polymers pMA^- and $pDMAEMA^+$ showed bad staining and cell death respectively (from live/dead analysis), small percentages of the polymers in pOx systems showed different behaviours. A preliminary study showed that cells are spreading when 5 mol% of the charged polymers are used with the pOx gels (not shown). The gels with $pDMAEMA^+$ do not show 100% cell death and the pMA^- effect on staining is reduced. These polymers could be useful tools to generate partially charged hydrogels which could potentially be used to study the interaction of proteins and cells with charged gels.

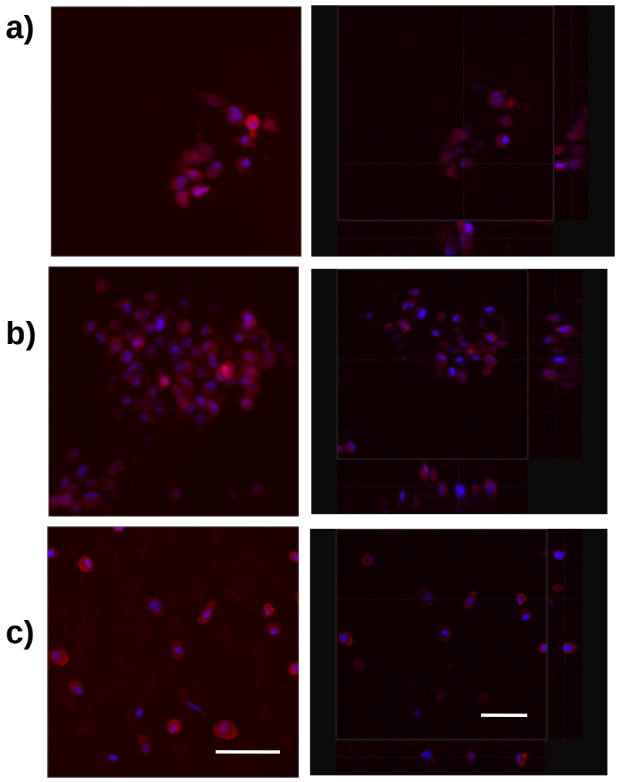

Figure 3.21 Dermal fibroblasts at day day 7 in pOx gels with 10% RGD, 0.5 mol% PI, 120 s UV and VPM:PEGDT 75:25 with varying stiffness a) S3, b) S4 and c) S5, stained with phalliodin (red) and DAPI (blue), 100k cells/well, scale bar 50 µm. Each image is represented with its corresponding z-stack on its right.

The results show that it is possible to generate a hydrogel system that supports cells and does not show cytotoxic behaviour, however, if the suitable microenvironment is not provided (backbone, stiffness, degradation, biofunctionality), cells will not spread. To assure we generate a hydrogel environment for 3D cell culture this material or similar materials needs to be further investigated with the implication of the factors reported.

A possible explanation for the failure to control cell spreading in pOx hydrogels could be related to the physio-chemical properties of the pOx polymer backbone, known to be anti-fouling[211, 234]. In other biomaterials, especially 2D, ECM proteins are adsorbed onto surfaces and cells subsequently adhere to these proteins via integrins. However, if proteins cannot interact with the pOx backbone in these gels, it may be proposed that cells are not able to deposit

new matrix allowing their spreading. However, this effect alone may not be sufficient to explain the absence of cell spreading observed as PEG-based hydrogel systems[142], such as those based on Michael addition coupling[199, 235], are also protein resistant[234, 236], yet are reported to allow 3D cell spreading.

Bott *et al*. showed the spreading of fibroblasts in 3D degradable PEG based hydrogels[142]. They manipulated the cell proliferation through the alteration of the gel stiffness and observed cell protrusions after 1 day in 0.6 kPa gels and spread cells for all gels after 7 days. They concluded that mechanical characteristics highly influence the cell behaviour, acting as a barrier at 1.2 kPa which could explain why the cells in our systems do not show the same behaviour compared to theirs. Enzyme-sensitive and insensitive crosslinked gels were compared; results showed reduced cell spreading for enzyme insensitive gels.

To our knowledge pOx gels have still not been used as 3D cell culture systems. Farrugia reported the live dead analysis with similar pOx gels, however, did not observe any changes in cell morphology and behaviour[40].

Another reason could be related to the percentage of alkene in the gels which is 13 or 17% per chain of which half are crosslinked. The enzymes produced by cells cleave the VPM crosslinks reducing the amount of crosslinks in the gel system. It is likely that the lack of crosslinks per polymer chain after partial degradation results in its partial dissolution and is unable to provide a scaffold to cells and therefore is unable to generate 3D culture materials. To overcome this factor, the percentage of alkene and therefore the density of crosslinks per chain should be increased, or the length of the polymer chains (degree of polymerisation) should be increased.

Choosing the most suitable peptide crosslinker is also a crucial factor, which could have an impact on the gel network and its interaction with cells and enzymes they may release. Enzymatically cleavable peptides have different kinetic profiles, of which specific sequences cleave more quickly or slowly in the presence of enzymes[171, 172]. Various peptide crosslinkers with slower degradability than VPM should be investigated, these systems may allow more time for cell-matrix interactions and therefore for cell spreading and 3D cell cultures. In addition, the design of the peptide sequence should be carefully carried out in order to maximise thiol-ene coupling efficiency and therefore increase the stability of the hydrogel network.

3.4 Summary

Chapter 3 focused on the production of hydrogels from 3 different alkene functional backbones with negative charge (pMA^-), positive charge ($pDMAEMA^+$) or neutral (pOx), crosslinked with PEGDT using photoinitiated thiol-ene coupling. This technique is an excellent tool to produce a series of gels of varying stiffness. Non-degradable gels from pOx-PEGDT were investigated as 3D culture materials. HUVECs showed near 80% cell viability in these matrices. The pOx gels were studied to achieve control over the enzymatic degradation of the gels by varying the ratio of degradable to non-degradable crosslinker. Gels were degraded in collagenase solution and followed using rheology. Dermal fibroblasts were encapsulated in the varying ratio of degradable gels (pOx-VPM: PEGDT) to observe the cell viability in these systems, and also to explore the effect of stiffness on the cell viability. Cells were viable (above 83%) in the studied gels. The control over the various features of the gel (stiffness, degradation, photo activation) and the good cell viability with 2 cell types support this material to be investigated further as a system for 3D cell culture. Thiol-ene coupling chemistry allowes hydrogels to be functionalised with a wide range of bioactive peptide sequences (i.e. RGD, PHSRN, YIGSR, and REDV). This gel system may provide good control over the chemical and mechanical properties of the ECM, which are not available in current 3D culture systems based on naturally-derived matrices (collagen, Matri-gel)[137] and may allow the systematic study of the impact of physio-chemical and biochemical parameters of the ECM on cell phenotype. However, the degradability and remodelling of pOx hydrogels needs to be improved before they can be applied more routinely in 3D cell culture systems.

3.5 Experimental section

3.5.1 Materials

Methanol (99.9%), ethanol (99.5%), 3-(trimethoxysilyl)propyl methacrylate (98%), PBS tablets, Dulbecco's PBS, IRG 2959 (98%), PEGDT (average M_n 1 kg/mol), PFA (95%), Triton-X 100, phalloidin–tetramethylrhodamine B isothiocyanate and DAPI (98%) and ECGF supplement: β-endothelial cell growth factor (25 µg), bovine neutral extract (75 mg), heparin (25KU), thymidine (28.1 mg) in dH_2O (40 mL) were obtained from Sigma Aldrich. Sylgard 184 and curing agent was purchased from Dow Corning Sylgard. Custom peptides GCGYGRGDSPG (RGD), GCRDVPMS↓MRGGDRCG (VPM) (↓ shows cleavage site) were purchased from Proteogenix, France. Penicillin streptomycin (5000 U/mL), DMEM and calcein were obtained from life technologies. FBS, South American Origin was purchased from Labtech. *l*-glutamine (200 mM), versene, trypsin (0.25%) phenol red and ethidium homodimer-1.were obtained from Thermo Fisher Scientific. HUVECs medium EBM-2 was purchased from Lonza. Polymer backbones (pOx, pMA^- and $pDMAEMA^+$) were synthesised as described previously (refer back to section 2.1.3).

3.5.2 Instrumentation

The UV light used to initiate reactions was the Omnicure series 1500. ILT 1400-A radiometer photometer from international light technologies was used to measure the UV light intensity. ATR-FTIR spectroscopy were produced using a Bruker Tensor 27 spectrometer equipped with a MCT detector, results were acquired at a resolution of 16 cm^{-1} and a total of 128 scans per run in the region of 600-4000 cm^{-1}. Leica DMI4000B epifluorescent microscope fitted with a HCX PL FLUOTAR 10x/0.3 PJ1 objective and a Leica DFC300 FX CCD camera was used to image cells in 3D hydrogels. Leica TCS SP2 confocal microscope fitted with a HCX PL APO 63x/1.40-0.60 oil objective and a Leica DFC420C CCD camera was used to image cells in 3D hydrogels. Image J analysis was used to merge images for the different channels, live (green) and dead (red) cell count was performed manually. Rheological measurements were performed using DHR-3 from TA Instruments fitted with a UV accessory and a 20 mm upper parallel plate. The UV curable gel was sandwiched between two coverslips (glued to the plates of the rheometer) with a fixed gap of 250 µm. Oscillations were set to controlled strain mode at 1% strain. For *in situ* monitoring of the progression of gelation, a time sweep was performed: 30 s of equilibrium without UV exposure, UV irradiation for 2 min and the UV light was turned off for the remaining part of the experiment. Frequency sweep and amplitude sweep measurements were conducted after the UV cure to examine the change in rheological behaviour. TGA measurements were performed using the TGA Q500 from TA instruments, 25-1000 ºC ramp, 3 ºC/min. TGA traces were analysed and the following equations (in section 3.5.4) were used to calculate the percentage of water and swelling of the gels.

3.5.3 Statistical analysis

All data were analysed by Tukey's test and significance was determined by * $p < 0.05$, ** $p < 0.01$: *** $p < 0.001$. A full summary of statistical analysis is provided in the Tables A2.1-2.2.

3.5.4 Percentage of water and swelling calculated from TGA

$$W = 100 - P \qquad \textbf{equation 3.128}$$

$$Ws\ (\%) = Wf - Wi \qquad \textbf{equation 3.2}$$

The percentage of water in the gel (W) was calculated from the percentage of polymer in gel (P) obtained from the TGA traces. The percentage swelling of gels (Ws) was calculated from the percentage of water in the gel before (Wi) and after (Wf) submersion in PBS or water obtained from the TGA traces.

3.5.5 Methacrylate functionalised coverslips for rheology

Glass coverslips (20 mm) were plasma oxidised for 10 minutes (power 95) and incubated in a solution of anhydrous toluene (30 mL) with 3-(trimethoxysilyl)propyl methacrylate (30 µL) and triethylamine (50 µL) for 24 h. The slides were washed with deionised water followed by ethanol and dried under a stream of nitrogen. The glass slides were glued to the quartz bottom plate and top geometry before rheology measurements.

3.5.6 Hydrogel preparation

To make hydrogels for characterisation, solutes were dissolved in PBS ($4.5x10^{-4}$ mol/mL, 450 mM): polymer backbone (pOx, pMA^- and $pDMAEMA^+$), crosslinkers (PEGDT, VPM) and IRG2959 in methanol (250 mg/mL). Crosslinked hydrogels (50 mol% w.r.t. to alkene) were generated using 0.5 mol% PI, the cocktails amounts are shown in Table 3.6, the mixture was transferred to the required location for rheology (quartz plate) or 8 mm cylindrical mould for TGA and FTIR spectroscopy samples, the gel mixture was cured using UV light (120 s, 17 mW/cm^2, power 2.04 J/cm^2). The stiffness of the gels increased with increasing concentrations of material in the gel S3 < S4 < S5. For gels with mixtures of degradable to non-degradable crosslinker, i.e. VPM: PEGDT 75:25 for S3, 22.5:7.5 µL was used. A solution of collagenase in PBS (0.25 mg/mL) was prepared for the rheological measurements and degradation studies.

Table 3.6 Protocol to make 200 µL gels, solutions were exposed to UV for 120s, 0.5 mol% PI, units in columns are in microlitres (except stiffness).

Stiffness	Polymer	Crosslinker	PI	PBS
S3	60	30	0.61	110
S4	80	40	0.81	80
S5	100	50	1.01	50

3.5.7 Preparation of PDMS wells

Glass bottom PDMS moulded wells were generated and used for the hydrogel studies performed with cells. Sylgard 184 silicone elastomer (50 g) was mixed with the base curing agent (5 g) (10:1) and stirred until the mixture was opaque. The bubbles in the mixture were removed under reduced pressure. The silicone mixture was poured into petridishes making sure that the silicone thickness was at least 1 cm. The PDMS was cured at 60-70 °C for 3 h. Once removed, the PDMS was cut (3 x 10 cm) using a blade and a series of holes (8 mm each) were made using a biopsy punch. Glass microscope slides (0 thickness) were coated with a very thin layer of PDMS and placed on top of the PDMS making sure all the holes were covered (pressure was applied with fingers to secure the bonding at the interface). The wells were cured in an oven (60-70 °C for 1 h) (Fig. 3.22). PDMS wells were sterilised using ethanol and UV before used for cell experiments.

Figure 3.22 Glass bottom PDMS wells in a petridish, diameter of each well is 8 mm.

3.5.8 Cell culture

HCA2 Dermal fibroblast strain was used[237]. Cells were routinely grown in DMEM supplemented with 10% FBS, 1% penicillin streptomycin and 1% glutamine. The medium was changed every 2-3 days and cells were sub-cultured each week using trypsin/versene. Cells were maintained at 37ºC in a humidified atmosphere containing 5% CO_2.

HUVECs (Lonza, C2519A) were routinely grown in EBM-2 supplemented with ECGF. The medium was changed every 2-3 days and cells were sub-cultured each week using trypsin/versene. Cells were maintained at 37ºC in a humidified atmosphere containing 5% CO_2.

3.5.9 Staining

Live/dead staining was performed on the 3D encapsulated cells at 24 h to study the cell viability. Cells were stained green with calcein (0.5 µL/mL) and red with ethidium homodimer-1 (2 µL/mL) in medium (serum-free) for 20 minutes, washed with medium and incubated 15 minutes before imaging. Epifluorescent images were produced using 10x objective and analysed using Image J.

To study the cell morphology, Cells were fixed and permeabilised simultaneously in 4% PFA and 0.2% Triton-X100, blocked for 1 h in 10% FBS containing 0.25% gelatin, incubated at room temperature with phalloidin (2 µL/mL) and DAPI (2 µL/mL) overnight and washed with PBS. Confocal images were generated using 63x objectives with z-axis scanning (500 nm), images were stacked and channels were merged.

3.5.10 Hydrogel preparation for 3D cell culture

To make hydrogels for cell culture, solutes were dissolved in PBS ($4.5x10^{-4}$ mol/mL, 450 mM): pOx polymer backbone, crosslinkers (PEGDT, VPM), monopeptide (RGD) and IRG2959 in ethanol (250 mg/mL). Solutions in PBS were filtered through a 0.2 µm supor membrane pore to sterilise. Crosslinked hydrogels (50 mol% w.r.t. to alkene) were generated with 10 mol% RGD using 0.5 mol% PI, cocktails shown in Table 3.7 were prepared, added (50 µL) into glass bottom PDMS wells and cured using UV light (120 s, 20 mW/cm^2, power 2.4 kJ), cells were added last (HUVECs passage 2-5, 1 million cells/mL gel; dermal fibroblasts passage 32-36, 0.5 million cells/mL gel). For gels with mixtures of degradable to non-degradable crosslinker, i.e. VPM: PEGDT 50:50 for S3, 15:15 µL was used. Gels with 3D encapsulated cells were washed with PBS (200 µL x3) and medium (200 µL x5) before adding medium (200 µL) and incubated for 24 h. The medium used for HUVECs was EBM-2 and for dermal fibroblasts was DMEM.

Table 3.7 Protocol to make 200 µL gels, 50 µL was put in each well and exposed to UV for 120s, 10 mol% RGD, 0.5 mol% PI, units in columns are in microlitres (except stiffness).

Stiffness	Polymer	Crosslinker	Monothiol	PI	Cells	PBS
S3	60	30	6	0.61	25	79
S4	80	40	8	0.81	25	47
S5	100	50	10	1.01	25	15

Chapter 4

Polymeric brushes as biomaterials

A successful approach to enable the spatial control over cell adhesion in 2D environments is to produce protein resistant surfaces. This can be achieved by growing polymer brushes on surfaces. ATRP is a well established method for the generation of pOEGMA brushes[106, 109, 238]. pOEGMA Brushes were the first to be known for their protein resistant properties, meaning proteins were unable to attach to their surface. The stability of pOEGMA brushes have been studied under ambient conditions and when exposed to cell culture conditions[106, 239]. The extreme protein repellent behaviour of pOEGMA brushes does not favour biofunctionalisation through the adsorption of proteins[109]. Although in some cases this is possible, Sielaff *et al.* immobilised fusion proteins on chemically modified pOEGMA brushes[240]. The immobilisation of proteins does not always provide sufficient control over biofunctionality or may not be compatible with the requirements of the system. Therefore, new platforms need to be developed for the selective biofunctionalisation of brushes. The biofunctionalisation of polymer brushes can also be achieved through the immobilisation of small molecules, peptides of surfaces.

Bioactive peptide sequences have been explored for their impact on cell behaviour. Some peptides such as RGD, REDV and GFOGER are used to promote the cell adhesion, migration and differentiation[21, 86, 111, 122, 123, 241]. Cells can bind to these peptides using via the interaction of specific integrins. The cell adhesive properties of such peptide sequences can be explored with protein resistant polymer brush surfaces to generate cell specific behaviour. pOEGMA Brushes decorated with peptides through thiol-ene coupling have specifically been used to control cell adhesion and this was recently used to develop dynamic patterns[21]. The thiol-ene functionalisation of brushes with peptides has also been studied in the case of pGMA brushes, but these brushes lack protein resistance[132]. Results showed that, in contrast to the small molecules biofunctionalisation such as *N*-acetyl *l*-cysteine, peptides only functionalised the upper part of the brush and did not seem to penetrate significantly. Therefore, a deeper understanding of thiol-ene chemistry at anti-fouling brushes is required to ensure their use as reliable and reproducible platforms for controlling cell adhesion. Here we explore the synthesis of pOEGMA brushes on silicon substrates and their functionalisation with alkene groups so that thiol-ene chemistry can be applied to couple biomolecules on the surface of the brushes. A series of peptides were coupled to promote cell adhesion, studied in the case of HUVECs. The brush protein resistance and peptide specific behaviour was confirmed in an experiment where silicon substrates were functionalised with silyl methacrylate which was reacted with peptidic thiols. Cells showed no specificity to these substrates, in contrast to results obtained with pOEGMA brushes. Furthermore, peptide patterned substrates were obtained using photo initiated thiol-ene chemistry and used for peptide specific adhesion studies.

4.1 Brush synthesis and activation via DSC

Simple protein adsorption doesn't always provide sufficient control over the biofunctionality and is not compatible with all polymer brush platforms; hence, it is necessary to use coupling agents to achieve the desired functionality. pOEGMA Brushes were synthesised on silicon substrates through ATRP initiation, which was further functionalised with DSC and allylamine to achieve alkene functional brushes.[109] Alkene functional brushes are capable of undergoing photo initiated thiol-ene chemistry whereby, biomolecules can be immobilised on these surfaces, below is a schematic showing this process (Fig. 4.1).

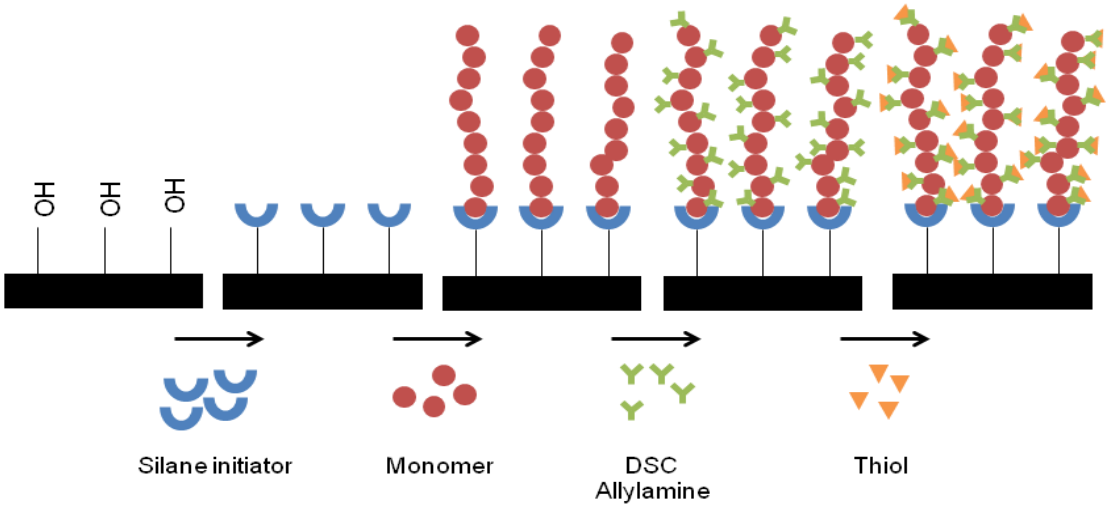

Figure 4.1 Scheme representing the polymer brush formation, functionalisation and thiol-ene reaction.

The pOEGMA brush synthesis and its growth kinetics was studied using ellipsometry (Scheme. 4.1). The polymerisation was performed under inert conditions to better control the brush growth and the reaction kinetics was monitored using ellipsometry. Gautrot *et al.* optimised the polymerisation kinetics of pOEGMA[106]. Results show the ability to achieve brushes of varying thickness by varying the polymerisation time. The brush length increased with

time, brushes used for further studies were obtained at 75 minutes. Ellipsometry is the technique used to measure the dry brush thickness on substrate surfaces. The equations used to calculate the degree of functionalisation at the different stages is shown in the experimental section. The functionalisation and conversion at each stage can be followed using this method.

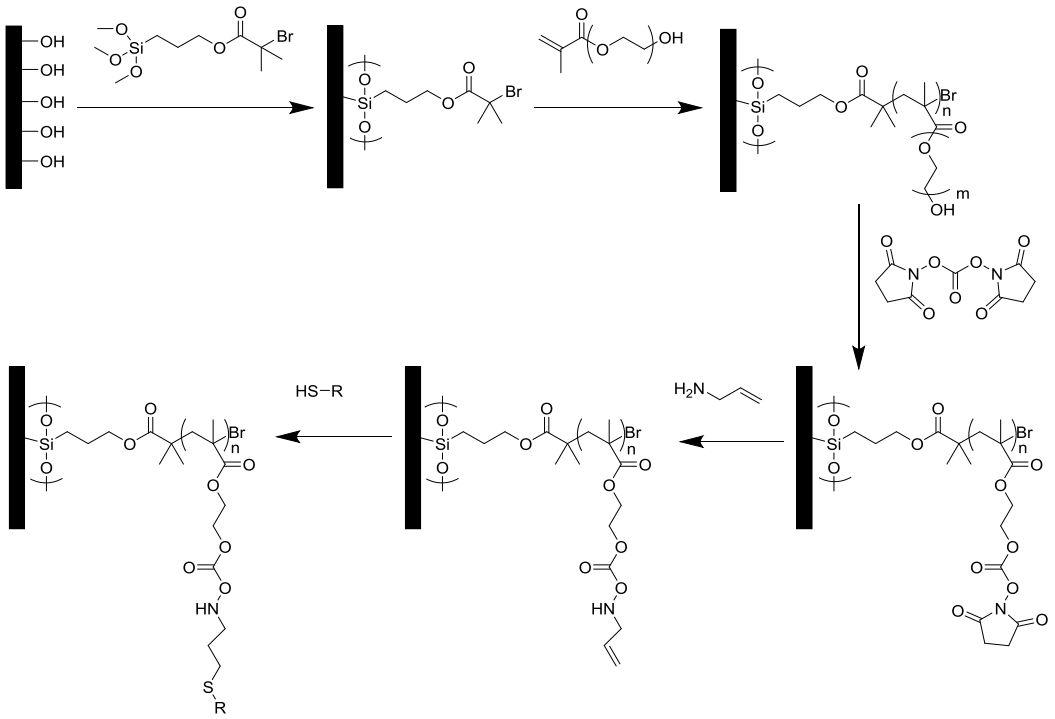

Scheme 4.1 A representation of the polymer brush synthesis, functionalisation and thiol-ene coupling reactions.

The brushes were further functionalised with allylamine through DSC coupling to achieve alkene functional surfaces. Trmcic-Cvitas *et al*. tested a series of coupling agents for capturing biomolecules, DSC was found to be the most efficient activating agent[109]. The thickness of the brush slightly increased with DSC functionalisation due to the addition of molecular size to the side chains (Fig. 4.2). However, this increase is minor (1 nm) as the increase in the molar mass of the side chain is relatively limited. The coupling efficiency for DSC was

calculated (5-15%), the degree of functionalisation was calculated using equation 4.1 and 4.2 in section 4.6.11 as previously reported by Tan *et al.*[132]. The brush thickness increased slightly with the substitution of DSC components with allylamine even though the molar mass is smaller; this is acceptable as the increase in thickness is within the error limits. The degree of allylamine functionalisation was calculated (5-27%) and used for further calculations for the thiol-ene reaction conversion. The degree of functionalisation for both DSC and allylamine with varying polymer brush thickness can be followed using ellipsometry. The degree of functionalisation is comparable to results previously reported for pGMA brushes[132], however relatively lower than what is reported by others (>50%), discussed in Krishnamoorthy *et al*.[101]. The percentage functionalisation for each step was considerably low compared to general organic reactions; the upper surface of the brush was more likely to be functionalised whilst closer to the solid substrate the steric hindrance from the architecture of the brush would not allow for functionalisation. However, this is not important when using these materials for cellular studies, since cells only interact with the uppermost surface of brushes.

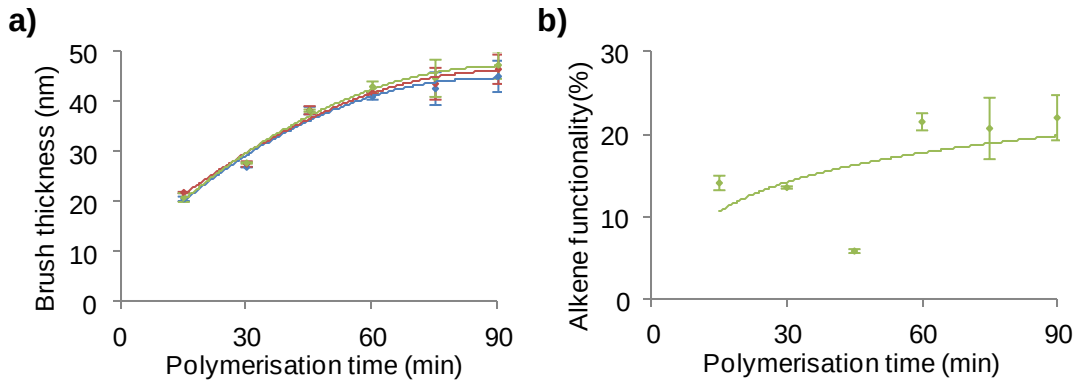

Figure 4.2 The polymerisation kinetics of pOEGMA brushes followed by ellipsometry and the functionalisation through DSC coupling to obtain alkene functional brushes. Blue pOEGMA, red pOEGMA-DSC and green pOEGMA-AA. a) The journey of the brush thickness and b) the degree of functionalisation of pOEGMA brushes. Trendlines were added to guide the eyes.

4.2 Thiol-ene coupling to POEGMA brushes

pOEGMA Brushes were known to be bioinert and therefore require the immobilisation of bioactive molecules to promote cell adhesion or bioactivity. Achieving biofunctional surfaces is essential for these systems to be applied to a wider range of biomedical applications. Having activated the terminal hydroxyl groups of oligo(ethylene glycol) side chains, we next examined thiol-ene coupling to the resulting brushes. Here we use thiol-ene coupling to immobilise relevant biomolecules on the surface of polymeric brushes. Thiol-ene coupling is particularly relevant for this application, since the thiol of cysteine residues within peptide sequences can be used to anchor onto alkene functional polymeric brushes. Having investigated thiol-ene coupling reactions in solution and for polymeric hydrogels in previous chapters, we set out to apply this chemistry to functionalise 2D solid surfaces. Fig. 4.4 shows a representation of the setup used for this process. Alkene functionalised pOEGMA brushes (30-40 nm) were generated (75 minutes polymerisation) and reacted with a series of thiols (Fig. 4.3) with the application of UV light. The coupling was investigated with varying amounts (mol%) of photoinitiator (IRG2959) and UV exposure time (5-300 s) to study the coupling efficiency.

N-Acetyl *l*-cysteine (S1) and *l*-glutathione (S3) were used as model thiols to study the efficiency of the reaction and to optimise the reaction conditions. Subsequently, cysteine-bearing peptide sequences were used to react with alkene functional surfaces using the developed protocol. The efficiency of the reactions was calculated using the brush thickness measurements obtained from ellipsometry (equations 4.2 and 4.3).

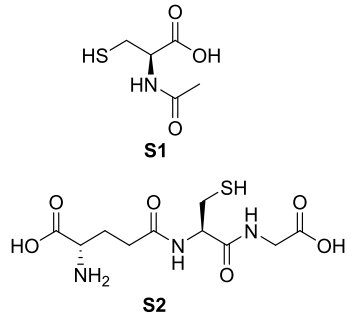

Thiol	Sequence
S3	GCGREDVSG
S4	GCGRVDESG
S5	GCGYGRGDSPG
S6	GCGYGRGESPG
S7	GCGPHSRNSG
S8	GCGYGRGESPG-Lys-FITC-G

Figure 4.3 Series of thiols and peptides (S1-S8) reacted with pOEGMA-AA brushes using thiol-ene coupling.

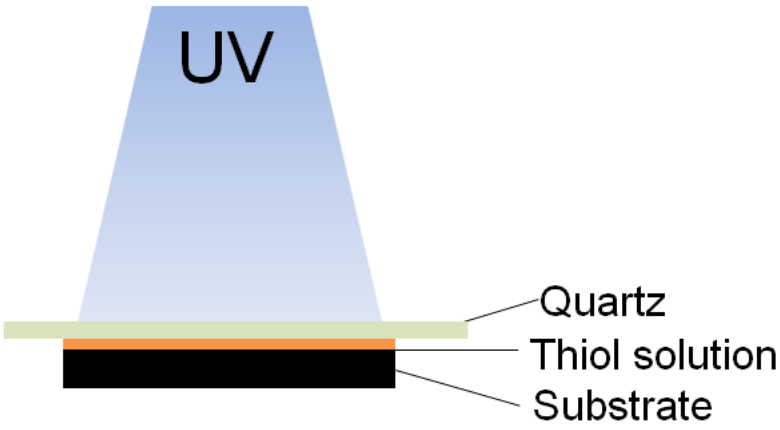

Figure 4.4 A representation the thiol-ene functionalisation setup

Reactions with *N*-acetyl *l*-cysteine (S1) and *l*-glutathione(S2) were performed with 2 mol% (1 mM) and 5 mol% (2.5 mM) photoinitiator (IRG2959) with respect to the thiol and exposed to varying times of UV light (17 mW/cm^2) to study the kinetics of the thiol-ene reaction on polymeric surfaces (Fig. 4.5). Results showed that an increase in the amount of PI from 2 to 5 mol% increased the degree of functionalisation. Conversions were higher for the S1 than for the S2 which is thought to be due to the steric hindrance associated with the size of the molecule used for further functionalisation. Tan *et al*. findings showed that the conversion for S1 was higher than S2 by ellipsometry, results by XPS did not show this and they concluded that S2 was functionalised on the uppermost surface of the brush[132]. Our conversion

results obtained for 5 mol% PI are slightly lower but very comparable with results reported for pGMA brushes, in particular for thiol S1. From the model studies we concluded that the conditions selected for further studies would consist in using 5 mol% photoinitiator and reacting for 300 s (UV exposure time).

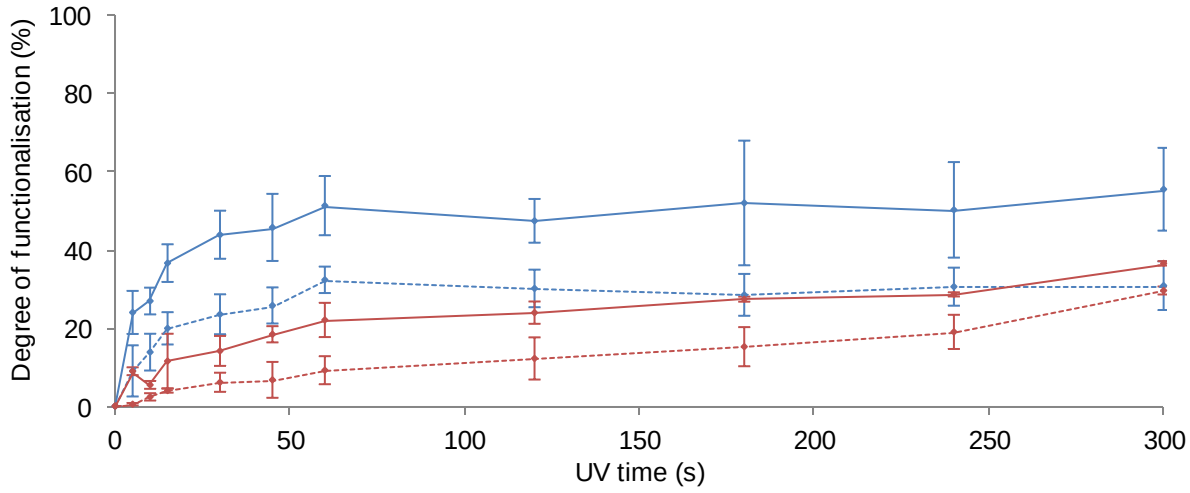

Figure 4.5 The effect of UV exposure time and PI concentration on the thiol-ene reaction with pOEGMA brushes. Blue represents the thiol-ene coupling with S1 and red S2. Solid lines represent thiol-ene coupling with 5 mol% PI, dotted lines 2 mol% PI with 300 s UV exposure time.

Brushes of different thicknesses were used to investigate the thiol-ene reaction efficiency (Fig. 4.6). A trendline was added to the graph to represent the general distribution of data. Reactions were performed with 5 mol% photoinitiator and 300 s UV exposure time. Results show that with increasing brush thickness, the thiol-ene reaction efficiency decreases slightly (not significant). This could be due to the steric hindrance/entanglement arising from increasing brush length. The same trend is observed for both S1 and S2. The conversion levels for S1 seem lower in Fig. 4.6 than Fig. 4.5, however within error limits.

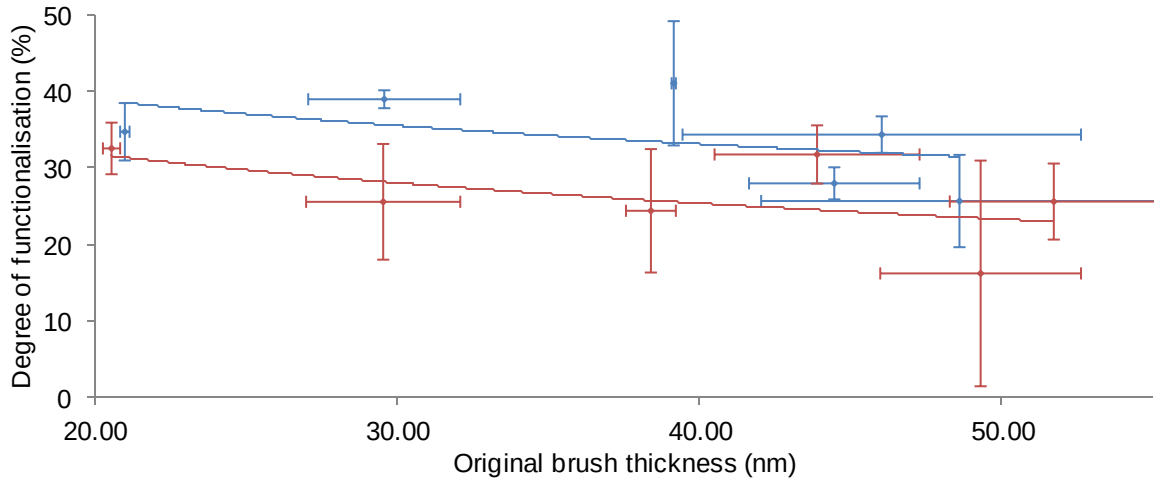

Figure 4.6 The effect of pOEGMA brush thickness on the thiol-ene reaction with 5 mol% PI, 300s UV exposure time, blue-S1 and red-S2. Trendline was added to guide the eyes.

The thiols in Fig. 4.3 were reacted with allylamine functional brushes to achieve immobilisation on the surface of the brushes. The reaction efficiencies are presented in Fig. 4.7. Thiol S1 was found to be coupled to significantly higher levels, compared to the other thiols tested, apart from S2. Hence, in the case of peptide sequences too, reaction efficiencies decreased with increasing molecular weight (in the range of 6 to 11%), a phenomenon also thought to be related to the steric hindrance associated with the size of the molecule and the high density of the polymer brushes used. Some of the cysteine-bearing peptides displayed lower reaction efficiencies compared to other peptides of similar molar mass. Peptide GCGPHSRNSG (S7) coupled with lower efficiencies (3%), although the reasons for this behaviour are unclear and should to be further investigated. However, the lower coupling efficiency could be associated with the presence of certain amino acids in the sequence not present in the other sequences studied (proline, histidine, asparagine) and resulting in a different conformation and/or local pH environment near the thiol of the corresponding cysteine, leading to decrease reaction efficiencies. In Chapter 2 the effect of the peptide sequence on thiol-ene coupling was studied

for selected peptide sequences and had identified such effect of local pH, although not with this sequence of amino acids.

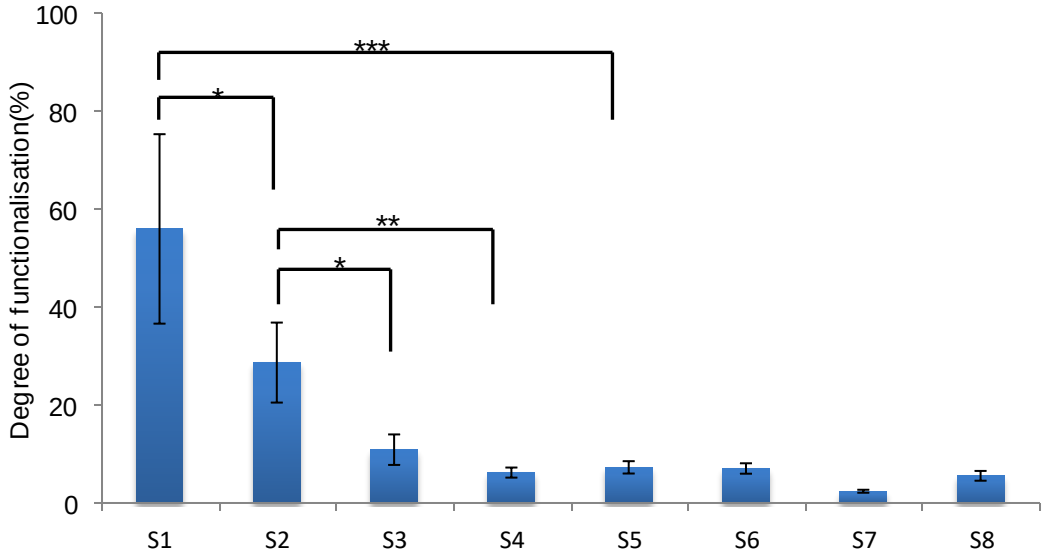

Figure 4.7 Representation of the degree of functionalisation of thiols (S1-8) on pOEGMA-AA (30-40 nm) surfaces. See Fig. A3.1 for corresponding statistical analysis.

To further analyse the chemical structure of the biofunctionalised brushes, grazing angle FTIR spectroscopy was used. Gold coated glass substrates coated with pOEGMA brushes and functionalised with allylamine were coupled with the series of thiols (Fig. 4.8). The broad peak at 3300-3600 cm^{-1} corresponds to the hydroxyl group (O-H symmetric stretch) present in pOEGMA brushes which disappears when the brush is functionalised with allylamine[230]. Carbonyl peak (C=O symmetric stretch) at ~1730 cm^{-1} and alkane peaks (C-H symmetric stretch) at 2860-2960 cm^{-1} are present for all samples from the pOEGMA brush. New peaks at 1530 cm^{-1} (C-N stretch and N-H bend) and 1650 cm^{-1} (C=O amide I band) appear after functionalisation of pOEGMA with allylamine, it is difficult to assign the peak due to the weak intensities. The alkene peak could not be assigned from the spectra. The 1650 cm^{-1} shoulder peak becomes more intense after functionalisation of the

allylamine with the thiols, and is most intense with the RGD functionalised substrate. This strengthens the argument that this peak is most probably the amide I band. The peak at 1250 cm^{-1} is relatively shallow for pOEGMA, this peak increases for the functionalised brushes. The peak at 1250 cm^{-1} is thought to be related to C-O symmetric stretching vibration, which increases due to the functionalities present in the thiols immobilised.

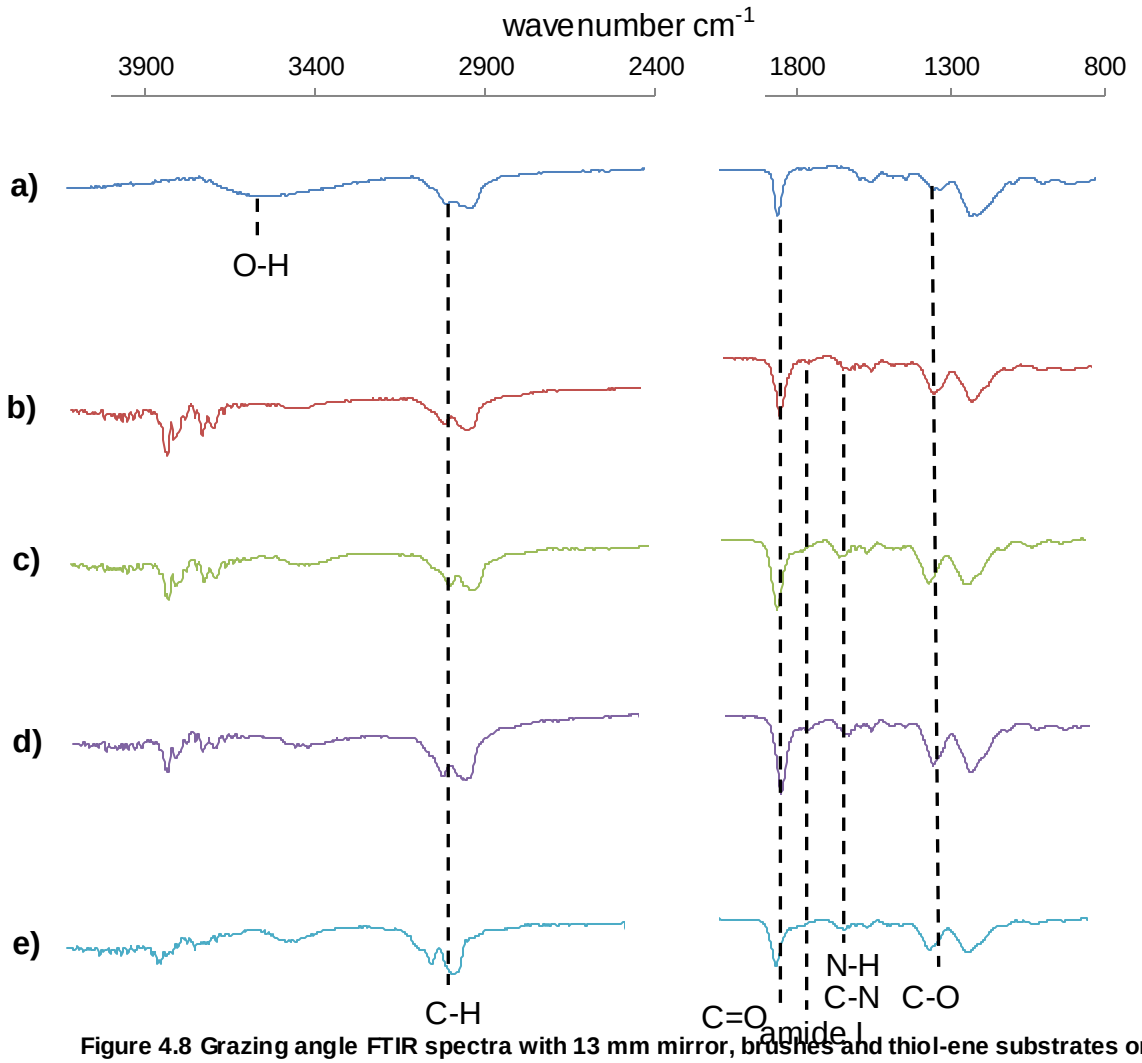

Figure 4.8 Grazing angle FTIR spectra with 13 mm mirror, brushes and thiol-ene substrates on gold coated glass surfaces plotted from 800-1900 cm^{-1} and 2600-4000 cm^{-1} for a more detailed view: a) pOEGMA, b) pOEGMA-AA, c) S1 functionalised pOEGMA d) S2 functioanlised pOEGMA and e) S5 functionalised pOEGMA. Thiol-ene coupling was performed with 5 mol% PI and 300 s UV exposure.

4.3 Cell adhesion to peptide functionalised polymer brushes

Having characterised the coupling of peptides to pOEGMA brushes via thiol-ene chemistry, we applied this system to the study of cell culture in 2D. In particular, we examined the specificity of the surfaces generated, to promote cell adhesion via the peptides selected. The immobilisation of biomolecules on polymeric brushes and the cell behaviour has been studied by other researchers[21, 87, 241]. Controlling the cell adhesion to 2D surfaces remains important to allow functionalisation of implants presenting 2D surfaces[86]. Raynor *et al.* functionalised the surface of titanium implants with polymer brushes to control protein and cell adhesion to the implant[111, 122]. Although medical implants are successful as devices, they are limited by infections and loosening over time. Polymer brush coatings are employed to improve the biocompatibility and enhance the implant integration within the host.

4.3.1 Adhesive motifs and cell attachment

HUVECs were seeded onto pOEGMA-coated substrates functionalised with peptides S3 to 6, to explore the role of the nature of the cell adhesive peptide in promoting their adhesion: RGD is derived from fibronectin and PHSRN from its synergy site[87, 117-121], REDV is also derived from a fibronectin fragment and is used to promote the adhesion of endothelial cells[242].

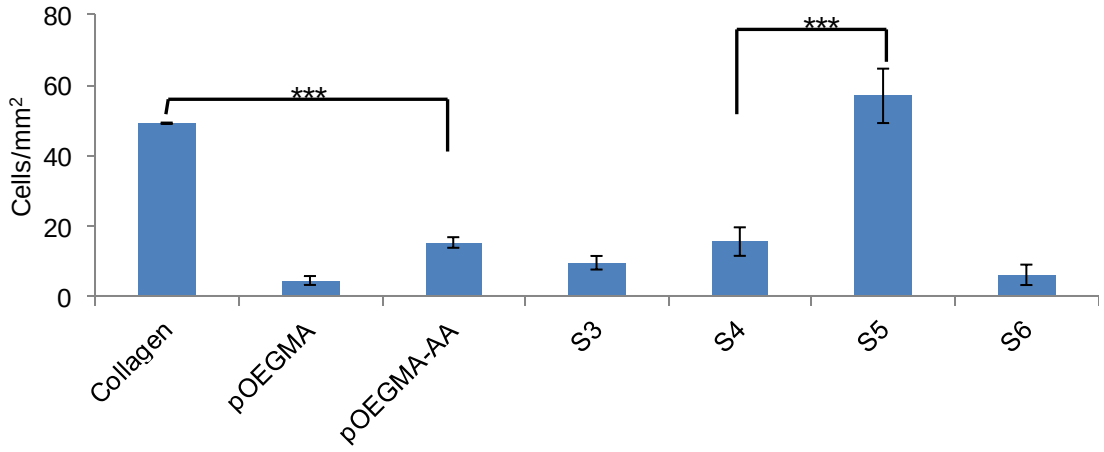

Figure 4.9 HUVEC cell count on polymer brush substrates functionalised with various peptides (S3-6) (5 mol%PI, 300s UV) and collagen control. See Fig. A3.2 for corresponding statistical analysis.

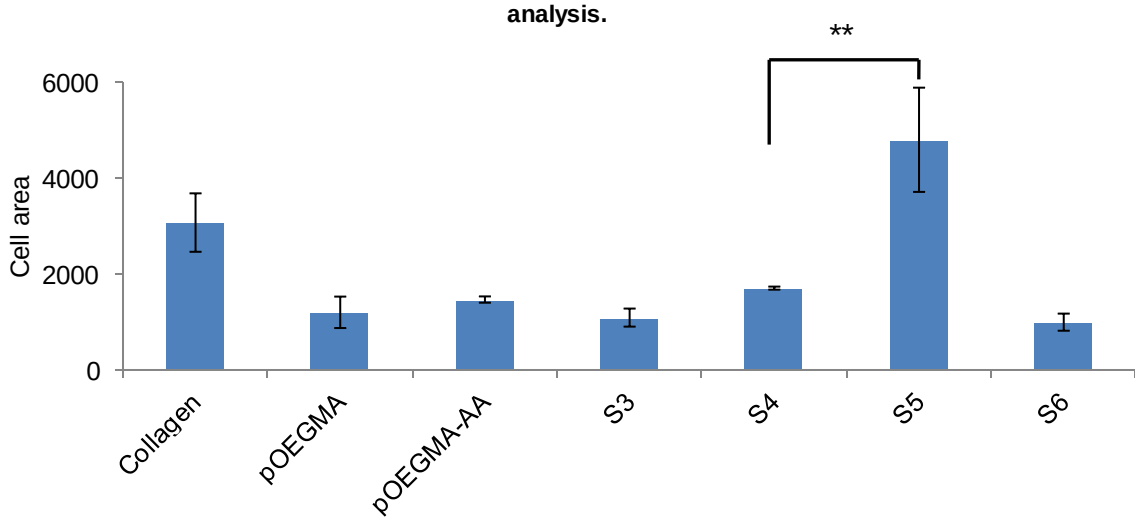

Figure 4.10 HUVEC cell area on polymer brush substrates functionalised with various peptides (S3-6) (5 mol%PI, 300s UV) and collagen control. See Fig. A3.3 for corresponding statistical analysis.

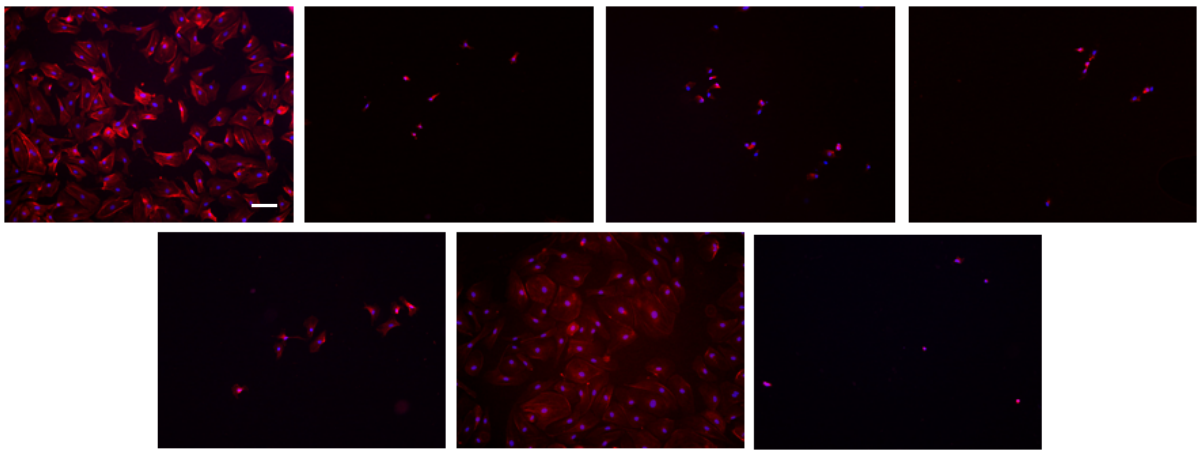

Figure 4.11 Epifluorescent images of HUVECs seeded (15,000 cells/mL) on substrates stained with phalliodin (red) and DAPI (blue). Substrates from left to right represent, collagen, pOEGMA, pOEGMA-AA, REDV (S3), RDVE (S4), RGD (S5) and RGE (S6). Reactions were performed with 5 mol%PI and 300 s UV.

Cells were allowed to spread for 24 h, fixed and stained, the number of cells adhered and their areas were characterised (Fig 4.9 and 4.10).Representative images for each condition studied are shown in Fig. 4.11, cells were stained with phalloidin (red), for the f-actin forming the cytoskeleton, and DAPI (blue) for the nucleus. Collagen coated surfaces were used as a positive control. pOEGMA Brushes are known to be protein resistant therefore were used as the negative control. Studies were also performed with allylamine functionalised brushes, to investigate whether the cell repellent behaviour still exists. The number of attached cells and their cell area were analysed using Image J. The collagen coated substrates gave rise to high numbers of cell attachment and spread cells, whereas pOEGMA brushes did not allow cell attachment and the few cells that were found at these surfaces displayed rounded morphologies. Cell numbers increased slightly for allylamine functionalised substrates indicating that the pOEGMA brushes lose some of their cell repellent properties, although the cells are not spread under these conditions. REDV (S3) is thought to promote some adhesive properties for HUVECs, as previously reported, mediated via the binding of $\alpha_4\beta_1$ integrins[241-244]. However, the HUVECs in this study did not show significant adhesion to the REDV (S3) substrates and also to its scrambled sequence RDVE (S4).

The triamino acid RGD is known to have cell adhesive properties for a range of cell types and has been studied intensively in many biomaterials fields[87]. It promotes adhesion via $\alpha_5\beta_1$ and $\alpha_v\beta_3$ integrins[199, 245]. Statistical analysis showed that RGD (S5) functionalised substrates allowed increased numbers of cells to adhere and these displayed significantly more spread morphologies than the other substrates studied. The cells in this study showed strong

adhesion and cell spreading to the thiol (S5) functionalised substrates, indicating that the RGD motif is an excellent tool for biofunctionalisation and promoting the adhesion of HUVECs. The S5 functionalised brushes even showed increased adhesion and cell spreading when compared to collagen, however, not statistically significant. In comparison the scrambled peptide RGE (S6) did not show adhesion or cell spreading, confirming the specificity of the RGD peptide.

A study was performed to investigate the selectivity of the peptides functionalised on the polymeric brushes compared to surfaces that had not been coated with polymer brushes. Silicon substrates were functionalised with silyl methacrylate to achieve alkene functional surfaces and coupled with the relevant peptides using thiol-ene coupling, using the same methodology as for polymer brushes. Results showed minimal difference in the number of cells adhered for all substrates with and without bioactive peptides (Fig. 4.12, 4.13 and 4.14).Collagen and S6 functionalised substrates show cells with slightly larger cell area, however,, these features were not as dominant as for the polymer brush systems and control peptides still gave rise to more cell spreading. This study confirms that the bioselectivity associated with cell adhesive peptides coupled to polymer brush substrates was preserved.

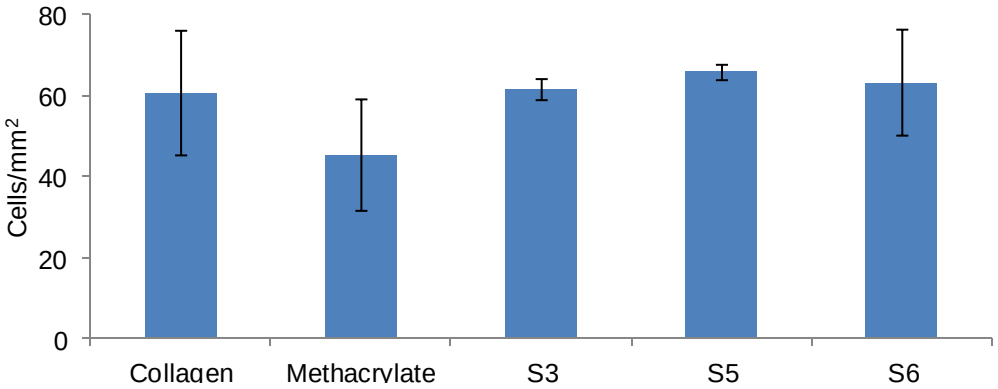

Figure 4.12 HUVEC cell count on methacrylate functionalised substrates functionalised with peptides (S3, S5-6)

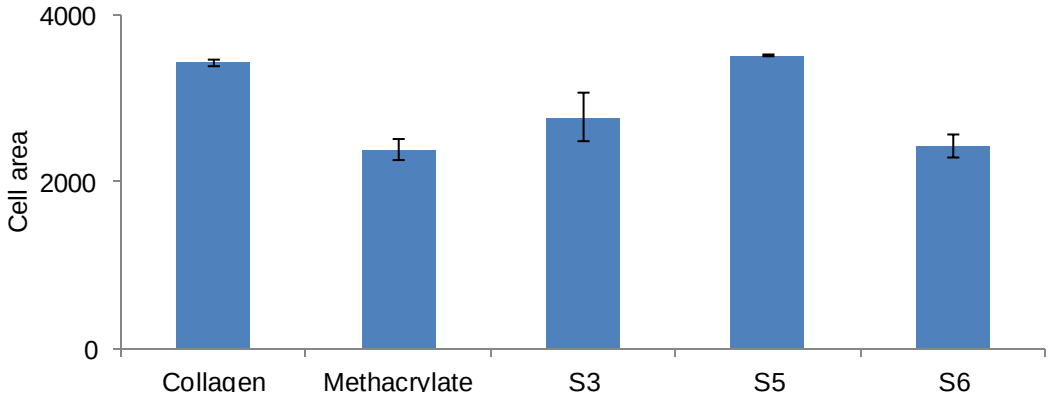

Figure 4.13 HUVEC cell area on methacrylate functionalised substrates functionalised with peptides (S3, S5-6)

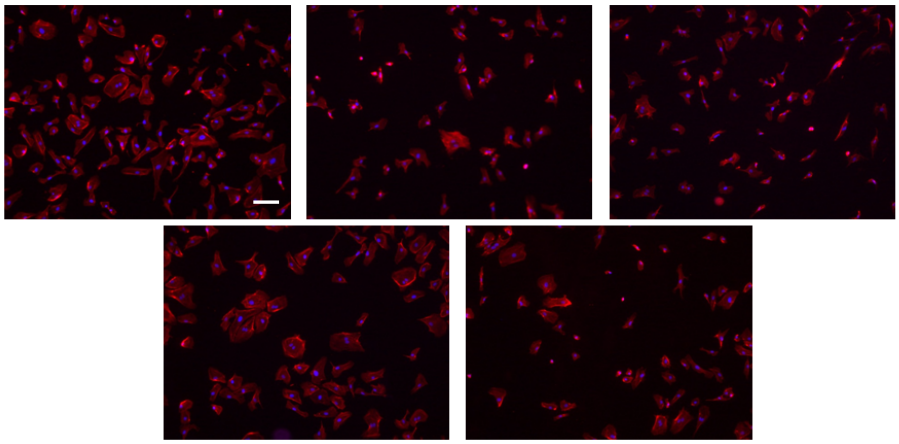

Figure 4.14 Epifluorescent images of HUVECs seeded (15,000 cells/mL) on substrates stained with phalliodin (red) and DAPI (blue). Substrates from left to right represent, collagen, methacrylate, REDV (S3), RGD (S5) and RGE (S6).

4.4 Patterning peptides on brushes

Cells are sensitive to geometrical and mechanical constraints from their environment *in vivo*[124]. These factors are not controlled under classic culture conditions. The ability to confine cells to specific microenvironments and the effect on cell behaviour plays a crucial role in the field of biomaterials. Cell patterning has been used to control the geometry and size of cells and help to understand cell response to physical properties in the microenvironment. Photo-patterning provides an excellent tool for this purpose. Thiol-ene coupling can be photo-triggered and therefore light can be used to pattern biomolecules onto the surfaces of polymeric brushes[21]. Here we applied thiol-ene coupling to create various patterned surfaces, using a model FITC labelled peptide. For this purpose, we used the method developed previously with the addition of a photomask to the system; Fig. 4.15 shows an illustration of the setup.

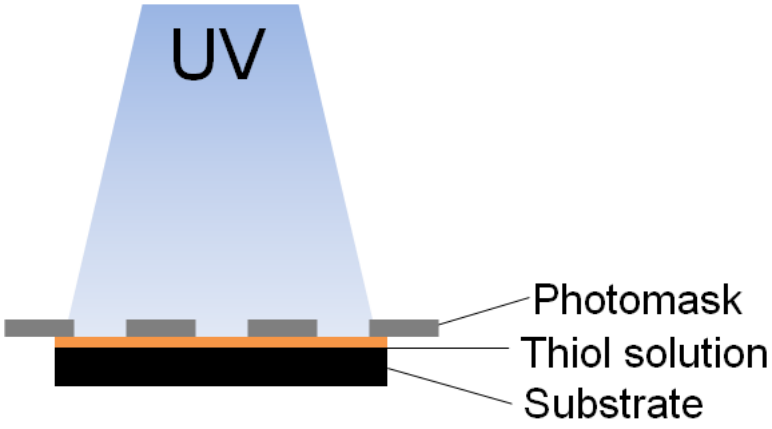

Figure 4.15 An illustration representing the thiol-ene patterning setup.

Two types of patterns were investigated, 50 µm circles and 50 µm lines were generated using a photomask and FITC labelled RGE (S8). Images were taken using an epifluorescent microscopy (Fig. 4.16) and analysed to characterise the definition of the patterns (Fig. 4.17), as determined by the

coupling efficiency of the batch studied. Images and analysis (Image J) clearly demonstrated the quality and definition of the patterns, although the expected 50 µm patterns measured 60 µm after the patterning of substrates. This could be a combination of the low resolution of the acetate masks, also because the masks were not in direct contact with the brushes therefore the light was able to diffract along the path.

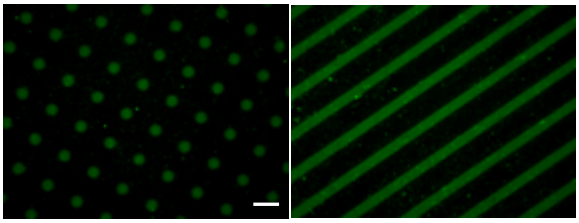

Figure 4.16 Epifluorescent images of FITC-RGE (S8) 50 µm circles and lined patterned substrates, scale 100µm. Reactions were performed with 5 mol% PI and 300 s UV exposure.

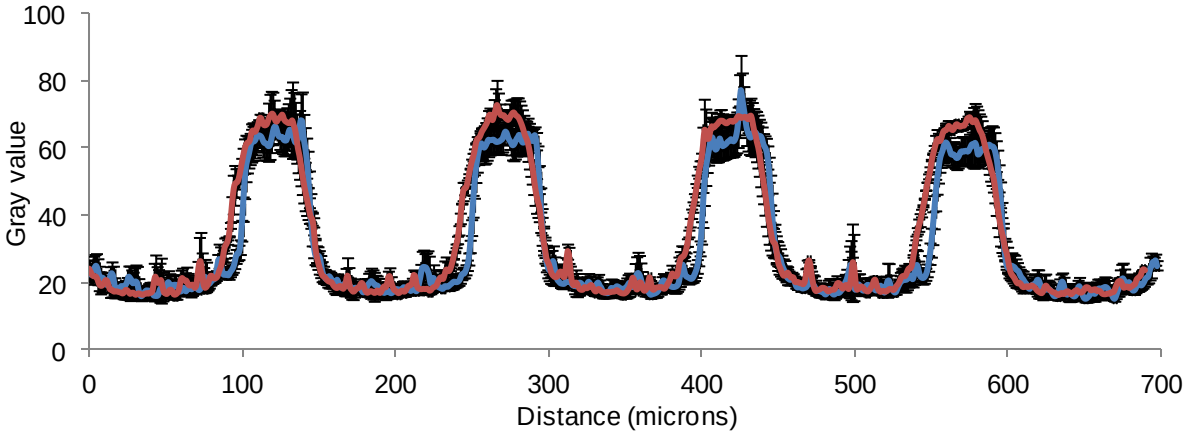

Figure 4.17 Gray values from epifluorescent images of S8 functionalised 50 µm lines (blue) and circles (red) patterned substrates. Reactions were performed with 5 mol% PI and 300 s UV exposure.

The impact of patterning conditions on coupling efficiency and pattern definition was assessed next. Substrates were reacted for different UV exposure times (60, 180, 300s UV). The corresponding epifluorescent images and analysis are presented in Fig. 4.18, 4.19, 4.20. Photopatterning usually requires optimum amount of time to achieve well defined patterns, these findings were from the method applied for the production of phoresists[151, 246,

[247]. However, this was not observed for our studies, as the width of the features did not broaden with longer exposure times. This may be because the coupling chemistry requires sufficient amount of light in order to achieve the required reaction efficiencies. Therefore, increased exposure of UV light allowed better functionalisation and therefore more defined patterns.

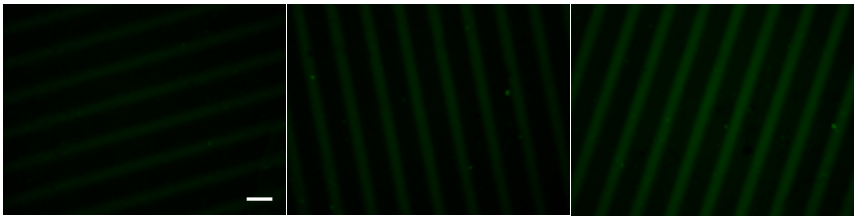

Figure 4.18 Epifluorescent images of S8 functionalised 50 µm line patterned substrates with differing UV exposure time, scale 100µm. Reactions were performed with 5 mol% PI.

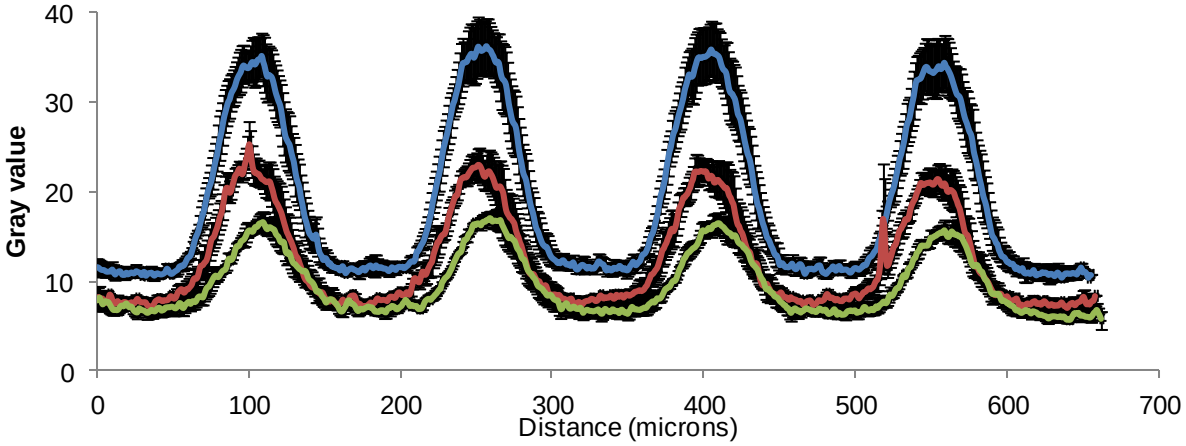

Figure 4.19 Gray value from epifluorescent images of S8 functionalised 50 µm line patterned substrates with differing UV exposure times: 300 s (blue), 180 s (red) and 60 s (green). Reactions were performed with 5 mol% PI.

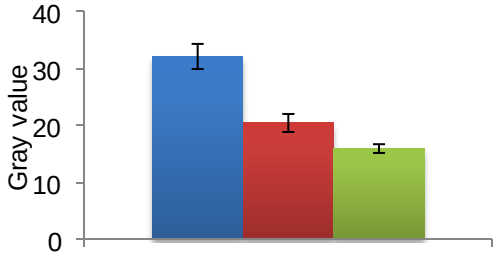

Figure 4.20 Average gray value from epifluorescent images of S8 functionalised 50 µm line patterned substrates with differing UV exposure times: 300 s (blue), 180 s (red) and 60 s (green). Reactions were performed with 5 mol% PI.

In order to show that photopatterning of polymeric brushes using thiol-ene coupling could be used as a tool for controlling the cell geometry, it is

important to achieve high enough resolution of the patterns. To this aim, 5 x 2 µm rectangles were patterned for different UV exposure times (60, 180, 300 s UV). Epifluorescence images and analysis are presented in Fig. 4.21, 4.22 and 4.23. As for larger patterns, increasing density of peptides coupled and pattern definition were observed with increasing UV exposure times. The patterns with FITC-RGE (S8) were also assessed using AFM, however patterns were not clearly visible using this technique, presumably owing to the relatively low reaction efficiency (confined to the surface of the brush) of the peptide coupling. To overcome this issue, the same patterns were generated with thiol S1, since its reaction efficiency was significantly higher compared to peptides (Fig. 4.7). Surfaces patterned with S1 with differing UV exposure (60, 180, 300s) were generated and AFM scans (Fig. 4.24) were produced to show the surface topography. The scans were analysed to observe the pattern definition (Fig. 4.25). AFM scans were performed by Stefania Di Cio. AFM scans clearly showed patterned surfaces with S1, due to the higher reaction efficiency with this thiol. The increase in UV exposure times (up to 300 s UV exposure) improved the definition of the patterns, confirming the results obtained by fluorescence microscopy for larger patterns (50 µm).

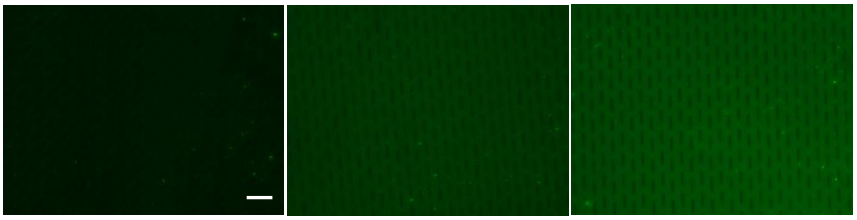

Figure 4.21 Epifluorescent images of S8 functionalised 5x2 µm rectangle patterned substrates with differing UV exposure time, scale 100µm. Reactions were performed with 5 mol% PI.

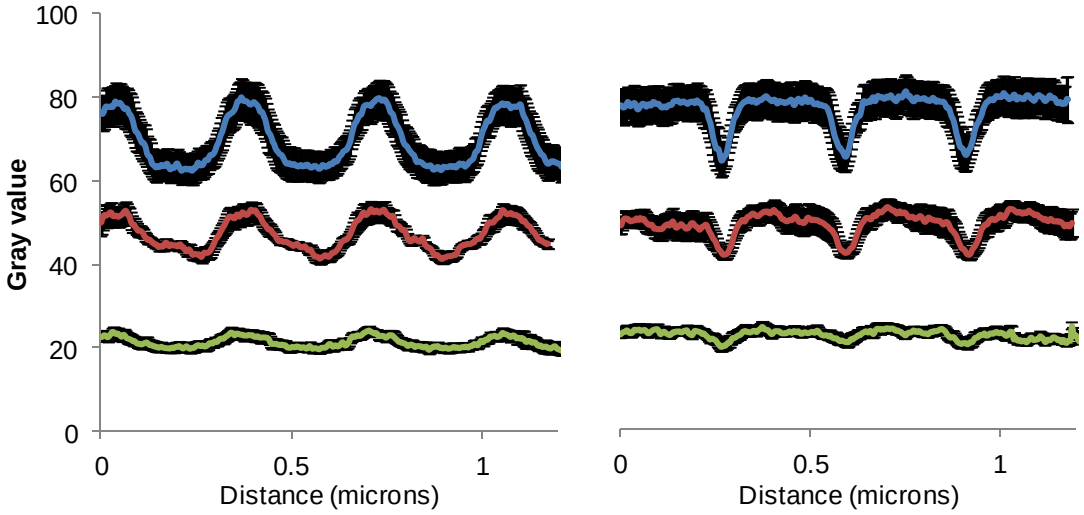

Figure 4.22 Gray values from epifluorescent images of S8 functionalised 5x2 µm reactangle patterned substrates with differing UV exposure times: 300 s (blue), 180 s (red) and 60 s (green). Reactions were performed with 5 mol% PI.

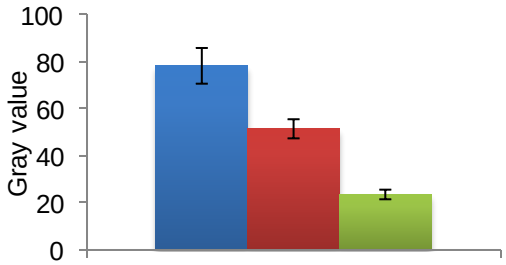

Figure 4.23 Average gray value from epifluorescent images of S8 functionalised 5x2 µm patterned substrates with differing UV exposure times: 300 s (blue), 180 s (red) and 60 s (green). Reactions were performed with 5 mol% PI.

Here the masks used were chromium masks so higher resolution was expected, this was thought to provide better control over the contact between the mask and the underlying substrate (as this mask is not flexible). Increasing the UV exposure results in improved patterns, the patterns by epifluorescence showed a 9 x 3 µm increase in dimension resulting in 14 x 5 µm patterned

rectangles (with thiol S8). When compared to patterns generated from S1 and analysed using AFM, the patterns are more defined and sized 7.5 x 3 µm, closer to the patterns on the mask (5 x 2 µm). Therefore, to control and generate a well defined pattern, it is important to use high efficiency coupling chemistry.

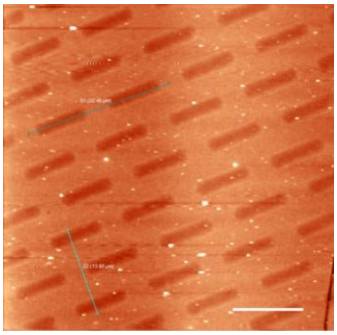

Figure 4.24 AFM topography scan of S1 rectangle (5x2µm) patterned substrate with 5 mol% PI and 300s UV exposure, scale 10µm.

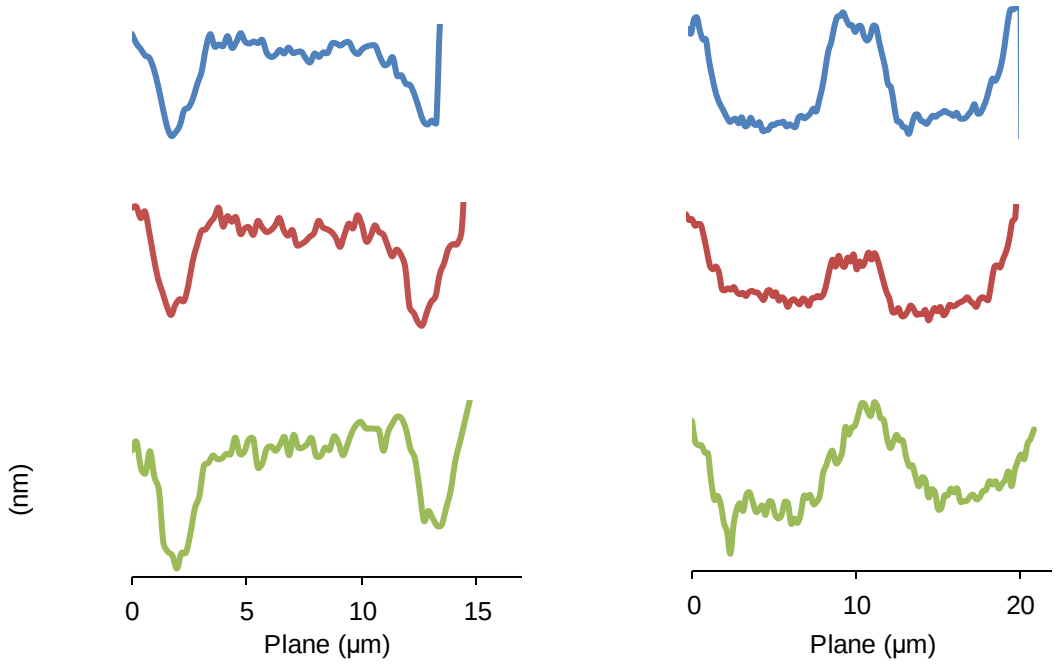

Figure 4.25 Pattern analysis of S1 rectangles with differing UV exposure times: 300 s (blue), 180 s (red) and 60 s (green). Reactions were performed with 5 mol% PI.

4.4.1 Cell interaction with thiol-ene patterned brushes

Finally, it is important to assess the cell behaviour with respect to the patterns generated. Based on our previous results and characterisation, homogeneous RGD functional substrates sustained suitable levels of cell adhesion and spreading. Therefore, this peptide was selected for surface patterning aimed at controlling the patterning of single cells. Others have also studied RGD patterned substrates with cells[21, 241].

Polymer brushes were patterned with mixtures of RGD (S5) and FITC-RGE (S8) (1:1) to generate the 50 µm rings. The FITC labelled RGE (S8) was used as the fluorescent component for imaging the patterns. The RGD (S5) peptide was used to adhere the cells to the patterns. HUVECs were seeded on S5:S8 patterned surfaces and allowed to spread for 24 hours. Cell were fixed and stained with phalloidin and DAPI and imaged using an epifluorescent microscope. Channels were merged using Image J and analysed manually. The aim was to recognise cells that adapted their morphology to the shape of the patterns. Results showed that 77% (± 3.1%) of the adhering cells recognised the RGD motifs and adhered to the ring-patterns (Fig. 4.26).

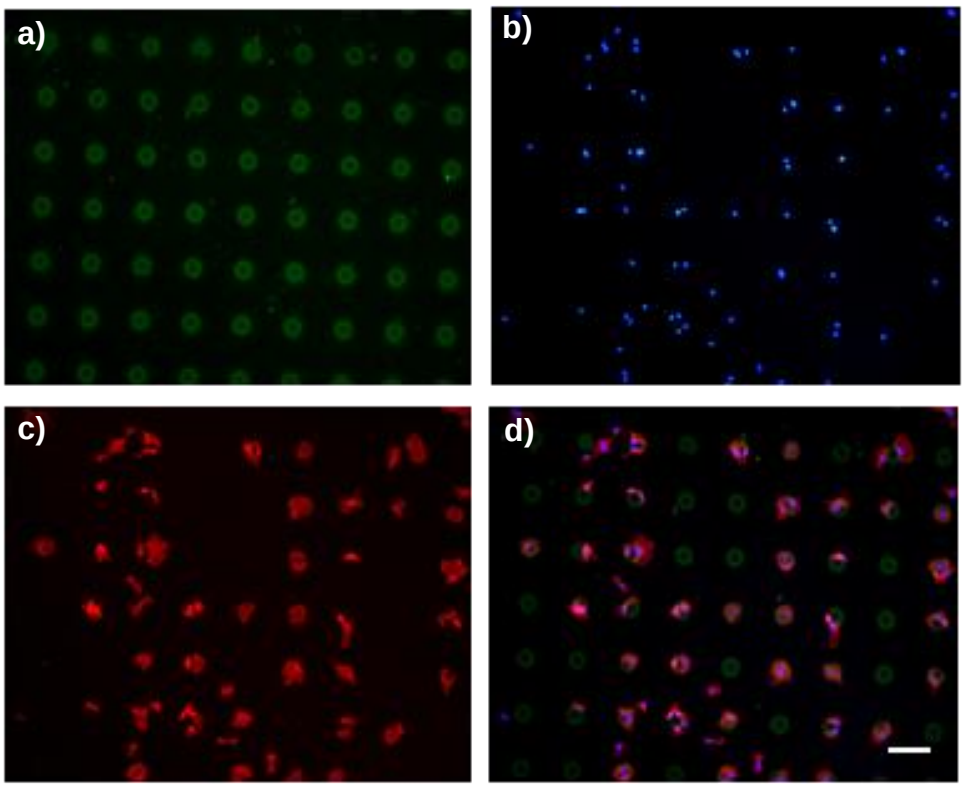

Figure 4.26 A representation of HUVECs (7 500 cells/mL) on S5 : S8 (1:1) ring patterned substrates, scale bar 100µm. Reactions were performed with 5 mol% PI and 300 s UV exposure. a) rings stained with FITC labelled peptide (green), b) nucleus were stained with DAPI (blue), c) cell cytoskeleton, actin were stained with phalliodin (red) an d) a representation of the merged channels.

4.5 Summary

Thiol-ene chemistry provides an excellent tool for the functionalisation of polymeric surfaces and to generate patterns or various shapes. The ability to generate various patterned surfaces for different cell types using defined peptides to control and quantify cell phenotype is an interesting feature for the development of novel cell-based assays, including single cell patterns allowing to isolate the role of different microenvironmental factors[248-250]. For example, the impact of specific integrin binding (which can be controlled via the choice of peptides coupled) on the sensing of the ECM geometry that has been shown to play an important role in directing the differentiation of stem cells has not been studied and will allow to explore further the role of different integrins in associated molecular signalling pathways.

4.6 Experimental section

4.6.1 Materials

Anhydrous toluene (99.8%), triethylamine (99%), ethanol (99.5%), 3-(trimethoxysilyl)propyl methacrylate (98%), methanol (99.9%), PBS tablets, Dulbecco's PBS, poly(ethylene glycol) methacrylate average M_n 360 g/mol (409537), bipyridine (99%), copper (II) bromide (99.999%), copper (I) chloride (99.995%), DSC (95%), DMAP (99%), DMF (pharmaceutical secondary standard), allylamine (98%), IRG2959 (98%), *N*-acetyl *l*-cysteine (S1, 99%), *l*-glutathione reduced (S2, 98%), PFA (95%), Triton-X 100, phalloidin–tetramethylrhodamine B isothiocyanate and DAPI (98%) were obtained from Sigma Aldrich. ATRP silane initiator, 3-trimethoxysilyl propyl 2-bromo-2 methylpropionate was purchased from Fluorochem. Medium 199, HEPES was purchased from life technologies. Collagen rat type I was purchased from BD Biosciences. Custom peptides GCGREDVSG (S3, REDV), GCGRVDESG (S4, RDVE), GCGYGRGDSPG (S5, RGD), GCGYGRGESPG (S6 RGE), GCGPHSRNSG (S7, PHSRN), GCGYGRGESPG-Lys-FITC-G (S8, FITC-RGE) were purchased from Proteogenix, France. Penicillin streptomycin (5000 U/mL) and medium 199 HEPES (22340020) were obtained from life technologies. FBS, South American Origin was purchased from Labtech. *l*-glutamine (200 mM), versene and trypsin (0.25%) phenol red, were obtained from Thermo Fisher Scientific.

4.6.2 Instrumentation

Dry brush thickness was measured using ellipsometry, J.A. Woolam Co., Inc. Ellipsometry solutions, α-SE. Grazing angle FTIR spectroscopy were produced using a Bruker Tensor 27 spectrometer equipped with a MCT detector; results were acquired at a resolution of 16 cm^{-1} and a total of 128 scans per run in the region of 600-4000 cm^{-1}. The UV light used to initiate reactions was the Omnicure series 1500. The radiometer used to measure the UV light intensity was from International light technologies, ILT 1400-A radiometer photometer. AFM was used to scan patterned surfaces, in semicontact mode and the row pictures were corrected with a first order function using Nova software. Non-contact NSG01 cantilevers from NT-MDT were used (force constant 1,45-15,1 N/m and resonant frequency 87-230 kHz). Leica DMI4000B epifluorescent microscope fitted with a HCX PL FLUOTAR 10x/0.3 PJ1 objective and a Leica DFC300 FX CCD camera was used to image patterned surfaces. Image J analysis was performed on all epifluorescent images; singe channel images were changed to grey scale then to black and white using a threshold (with cells appearing black), binary watershed was performed to separate into individual cells, requires measurements were set and the particles were analysed (excluding on the edges and including holes). Images from channels were merged for illustration purposes.

4.6.3 Statistical analysis

All data were analysed by Tukey's test and significance was determined by * $p < 0.05$, ** $p < 0.01$: *** $p < 0.001$. A full summary of statistical analysis is provided in Tables A3.1-3.3.

4.6.4 Brush synthesis and functionalisation

Polymer brushes were generated using a previously published method[109, 238]. Silicon wafer substrates were functionalised with an ATRP initiator using the following method. The substrates were plasma oxidised for 10 minutes (power 95) and incubated in a solution of anhydrous toluene (30 mL) with 3-trimethoxysilyl propyl 2-bromo-2 methylpropionate (30 µL) and triethylamine (50 µL) for 24 h. The wafer was washed with deionised water followed by ethanol and dried under a stream of nitrogen.

pOEGMA Brushes were grown on the surface of the silicon substrates. PEG methacrylate (17.5 mmol), bipyridine (1.0 mmol), Cu(II)Br_2 (40 µmol) and water: ethanol 4:1 (12:3 mL) were measured into a round bottom flask and dissolved. The solution was bubbled with argon for 45 minutes whilst stirring. Then was added Cu(I)Cl (410 µmol), the contents were sonicated and bubbled with argon for a further 10 minutes. The polymerisation solution was added into carousels containing substrates and reacted under inert atmosphere for a given time. The substrates were washed with plenty of water then ethanol and dried under a stream of nitrogen. The thicknesses of the brushes were measured using ellipsometry.

The brushes contain a hydroxyl group that can be used for further functionalisation of the brush. The brushes were functionalised with a solution of DSC (60 mmol) and DMAP (60 mmol) in anhydrous DMF (60 mL) under inert atmosphere for 24 h. The substrates were washed with DMF followed by water and ethanol and dried under a stream of nitrogen. The thickness of the brush was measured using ellipsometry.

To achieve brushes with alkene functionality, the DSC functionalised brushes were incubated in a solution of 1% allylamine in DMF (10 µL/mL) for 24 h. The substrates were washed with DMF, water, ethanol and dried under a stream of nitrogen. The thickness of the brush was measured using ellipsometry.

4.6.5 Methacrylate functionalised substrates

Silicon wafers were plasma oxidised for 10 minutes (power 95) and incubated in a solution of anhydrous toluene (30 mL) with 3-(trimethoxysilyl)propyl methacrylate (30 µL) and triethylamine (50 µL) for 24 h. The wafer was washed with deionised water followed by ethanol and dried under a stream of nitrogen.

4.6.6 Thiol-ene on substrates

A series of thiols (S1-7) were dissolved in PBS ($4.5x10^{-5}$ mol/mL), thiol S8 was dissolved in DMF: PBS (2: 8). Photoinitiator 5 mol% was added to the thiol solution (25 µL/mL of 250 mg/mL in methanol). The mixture was added onto a quartz plate (10 µL) and alkene or methacrylate functional substrates were placed on top. Substrates were cured with UV (300 s) as shown in setup (Fig.

4.4). Substrates were washed with deionised water then ethanol and dried under a stream of nitrogen before being measured using ellipsometry.

4.6.7 Cell culture

HUVECs were routinely grown in medium 199 supplemented with 10% FBS, 1% penicillin streptomycin and 1% glutamine. The medium was changed every 2-3 days and cells were sub-cultured each week using trypsin/versene. Cells were maintained at 37 ºC in a humidified atmosphere containing 5% CO_2.

4.6.8 Cells on brushes

Collagen rat, type I was dissolved in PBS (400 µg/mL) and filtered through a 0.2 µm pore membrane. The collagen mixture was added to a well containing a coverslip and allowed to set for 30 minutes. The solution was removed and replaced with PBS before cell seeding cells. Thiol-ene functionalised substrates were sterilised with ethanol and sterile PBS. HUVECs passage 4-12 (15,000 cells/mL) in medium (1 mL) were seeded on the substrates and cultured for 24 h. Cells were fixed and permeabilised simultaneously in 4% PFA and 0.2% Triton-X100, blocked for 1 h in 10% FBS containing 0.25% gelatin, incubated at room temperature with phalloidin (2 µL/mL) and DAPI (2 µL/mL) for 1 h and mounted on glass slides in Mowiol. Epifluorescent microscopy was used to image the cells on the surfaces, images were merged using image J and analysed for the number of cells and cell area.

4.6.9 Patterning peptides on brushes

Patterned substrates were generated as for the homogeneous substrates (with *N*-acetyl *l*-cysteine S1 and FITC RGE S8 only). Instead of adding the reaction mixture (with 5 mol% PI) to the quartz, it was added to the photomask (acetate mask-circles, lines, chromium mask-rectangles and rings) as in setup shown previously (Fig. 4.15) and the remainder of the process was as for the homogeneous substrates. Substrates were analysed using epifluorescent microscopy or AFM.

4.6.10 Cells on patterned brushes

Patterned substrates were generated with 1:1 S5: S8 mixed solutions. Thiol solution with PI was used to generate ring patterns. Substrates were sterilised with ethanol and sterile PBS. HUVECs (7,500 cells/mL) in medium (1 mL) were seeded on the substrates and cultured for 24 h. Patterned cells were fixed and permeabilised simultaneously in 4% PFA and 0.2% Triton-X100, blocked for 1 h in 10% FBS containing 0.25% gelatin, incubated at room temperature with phalloidin (2 µL/mL) and DAPI (2 µL/mL) for 1 h and mounted on glass slides in Mowiol. Epifluorescent microscopy was used to image the cells on the patterned surfaces, images were merged using image J and analysed. Cell count analysis was performed manually and percentage of patterned cells was calculated using equation 4.1.

$$Patterned\ cells\ (\%) = \left(\frac{no.of\ cells\ not\ on\ patterns}{no.of\ cells\ on\ patterns}\right) \times 100 \qquad \textbf{equation 4.1}$$

4.6.11 Percentage conversion calculated from ellipsometry

$$\Delta T = Tn - Ti \qquad \textbf{equation 4.2}$$

ΔT Difference in dry brush thickness (nm)

Ti Initial dry brush thickness (nm)

Tn New dry brush thickness (nm)

$$fn = \left(\frac{\Delta T}{Ti} \times \frac{M1}{M2}\right) \times 100 \qquad \textbf{equation 4.3}$$

fn Degree of functionalisation (%)

M1 Molecular weight of initial monomers (g/mol)

M2 Molecular weight of added molecule (g/mol)

Initial monomers g/mol (M1)		**Added molecules g/mol (M2)**	
pOEGMA	360	DSC cleaved M_w	141
pOEGMA-DSC	360	Allylamine (part DSC)	83
pOEGMA-AA	510.09	*N*-Acetyl *l*-cysteine (S1)	163.19
pOEGMA-AA	510.09	*l*-Glutathione (S2)	307.32
pOEGMA-AA	510.09	GCGREDVSG (S3)	878.91
pOEGMA-AA	510.09	GCGRVDESG (S4)	878.91
pOEGMA-AA	510.09	GCGYGRGDSPG (S5)	1025.06
pOEGMA-AA	510.09	GCGYGRGESPG (S6)	1039.09
pOEGMA-AA	510.09	GCGPHSRNSG (S7)	971.02
pOEGMA-AA	510.09	FITC RGE (S8)	1025.06
Methacrylate	248.35	GCGREDVSG (S3)	878.91
Methacrylate	248.35	GCGYGRGDSPG (S5)	1025.06
Methacrylate	248.35	GCGYGRGESPG (S6)	1039.09

Chapter 5

Conclusion and future directions

This thesis investigates the chemistry of photoinitiated thiol-ene coupling and proves it a useful tool for the generation of biomaterials. Thiol-ene coupling is widely used in the biomaterials field however; little is known about the chemistry under the relevant conditions. Chemistries are mainly investigated in organic solvents, however, many biomaterials of interest are produced in aqueous buffers, and the chemistry under these conditions differs to organic solvents. A detailed study of thiol-ene chemistry in buffered conditions was performed and the factors impacting the coupling were investigated. Results showed that one of the main factors impacting the coupling different than in organic solvent is the pH of the buffer. Thiol-ene coupling works best at neutral or slightly acidic pH and ceases at alkaline pH and the working range of pH is affected by the chosen thiol. Since the cysteine amino acid contains a thiol on its side chain, it opens up doors to do thiol-ene coupling with peptide sequences of choice. This is an important step for the biofunctionalisation of materials. Thiol-ene coupling was further explored with a series of peptides to investigate the affect of the changes in the local structure of the peptide on the reaction efficiency. The results showed that the presence of specific aromatic

groups in the sequence (tyrosine: cysteine 1:1) affected the reaction efficiency, however, the same observations are not made when this is decreased to 10%. One of the main factors affecting the reaction efficiency was the position of the cysteine in the sequence and the presence of charged amino acids near the cysteine. When the cysteine was placed as the terminal position in the sequence it reacted with lower efficiency than when it was placed second position near a glycine. Also, the cysteine performed better when with glycine neighbours rather than charged neighbours. Understanding the chemistry behind the choice of peptide is crucial especially when using for biofunctionalisation and where reaction efficiencies are important.

The potential for thiol-ene is greater than what is reported in this work. The chemistry and knowledge involved with the peptide studies is crucial for the field of biomaterials and requires more investigation into the mechanistic detail of the reasons why certain amino acids at specific distances from the cysteine affect the reactivity of the thiol. Also, why the reaction efficiency is lower when the cysteine is placed at the terminal position compared to when it placed second position near a glycine residue. Many more cysteine containing sequences can be studied to generate guidelines and help researchers with their choice of peptide sequences for thiol-ene coupling. Since many biomaterials are generated using aqueous buffer systems, the effect of various buffers on the thiol-ene coupling could be investigated to provide a library of buffers where the thiol-ene coupling works best.

Thiol-ene coupling was investigated for the biofunctionalisation of polymer brush surfaces. Many biofunctional peptides of choice were immobilised on these surfaces, making them attractive tools for the study of biomolecule-cell

interactions. Biomolecules can be immobilised with ease and their affects on cell behaviour can be observed quickly. This method generates a tool for high throughput systems. Since the chemistry of interest is photo-initiated, photomasks can be used to generate various patterns using the biomolecules, and therefore directing the cell attachment to required shapes for the investigation of microenvironmental effects.

In the future, biofunctional patterns may be used to direct cell attachment to templates, i.e. HUVECs on 2D lines or branched patterns, when provided with a 3D environment i.e. coating with hydrogels, the cells could possibly be directed to generate line patterned vascular structures. The simple tool of thiol-ene used for the biofunctionalisation of surfaces could also help generate high-throughput systems; many peptide sequences of choice could be functionalised on solid supports to investigate their bioactivity with a variety of cell types. The ability to immobilise bioactive peptides on solid supports also shows potential in the biosensing field.

Synthetic biomimetic hydrogel systems are currently receiving much attention in the biomaterials field as they have a great potential for many bioengineering and cell culture applications. The ability to control the thiol-ene coupling reaction enables good control over the crosslinking kinetics for network formation and therefore the gelation properties of hydrogels. Many features of the hydrogel can be manipulated by choice (stiffness, biofunctionality, degradation, choice of polymeric material). This makes this hydrogel system very attractive to users with specific requirements that require change of various features of the gel that other commercially used gel systems cannot provide.

The hydrogels generated in this work are UV crosslinked with either a PEG or/and an enzymatically degradable peptide crosslinker to achieve networks of varying stiffness and degradation kinetics. The hydrogel systems were investigated as 3D cell culture materials and showed good cell viability and potential for the use of these materials in the bioengineering field. However, there were some problems with the hydrogel material and 3D cell encapsulation. Cells showed very rounded behaviour throughout all systems studied and preferred not to spread and form cell networks. Reasons for this behaviour and the factors required for investigation are discussed at the end of Chapter 3. Briefly the future work with hydrogels should be implemented to achieve cells that are happy in the hydrogel system over a long term in order to increase the potential for this material compared to all others on the market. Once the hydrogel system meets all the requirements needed, there is a huge potential for its application in many fields involved with biology. Also, since thiol-ene chemistry is UV activated, like the polymer brush systems; patterned hydrogel systems can be generated. The ability for patterning could also provide a potential for this material to generate devices (i.e. microfludic systems) that the standard materials on the market are not able to achieve.

References

1. F. Ullah, M. B. H. Othman, F. Javed, Z. Ahmad and H. M. Akil, *Mater. Sci. Eng. C Mater. Biol. Appl.*, 2015, **57**, 414-433.
2. E. Jabbari, *Curr. Opin. Biotechnol.*, 2011, **22**, 655-660.
3. H. Schlaad, C. Diehl, A. Gress, M. Meyer, A. L. Demirel, Y. Nur and A. Bertin, *Macromol. Rapid Comm.*, 2010, **31**, 511-525.
4. J. A. Burdick and W. L. Murphy, *Nat. Comm.*, 2012, **3,** 1-8.
5. M. Guvendiren and J. A. Burdick, *Nat. Comm.*, 2012, **3**, 1-9.
6. R. Sunyer, A. J. Jin, R. Nossal and D. L. Sackett, *Plos One*, 2012, **7,** 1-9.
7. T. Yeung, P. C. Georges, L. A. Flanagan, B. Marg, M. Ortiz, M. Funaki, N. Zahir, W. Y. Ming, V. Weaver and P. A. Janmey, *Cell Motil Cytoskeleton*, 2005, **60**, 24-34.
8. S. Khetan, M. Guvendiren, W. R. Legant, D. M. Cohen, C. S. Chen and J. A. Burdick, *Nat. Mater.*, 2013, **12**, 458-465.
9. B. D. Fairbanks, M. P. Schwartz, A. E. Halevi, C. R. Nuttelman, C. N. Bowman and K. S. Anseth, *Adv. Mater.*, 2009, **21**, 5050-5010.
10. H. C. Kolb, M. G. Finn and K. B. Sharpless, *Angew. Chem. Int. Edit.*, 2001, **40**, 2004-2021.
11. A. B. Lowe, *Polym. Chem.*, 2014, **5**, 4820-4870.
12. M. Le Neindre and R. Nicolay, *Polym. Chem.*, 2014, **5**, 4601-4611.
13. K. Kempe, A. Krieg, C. R. Becer and U. S. Schubert, *Chem. Soc. Rev.*, 2012, **41**, 176-191.
14. M. J. Kade, D. J. Burke and C. J. Hawker, *J. Polym. Sci. A Polym. Chem.*, 2010, **48**, 743-750.
15. V. V. Rostovtsev, L. G. Green, V. V. Fokin and K. B. Sharpless, *Angew. Chem. Int. Edit.*, 2002, **41**, 2596-2599.
16. G. Delaittre, N. K. Guimard and C. Barner-Kowollik, *Acc. Chem. Res.*, 2015, **48**, 1296-1307.
17. R. M. Hensarling, V. A. Doughty, J. W. Chan and D. L. Patton, *J. Am. Chem. Soc.*, 2009, **131,** 14673-14675.
18. R. Hoogenboom, *Angew. Chem. Int. Edit.*, 2010, **49**, 6288-6308.
19. L. M. Campos, K. L. Killops, R. Sakai, J. M. J. Paulusse, D. Damiron, E. Drockenmuller, B. W. Messmore and C. J. Hawker, *Macromolecules*, 2008, **41**, 7063-7070.
20. W. M. Gramlich, I. L. Kim and J. A. Burdick, *Biomaterials*, 2013, **34**, 9803-9811.

21. P. Costa, J. E. Gautrot and J. T. Connelly, *Acta Biomater.*, 2014, **10**, 2415-2422.
22. A. Gress, A. Volkel and H. Schlaad, *Macromolecules*, 2007, **40**, 7928-7933.
23. V. Schenk, L. Ellmaier, E. Rossegger, M. Edler, T. Griesser, G. Weidinger and F. Wiesbrock, *Macromol. Rapid Comm.*, 2012, **33**, 396-400.
24. A. Dondoni, *Angew. Chem. Int. Edit.*, 2008, **47**, 8995-8997.
25. N. Gupta, B. F. Lin, L. Campos, M. D. Dimitriou, S. T. Hikita, N. D. Treat, M. V. Tirrell, D. O. Clegg, E. J. Kramer and C. J. Hawker, *Nat. Chem.*, 2010, **2**, 138-145.
26. B. D. Mather, K. Viswanathan, K. M. Miller and T. E. Long, *Prog. Polym. Sci.*, 2006, **31**, 487-531.
27. C. E. Hoyle and C. N. Bowman, *Angew. Chem. Int. Edit.*, 2010, **49**, 1540-1573.
28. N. B. Cramer, T. Davies, A. K. O'Brien and C. N. Bowman, *Macromolecules*, 2003, **36**, 4631-4636.
29. B. H. Northrop and R. N. Coffey, *J.Am. Chem. Soc.*, 2012, **134**, 13804-13817.
30. M. Uygun, M. A. Tasdelen and Y. Yagci, *Macromol. Chem. Physic.*, 2010, 211, 103-110.
31. P. M. Johnson, J. W. Stansbury and C. N. Bowman, *J. Polym. Sci. A Polym. Chem.*, 2008, 46, 1502-1509.
32. L. Lecamp, F. Houllier, B. Youssef and C. Bunel, *Polymer*, 2001, **42**, 2727-2736.
33. N. B. Cramer and C. N. Bowman, *J. Polym. Sci. A Polym. Chem.*, 2001, **39**, 3311-3319.
34. C. E. Hoyle, A. B. Lowe and C. N. Bowman, *Chem. Soc. Rev.*, 2010, **39**, 1355-1387.
35. S. P. S. Koo, M. M. Stamenovic, R. A. Prasath, A. J. Inglis, F. E. Du Prez, C. Barner-Kowollik, W. Van Camp and T. Junkers, *J. Polym. Sci. A Polym. Chem.*, 2010, **48**, 1699-1713.
36. C. E. Hoyle, T. Y. Lee and T. Roper, *J. Polym. Sci. A Polym Chem.*, 2004, **42**, 5301-5338.
37. G. Povie, T. Anh-Tuan, D. Bonnaffe, J. Habegger, Z. Hu, C. Le Narvor and P. Renaud, *Angew. Chem. Int. Edit.*, 2014, **53**, 3894-3898.
38. N. B. Cramer, S. K. Reddy, A. K. O'Brien and C. N. Bowman, *Macromolecules*, 2003, **36**, 7964-7969.
39. P. Derboven, D. R. D'Hooge, M. M. Stamenovic, P. Espeel, G. B. Marin, F. E. Du Prez and M.-F. Reyniers, *Macromolecules*, 2013, **46**, 1732-1742.
40. B. L. Farrugia, K. Kempe, U. S. Schubert, R. Hoogenboom and T. R. Dargaville, *Biomacromolecules*, 2013, **14**, 2724-2732.
41. C. Weber, R. Hoogenboom and U. S. Schubert, *Prog. Polym. Sci.*, 2012, **37**, 686-714.
42. R. Hoogenboom, *Angew. Chem. Int. Edit.*, 2009, **48**, 7978-7994.
43. N. Adams and U. S. Schubert, *Adv. Drug Deliv. Rev.*, 2007, **59**.
44. V. R. de la Rosa, *J. Mater. Sci. Mater. Med.*, 2014, **25**, 1211-1225.
45. R. Luxenhofer, G. Sahay, A. Schulz, D. Alakhova, T. K. Bronich, R. Jordan and A. V. Kabanov, *J. Control. Release*, 2011, **153**, 73-82.

46. S. Cesana, A. Kurek, M. A. Baur, J. Auernheirner and O. Nuyken, *Macromol. Rapid Comm.*, 2007, **28**, 608-615.
47. A. M. Kelly, A. Hecke, B. Wirnsberger and F. Wiesbrock, *Macromol. Rapid Comm.*, 2011, **32**, 1815-1819.
48. F. Wiesbrock, R. Hoogenboom, M. A. M. Leenen, M. A. R. Meier and U. S. Schubert, *Macromolecules*, 2005, **38**, 5025-5034.
49. R. Hoogenboom, F. Wiesbrock, H. Y. Huang, M. A. M. Leenen, H. M. L. Thijs, S. van Nispen, M. Van der Loop, C. A. Fustin, A. M. Jonas, J. F. Gohy and U. S. Schubert, *Macromolecules*, 2006, **39**, 4719-4725.
50. T. A. Petrie, J. E. Raynor, D. W. Dumbauld, T. T. Lee, S. Jagtap, K. L. Templeman, D. M. Collard and A. J. Garcia, *Sci. Transl. Med.*, 2010, **2**, 45-60.
51. S. R. Meyers, D. J. Kenan, X. Khoo and M. W. Grinstaff, *Biomacromolecules*, 2011, **12**, 533-539.
52. S. Kusuma, Y.-I. Shen, D. Hanjaya-Putra, P. Mali, L. Cheng and S. Gerecht, *Proc. Natl Acad. Sci. USA*, 2013, **110**, 12601-12606.
53. Z. Melkoumian, J. L. Weber, D. M. Weber, A. G. Fadeev, Y. Zhou, P. Dolley-Sonneville, J. Yang, L. Qiu, C. A. Priest, C. Shogbon, A. W. Martin, J. Nelson, P. West, J. P. Beltzer, S. Pal and R. Brandenberger, *Nat. Biotechnol.*, 2010, **28**, 606-695.
54. S. Dhar, F. X. Gu, R. Langer, O. C. Farokhzad and S. J. Lippard, *Proc. Natl Acad. Sci. USA*, 2008, **105**, 17356-17361.
55. S. Khetan, J. S. Katz and J. A. Burdick, *Soft Matter*, 2009, **5**, 3412-3416.
56. H. Shih and C.-C. Lin, *Macromol. Rapid Comm.*, 2013, **34**, 269-273.
57. M. Bracher, D. Bezuidenhout, M. P. Lutolf, T. Franz, M. Sun, P. Zilla and N. H. Davies, *Biomaterials*, 2013, **34**, 6797-6803.
58. M. Caiazzo, Y. Okawa, A. Ranga, A. Piersigilli, Y. Tabata and M. P. Lutolf, *Nat. Mater.*, 2016, **15**, 344-352.
59. S. B. Anderson, C.-C. Lin, D. V. Kuntzler and K. S. Anseth, *Biomaterials*, 2011, **32**, 3564-3574.
60. N. B. Cramer, S. K. Reddy, M. Cole, C. Hoyle and C. N. Bowman, *J. Polym. Sci. A Polym. Chem.*, 2004, **42**, 5817-5826.
61. M. H. Fittkau, P. Zilla, D. Bezuidenhout, M. Lutolf, P. Human, J. A. Hubbell and N. Davies, *Biomaterials*, 2005, **26**, 167-174.
62. M. W. Toepke, N. A. Impellitteri, J. M. Theisen and W. L. Murphy, *Macromol. Mater. Eng.*, 2013, **298**, 699-703.
63. M. A. C. Stuart, W. T. S. Huck, J. Genzer, M. Mueller, C. Ober, M. Stamm, G. B. Sukhorukov, I. Szleifer, V. V. Tsukruk, M. Urban, F. Winnik, S. Zauscher, I. Luzinov and S. Minko, *Nat. Mater.*, 2010, **9**, 101-113.
64. M. Liu and L. Jiang, *Adv. Funct. Mater.*, 2010, **20**, 3753-3764.
65. A. Hucknall, S. Rangarajan and A. Chilkoti, *Adv. Mater.*, 2009, **21**, 2441-2446.
66. A. Malinauskas, *Polymer*, 2001, **42**, 3957-3972.
67. M. E. Alf, A. Asatekin, M. C. Barr, S. H. Baxamusa, H. Chelawat, G. Ozaydin-Ince, C. D. Petruczok, R. Sreenivasan, W. E. Tenhaeff, N. J. Trujillo, S. Vaddiraju, J. Xu and K. K. Gleason, *Adv. Mater.*, 2010, **22**, 1993-2027.
68. O. Azzaroni, *J. Polym. Sci. A Polym. Chem.*, 2012, **50**, 3225-3258.

69. R. Barbey, L. Lavanant, D. Paripovic, N. Schuewer, C. Sugnaux, S. Tugulu and H.-A. Klok, *Chem. Rev.*, 2009, **109**, 5437-5527.
70. B. Zhao and W. J. Brittain, *Prog. Polym. Sci.*, 2000, **25**, 677-710.
71. J. Ruhe, M. Ballauff, M. Biesalski, P. Dziezok, F. Grohn, D. Johannsmann, N. Houbenov, N. Hugenberg, R. Konradi, S. Minko, M. Motornov, R. R. Netz, M. Schmidt, C. Seidel, M. Stamm, T. Stephan, D. Usov and H. N. Zhang, *Adv. Polym. Sci*, 2004, **165**, 79-150.
72. S. Edmondson, V. L. Osborne and W. T. S. Huck, *Chem. Soc. Rev.*, 2004, **33**, 14-22.
73. F. Zhou and W. T. S. Huck, *Phys. Chem. Chem. Phys.*, 2006, **8**, 3815-3823.
74. K. Y. Tan, J. E. Gautrot and W. T. S. Huck, *Soft Matter*, 2011, **7**, 7013-7020.
75. F. Liu, C.-H. Du, B.-K. Zhu and Y.-Y. Xu, *Polymer*, 2007, **48**, 2910-2918.
76. Y.-F. Yang, Y. Li, Q.-L. Li, L.-S. Wan and Z.-K. Xu, *J. Membr. Sci.*, 2010, **362**, 255-264.
77. R. Oren, Z. Liang, J. S. Barnard, S. C. Warren, U. Wiesner and W. T. S. Huck, *J. Am. Chem. Soc.*, 2009, **131**, 1670-1671.
78. M. J. Rodriguez Presa, L. M. Gassa, O. Azzaroni and C. A. Gervasi, *Anal. Chem.*, 2009, **81**, 7936-7943.
79. H.-S. Lee and L. S. Penn, *Langmuir*, 2009, **25**, 7983-7989.
80. S. Gupta, M. Agrawal, P. Uhlmann, F. Simon, U. Oertel and M. Stamm, *Macromolecules*, 2008, **41**, 8152-8158.
81. H. Murata, O. Prucker and J. Ruehe, *Macromolecules*, 2007, **40**, 5497-5503.
82. H. Kitano, Y. Takahashi, K. Mizukami and K. Matsuura, *Colloids Surf. B*, 2009, **70**, 91-97.
83. Y. Anraku, Y. Takahashi, H. Kitano and M. Hakari, *Colloids Surf. B*, 2007, **57**, 61-68.
84. J. E. Gautrot, W. T. S. Huck, M. Welch and M. Ramstedt, *ACS Appl. Mater. Interfaces*, 2010, **2**, 193-202.
85. T. Kawai, K. Saito and W. Lee, *J. Chromatogr. B Analyt. Technol. Biomed. Life Sci.*, 2003, **790**, 131-142.
86. J. E. Raynor, J. R. Capadona, D. M. Collard, T. A. Petrie and A. J. Garcia, *Biointerphases*, 2009, **4**, 3-16.
87. S. Tugulu, P. Silacci, N. Stergiopulos and H.-A. Klok, *Biomaterials*, 2007, **28**, 2536-2546.
88. C. D. H. Alarcon, T. Farhan, V. L. Osborne, W. T. S. Huck and C. Alexander, *J. Mater. Chem.*, 2005, **15**, 2089-2094.
89. H. W. Ma, J. H. Hyun, P. Stiller and A. Chilkoti, *Adv. Mater.*, 2004, **16**.
90. K. Matyjaszewski, *Macromolecules*, 2012, **45**, 4015-4039.
91. D. J. Siegwart, J. K. Oh and K. Matyjaszewski, *Prog. Polym. Sci.*, 2012, **37**, 18-37.
92. G. Moad, E. Rizzardo and S. H. Thang, *Polymer*, 2008, **49**, 1079-1131.
93. A. B. Lowe and C. L. McCormick, *Prog. Polym. Sci.*, 2007, **32**, 283-351.
94. S. Perrier and P. Takolpuckdee, *J. Polym. Sci. A Polym. Chem.*, 2005, **43**, 5347-5393.
95. V. Sciannamea, R. Jerome and C. Detrembleur, *Chem. Rev.*, 2008, **108**, 1104-1126.
96. R. B. Grubbs, *Polym. Rev.*, 2011, **51**, 104-137.
97. T. Otsu, *J. Polym. Sci. A Polym. Chem.*, 2000, **38**, 2121-2136.

98. B. Zhao and L. Zhu, *Macromolecules*, 2009, **42**, 9369-9383.
99. T. Chen, R. Ferris, J. Zhang, R. Ducker and S. Zauscher, *Prog. Polym. Sci.*, 2010, **35**, 94-112.
100. S. Peng and B. Bhushan, *RSC Adv.*, 2012, **2**, 8557-8578.
101. M. Krishnamoorthy, S. Hakobyan, M. Ramstedt and J. E. Gautrot, *Chem. Rev.*, 2014, **114**, 10976-11026.
102. A. L. Becker, K. Henzler, N. Welsch, M. Ballauff and O. Borisov, *Curr. Opin. Colloid Interface Sci.*, 2012, **17**, 90-96.
103. S. Sakata, Y. Inoue and K. Ishihara, *Langmuir*, 2014, **30**, 2745-2751.
104. A. Halperin, G. Fragneto, A. Schollier and M. Sferrazza, *Langmuir*, 2007, **23**, 10603-10617.
105. H. W. Ma, D. J. Li, X. Sheng, B. Zhao and A. Chilkoti, *Langmuir*, 2006, **22**, 3751-3756.
106. J. E. Gautrot, B. Trappmann, F. Oceguera-Yanez, J. Connelly, X. He, F. M. Watt and W. T. S. Huck, *Biomaterials*, 2010, **31**, 5030-5041.
107. K. L. Christman, V. Vazquez-Dorbatt, E. Schopf, C. M. Kolodziej, R. C. Li, R. M. Broyer, Y. Chen and H. D. Maynard, *J. Am. Chem. Soc.*, 2008, **130**, 16585-16591.
108. A. Hucknall, D.-H. Kim, S. Rangarajan, R. T. Hill, W. M. Reichert and A. Chilkoti, *Adv. Mater.*, 2009, **21**, 1968-1971.
109. J. Trmcic-Cvitas, E. Hasan, M. Ramstedt, X. Li, M. A. Cooper, C. Abell, W. T. S. Huck and J. E. Gautrot, *Biomacromolecules*, 2009, **10**, 2885-2894.
110. S. Diamanti, S. Arifuzzaman, A. Elsen, J. Genzer and R. A. Vaia, *Polymer*, 2008, **49**, 3770-3779.
111. J. E. Raynor, T. A. Petrie, A. J. Garcia and D. M. Collard, *Adv. Mater.*, 2007, **19**, 1724-1728.
112. N. Schuewer, T. Geue, J. P. Hinestrosa and H.-A. Klok, *Macromolecules*, 2011, **44**, 6868-6874.
113. K. Glinel, A. M. Jonas, T. Jouenne, J. Leprince, L. Galas and W. T. S. Huck, *Bioconjugate Chem.*, 2009, **20**, 71-77.
114. S. Yuan, D. Wan, B. Liang, S. O. Pehkonen, Y. P. Ting, K. G. Neoh and E. T. Kang, *Langmuir*, 2011, **27**, 2761-2774.
115. F. J. Xu, L. Y. Liu, W. T. Yang, E. T. Kang and K. G. Neoh, *Biomacromolecules*, 2009, **10**, 1665-1674.
116. M. E. Smithmyer, L. A. Sawicki and A. M. Kloxin, *Biomater. Sci.*, 2014, **2**, 634-650.
117. N. Singh, X. Cui, T. Boland and S. M. Husson, *Biomaterials*, 2007, **28**, 763-771.
118. F. He, B. Luo, S. Yuan, B. Liang, C. Choong and S. O. Pehkonen, *RSC Adv.*, 2014, **4**, 105-117.
119. P. Koegler, P. Pasic, J. Gardiner, V. Glattauer, P. Kingshott and H. Thissen, *Biomacromolecules*, 2014, **15**, 2265-2273.
120. S. E. Ochsenhirt, E. Kokkoli, J. B. McCarthy and M. Tirrell, *Biomaterials*, 2006, **27**, 3863-3874.
121. J.-H. Seo, S. Kakinoki, Y. Inoue, T. Yamaoka, K. Ishihara and N. Yui, *J. Am. Chem. Soc.*, 2013, **135**, 5513-5516.
122. J. E. Raynor, T. A. Petrie, K. P. Fears, R. A. Latour, A. J. Garcia and D. M. Collard, *Biomacromolecules*, 2009, **10**, 748-755.
123. Y. Wei, Y. Ji, L. Xiao, Q. Lin and J. Ji, *Colloids Surf. B*, 2011, **84**, 369-378.

124. M. Thery, *J. Cell Sci.*, 2010, **123**, 4201-4213.
125. W. K. Cho, B. Kong, H. J. Park, J. Kim, W. Chegal, J. S. Choi and I. S. Choi, *Biomaterials*, 2010, **31**, 9565-9574.
126. E. N. Chiang, R. Dong, C. K. Ober and B. A. Baird, *Langmuir*, 2011, **27**, 7016-7023.
127. C. Li, A. Glidle, X. Yuan, Z. Hu, E. Pulleine, J. Cooper, W. Yang and H. Yin, *Biomacromolecules*, 2013, **14**, 1278-1286.
128. R. Iwata, P. Suk-In, V. P. Hoven, A. Takahara, K. Akiyoshi and Y. Iwasaki, *Biomacromolecules*, 2004, **5**, 2308-2314.
129. A. Steinbach, A. Tautzenberger, A. Ignatius, M. Pluntke, O. Marti and D. Volkmer, *J. Mater. Sci. Mater. Med.*, 2012, **23**, 573-579.
130. J. E. Gautrot, C. Wang, X. Liu, S. J. Goldie, B. Trappmann, W. T. S. Huck and F. M. Watt, *Biomaterials*, 2012, **33**, 5221-5229.
131. P. Jonkheijm, D. Weinrich, M. Koehn, H. Engelkamp, P. C. M. Christianen, J. Kuhlmann, J. C. Maan, D. Nuesse, H. Schroeder, R. Wacker, R. Breinbauer, C. M. Niemeyer and H. Waldmann, *Angew. Chem. Int. Edit.*, 2008, **47**, 4421-4424.
132. K. Y. Tan, M. Ramstedt, B. Colak, W. T. S. Huck and J. E. Gautrot, *Polym. Chem.*, 2016, **7**, 979-990.
133. A. E. Rydholm, N. L. Held, D. S. W. Benoit, C. N. Bowman and K. S. Anseth, *J. Biomed. Mater. Res. A*, 2008, **86A**, 23-30.
134. R. J. Wade and J. A. Burdick, *Mater. Today*, 2012, **15**, 454-459.
135. R. A. Marklein and J. A. Burdick, *Adv. Mater.*, 2010, **22**, 175-189.
136. S. R. Caliari and J. Burdick, *Nat. Methods*, 2016, **13**, 405-414.
137. T. R. Dargaville, B. G. Hollier, A. Shokoohmand and R. Hoogenboom, *Cell Adh. Migr.*, 2014, **8**, 88-93.
138. J. A. Burdick and G. D. Prestwich, *Adv. Mater.*, 2011, **23**, H41-H56.
139. M. Ehrbar, A. Sala, P. Lienemann, A. Ranga, K. Mosiewicz, A. Bittermann, S. C. Rizzi, F. E. Weber and M. P. Lutolf, *Biophys. J.*, 2011, **100**, 284-293.
140. G. P. Raeber, M. P. Lutolf and J. A. Hubbell, *Biomech. Model. Mechanobiol.*, 2008, **7**, 215-225.
141. D. Loessner, K. S. Stok, M. P. Lutolf, D. W. Hutmacher, J. A. Clements and S. C. Rizzi, *Biomaterials*, 2010, **31**, 8494-8506.
142. K. Bott, Z. Upton, K. Schrobback, M. Ehrbar, J. A. Hubbell, M. P. Lutolf and S. C. Rizzi, *Biomaterials*, 2010, **31**, 8454-8464.
143. Z. Munoz, H. Shih and C.-C. Lin, *Biomater. Sci.*, 2014, **2**, 1063-1072.
144. Y. Hao, H. Shih, Z. Munoz, A. Kemp and C.-C. Lin, *Acta Biomaterialia*, 2014, **10**, 104-114.
145. H. Shih and C.-C. Lin, *Biomacromolecules*, 2012, **13**, 2003-2012.
146. K. Olofsson, M. Malkoch and A. Hult, *RSC Adv.*, 2014, **4**, 30118-30128.
147. H. Shih, A. K. Fraser and C.-C. Lin, *ACS Appl. Mater. Interfaces*, 2013, **5**, 1673-1680.
148. A. Fu, K. Gwon, M. Kim, G. Tae and J. A. Kornfield, *Biomacromolecules*, 2015, **16**, 497-506.
149. H. Shih, R. G. Mirmira and C.-C. Lin, *J. Mater. Chem. B*, 2015, **3**, 170-175.
150. J. Mergy, A. Fournier, E. Hachet and R. Auzely-Velty, *J. Polym. Sci. A Polym. Chem.*, 2012, **50**, 4019-4028.

151. T. R. Dargaville, R. Forster, B. L. Farrugia, K. Kempe, L. Voorhaar, U. S. Schubert and R. Hoogenboom, *Macromol. Rapid Comm.*, 2012, **33**, 1695-1700.
152. V. X. Truong, I. A. Barker, M. Tan, L. Mespouille, P. Dubois and A. P. Dove, *J. Mater. Chem. B*, 2013, **1**, 221-229.
153. T. Iskratsch, H. Wolfenson and M. P. Sheetz, *Nat. Rev. Mol. Cell Biol.*, 2014, **15**, 825-833.
154. S. T. Gould, N. J. Darling and K. S. Anseth, *Acta Biomater.*, 2012, **8**, 3201-3209.
155. T. Yang, M. Malkoch and A. Hult, *J. Polym. Sci. A Polym. Chem.*, 2013, **51**, 363-371.
156. K. A. Mosiewicz, L. Kolb, A. J. van der Vlies and M. P. Lutolf, *Biomaterials Science*, 2014, **2**, 1640-1651.
157. M. W. Tibbitt, A. M. Kloxin, L. A. Sawicki and K. S. Anseth, *Macromolecules*, 2013, **46**, 2785-2792.
158. S. Grube and W. Oppermann, *Macromolecules*, 2013, **46**, 1948-1955.
159. J. E. Frith, R. J. Mills, J. E. Hudson and J. J. Cooper-White, *Stem Cells Dev.*, 2012, **21**, 2442-2456.
160. J. A. Craig, E. L. Rexeisen, A. Mardilovich, K. Shroff and E. Kokkoli, *Langmuir*, 2008, **24**, 10282-10292.
161. H. Du, G. Zha, L. Gao, H. Wang, X. Li, Z. Shen and W. Zhu, *Polym. Chem.*, 2014, **5**, 4002-4008.
162. P. Lundberg, A. Bruin, J. W. Klijnstra, A. M. Nystrom, M. Johansson, M. Malkoch and A. Hult, *ACS Appl. Mater. Interfaces*, 2010, **2**, 903-912.
163. R. T. C. Cleophas, J. Sjollema, H. J. Busscher, J. A. W. Kruijtzer and R. M. J. Liskamp, *Biomacromolecules*, 2014, **15**, 3390-3395.
164. R. T. C. Cleophas, M. Riool, H. C. Q. van Ufford, S. A. J. Zaat, J. A. W. Kruijtzer and R. M. J. Liskamp, *ACS Macro Lett.*, 2014, **3**, 477-480.
165. N. Gupta, B. F. Lin, L. M. Campos, M. D. Dimitriou, S. T. Hikita, N. D. Treat, M. V. Tirrell, D. O. Clegg, E. J. Kramer and C. J. Hawker, *Nat. Chem.*, 2012, **4**, 138-145.
166. M. S. Rehmann, A. C. Garibian and A. M. Kloxin, *Macromol. Symp.*, 2013, **329**, 58-65.
167. P. M. Kharkar, K. L. Kiick and A. M. Kloxin, *Polym. Chem.*, 2015, **6**, 5565-5574.
168. K. S. Anseth, A. T. Metters, S. J. Bryant, P. J. Martens, J. H. Elisseeff and C. N. Bowman, *J. Control. Release*, 2002, **78**, 199-209.
169. C. S. Ki, H. Shih and C.-C. Lin, *Polymer*, 2013, **54**, 2115-2122.
170. D. R. Jones, R. E. Marchant, H. von Recum, A. Sen Gupta and K. Kottke-Marchant, *Acta Biomater.*, 2015, **13**, 52-60.
171. J. Patterson and J. A. Hubbell, *Biomaterials*, 2010, **31**, 7836-7845.
172. J. Patterson and J. A. Hubbell, *Biomaterials*, 2011, **32**, 1301-1310.
173. K. Chwalek, K. R. Levental, M. V. Tsurkan, A. Zieris, U. Freudenberg and C. Werner, *Biomaterials*, 2011, **32**, 9649-9657.
174. A. A. Aimetti, A. J. Machen and K. S. Anseth, *Biomaterials*, 2009, **30**, 6048-6054.
175. J. L. Holloway, H. Ma, R. Rai and J. A. Burdick, *J. Control Release*, 2014, **191**, 63-70.
176. Y. S. Jo, S. C. Rizzi, M. Ehrbar, F. E. Weber, J. A. Hubbel and M. P. Lutolf, *J. Biomed. Mater. Res. A*, 2010, **93A**, 870-877.

177. M. Ehrbar, S. C. Rizzi, R. G. Schoenmakers, B. San Miguel, J. A. Hubbell, F. E. Weber and M. P. Lutolf, *Biomacromolecules*, 2007, **8**, 3000-3007.
178. D. Missirlis and J. P. Spatz, *Biomacromolecules*, 2014, **15**, 195-205.
179. M. Goktas, G. Cinar, I. Orujalipoor, S. Ide, A. B. Tekinay and M. O. Guler, *Biomacromolecules*, 2015, **16**, 1247-1258.
180. A. Saez, M. Ghibaudo, A. Buguin, P. Silberzan and B. Ladoux, *Proc. Natl. Acad. Sci. USA*, 2007, **104**, 8281-8286.
181. E. Hadjipanayi, V. Mudera and R. A. Brown, *J. Tissue Eng. Regen. Med.*, 2009, **3**, 77-84.
182. A. Singh, J. Zhan, Z. Ye and J. H. Elisseeff, *Adv. Func. Mater.*, 2013, **23**, 575-582.
183. K. A. Mosiewicz, L. Kolb, A. J. van der Vlies, M. M. Martino, P. S. Lienemann, J. A. Hubbell, M. Ehrbar and M. P. Lutolf, *Nat. Mater.*, 2013, **12**, 1071-1077.
184. L. Beria, T. N. Gevrek, A. Erdog, R. Sanyal, D. Pasini and A. Sanyal, *Biomater. Sci.*, 2014, **2**, 67-75.
185. R. A. Marklein and J. A. Burdick, *Soft Matter*, 2010, **6**, 136-143.
186. C. A. DeForest, B. D. Polizzotti and K. S. Anseth, *Nat. Mater.*, 2009, **8**, 659-664.
187. C. A. DeForest and K. S. Anseth, *Angew. Chem. Int. Edit.*, 2012, **51**, 1816-1819.
188. M. P. Lutolf and J. A. Hubbell, *Nat. Biotechnol.*, 2005, **23**, 47-55.
189. L. A. Sawicki and A. M. Kloxin, *Biomater. Sci.*, 2014, **2**, 1612-1626.
190. J. J. Roberts and S. J. Bryant, *Biomaterials*, 2013, **34**, 9969-9979.
191. T. R. Dargaville, B. G. Hollier, A. Shokoohmand and R. Hoogenboom, *Cell Adh. Migr.*, 2014, **8**, 88-93.
192. A. J. Neumann, T. Quinn and S. J. Bryant, *Acta biomater.*, 2016, **39**, 1-11.
193. A. J. Engler, S. Sen, H. L. Sweeney and D. E. Discher, *Cell*, 2006, **126**, 677-689.
194. N. Huebsch, P. R. Arany, A. S. Mao, D. Shvartsman, O. A. Ali, S. A. Bencherif, J. Rivera-Feliciano and D. J. Mooney, *Nat. Mater.*, 2010, **9**, 518-526.
195. Y. Fu, K. Xu, X. Zheng, A. J. Giacomin, A. W. Mix and W. J. Kao, *Biomaterials*, 2012, **33**, 48-58.
196. S. Khetan and J. A. Burdick, *Biomaterials*, 2010, **31**, 8228-8234.
197. T. Y. Lin, C. S. Ki and C. C. Lin, *Biomaterials*, 2014, **35**, 6898-6906.
198. C. S. Ki, T.-Y. Lin, M. Korc and C.-C. Lin, *Biomaterials*, 2014, **35**, 9668-9677.
199. T. P. Kraehenbuehl, P. Zammaretti, A. J. Van der Vlies, R. G. Schoenmakers, M. P. Lutolf, M. E. Jaconi and J. A. Hubbell, *Biomaterials*, 2008, **29**, 2757-2766.
200. M. Uygun, M. A. Tasdelen and Y. Yagci, *Macromol. Chem. Phys.*, 2010, **211**.
201. K. Kempe, R. Hoogenboom and U. S. Schubert, *Macromol. Rapid Comm.*, 2011, **32**, 1484-1489.
202. H. Tang, L. Yin, H. Lu and J. Cheng, *Biomacromolecules*, 2012, **13**, 2609-2615.
203. M. A. Cortez and S. M. Grayson, *Macromolecules*, 2010, **43**, 4081-4090.

204. A. Raza, C. S. Ki and C.-C. Lin, *Biomaterials*, 2013, **34**, 5117-5127.
205. C. Wu, S. Wang, L. Bruelisauer, J.-C. Leroux and M. A. Gauthier, *Biomacromolecules*, 2013, **14**, 2383-2388.
206. C. Wu, C. Belenda, J.-C. Leroux and M. A. Gauthier, *Chem. Eur. J.*, 2011, **17**, 10064-10070.
207. B. Colak, J. C. S. Da Silva, T. A. Soares and J. E. Gautrot, *Bioconjugate Chem.*, 2016, **27**, 2111-2123.
208. M. Hartlieb, K. Kempe and U. S. Schubert, *J. Mater. Chem. B*, 2015, **3**, 526-538.
209. C. Weber, C. R. Becer, A. Baumgaertel, R. Hoogenboom and U. S. Schubert, *Des. Monomers Polym.*, 2009, **12**.
210. C. Weber, A. Krieg, R. M. Paulus, H. M. L. Lambermont-Thijs, C. R. Becer, R. Hoogenboom and U. S. Schubert, *Ionic Polymerization*, 2011, **308**, 17-24.
211. L. Tauhardt, M. Frant, D. Pretzel, M. Hartlieb, C. Buecher, G. Hildebrand, B. Schroeter, C. Weber, K. Kempe, M. Gottschaldt, K. Liefeith and U. S. Schubert, *J. Mater. Chem. B*, 2014, **2**, 4883-4893.
212. D. A. Brafman, C. W. Chang, A. Fernandez, K. Willert, S. Varghese and S. Chien, *Biomaterials*, 2010, **31**, 9135-9144.
213. B. Isaac Cerda-Cristerna, H. Flores, A. Pozos-Guillen, E. Perez, C. Sevrin and C. Grandfils, *J. Control. Release*, 2011, **153**, 269-277.
214. A. Mathew, H. Cao, E. Collin, W. Wang and A. Pandit, *Int. J. Pharm.*, 2012, **434**, 99-105.
215. X. Liu, H. Zhang, Z. Tian, A. Sen and H. R. Allcock, *Polym. Chem.*, 2012, **3**, 2082-2091.
216. A. E. Oezcam, K. E. Roskov, R. J. Spontak and J. Genzer, *J. Mater. Chem.*, 2012, **22**, 5855-5864.
217. L. Zhou, W. Yuan, J. Yuan and X. Hong, *Mater. Lett.*, 2008, **62**, 1372-1375.
218. Z. Dong, H. Wei, J. Mao, D. Wang, M. Yang, S. Bo and X. Ji, *Polymer*, 2012, **53**, 2074-2084.
219. F. Yu, X. Tang and M. Pei, *Microporous Mesoporous Mater.*, 2013, **173**, 64-69.
220. M. Schmitz, M. Kuhlmann, O. Reimann, C. P. R. Hackenberger and J. Groll, *Biomacromolecules*, 2015, **16**, 1088-1094.
221. J. Najbar and M. Mac, *J. Chem. Soc. Faraday Trans.*, 1991, **87**, 1523-1529.
222. A. A. Isse, C. Y. Lin, M. L. Coote and A. Gennaro, *J. Phys. Chem. B*, 2011, **115**, 678-684.
223. J. Brandrup and E. H. Immergut, *Polymer Handbook*, Wiley-Interscience, New York, 2nd ed. edn., 1975.
224. J. Brandrup, E. H. Immergut and E. A. Gulke, *Polymer Handbook*, Wiley-Interscience, New York, 4th e. edn., 1999, 1-2336.
225. P. Prediger, L. F. Barbosa, Y. Genisson and C. R. Duarte Correia, *J. Org. Chem.*, 2011, **76**, 7737-7749.
226. S. Kulchat and J.-M. Lehn, *Chem. Asian J.*, 2015, **10**, 2484-2496.
227. E. Hachet, N. Sereni, I. Pignot-Paintrand, V. Ravaine, A. Szarpak-Jankowska and R. Auzely-Velty, *J. Colloid Interface Sci.*, 2014, **419**, 52-55.
228. P. Lundberg, A. Bruin, J. W. Klijnstra, A. M. Nystrom, M. Johansson, M. Malkoch and A. Hult, *ACS Appl. Mater. Interfaces*, 2010, **2**, 903-912.

229. S. Allazetta, T. C. Hausherr and M. P. Lutolf, *Biomacromolecules*, 2013, **14**, 1122-1131.
230. B. Stuart, *Infrared Spectroscopy: Fundamentals and Applications*, Wiley, 2004.
231. M. L. Oyen, *Int. Mater. Rev.*, 2014, **59**, 44-59.
232. M. V. Turturro, M. C. Christenson, J. C. Larson, D. A. Young, E. M. Brey and G. Papavasiliou, *Plos One*, 2013, **8**, 1-14.
233. K. T. Morin and R. T. Tranquillo, *Exp. Cell Res.*, 2013, **319**, 2409-2417.
234. S. Lowe, N. M. O'Brien-Simpson and L. A. Connal, *Polym. Chem.*, 2015, **6**, 198-212.
235. M. S. Weiss, B. P. Bernabe, A. Shikanov, D. A. Bluver, M. D. Mui, S. Shin, L. J. Broadbelt and L. D. Shea, *Biomaterials*, 2012, **33**, 3548-3559.
236. R. Konradi, C. Acikgoz and M. Textor, *Macromol. Rapid Comm.*, 2012, **33**, 1663-1676.
237. P. Stephens, P. Grenard, P. Aeschilmann, M. Langley, E. Blain, R. Errington, D. Kipling, D. Thomas and D. Aeschlimann, *J. Cell Sci.*, 2004, **117**, 3389-3403.
238. A. A. Brown, N. S. Khan, L. Steinbock and W. T. S. Huck, *Eur. Polym. J.*, 2005, **41**, 1757-1765.
239. S. Tugulu and H.-A. Klok, *Biomacromolecules*, 2008, **9**, 906-912.
240. I. Sielaff, A. Arnold, G. Godin, S. Tugulu, H. A. Klok and K. Johnsson, *ChemBioChem*, 2006, **7**, 194-202.
241. E. Monchaux and P. Vermette, *Biomacromolecules*, 2007, **8**, 3668-3673.
242. S. P. Massia and J. A. Hubbell, *J. Biol. Chem.*, 1992, **267**, 14019-14026.
243. W. J. Seeto, Y. Tian and E. A. Lipke, *Acta Biomater.*, 2013, **9**, 8279-8289.
244. B. D. Plouffe, M. Radisic and S. K. Murthy, *Lab Chip*, 2008, **8**, 462-472.
245. J. Chen, T. Maeda, K. Sekiguchi and D. Sheppard, *Cell Adhesion Comm.*, 1996, **4**, 237-250.
246. M. Shirai and H. Okamura, *Polym. Int.*, 2016, **65**, 362-370.
247. A. del Campo and C. Greiner, *J. Micromech. Microeng.*, 2007, **17**, 81-95.
248. J. T. Connelly, A. Mishra, J. E. Gautrot and F. M. Watt, *Plos One*, 2011, **6**, 1-10.
249. J. T. Connelly, J. E. Gautrot, B. Trappmann, D. W.-M. Tan, G. Donati, W. T. S. Huck and F. M. Watt, *Nat. Cell Biol.*, 2010, **12**, 711-U177.
250. K. Y. Tan, H. Lin, M. Ramstedt, F. M. Watt, W. T. S. Huck and J. E. Gautrot, *Integr. Biol.*, 2013, **5**, 899-910.

Appendix 1

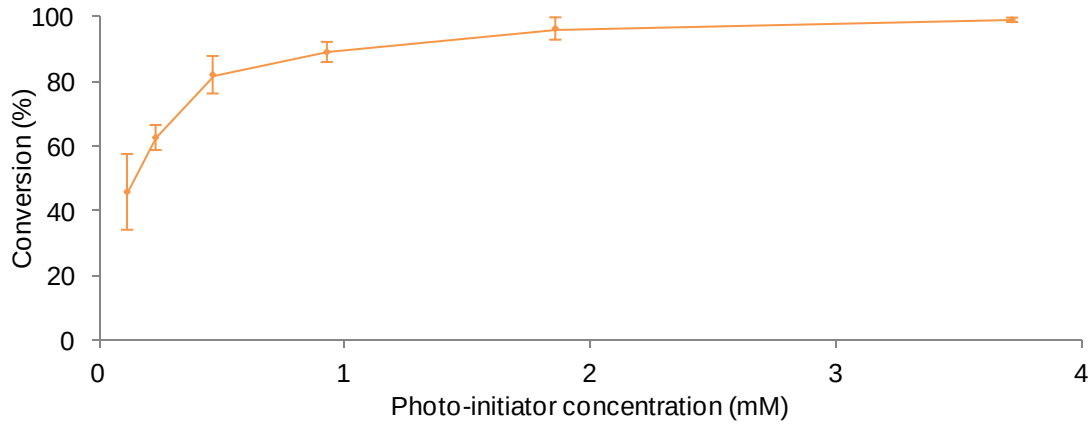

Figure A1.1 The impact of PI concentration on the thiol-ene extent of reaction between PEG methyl ether thiol S5 and alkene A1 (45 µmol/mL) with 60 s UV.

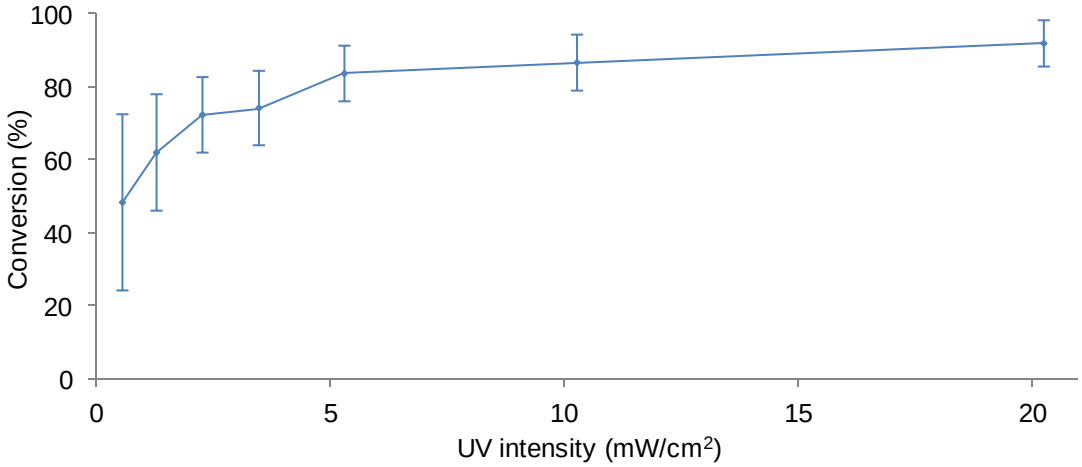

Figure A1.2 The impact of UV intensity on the thiol-ene extent of reaction between alkene A1 and thiols S1 (blue line) and S5 (orange line) (45 µmol/mL), using 2 mol% of PI with respect to the thiol with 60 s UV.

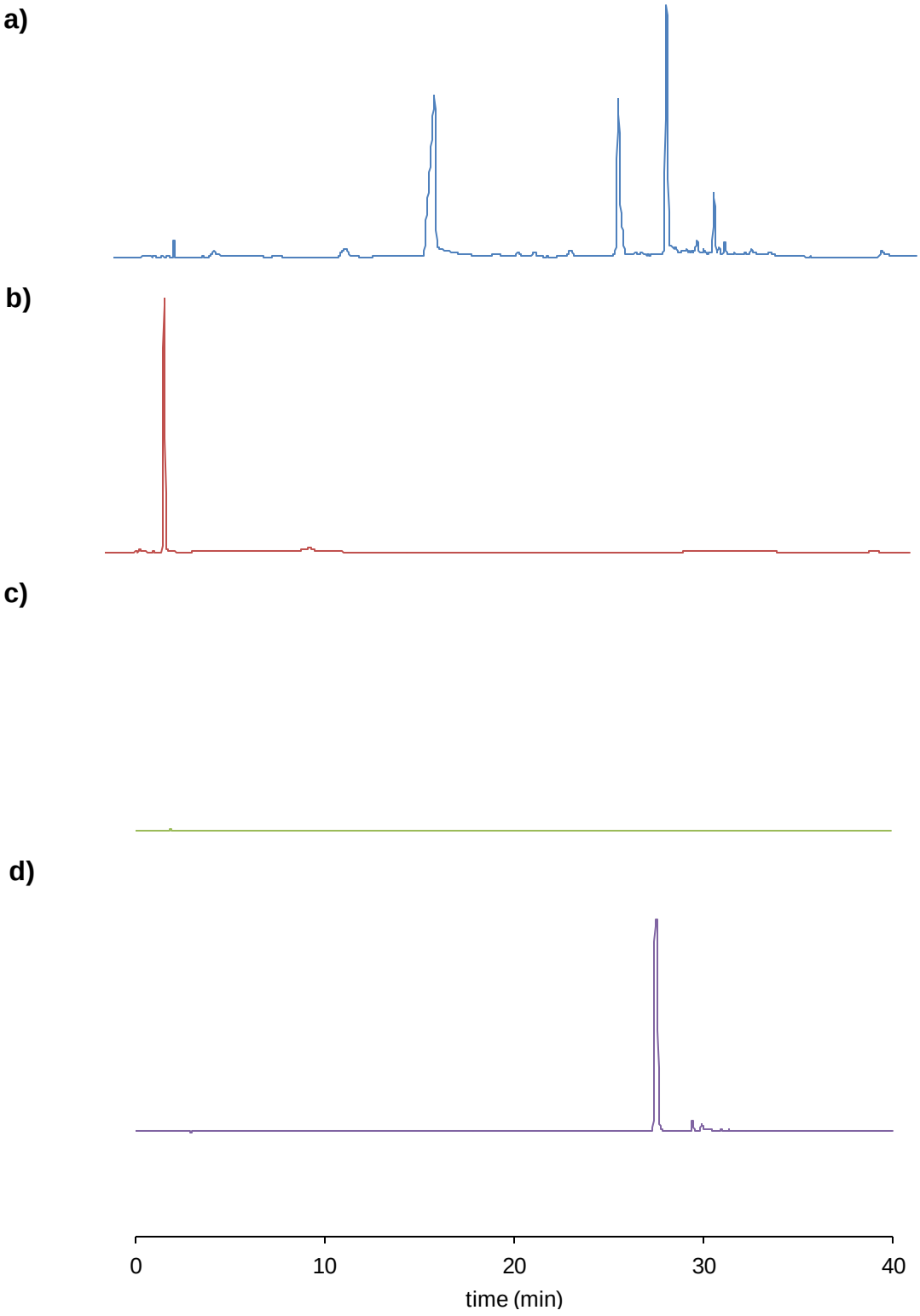

Figure A1.3 HPLC traces for a) thiol-ene coupling reaction (45 mM) between GCGSY and pentenoic acid (A1), b) unreacted peptide GCGSY, c) pentenoic acid and d) PI IRG2959.

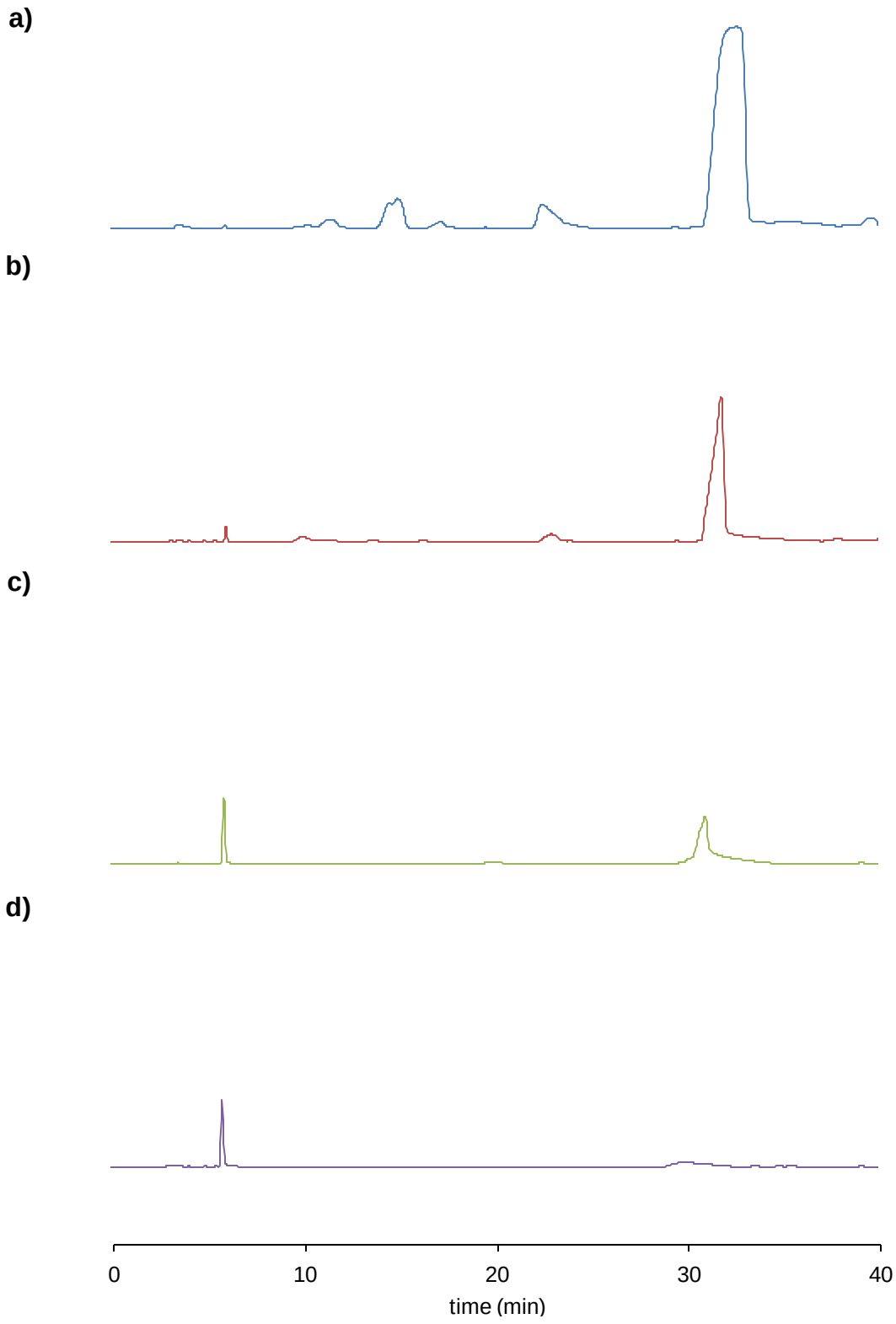

Figure A1.4 HPLC traces for the low concentration reaction with GCGSY and pentenoic acid (A1) from high to low concentration a) 45 mM, b) 9 mM, c) 4,5 mM and d) 1.8 mM. Reactions were performed with 5 mol% PI and 300 s UV exposure.

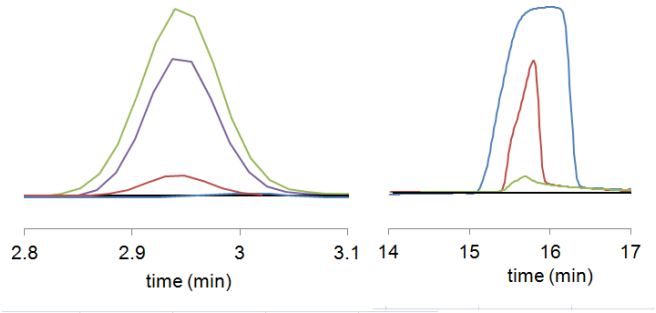

Figure A1.5 Normalised traces for unreacted peptide GCGSY (2.95 min)) and product peaks (15.9 min) for GCGSY and pentenoic acid (A1) at different reaction concentrations: 45 mM, 9 mM, 4,5 mM and 1.8 mM. Reactions were performed with 5 mol% PI and 300 s UV exposure.

Table A1.1 Summary of statistical data analysis obtained for the percentage conversion with S1 and A2-A9 (see Fig. 2.13). n.s., non significant; *, p < 0.05; **, p < 0.01: ***, p < 0.001.

		MeanDiff	Prob	
A3	**A2**	-43.53	0.0118	*
A4	**A2**	-68.43	0.000126	***
A4	**A3**	-24.90	0.300	n.s.
A5	**A2**	0.42	1.00	n.s.
A5	**A3**	43.95	0.0109	**
A5	**A4**	68.85	0.000117	***
A6	**A2**	12.53	0.916	n.s.
A6	**A3**	56.06	0.00114	**
A6	**A4**	80.96	0.0000161	***
A6	**A5**	12.11	0.928	n.s.
A7	**A2**	-68.19	0.000131	***
A7	**A3**	-24.66	0.310	n.s.
A7	**A4**	0.23	1.00	n.s.
A7	**A5**	-68.61	0.000122	***
A7	**A6**	-80.72	0.0000167	***
A8	**A2**	26.47	0.239	n.s.
A8	**A3**	70.00	0.0000966	***
A8	**A4**	94.90	0.0000019	***
A8	**A5**	26.05	0.254	n.s.
A8	**A6**	13.94	0.866	n.s.
A8	**A7**	94.66	0.0000020	***
A9	**A2**	26.80	0.227	n.s.
A9	**A3**	70.33	0.0000913	***
A9	**A4**	95.23	0.0000018	***

A9	**A5**	26.38	0.242	n.s.
A9	**A6**	14.27	0.853	n.s.
A9	**A7**	95.00	0.0000019	***
A9	**A8**	0.33	1.00	n.s.

Table A1.2 Summary of statistical data analysis obtained for the percentage peptide product formation via ^{1}H NMR spectroscopy (see Fig. 2.16). n.s., non significant; *, p < 0.05; **, p < 0.01: ***, p < 0.001.

		MeanDiff	Prob	
GCGSF	**GCGSY**	28.17	0.0202	***
CRGSF	**GCGSY**	6.78	0.791	n.s.
CRGSF	**GCGSF**	-21.39	0.0738	n.s.
CDGSF	**GCGSY**	8.64	0.653	n.s.
CDGSF	**GCGSF**	-19.53	0.105	n.s.
CDGSF	**CRGSF**	1.86	0.993	n.s.

Table A1.3 Summary of statistical data analysis obtained for the percentage peptide product formation via HPLC (see Fig. 2.16). n.s., non significant; *, p < 0.05; **, p < 0.01: ***, p < 0.001.

	MeanDiff	Prob	
GCGSF GCGSY	26.38	0.262	n.s.
CGGSF GCGSY	-5.26	0.998	n.s.
CGGSF GCGSF	-31.65	0.123	n.s.
CRGSF GCGSY	-15.39	0.789	n.s.
CRGSF GCGSF	-41.78	0.0241	*
CRGSF CGGSF	-10.13	0.961	n.s.
CGRSF GCGSY	-15.62	0.778	n.s.
CGRSF GCGSF	-42.01	0.0232	*
CGRSF CGGSF	-10.36	0.957	n.s.
CGRSF CRGSF	-0.23	1.00	n.s.
CDGSF GCGSY	22.05	0.446	n.s.
CDGSF GCGSF	-4.33	0.999	n.s.
CDGSF CGGSF	27.32	0.231	n.s.
CDGSF CRGSF	37.45	0.0492	*
CDGSF CGRSF	37.68	0.0474	*
CGDSF GCGSY	1.36	1.00	n.s.
CGDSF GCGSF	-25.02	0.313	n.s.
CGDSF CGGSF	6.63	0.995	n.s.
CGDSF CRGSF	16.76	0.723	n.s.
CGDSF CGRSF	16.99	0.711	n.s.
CGDSF CDGSF	-20.69	0.515	n.s.

Table A1.4 Summary of statistical data analysis obtained for the percentage reaction conversion in the presence of amino acids and electrolytes (see Fig. 2.15). n.s., non significant; *, p < 0.05; **, p < 0.01: ***, p < 0.001.

	MeanDiff	Prob	
tyr 10 control	-5.45	1	n.s.
trp 10 control	-6.21	1	n.s.
trp 10 tyr 10	-0.76	1	n.s.
trp 100 control	-15.83	1	n.s.
trp 100 tyr 10	-10.38	1	n.s.
trp 100 trp 10	-9.62	1	n.s.
phe 10 control	-2.52	1	n.s.
phe 10 tyr 10	2.92	1	n.s.
phe 10 trp 10	3.68	1	n.s.
phe 10 trp 100	13.31	1	n.s.
phe 100 control	-6.75	1	n.s.
phe 100 tyr 10	-1.30	1	n.s.
phe 100 trp 10	-0.54	1	n.s.
phe 100 trp 100	9.08	1	n.s.
phe 100 phe 10	-4.22	1	n.s.
leu 10 control	-11.61	1	n.s.
leu 10 tyr 10	-6.16	1	n.s.
leu 10 trp 10	-5.40	1	n.s.
leu 10 trp 100	4.21	1	n.s.
leu 10 phe 10	-9.09	1	n.s.
leu 10 phe 100	-4.86	1	n.s.
leu 100 control	-11.02	1	n.s.
leu 100 tyr 10	-5.57	1	n.s.
leu 100 trp 10	-4.81	1	n.s.
leu 100 trp 100	4.80	1	n.s.
leu 100 phe 10	-8.50	1	n.s.
leu 100 phe 100	-4.27	1	n.s.
leu 100 leu 10	0.58	1	n.s.
his 10 control	-5.60	1	n.s.
his 10 tyr 10	-0.15	1	n.s.
his 10 trp 10	0.60	1	n.s.
his 10 trp 100	10.23	1	n.s.
his 10 phe 10	-3.08	1	n.s.
his 10 phe 100	1.14	1	n.s.

his 10 leu 10	6.01	1	n.s.
his 10 leu 100	5.42	1	n.s.
his 100 control	-14.34	1	n.s.
his 100 tyr 10	-8.89	1	n.s.
his 100 trp 10	-8.13	1	n.s.
his 100 trp 100	1.49	1	n.s.
his 100 phe 10	-11.81	1	n.s.
his 100 phe 100	-7.59	1	n.s.
his 100 leu 10	-2.72	1	n.s.
his 100 leu 100	-3.31	1	n.s.
his 100 his 10	-8.73	1	n.s.
lys 10 control	-16.45	0.997	n.s.
lys 10 tyr 10	-11.00	1	n.s.
lys 10 trp 10	-10.24	1	n.s.
lys 10 trp 100	-0.62	1	n.s.
lys 10 phe 10	-13.93	1	n.s.
lys 10 phe 100	-9.70	1	n.s.
lys 10 leu 10	-4.83	1	n.s.
lys 10 leu 100	-5.42	1	n.s.
lys 10 his 10	-10.85	1	n.s.
lys 10 his 100	-2.11	1	n.s.
lys 100 control	-19.39	0.976	n.s.
lys 100 tyr 10	-13.94	1	n.s.
lys 100 trp 10	-13.18	1	n.s.
lys 100 trp 100	-3.55	1	n.s.
lys 100 phe 10	-16.86	0.995	n.s.
lys 100 phe 100	-12.64	1	n.s.
lys 100 leu 10	-7.77	1	n.s.
lys 100 leu 100	-8.36	1	n.s.
lys 100 his 10	-13.78	1	n.s.
lys 100 his 100	-5.05	1	n.s.
lys 100 lys 10	-2.93	1	n.s.
arg 10 control	-8.15	1	n.s.
arg 10 tyr 10	-2.70	1	n.s.
arg 10 trp 10	-1.94	1	n.s.
arg 10 trp 100	7.67	1	n.s.
arg 10 phe 10	-5.63	1	n.s.

arg 10 phe 100	-1.40	1	n.s.
arg 10 leu 10	3.46	1	n.s.
arg 10 leu 100	2.87	1	n.s.
arg 10 his 10	-2.55	1	n.s.
arg 10 his 100	6.18	1	n.s.
arg 10 lys 10	8.29	1	n.s.
arg 10 lys 100	11.23	1	n.s.
arg 100 control	-14.70	1	n.s.
arg 100 tyr 10	-9.25	1	n.s.
arg 100 trp 10	-8.49	1	n.s.
arg 100 trp 100	1.12	1	n.s.
arg 100 phe 10	-12.18	1	n.s.
arg 100 phe 100	-7.95	1	n.s.
arg 100 leu 10	-3.09	1	n.s.
arg 100 leu 100	-3.68	1	n.s.
arg 100 his 10	-9.10	1	n.s.
arg 100 his 100	-0.36	1	n.s.
arg 100 lys 10	1.74	1	n.s.
arg 100 lys 100	4.68	1	n.s.
arg 100 arg 10	-6.55	1	n.s.
asp 10 control	-9.91	1	n.s.
asp 10 tyr 10	-4.46	1	n.s.
asp 10 trp 10	-3.70	1	n.s.
asp 10 trp 100	5.91	1	n.s.
asp 10 phe 10	-7.39	1	n.s.
asp 10 phe 100	-3.16	1	n.s.
asp 10 leu 10	1.70	1	n.s.
asp 10 leu 100	1.11	1	n.s.
asp 10 his 10	-4.31	1	n.s.
asp 10 his 100	4.42	1	n.s.
asp 10 lys 10	6.54	1	n.s.
asp 10 lys 100	9.47	1	n.s.
asp 10 arg 10	-1.75	1	n.s.
asp 10 arg 100	4.79	1	n.s.
asp 100 control	-13.74	1	n.s.
asp 100 tyr 10	-8.29	1	n.s.
asp 100 trp 10	-7.53	1	n.s.

asp 100 trp 100	2.09	1	n.s.
asp 100 phe 10	-11.21	1	n.s.
asp 100 phe 100	-6.99	1	n.s.
asp 100 leu 10	-2.12	1	n.s.
asp 100 leu 100	-2.71	1	n.s.
asp 100 his 10	-8.13	1	n.s.
asp 100 his 100	0.59	1	n.s.
asp 100 lys 10	2.71	1	n.s.
asp 100 lys 100	5.65	1	n.s.
asp 100 arg 10	-5.58	1	n.s.
asp 100 arg 100	0.96	1	n.s.
asp 100 asp 10	-3.82	1	n.s.
pro 10 control	-2.08	1	n.s.
pro 10 tyr 10	3.36	1	n.s.
pro 10 trp 10	4.12	1	n.s.
pro 10 trp 100	13.74	1	n.s.
pro 10 phe 10	0.43	1	n.s.
pro 10 phe 100	4.66	1	n.s.
pro 10 leu 10	9.53	1	n.s.
pro 10 leu 100	8.94	1	n.s.
pro 10 his 10	3.51	1	n.s.
pro 10 his 100	12.25	1	n.s.
pro 10 lys 10	14.37	1	n.s.
pro 10 lys 100	17.30	0.993	n.s.
pro 10 arg 10	6.07	1	n.s.
pro 10 arg 100	12.62	1	n.s.
pro 10 asp 10	7.83	1	n.s.
pro 10 asp 100	11.65	1	n.s.
pro 100 control	-2.96	1	n.s.
pro 100 tyr 10	2.48	1	n.s.
pro 100 trp 10	3.24	1	n.s.
pro 100 trp 100	12.87	1	n.s.
pro 100 phe 10	-0.43	1	n.s.
pro 100 phe 100	3.78	1	n.s.
pro 100 leu 10	8.65	1	n.s.
pro 100 leu 100	8.06	1	n.s.
pro 100 his 10	2.64	1	n.s.

pro 100 his 100	11.37	1	n.s.
pro 100 lys 10	13.49	1	n.s.
pro 100 lys 100	16.43	0.997	n.s.
pro 100 arg 10	5.19	1	n.s.
pro 100 arg 100	11.74	1	n.s.
pro 100 asp 10	6.95	1	n.s.
pro 100 asp 100	10.77	1	n.s.
pro 100 pro 10	-0.87	1	n.s.
gly 10 control	-2.00	1	n.s.
gly 10 tyr 10	3.44	1	n.s.
gly 10 trp 10	4.20	1	n.s.
gly 10 trp 100	13.83	1	n.s.
gly 10 phe 10	0.52	1	n.s.
gly 10 phe 100	4.74	1	n.s.
gly 10 leu 10	9.61	1	n.s.
gly 10 leu 100	9.02	1	n.s.
gly 10 his 10	3.60	1	n.s.
gly 10 his 100	12.33	1	n.s.
gly 10 lys 10	14.45	1	n.s.
gly 10 lys 100	17.39	0.993	n.s.
gly 10 arg 10	6.15	1	n.s.
gly 10 arg 100	12.70	1	n.s.
gly 10 asp 10	7.91	1	n.s.
gly 10 asp 100	11.74	1	n.s.
gly 10 pro 10	0.083	1	n.s.
gly 10 pro 100	0.96	1	n.s.
gly 100 control	-8.82	1	n.s.
gly 100 tyr 10	-3.37	1	n.s.
gly 100 trp 10	-2.61	1	n.s.
gly 100 trp 100	7.00	1	n.s.
gly 100 phe 10	-6.30	1	n.s.
gly 100 phe 100	-2.07	1	n.s.
gly 100 leu 10	2.79	1	n.s.
gly 100 leu 100	2.20	1	n.s.
gly 100 his 10	-3.23	1	n.s.
gly 100 his 100	5.51	1	n.s.
gly 100 lys 10	7.62	1	n.s.

gly 100 lys 100	10.56	1	n.s.
gly 100 arg 10	-0.67	1	n.s.
gly 100 arg 100	5.88	1	n.s.
gly 100 asp 10	1.08	1	n.s.
gly 100 asp 100	4.91	1	n.s.
gly 100 pro 10	-6.74	1	n.s.
gly 100 pro 100	-5.86	1	n.s.
gly 100 gly 10	-6.82	1	n.s.
glu 10 control	-11.28	1	n.s.
glu 10 tyr 10	-5.83	1	n.s.
glu 10 trp 10	-5.07	1	n.s.
glu 10 trp 100	4.55	1	n.s.
glu 10 phe 10	-8.75	1	n.s.
glu 10 phe 100	-4.53	1	n.s.
glu 10 leu 10	0.33	1	n.s.
glu 10 leu 100	-0.25	1	n.s.
glu 10 his 10	-5.67	1	n.s.
glu 10 his 100	3.05	1	n.s.
glu 10 lys 10	5.17	1	n.s.
glu 10 lys 100	8.11	1	n.s.
glu 10 arg 10	-3.12	1	n.s.
glu 10 arg 100	3.42	1	n.s.
glu 10 asp 10	-1.36	1	n.s.
glu 10 asp 100	2.45	1	n.s.
glu 10 pro 10	-9.19	1	n.s.
glu 10 pro 100	-8.31	1	n.s.
glu 10 gly 10	-9.28	1	n.s.
glu 10 gly 100	-2.45	1	n.s.
glu 100 control	-12.83	1	n.s.
glu 100 tyr 10	-7.37	1	n.s.
glu 100 trp 10	-6.61	1	n.s.
glu 100 trp 100	3.00	1	n.s.
glu 100 phe 10	-10.30	1	n.s.
glu 100 phe 100	-6.07	1	n.s.
glu 100 leu 10	-1.20	1	n.s.
glu 100 leu 100	-1.79	1	n.s.
glu 100 his 10	-7.22	1	n.s.

glu 100 his 100	1.51	1	n.s.
glu 100 lys 10	3.63	1	n.s.
glu 100 lys 100	6.56	1	n.s.
glu 100 arg 10	-4.66	1	n.s.
glu 100 arg 100	1.88	1	n.s.
glu 100 asp 10	-2.90	1	n.s.
glu 100 asp 100	0.91	1	n.s.
glu 100 pro 10	-10.73	1	n.s.
glu 100 pro 100	-9.86	1	n.s.
glu 100 gly 10	-10.82	1	n.s.
glu 100 gly 100	-3.99	1	n.s.
glu 100 glu 10	-1.54	1	n.s.
ser 10 control	-13.49	1	n.s.
ser 10 tyr 10	-8.04	1	n.s.
ser 10 trp 10	-7.28	1	n.s.
ser 10 trp 100	2.34	1	n.s.
ser 10 phe 10	-10.96	1	n.s.
ser 10 phe 100	-6.74	1	n.s.
ser 10 leu 10	-1.87	1	n.s.
ser 10 leu 100	-2.46	1	n.s.
ser 10 his 10	-7.88	1	n.s.
ser 10 his 100	0.84	1	n.s.
ser 10 lys 10	2.96	1	n.s.
ser 10 lys 100	5.90	1	n.s.
ser 10 arg 10	-5.33	1	n.s.
ser 10 arg 100	1.21	1	n.s.
ser 10 asp 10	-3.57	1	n.s.
ser 10 asp 100	0.25	1	n.s.
ser 10 pro 10	-11.40	1	n.s.
ser 10 pro 100	-10.52	1	n.s.
ser 10 gly 10	-11.48	1	n.s.
ser 10 gly 100	-4.66	1	n.s.
ser 10 glu 10	-2.20	1	n.s.
ser 10 glu 100	-0.66	1	n.s.
ser 100 control	-7.77	1	n.s.
ser 100 tyr 10	-2.32	1	n.s.
ser 100 trp 10	-1.56	1	n.s.

ser 100 trp 100	8.06	1	n.s.
ser 100 phe 10	-5.24	1	n.s.
ser 100 phe 100	-1.02	1	n.s.
ser 100 leu 10	3.84	1	n.s.
ser 100 leu 100	3.25	1	n.s.
ser 100 his 10	-2.16	1	n.s.
ser 100 his 100	6.56	1	n.s.
ser 100 lys 10	8.68	1	n.s.
ser 100 lys 100	11.62	1	n.s.
ser 100 arg 10	0.38	1	n.s.
ser 100 arg 100	6.93	1	n.s.
ser 100 asp 10	2.14	1	n.s.
ser 100 asp 100	5.97	1	n.s.
ser 100 pro 10	-5.68	1	n.s.
ser 100 pro 100	-4.80	1	n.s.
ser 100 gly 10	-5.77	1	n.s.
ser 100 gly 100	1.05	1	n.s.
ser 100 glu 10	3.51	1	n.s.
ser 100 glu 100	5.05	1	n.s.
ser 100 ser 10	5.71	1	n.s.
KBr 100 control	-8.50	1	n.s.
KBr 100 tyr 10	-3.05	1	n.s.
KBr 100 trp 10	-2.29	1	n.s.
KBr 100 trp 100	7.33	1	n.s.
KBr 100 phe 10	-5.97	1	n.s.
KBr 100 phe 100	-1.75	1	n.s.
KBr 100 leu 10	3.11	1	n.s.
KBr 100 leu 100	2.52	1	n.s.
KBr 100 his 10	-2.89	1	n.s.
KBr 100 his 100	5.84	1	n.s.
KBr 100 lys 10	7.95	1	n.s.
KBr 100 lys 100	10.89	1	n.s.
KBr 100 arg 10	-0.34	1	n.s.
KBr 100 arg 100	6.20	1	n.s.
KBr 100 asp 10	1.41	1	n.s.
KBr 100 asp 100	5.24	1	n.s.
KBr 100 pro 10	-6.41	1	n.s.

KBr 100 pro 100	-5.53	1	n.s.
KBr 100 gly 10	-6.49	1	n.s.
KBr 100 gly 100	0.32	1	n.s.
KBr 100 glu 10	2.78	1	n.s.
KBr 100 glu 100	4.32	1	n.s.
KBr 100 ser 10	4.99	1	n.s.
KBr 100 ser 100	-0.72	1	n.s.
KI 10 control	-65.50	0.0000496	***
KI 10 tyr 10	-60.05	0.000294	***
KI 10 trp 10	-59.29	0.000375	***
KI 10 trp 100	-49.66	0.00713	**
KI 10 phe 10	-62.97	0.000114	***
KI 10 phe 100	-58.75	0.000446	***
KI 10 leu 10	-53.88	0.00204	**
KI 10 leu 100	-54.47	0.0017	**
KI 10 his 10	-59.89	0.000309	***
KI 10 his 100	-51.16	0.00461	**
KI 10 lys 10	-49.04	0.00853	**
KI 10 lys 100	-46.10	0.01934	*
KI 10 arg 10	-57.34	0.000697	***
KI 10 arg 100	-50.79	0.00514	**
KI 10 asp 10	-55.58	0.00121	**
KI 10 asp 100	-51.75	0.00387	**
KI 10 pro 10	-63.41	0.0000986	***
KI 10 pro 100	-62.53	0.000131	***
KI 10 gly 10	-63.49	0.0000959	***
KI 10 gly 100	-56.67	0.000860	***
KI 10 glu 10	-54.21	0.00184	**
KI 10 glu 100	-52.67	0.00294	**
KI 10 ser 10	-52.00	0.00359	**
KI 10 ser 100	-57.72	0.000617	***
KI 10 KBr 100	-57.00	0.000776	***
KI 100 control	-77.16	0.00000110	***
KI 100 tyr 10	-71.71	0.00000641	***
KI 100 trp 10	-70.95	0.00000821	***
KI 100 trp 100	-61.33	0.000194	***
KI 100 phe 10	-74.64	0.00000310	***

KI 100 phe 100	-70.41	0.00000980	***
KI 100 leu 10	-65.54	0.0000488	***
KI 100 leu 100	-66.13	0.0000402	***
KI 100 his 10	-71.56	0.00000673	***
KI 100 his 100	-62.82	0.000120	***
KI 100 lys 10	-60.71	0.000238	***
KI 100 lys 100	-57.77	0.000608	***
KI 100 arg 10	-69.01	0.0000154	***
KI 100 arg 100	-62.45	0.000135	***
KI 100 asp 10	-67.25	0.0000278	***
KI 100 asp 100	-63.42	0.0000983	***
KI 100 pro 10	-75.08	0.00000280	***
KI 100 pro 100	-74.20	0.00000346	***
KI 100 gly 10	-75.16	0.00000275	***
KI 100 gly 100	-68.33	0.0000193	***
KI 100 glu 10	-65.88	0.0000437	***
KI 100 glu 100	-64.34	0.0000727	***
KI 100 ser 10	-63.67	0.0000905	***
KI 100 ser 100	-69.39	0.0000136	***
KI 100 KBr 100	-68.66	0.0000173	***
KI 100 KI 10	-11.66	1	n.s.

Appendix 2

Table A2.1 Summary of statistical data analysis obtained for the percentage cell viability of HUVECs encapsulated in different stiffness gels (see Fig. 3.14). n.s., non significant; *, p < 0.05; **, p < 0.01: ***, p < 0.001.

		MeanDiff	Prob	
S3 0:100	**control**	-10.77	0.433	n.s.
S4 0:100	**control**	-9.84	0.503	n.s.
S4 0:100	**S3 0:100**	0.93	0.998	n.s.
S5 0:100	**control**	-4.88	0.885	n.s.
S5 0:100	**S3 0:100**	5.88	0.820	n.s.
S5 0:100	**S4 0:100**	4.95	0.881	n.s.

Table A2.2 Summary of statistical data analysis obtained for the percentage cell viability of dermal fibroblasts encapsulated in hydrogels (see Fig. 3.16). n.s., non significant; *, p < 0.05; **, p < 0.01: ***, p < 0.001.

		MeanDiff	Prob	
S3 100:0	**control**	-6.43	0.883	n.s.
S3 25:75	**control**	-41.55	0.0000331	***
S3 25:75	**S3 100:0**	-35.12	0.000209	**
S3 50:50	**control**	-12.46	0.300	*
S3 50:50	**S3 100:0**	-6.02	0.911	n.s.
S3 50:50	**S3 25:75**	29.09	0.00137	*
S3 75:25	**control**	-11.11	0.419	n.s.
S3 75:25	**S3 100:0**	-4.68	0.971	n.s.
S3 75:25	**S3 25:75**	30.44	0.000891	***
S3 75:25	**S3 50:50**	1.34	0.999	n.s.
S4 75:25	**control**	-10.50	0.480	*
S4 75:25	**S3 100:0**	-4.06	0.985	n.s.
S4 75:25	**S3 25:75**	31.05	0.000733	n.s.
S4 75:25	**S3 50:50**	1.95	0.999	n.s.
S4 75:25	**S3 75:25**	0.61	1	n.s.
S5 75:25	**control**	-8.77	0.665	**
S5 75:25	**S3 100:0**	-2.34	0.9998	n.s.
S5 75:25	**S3 25:75**	32.78	0.000427	n.s.
S5 75:25	**S3 50:50**	3.68	0.991	n.s.
S5 75:25	**S3 75:25**	2.34	0.999	n.s.
S5 75:25	**S4 75:25**	1.72	0.999	n.s.

Appendix 3

Table A3.1 Summary of statistical data analysis obtained for the percentage functionalisation with a series of thiols (see Fig. 4.7). n.s., non significant; *, p < 0.05; **, p < 0.01: ***, p < 0.001.

	MeanDiff	Prob	
S2 S1	-23.64	0.0160	*
S3 S1	-44.98	0.0000195	***
S3 S2	-21.34	0.0343	*
S4 S1	-49.58	0.00000551	***
S4 S2	-25.93	0.00746	**
S4 S3	-4.59	0.991	n.s.
S5 S1	-48.67	0.00000703	***
S5 S2	-25.03	0.0101	**
S5 S3	-3.69	0.997	n.s.
S5 S4	0.90	1	n.s.
S6 S1	-48.74	0.00000690	***
S6 S2	-25.10	0.00987	**
S6 S3	-3.76	0.997	n.s.
S6 S4	0.83	1	n.s.
S6 S5	-0.07	1	n.s.
S7 S1	-53.44	0.00000198	***
S7 S2	-29.79	0.00206	**
S7 S3	-8.45	0.821	n.s.
S7 S4	-3.86	0.996	n.s.
S7 S5	-4.76	0.989	n.s.
S7 S6	-4.69	0.990	n.s.
S8 S1	-50.79	0.00000398	***
S8 S2	-27.15	0.00496	**
S8 S3	-5.81	0.968	n.s.

S8 S4	-1.21	1	n.s.
S8 S5	-2.12	0.999	n.s.
S8 S6	-2.05	0.999	n.s.
S8 S7	2.64	0.999	n.s.

Table A3.2 Summary of statistical data analysis obtained for the number of cells on substrates (see Fig. 4.9). n.s., non significant; *, p < 0.05; **, p < 0.01: ***, p < 0.001.

	MeanDiff	Prob	
pOEGMA collagen	-44.50	0.00000839	***
pOEGMA-AA collagen	-33.75	0.000189	***
pOEGMA-AA pOEGMA	10.75	0.401	n.s.
S3 collagen	-39.48	0.0000338	***
S3 pOEGMA	5.021	0.950	n.s.
S3 pOEGMA-AA	-5.73	0.911	n.s.
S4 collagen	-33.49	0.000205	***
S4 pOEGMA	11.01	0.376	n.s.
S4 pOEGMA-AA	0.25	1	n.s.
S4 S3	5.99	0.893	n.s.
S5 collagen	7.77	0.730	n.s.
S5 pOEGMA	52.28	0.00000114	***
S5 pOEGMA-AA	41.52	0.0000190	***
S5 S3	47.25	0.00000407	***
S5 S4	41.26	0.0000204	***
S6 collagen	-42.91	0.0000129	***
S6 pOEGMA	1.59	0.999	n.s.
S6 pOEGMA-AA	-9.15	0.574	n.s.
S6 S3	-3.42	0.992	n.s.
S6 S4	-9.41	0.545	n.s.
S6 S5	-50.63	0.00000170	***

Table A3.3 Summary of statistical data analysis obtained for the cell area on substrates (see Fig. 4.10). n.s., non significant; *, p < 0.05; **, p < 0.01: ***, p < 0.001.

	MeanDiff	Prob	
pOEGMA collagen	-1875.99	0.180	n.s.
pOEGMA-AA collagen	-1609.28	0.316	n.s.
pOEGMA-AA pOEGMA	266.70	0.999	n.s.
S3 collagen	-1986.51	0.139	n.s.
S3 pOEGMA	-110.52	1	n.s.
S3 pOEGMA-AA	-377.22	0.997	n.s.
S4 collagen	-1370.41	0.486	n.s.
S4 pOEGMA	505.57	0.989	n.s.
S4 pOEGMA-AA	238.87	0.999	n.s.
S4 S3	616.10	0.971	n.s.
S5 collagen	1730.49	0.247	n.s.
S5 pOEGMA	3606.48	0.0023	**
S5 pOEGMA-AA	3339.77	0.00457	n.s.
S5 S3	3717.00	0.00176	n.s.
S5 S4	3100.90	0.00843	**
S6 collagen	-2082.02	0.111	n.s.
S6 pOEGMA	-206.03	0.999	n.s.
S6 pOEGMA-AA	-472.74	0.992	n.s.
S6 S3	-95.51	1	n.s.
S6 S4	-711.61	0.943	n.s.
S6 S5	-3812.52	0.00139	**